# N/Z EQUILIBRATION IN DEEP INELASTIC COLLISIONS AND THE FRAGMENTATION OF THE RESULTING QUASIPROJECTILES

A Dissertation

by

AUGUST LAWRENCE KEKSIS

Submitted to the Office of Graduate Studies of
Texas A&M University
in partial fulfillment of the requirements for the degree of

DOCTOR OF PHILOSOPHY

May 2007

Major Subject: Chemistry

# N/Z EQUILIBRATION IN DEEP INELASTIC COLLISIONS AND THE FRAGMENTATION OF THE RESULTING QUASIPROJECTILES

A Dissertation

by

AUGUST LAWRENCE KEKSIS

Submitted to the Office of Graduate Studies of
Texas A&M University
in partial fulfillment of the requirements for the degree of

DOCTOR OF PHILOSOPHY

Approved by:

| | |
|---|---|
| Chair of Committee, | Sherry J. Yennello |
| Committee Members, | Che-Ming Ko |
| | Rand L. Watson |
| | Joseph B. Natowitz |
| Head of Department, | David H. Russell |

May 2007

Major Subject: Chemistry

# ABSTRACT

N/Z Equilibration in Deep Inelastic Collisions and the Fragmentation of the Resulting Quasiprojectiles. (May 2007)

August Lawrence Keksis, B.S., Northern Arizona University

Chair of Advisory Committee: Dr. Sherry J. Yennello

When target and projectile nuclei have a difference in neutron to proton ratio (N/Z), the quasiprojectiles formed in a deep inelastic collision (DIC) should have a mean N/Z between the N/Z of the target and the N/Z of the projectile, depending on the amount of N/Z equilibration that occurred. Data from six reaction systems at two beam energies (32 and 45 MeV/nucleon) were collected. The systems in order of increasing difference between target and projectile N/Z (shown in parentheses) are $^{40}$Ar + $^{112}$Sn ($\Delta$N/Z = 0.018), $^{48}$Ca + $^{124}$Sn ($\Delta$N/Z = 0.080), $^{48}$Ca + $^{112}$Sn ($\Delta$N/Z = 0.160), $^{40}$Ca + $^{112}$Sn ($\Delta$N/Z = 0.240), $^{40}$Ar + $^{124}$Sn ($\Delta$N/Z = 0.258) and $^{40}$Ca + $^{124}$Sn ($\Delta$N/Z = 0.480).

The quasiprojectile N/Z was determined by two techniques. The first technique used the isotopically resolved fragments to reconstruct the quasiprojectile N/Z. The second technique, developed in this thesis, used fragment yield ratios and a simple equation to simultaneously fit all six systems to determine the quasiprojectile N/Z. Simulations and a filter of the FAUST (Forward Array Using Silicon Technology) acceptance were used to calculate neutron loss; this accounted for the difference between the two techniques.

To study the fragmentation of quasiprojectiles the fragment yields were used to calculate the isobaric, isotopic, fractional and mean N/Z yields. The results showed that as neutron richness increased, more neutron-rich fragments were produced. In

addition observation showed evidence for an inhomogeneous distribution of N/Z between the light charged particles (LCPs Z less than 3) and intermediate mass fragments (IMFs Z greater than 2).

The theoretical results, which used different values of the symmetry energy, were compared to experimental data to determine which symmetry energy best represents the experimental data. The comparison showed the experimental data was the overall best fit with a lower value of the symmetry energy. These results were not conclusive and further investigation is required.

To Andy, Mona and Monika Keksis

# ACKNOWLEDGMENTS

It was a pleasure working at the Cyclotron Institute at Texas A&M University with such a wonderful, friendly and helpful staff. First and foremost I want to thank my advisor, Dr. Sherry Yennello, for all her advice, support and brainstorming. In her group I was able to see all aspects of research from concept, setup, testing, acquisition, analysis, simulations, to conferences and publications, which is extremely important to prepare for your career after graduate school. I also want to thank all the SJY group members I have worked with through the years for their advice and support. I also want to thank my committee members Dr. Ko, Dr. Natowitz and Dr. Watson and my family and friends for all their encouragement and support. Last but not least I want to thank the Department of Energy (Grant DE-FG03-93ER40773) and the Robert A. Welch Foundation (Grant A-1266) for funding, which made this research possible.

TABLE OF CONTENTS

CHAPTER Page

CHAPTER Page

# LIST OF TABLES

TABLE Page

TABLE Page

# LIST OF FIGURES

FIGURE Page

FIGURE Page

FIGURE Page

FIGURE Page

FIGURE Page

FIGURE Page

FIGURE Page

FIGURE Page

FIGURE Page

FIGURE Page

FIGURE Page

FIGURE Page

FIGURE Page

FIGURE Page

FIGURE Page

FIGURE Page

# CHAPTER I

## INTRODUCTION

With many facilities upgrading to produce radioactive beams (and targets) and a rare isotope accelerator laboratory being planned by the community, the study of N/Z equilibration and the distribution of N/Z in the fragment yields are important areas of research. In the next section N/Z equilibration is discussed, followed by a section on distribution of N/Z in the fragment yields. Then a section describing the reaction mechanism being used, the deep inelastic collision, is given. The last section discusses the symmetry energy of the nuclear Equation-of-State (nEOS), which is studied through comparison of experimental results with theoretical results.

Chapter II discusses the experimental details, while chapter III discusses the calibrations, gating and analysis. The experimental results are discussed in chapter IV. Then chapter V reviews details about all the simulations used as well as the FAUST filter program. Chapter VI compares the experimental and theoretical results. Finally chapter VII states the conclusions from this thesis project. Appendix A has a complete step-by-step walk-through of quasiprojectile reconstruction. Appendices B through E contain additional experimental fractional yield plots, isotopic yield ratio plots, isobaric yield plots and mean N/Z versus Z plots, respectively.

### A. N/Z Equilibration

When target and projectile nuclei have different neutron to proton ratios (N/Z), the sources formed should have an N/Z between that of the N/Z of the target and the N/Z of the projectile depending on the amount of N/Z equilibration that occurred

---

The journal model is Physical Review C.

during the collision. If full N/Z equilibration occurred then the N/Z of the source should be identical to the N/Z of the composite system, which is given by equation 1.1 [1]. The composite system is a system having proton number equal to the number of protons in the target plus the number of protons in the projectile; and neutron number equal to the number of neutrons in the target plus the number of neutrons in the projectile.

$$(N/Z)_{CompositeSystem} = \frac{N_{Projectile} + N_{Target}}{Z_{Projectile} + Z_{Target}} \tag{1.1}$$

The N/Z equilibration, also referred to as N/Z relaxation, N/Z diffusion and N/Z mixing, is a way to study nuclear stopping, which is a measure of the conversion of kinetic energy into other degrees of freedom (i.e. N/Z, thermal, spin). The dynamics of the reaction provide the energy density and volume of the interaction region, called the participant zone, which determines the nuclear stopping. In turn this depends on the nucleon-nucleon cross sections and the nEOS.

The early work on N/Z equilibration showed its statistical nature using both N/Z diffusion and drift [2]. The diffusion is from the difference in the N/Z between the target and the projectile, while the drift is due to density gradients of the neutrons and the protons in the interaction zone [3]. Neutrons are preferentially transferred early on during the interaction, because protons must overcome the Coulomb barrier [4]. With increasing interaction time the energy dissipation provides the needed energy for protons to start exchanging.

The source being used must be well defined in order to get the N/Z value. If nucleons in the projectile and target could be individually tagged like they tag sharks, then the exact equilibration could be calculated by observing the composition of one of the sources, however protons and neutrons cannot be tagged. This means nucleons

coming from the target and those from the projectile cannot be discerned from one another. In order to find the amount of N/Z equilibration there are several methods that could be used. The first method is reconstruction of the source [5]. In this case all the fragments emitted from the source must be collected, which is difficult experimentally. The fragments are then added together in the center of mass frame to reconstruct the source. In this work the reconstruction based on collected charged particles was done, as described in detail in chapter III and appendix A.

Another method uses a multi-source fit of the fragment energy spectra, which on average attribute the nucleons to the target or the projectile [6]. Rapidity, which is the momentum distribution of the secondary fragments in the center of mass frame, can also be used to find the N/Z of the source. The N/Z versus rapidity plot shown in figure 1 shows the initial target and beam N/Z as ovals. For a bounce back reaction the rapidity distribution increases from the lower left to upper right, while for partial transparency the rapidity distribution decreases from the upper left to lower right. Complete equilibration results in a flat rapidity distribution shown by the horizontal line at intermediate N/Z. Average rapidity loss is the beam rapidity minus the average nucleon rapidity. The rapidity is defined by equation 1.2, where y is the rapidity, $p_L$ is the longitudinal momentum in beam direction, and E is the energy. Solving for y rearranges to form equation 1.3 [7].

$$tanh(y) = p_L/E \tag{1.2}$$

$$y = \frac{1}{2} ln \frac{E + P_L}{E - P_L} \tag{1.3}$$

If the final state nucleon rapidity distribution peaks at mid-rapidity, then there was complete stopping, which is a requirement for complete thermal equilibrium [8].

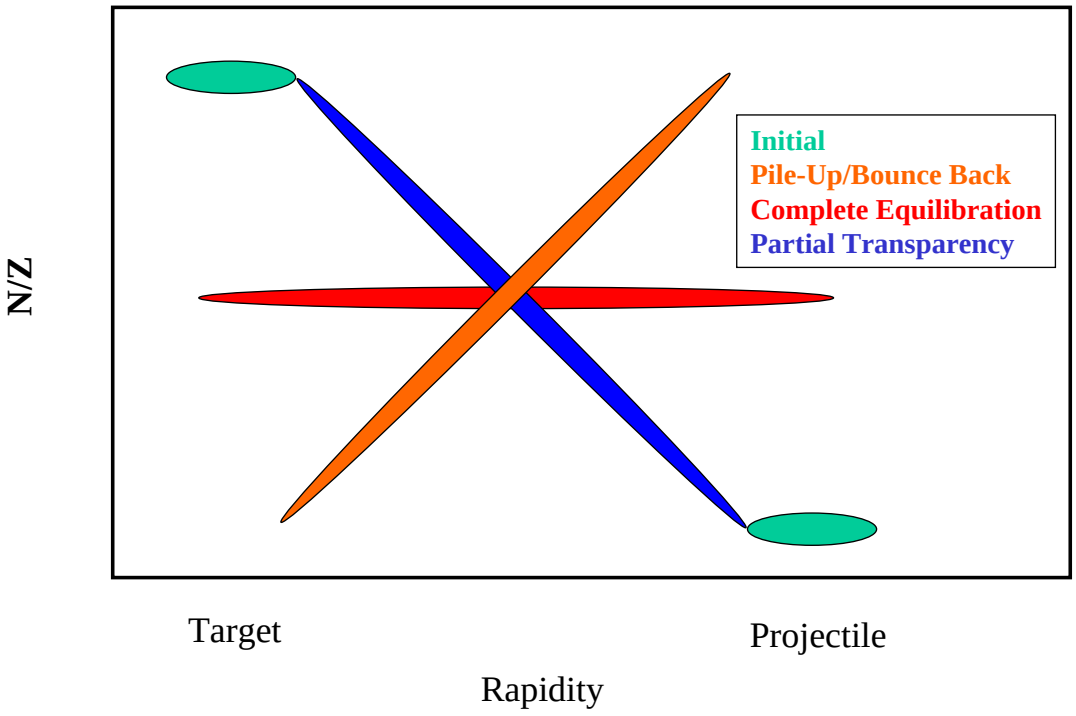


FIG. 1. (Color online) N/Z versus rapidity.

Some other methods include: looking at the energy deficit of the remaining baryons after the reaction, using the transverse energy distributions, using the quadrupole moments, and using isobaric yield ratios in symmetric systems [9, 10, 11, 12].

In this work the fragment yields are available and so the procedure of Bell was followed. The original method was the $R_z$ method, which measured the amount of mixing using symmetric systems and calculating the charge in a given area shown in equation 1.4. The equation uses the original symmetric systems of Rami *et al.*, which were Zr + Zr, Ru + Ru and the cross systems ($Z_{Source}$) [9]. If the cross systems had a $R_Z$ of +1, they would be like Zr + Zr. If the cross systems had a $R_Z$ of -1, they would be like Ru + Ru. If they were fully equilibrated in N/Z, then the $R_Z$ value would equal 0.

$$R_Z = \frac{2(Z_{Source}) - Z_{ZrZr} - Z_{RuRu}}{Z_{ZrZr} - Z_{RuRu}} \tag{1.4}$$

The N/Z tracer method was developed by Bell *et al.* from the $R_Z$ method to use the proton to triton (p/t) ratio. The formula used is given by equation 1.5 using their systems [11]. The $R_Z$ and N/Z tracer methods cannot be applied to non-symmetric systems, so a new method has been developed in this work and discussed further in chapter IV.

$$N/Z_{tracer} = \frac{2(p/t)_{Source} - (p/t)_{NiNi} - (p/t)_{FeFe}}{(p/t)_{NiNi} - (p/t)_{FeFe}} \tag{1.5}$$

Complete N/Z equilibration occurs below the Fermi energy, because the N/Z equilibration time is shorter than the momentum relaxation time [13]. With increasing energy full equilibration cannot be reached and the reactions have increased transparency. This is caused by dynamical instabilities that occur before the N/Z or thermal equilibrium was reached. The reason is that the projectile nucleons have

large incoming momenta, so the mean field potential cannot reverse the direction of motion of many nucleons in the short interaction time. Another factor comes into play at higher energies, where there comes a point when another degree of freedom is reached: particle production (i.e. pions at a threshold of 280 MeV) [14]. However, in the energy range in this work (32 and 45 MeV/nucleon) pion production can be neglected.

To find the percent equilibration one could use an equation such as equation 1.6, where the numerator is the absolute value of the difference between the N/Z of the source ($N_{Source}/Z_{Source}$) and the N/Z of the projectile ($N_{Projectile}/Z_{Projectile}$) (i.e. the amount of N/Z equilibration of the source relative to the projectile). The denominator is the absolute value of the difference between the N/Z of the compound system ($N_{Composite}/Z_{Composite}$) and the N/Z of the projectile (i.e. the amount of N/Z equilibration needed to be completely N/Z equilibrated). If the source did not undergo any equilibration, then the ($N_{Source}/Z_{Source}$) would be equal to the ($N_{Projectile}/Z_{Projectile}$) and the percent equilibration would be 0%. If the source was completely equilibrated, then ($N_{Source}/Z_{Source}$) would equal the ($N_{Composite}/Z_{Composite}$) and the percent equilibration would be 100%.

$$PercentEquilibration = \frac{|\frac{N_{Source}}{Z_{Source}} - \frac{N_{Projectile}}{Z_{Projectile}}|}{|\frac{N_{Composite}}{Z_{Composite}} - \frac{N_{Projectile}}{Z_{Projectile}}|}100\% \tag{1.6}$$

The simulation SMM/DIT, discussed in chapter V, was used to study the differences between the reconstruction and yield ratio methods. The simulations allow for direct tracking of the evolution of the systems. Then using the two methods on the simulated fragments the quasiprojectile N/Z can be calculated and compared with the theoretical quasiprojectile N/Z.

## B. Distribution of N/Z in the Fragment Yields

The N/Z distribution in the fragment yields can be used to look for an inhomogeneous distribution in N/Z between the light charged particles (LCPs, which have charge less than 3) and intermediate mass fragments (IMFs, which have charge greater than 2) [15]. If this occurs the asymmetry of the system goes into the LCPs, leaving more symmetric IMFs, which can be thought of as a liquid-gas phase transition, with the asymmetry given to the gas, leaving a more symmetric liquid.

There are several observables that can be used to study the inhomogeneous distribution of N/Z in the fragment yields. The first is the multiplicity of LCPs and IMFs. Previous studies have shown that with increased proton richness the LCP multiplicity increases dramatically, while the IMF multiplicity remains nearly constant [16]. It was suggested that with increasing neutron richness more neutron-rich light charged particles would be produced [16]. This work sets out to make these observations.

Another observable for inhomogeneous distribution of N/Z is the mean N/Z of the IMF divided by the mean N/Z of the LCP. Earlier studies showed there is an increase in this ratio with increasing proton richness and an asymptote developing around unity for neutron-rich sources [16]. The earlier studies accounted for this trend by the dependence of the mean N/Z of the LCPs with the N/Z of the source. In the current study the mean N/Z of the IMFs with the N/Z of the source was examined.

Finally the t/$^3$He mirror ratio has been used in the past to observe an enhancement of the neutron-rich nuclides with increasing neutron-richness of the source [16]. This study will see if this trend holds for other mirror-nuclei ratios: $^7$Li/$^7$Be, $^{11}$B/$^{11}$C and $^{15}$N/$^{15}$O.

## C. Deep Inelastic Collisions

The type of collision that occurs between a target and a projectile in a heavy-ion reaction is determined by impact parameter and energy. At the largest impact parameters at all energies the reactions are Coulomb, or Rutherford, scattering, elastic diffraction and inelastic Coulomb excitation. At peripheral impact parameter and low energies there are stripping and pickup reactions, with increasing energy projectile fragmentation occurs. Then in mid-peripheral impact parameters at low energy there are deep inelastic collisions, also called damped collisions, at higher energies there are neck formation, then at still higher energies there can be abrasion-ablation, also called participant-spectator reactions. Finally at near central impact parameters at low energy there are direct reactions and fusion, then with increasing energy there is incomplete fusion, also called massive transfer, at higher energies the multifragmentation regime is reached, then at higher energies spallation occurs, finally at the highest energies quark-gluon plasma could be formed. There are no specific cut offs between reaction mechanisms with energy or impact parameter, so the different mechanisms compete between one another.

Now the focus will be on the Fermi energy regime, where the reactions of this work are in. The excitation energy depends on the stopping and nucleon exchange between the projectile and target. Central collisions, where most of the beam energy is transferred into internal degrees of freedom, can create highly excited nuclear matter, however the fragmenting source size, density and N/Z are difficult to define. Also central collisions can undergo greater equilibration, and therefore reduce the amount of N/Z of the composite system, so this is not a preferred way to achieve production of rare nuclides [17]. With deep inelastic collisions there are well defined target-like and projectile-like sources with possible wider range in N/Z [18].

Figure 2 shows an example of a deep inelastic collisions. In the first frame there is a projectile and target. Then the two sources start interacting through the deep inelastic transfer of nucleons between the two sources. Once the two sources separate there is a quasiprojectile, or projectile-like source, and a quasitarget, or target-like source. The amount of N/Z equilibration that occurred can then be determined by measuring the N/Z of the quasiprojectile source and comparing with the N/Z of the target, the N/Z of the projectile, and the N/Z of the composite system. The composite system, as defined in equation 1.1, represents the N/Z of a fully equilibrated source.

Both the quasiprojectile and quasitarget are in excited states after the interaction and undergo fragmentation to dissipate the energy. The primary fragments formed, or the first set of fragments, may be excited themselves or be unstable, such as $^{8}$Be. These primary fragments then undergo secondary decay forming the final fragments, which are detected experimentally. The quasiprojectile fragments are traveling near beam velocity, so high threshold detectors can be used, effectively screening out quasitarget fragments. Also the quasiprojectile fragments are forward focused, so a high granularity forward array must be used. FAUST, the Forward Array Using Silicon Technology, used in this work is described further in chapter II.

When target and projectile nuclei have a wide distribution in N/Z, the quasiprojectiles formed should have an N/Z between that of the N/Z of the target and the N/Z of the projectile depending on the amount of N/Z equilibration that occurred. In this study of N/Z equilibration, six systems at two energies (32 and 45 MeV/nucleon) with differing N/Z between targets and projectiles were collected. The systems in order of increasing difference between target and projectile N/Z (shown in parentheses) are $^{40}$Ar on $^{112}$Sn (0.018), $^{48}$Ca on $^{124}$Sn (0.080), $^{48}$Ca on $^{112}$Sn (0.160), $^{40}$Ca on $^{112}$Sn (0.240), $^{40}$Ar on $^{124}$Sn (0.258), and $^{40}$Ca on $^{124}$Sn (0.480).

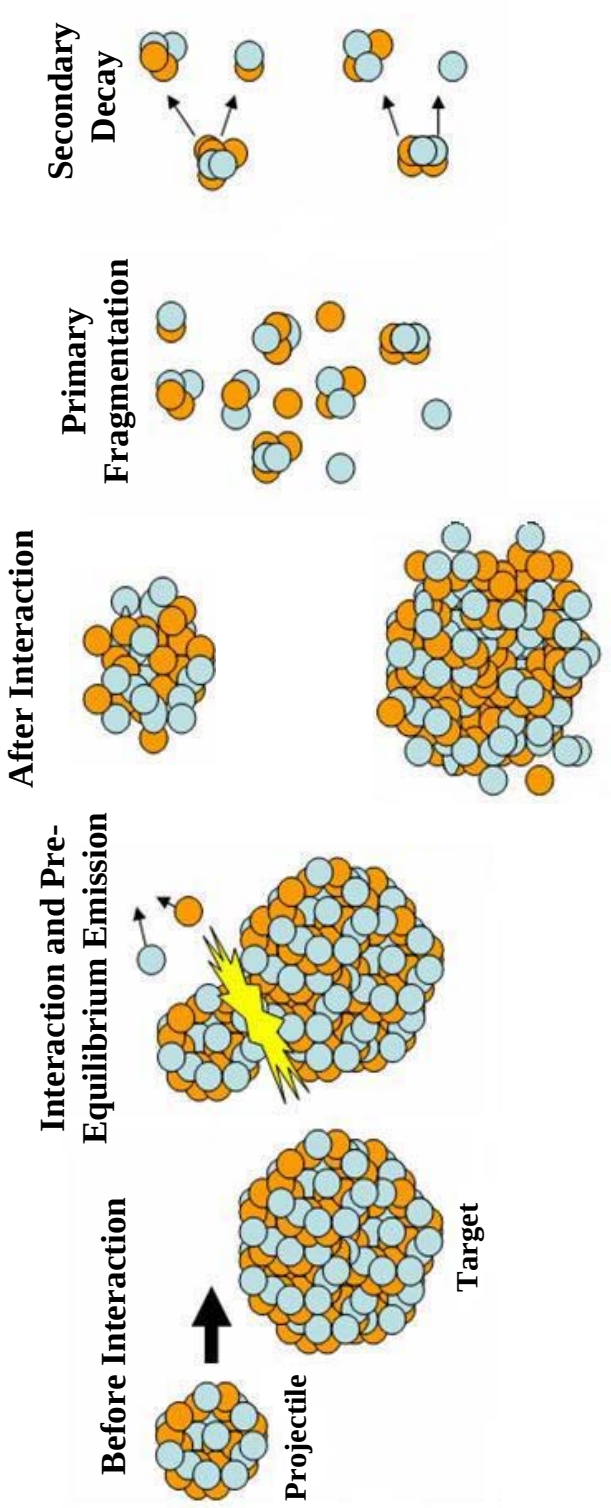


FIG. 2. (Color online) Cartoon of a deep inelastic collision of $^{40}$Ca on $^{124}$Sn.

D. Symmetry Energy

The symmetry energy is a parameter in the nEOS. An equation-of-state describes the relationship between measurable properties of a system. The nEOS shown in equation 1.7, relates the density ($\rho$), temperature (T), and asymmetry ($\delta$) with the binding energy [19]. The asymmetry is given by equation 1.8, where N is the neutron number and Z is the proton number. When Z is equal to 0 (for the case of pure neutron matter) $\delta = 1$, while if Z is equal to N (for the case of symmetric nuclear matter) $\delta = 0$, and if N is equal to 0 (for the case of pure proton matter) $\delta = -1$. There are two parts to the nEOS, the symmetric part and the asymmetric part, which both depend on the density and temperature.

$$BE_{AsymmetricMatter}(\rho, T, \delta) = BE_{SymmetricMatter}(\rho, T) + C_{sym}(\rho, T)\delta^2 \tag{1.7}$$

$$\delta = (N - Z)/(N + Z) \tag{1.8}$$

The binding energy is an inherent property of nuclei and to first order there is a linear dependence with mass number. To compare the binding energies of different nuclei, the binding energy is divided by the mass number to get the binding energy per nucleon (MeV/nucleon) shown in figure 3. The binding energy equation is shown in equation 1.9, where BE is the binding energy, Z is the number of protons, $m_H$ is the mass of hydrogen atom, N is the neutron number, $m_n$ is the mass of the neutron and $m_{Nuclide}$ is the mass of the nuclide. 931.5 is a constant to convert mass to energy and by using the isotopic mass of the nuclide and the hydrogen atomic mass account for the electrons.

$$BE = (Zm_H + Nm_n - m_{Nuclide})931.5 \tag{1.9}$$

Figure 3 shows the plot of binding energy per nucleon as a function of mass number for the most bound nuclide at each mass (data taken from the AME 2003 data files [22, 21, 20]). There is a peak in the binding energy per nucleon around iron with $^{62}$Ni the most tightly bound nucleus. This peak divides the nuclides into two groups, with those having lower masses able to provide energy from fusion, and the higher masses able to provide energy from fission.

For nuclides in the ground state at normal nuclear density that have unknown masses their binding energy can be calculated using Weizsacker's phenomenological formula developed in 1935 [23]:

$$BE(A,Z) = -a_b A + a_s A^{2/3} + a_a \frac{(A-2Z)^2}{A} + a_c \frac{Z(Z-1)}{A^{1/3}} - B \tag{1.10}$$

The binding energy (BE) for a given nuclide (A, Z) is determined using the five terms which depend on the mass (A) and/or charge (Z). The first term is called the bulk term, and the asymmetry term is the third term. The other three terms arise from the finite size of the nucleus. The second term, or surface term, corrects for the nuclear surface. The fourth term, or Coulomb term, corrects for the repulsion of the protons. The fifth term, or pairing term, corrects for the neutron and proton pairing. The constants for each of the terms are determined by fitting experimental data and are: $a_b = 15.835$ MeV/c$^2$, $a_s = 18.33$ MeV/c$^2$, $a_c = 0.714$ MeV/c$^2$, $a_a = 23.2$ MeV/c$^2$, and the pairing term, B, is 0 MeV/c$^2$ for odd-even or even-odd nuclei, -11.2 MeV/c$^2$ for even-even nuclei and +11.2 MeV/c$^2$ for odd-odd nuclei [24].

The effects of each term are shown schematically in figure 4 as a function of mass

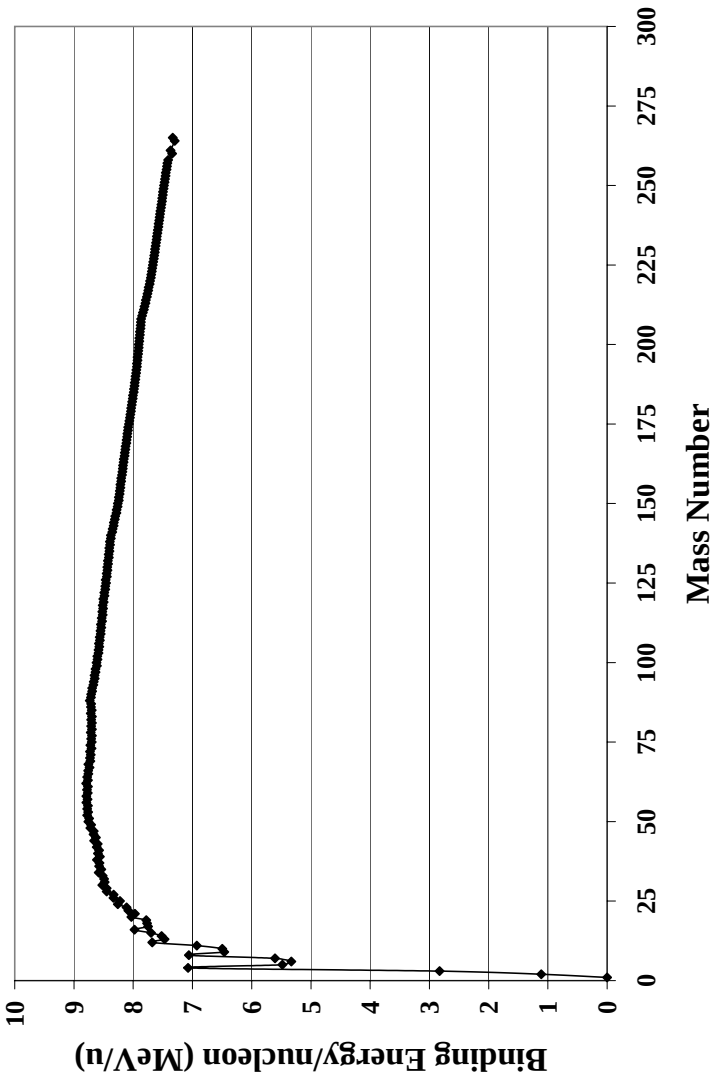


FIG. 3. Binding energy per nucleon as a function of mass number. In this plot only the most bound nucleus at each mass is used.

TABLE I. List of parameters used in the binding energy equation. Note that the pairing term has a different form in Krane.

| Parameter | Friedlander [29] | Krane [30] | Cottingham [24] |
|---|---|---|---|
| Volume ($MeV/c^2$) | 15.677 | 15.5 | 15.835 |
| Surface ($MeV/c^2$) | 18.56 | 16.8 | 18.33 |
| Symmetry ($MeV/c^2$) | 1.211 (k = 1.79) | 23 | 23.20 |
| Coulomb ($MeV/c^2$) | 0.717 | 0.72 | 0.714 |
| Pairing ($MeV/c^2$) | +11,0,-11 | 34 MeV | +11.2,0,-11.2 |

number (again using the most bound nucleus at each A from the AME 2003 Data [22, 21, 20]). The bulk energy is uniform at 15.835 MeV/nucleon, then adding the surface energy dramatically reduces the binding energy for the low mass nuclides, since they have large surface to volume ratio. With increasing mass the surface to volume decreases and the binding energy increases slowly approaching the bulk binding energy. Taking into account the Coulomb term decreases the binding energy with increasing mass. Adding the symmetry term decreases the binding energy further with increasing mass. The pairing term is not shown since it can either reduce, increase or not change the binding energy based on which nuclide is used. Table 1 shows the various parameters used for this equation from several sources.

Each parameter in this equation can be broken down into evermore complex dependencies. The Weizsacker mass formula has been modified extensively through the years [25]. First to a droplet model created by Hilf *et al.* in 1976 [26]. The model was then updated by Moller *et al.* in 1995 and is called the finite-range droplet model [27]. The first two terms were further modified by Myers *et al.* [28] to include the effect that for sufficiently large asymmetry, |N-Z|, that would make the bulk term 0,

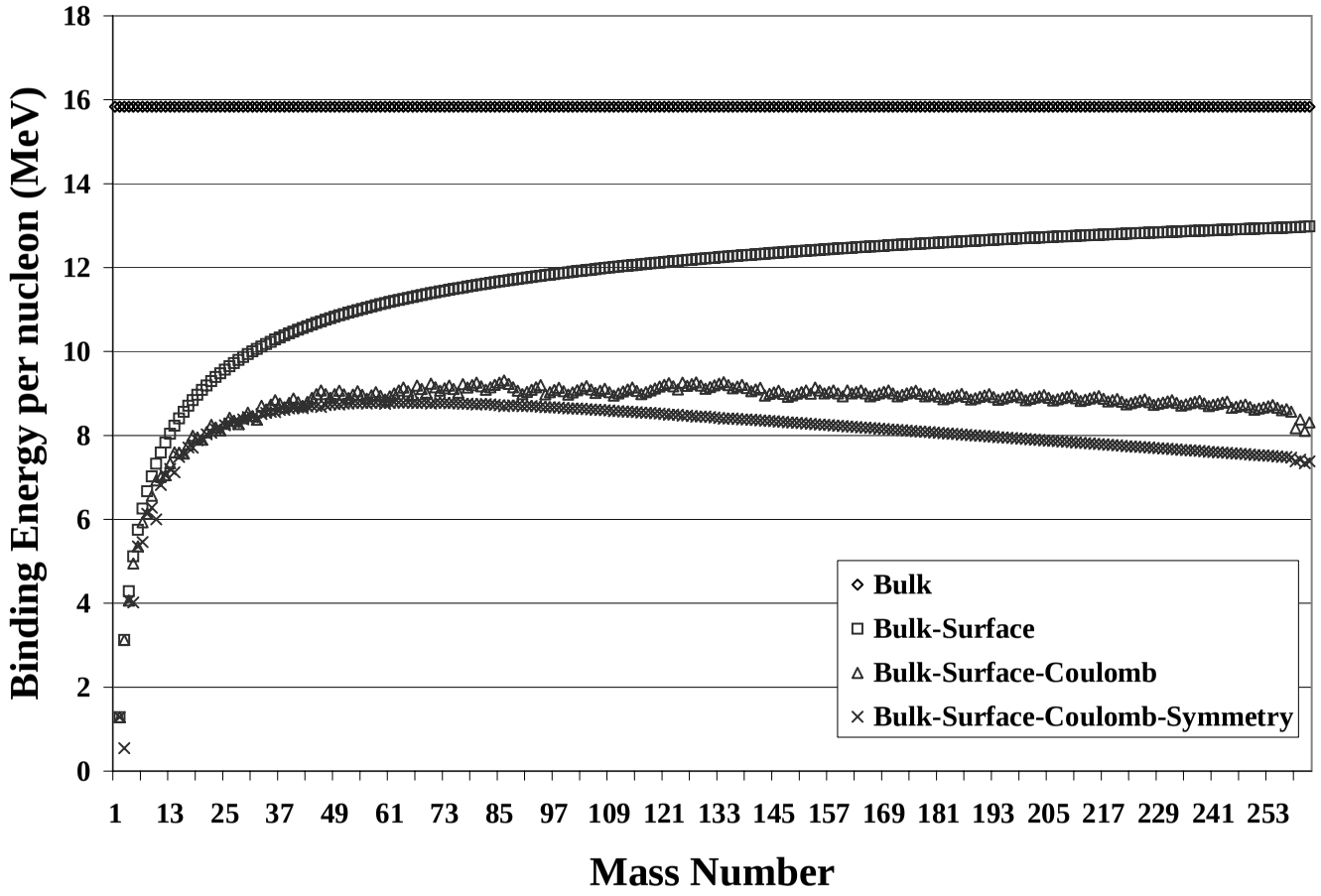


FIG. 4. Binding energy effects from each term in Weizsacker's phenomenological formula as a function of A. Values calculated with constants from Cottingham in Table I for the most stable nuclide at each A as used in Figure 3 [24].

the surface term should also go to 0. Wanajo *et al.* then modified the mass formula so that it predicted 2,135 measured masses with root mean square error of 0.670 MeV for nuclei with N and Z greater than 7 [31]. It has even been modified to include hypernuclei, which are nuclei containing hyperons as well as neutrons and protons [32].

The symmetry energy is the energy difference between symmetric nuclear matter and pure neutron matter at a given density. The left side of figure 5 shows an example of the binding energy difference between pure neutron matter and symmetric matter as a function of density. At a given density the difference between symmetric nuclear matter and pure neutron matter is the symmetry energy at that density and is plotted in the right side of figure 5. Around normal nuclear density, i.e. $\rho/\rho_0 = 1$, and temperature, i.e. T = 0, the symmetry energy is approximately 23.5 MeV/nucleon for finite nuclear matter [13] and 30 MeV/nucleon for infinite nuclear matter. In nuclear reactions density changes from normal nuclear density before interaction, to higher density during the interaction, then lower density when freeze-out occurs and fragments are formed. The lower density region can be probed using the fragments formed and the high density region can be probed using early emission gammas, neutron and proton differential flow [33], pion ratio: $\pi^-/\pi^+$ [33] and kaon ratio: $K^0/K^+$ [34].

The strength of the density dependence on the first term of the nEOS can be soft, also called weak, or strong, also called stiff, as shown in figure 5. This is also the case for the second term, but called asy-stiff and asy-soft in order to differentiate between the two terms. In neutron-rich systems the effect of asy-soft dependence is increased interaction time, leading to more equilibration and a larger dissipation of energy, while an asy-stiff dependence decreases interaction time, leading to less equilibration and less dissipation of energy. For proton-rich systems this is reversed, so an asy-

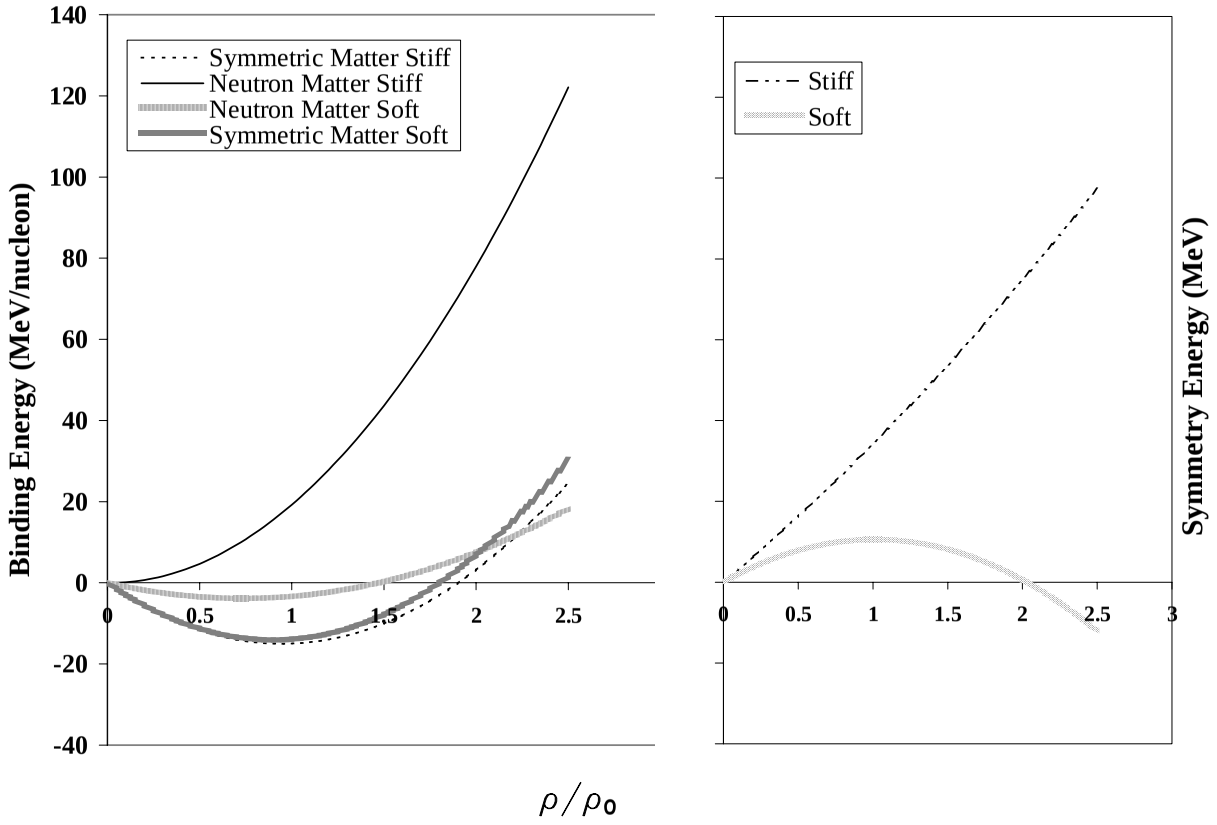


FIG. 5. Left: Example of binding energy as a function of density for pure neutron matter and symmetric matter for a soft and a stiff parameterization. Right: Symmetry energy as a function of density.

soft dependence would decrease interaction time, leading to less equilibration and less dissipation of energy, while an asy-stiff dependence would increase interaction time leading to more equilibration and larger dissipation of energy. Recent studies of excited, i.e. low density and high temperature, nuclear matter have shown a decrease in the symmetry energy with increasing excitation energy down to approximately 15 MeV [35, 36, 37, 38]. This work will see if the current data sets also agree with this lowering.

There are many ways to measure and constrain the symmetry energy. The strength of the density dependence of the symmetry energy effects neutron star mass and radii. Neutron stars are very dense forms of nuclear material and could contain exotic phases of matter such as hyperons and QGP, the quark gluon plasma. A stiffer dependence of the symmetry energy on the density allows for the creation of massive neutron stars with large radii. Astronomers can measure the masses and radii of neutron stars to establish high and low thresholds to help constrain the nEOS. Schulze *et al*. found the maximum mass of a neutron star before collapse to a black hole to be about 1.4 solar masses ($M_{\odot}$) [39]. At densities double to triple normal nuclear densities hyperons appear and soften the nEOS, which then reduces the maximum mass. The heaviest neutron star observed is PSRJ0751+1807 , which is a 2.1 $M_{\odot}$ millisecond pulsar deduced using relativistic orbital decay [40]. This could be evidence for existence of strange or quark stars.

The masses and radii of neutron stars are also confined by other requirements, which in turn constrain the nEOS. First there is a mass-shedding limit, which is a limit to how fast the star can rotate without breaking apart. At this limit the velocity of a particle on the surface of the neutron star is equal to an orbiting particle just above the surface and the star can then shed the particle. The fastest spinning neutron star observed is PSR B1937+21, which rotates 641 times a second, giving

a limit of the radius to 15.5 km for a 1.4 $M_{\odot}$ star [41]. Second general relativity prohibits the Schwarzschild condition $R \leq 2GM/c^2$, where R is the radius, G is the gravitational constant, M is the mass and c is the speed of light [42]. This occurs at the maximum energy density, where the maximum mass is equal to the half radius in Plank units. Finally the condition of causality prohibits $R \leq 3GM/c^2$ [42].

The nEOS determines the percent deleptonization, or electron capture by protons in neutron stars, which comes into play when determining the inner core size and bounce densities during supernovae explosions [43]. The bounce density of the inner core occurs around 3 $10^{14}$ g/cm$^3$ near normal nuclear densities, where the nuclear force slows down the collapse and generates a shockwave into the outer core.

Neutron star mergers and neutron star/black hole mergers also depend on the radii and masses of the objects and therefore depends on the nEOS [43, 44]. The mass transfer and evolution between the systems are dependent on the stiffness of the nEOS [44]. Lee found that a neutron star with a stiff nEOS would break apart, while a neutron star with a stiffer nEOS would hold together and form an accretion stream. Then the eccentricity of the neutron star with the stiffer nEOS creates peaks in the gravitational wave luminosity, which may be seen by LIGO, the Laser Interferometer Gravitational Wave Observatory, and help constrain the nEOS.

The r-process, or rapid neutron capture process, of nucleosynthesis is highly dependent upon the binding energies of the nuclides involved [31]. A smaller symmetry energy results in rare nuclides having greater binding energies, therefore being more stable, allowing them to persist longer during the r-process. These values can then be compared to the observed abundances of r-process daughter nuclides that can only be formed via the r-process.

Neutron stars cool via the URCA process, named after Casino da URCA in Rio de Janeiro by George Gamov, who said *the energy disappears in the nucleus of*

*the supernova as quickly as the money disappeared at that roulette table.* The direct URCA process is given by two reactions shown in equations 1.11 and 1.12, where n is a neutron, p is a proton, $e^-$ is an electron an $\bar{\nu}_e$ is an anti-neutrino and $\nu_e$ is a neutrino. The modified URCA process is given by equations 1.13 and 1.14, where the reactions now take place in the vicinity of other nucleons. The star cools from the energy carried off by the neutrinos. Having a modified URCA process could explain why neutron star 3C58 (1186 AD Supernova) is unexpectedly so cool [45]. A stronger, or stiffer, density dependence of the symmetry energy, leads to more rapid cooling through the modified URCA process.

$$n \longrightarrow p + e^- + \bar{\nu}_e \tag{1.11}$$

$$p + e^- \longrightarrow n + \nu_e \tag{1.12}$$

$$(n,p) + n \longrightarrow (n,p) + p + e^- + \bar{\nu}_e \tag{1.13}$$

$$(n,p) + p + e^- \longrightarrow (n,p) + n + \nu_e \tag{1.14}$$

The neutron skin thickness of nuclei is also effected. A larger density dependence of the symmetry energy produces a thicker neutron skin. A new study P-REX ($^{208}$Pb Radius Experiment) is trying to measure this thickness accurately in $^{208}$Pb [46]. They are using the parity violating weak interaction via polarized electron scattering to probe the neutron distribution to about 1% accuracy.

Low mass neutron stars (i.e. 0.5 $M_\odot$) have central densities near normal nuclear density, but these stars are rare [47]. However, the neutron density of $^{208}$Pb is correlated with the neutron star radius for these light neutron stars. By comparing this

density and the density of heavier neutron stars can put a constraint on the density dependence of the nEOS.

Neutron skin thickness is also correlated to the amount of N/Z diffusion in heavy-ion collisions [48]. Steiner *et al.* have shown that the skin thickness must be greater than 0.15 fm, from the current N/Z diffusion data [48]. The strength of the N/Z diffusion can also be studied using rapidity distributions of free nucleons and their corresponding N/Z asymmetries [33].

Another way to find the symmetry energy experimentally is through the technique of isoscaling, or the scaling of the fragment yields [49, 50]. Tsang *et al.* has shown a relation of the isoscaling parameter $\alpha$ with the symmetry energy by equation 1.15, where T is the temperature and the $Z_1$ and $A_1$ are the neutron and proton numbers from the first system and $Z_2$ and $A_2$ are the neutron and proton numbers from the second system [49].

$$\alpha = 4\frac{C_{sym}}{T}[\frac{Z_1}{A_1} - \frac{Z_2}{A_2}] \tag{1.15}$$

The symmetry energy was studied in this work using several parameterization of the symmetry energy in SMM using the same DIT input. BNV and iBUU were also run with different nEOS parameterizations, but the results were not conclusive for BNV and iBUU was found to be having compiler problems. All the simulations will be discussed in further detail in chapter V and comparisons with the experimental data will be made in chapter VI.

# CHAPTER II

# EXPERIMENTAL

This chapter discusses the experimental details. The first section describes the beams, targets and event statistics. The FAUST array will then be described, followed by other supplementary detectors. Signal transmission from the preamplifiers through to CAMAC and VME is then discussed. Finally the data transfer to computer and storage as root files is described in the last section.

## A. Target and Beam Details

This experiment was carried out at the Texas A&M University Cyclotron Institute. Beams of 32 and 45 MeV/nucleon $^{40}$Ar with N/Z = 1.22, $^{40}$Ca with N/Z = 1.00 and $^{48}$Ca with N/Z = 1.40 were extracted out of the K500 superconducting cyclotron. The list of beams, their energies and charge states injected into the cyclotron are listed in table II. After the K500 there was a stripper foil, to create fully stripped beams.

The two targets were 2 x 2 cm self supporting $^{112}$Sn with N/Z = 1.24 at 1.30 mg/cm$^2$ and $^{124}$Sn with N/Z = 1.48 at 1.15 mg/cm$^2$. They were mounted on a target ladder along with magnets, which were used to deflect electrons. A $^{228}$Th calibration source was also mounted on the target ladder for calibrating the silicon detectors. To maintain a reasonable dead time the event rate was kept below 400 events per second by using an attenuator and an iris, for fine tuning.

The number of events collected for each system are listed in table III. An effort was made to try to obtain similar statistics for each beam-target combination. Alpha source runs were taken before, during and after each beam for calibrations.

TABLE II. List of beams, energies and charge states out of the advanced ECRIS.

| Beam | Z | N | N/Z | E | Charge State |
|---|---|---|---|---|---|
| $^{40}$Ar | 18 | 22 | 1.22 | 32 | 13 |
| $^{40}$Ar | 18 | 22 | 1.22 | 45 | 16 |
| $^{40}$Ca | 20 | 20 | 1.00 | 32 | 13 |
| $^{40}$Ca | 20 | 20 | 1.00 | 45 | 16 |
| $^{48}$Ca | 20 | 28 | 1.40 | 32 | 14 |
| $^{48}$Ca | 20 | 28 | 1.40 | 45 | 17 |

TABLE III. Table of number of events for each system and source.

| Beam | Target | Energy | Events | Energy | Events |
|---|---|---|---|---|---|
| $^{40}$Ar | $^{112}$Sn | 32 | 8,122,211 | 45 | 6,639,425 |
| $^{40}$Ar | $^{124}$Sn | 32 | 4,851,988 | 45 | 8,520,048 |
| $^{40}$Ca | $^{112}$Sn | 32 | 15,870,175 | 45 | 22,734,153 |
| $^{40}$Ca | $^{124}$Sn | 32 | 18,943,162 | 45 | 17,246,320 |
| $^{48}$Ca | $^{112}$Sn | 32 | 11,552,202 | 45 | 6,396,584 |
| $^{48}$Ca | $^{124}$Sn | 32 | 13,349,003 | 45 | 9,828,418 |
| $^{228}$Th | | Source | 22,741,754 | | |

## B. F.A.U.S.T.

FAUST, the Forward Array Using Silicon Technology, was used to isotopically identify the fragments [51, 52, 53, 54, 5]. FAUST is composed of 68 detector telescopes, each having an edge mounted 2 x 2 cm 300 $\mu$m Si (Silicon) detector, model MSI-MSX04-300 from Micron Semiconductor [1], followed by a CsI(Tl) (Cesium Iodide crystal doped with Thallium) crystal from Bicron [2]. The CsI(Tl) crystals are 1.181" thick in rings A through D and 0.890" thick in ring E. The CsI(Tl) crystals light output is focused onto a PD (Photodiode), model S5107 by Hammamatsu Corporation [3], using a LLG (Lucite Light Guide), produced in-house. An example telescope is shown in figure 6 with the inset showing the face of the edge mounted Si. The telescopes in FAUST provide isotopic identification up to Oxygen.

The detectors are arranged in 5 rings, see figure 7, with angular coverage of 90% from 2.31° to 33.63°, 71% from 1.64° to 2.31° and 25% from 33.63° to 44.85°. Ring A covers 1.64° to 6.36° and has 8 detector telescopes. Ring B covers 4.60° to 12.28° and has 12 detector telescopes. Rings C, D and E cover 8.84° to 19.73°, 14.30° to 30.77° and 22.63° to 44.85°, respectfully, and each with 16 detector telescopes. The cross section of FAUST is shown in figure 8. The inactive area of a ring is blocked by the active area of the ring in front, which maximizes the forward angular coverage.

FAUST was constructed to provide bias and power to the full ring for ring A and half rings for rings B through E. Silicon biases were matched as closely as possible for each section as each Si detector has an optimal bias. The bias voltages were provided by Tennelec 953/953A power supplies. The biases and leakage currents from the start

[1]Micron Semiconductor Inc., 126 Baywood Avenue, Longwood, Florida.

[2]Bicron (Currently Saint Gobain), 6801 Cochran Road, Solon, Ohio.

[3]Hammamatsu Corporation, 360 Foothill Road Box 6910, Bridgewater, New Jersey.

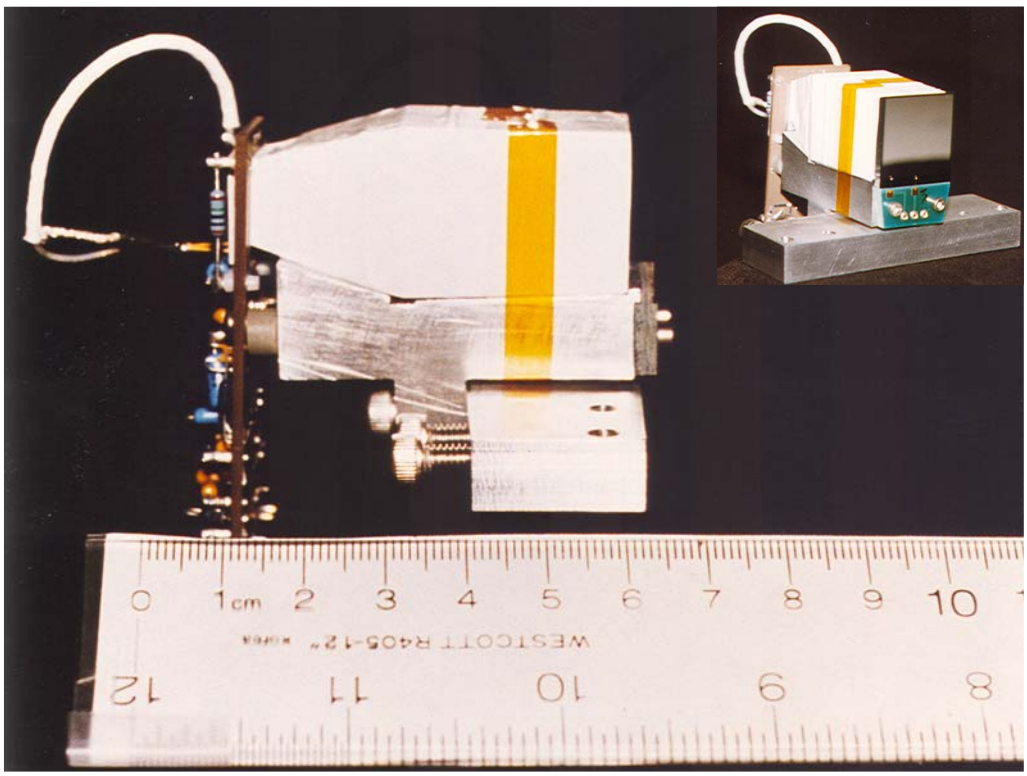


FIG. 6. (Color online). Example of a telescope from FAUST. Inset shows edge mounted Silicon wafer. (Courtesy of Doug Rowland)

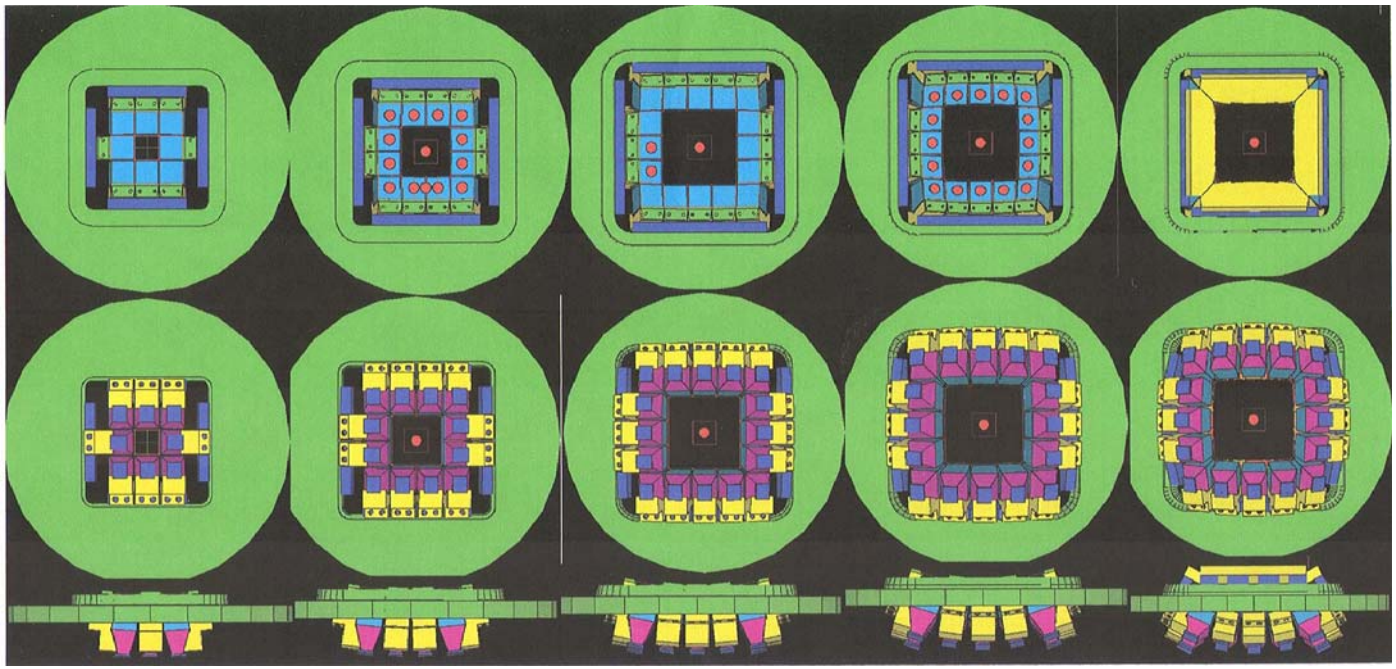

FIG. 7. (Color online). AutoCAD rendering of the FAUST Rings. From left to right, rings A through E. Top: front view, middle: back view, and bottom: side view. Note that Ring E is shown with the protective brass plates in place, which protect the preamp electronics. (Courtesy of Robert Olsen)

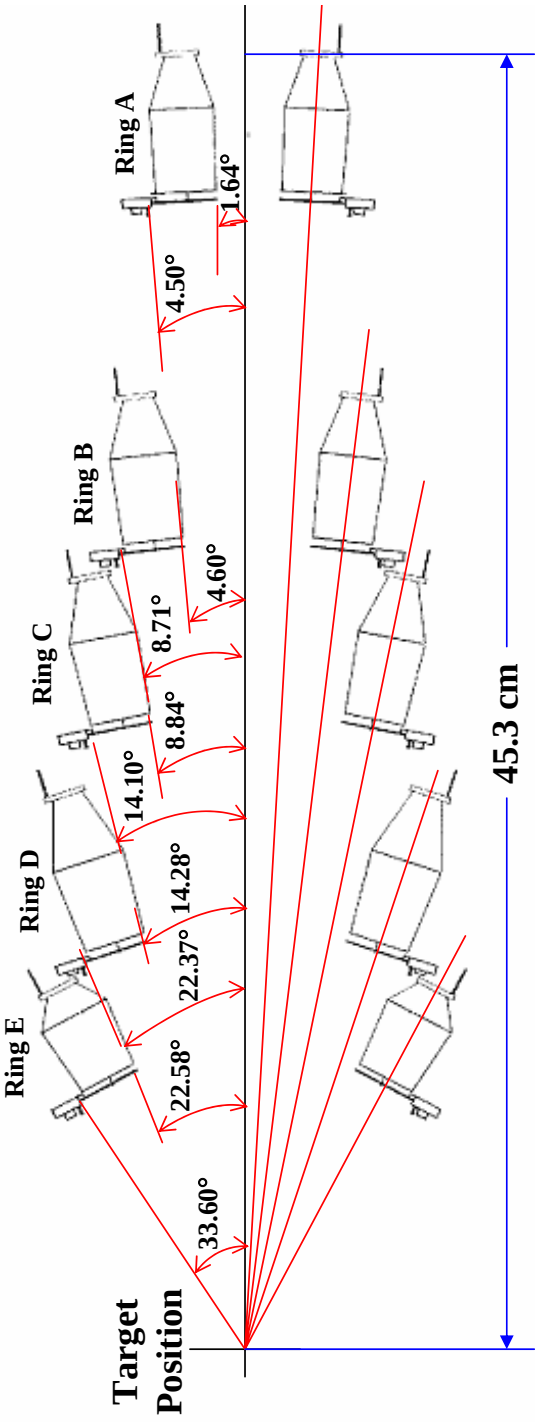


FIG. 8. Cross section of the FAUST array.

TABLE IV. List of half rings and their bias voltage and leakage currents.

| Half Ring | Bias (+V) | Leakage Current ($\mu$A) |
|---|---|---|
| A1-2 | 22.5 | 0.93 |
| B1 | 27.2 | 0.31 |
| B2 | 28.4 | 0.39 |
| C1 | 27.1 | 0.20 |
| C2 | 27.4 | 0.31 |
| D1 | 22.8 | 0.17 |
| D2 | 22.6 | 0.25 |
| E1 | 26.9 | 0.23 |
| E2 | 26.6 | 0.18 |

of the run are listed in table IV.

The PD bias of +16 V was provided by a Topward 6302D power supply, which had a leakage current of 0.10 $\mu$A. Over the course of the experiment all of the leakage currents were stable as shown in figure 9.

FAUST was aligned to the beam line using alignment bars that fit onto both ends of the FAUST array. Then using a transit upstream and the 8 positioning fingers on the FAUST chamber, the back and front of FAUST were aligned to the beam line.

### C. Other Detectors

Faraday cups were used after the K500 cyclotron, to determine the initial beam current, and at the end of the beam line, to collect unreacted beam and measure the final beam current. Phosphors were used on the target ladder and at the end of the

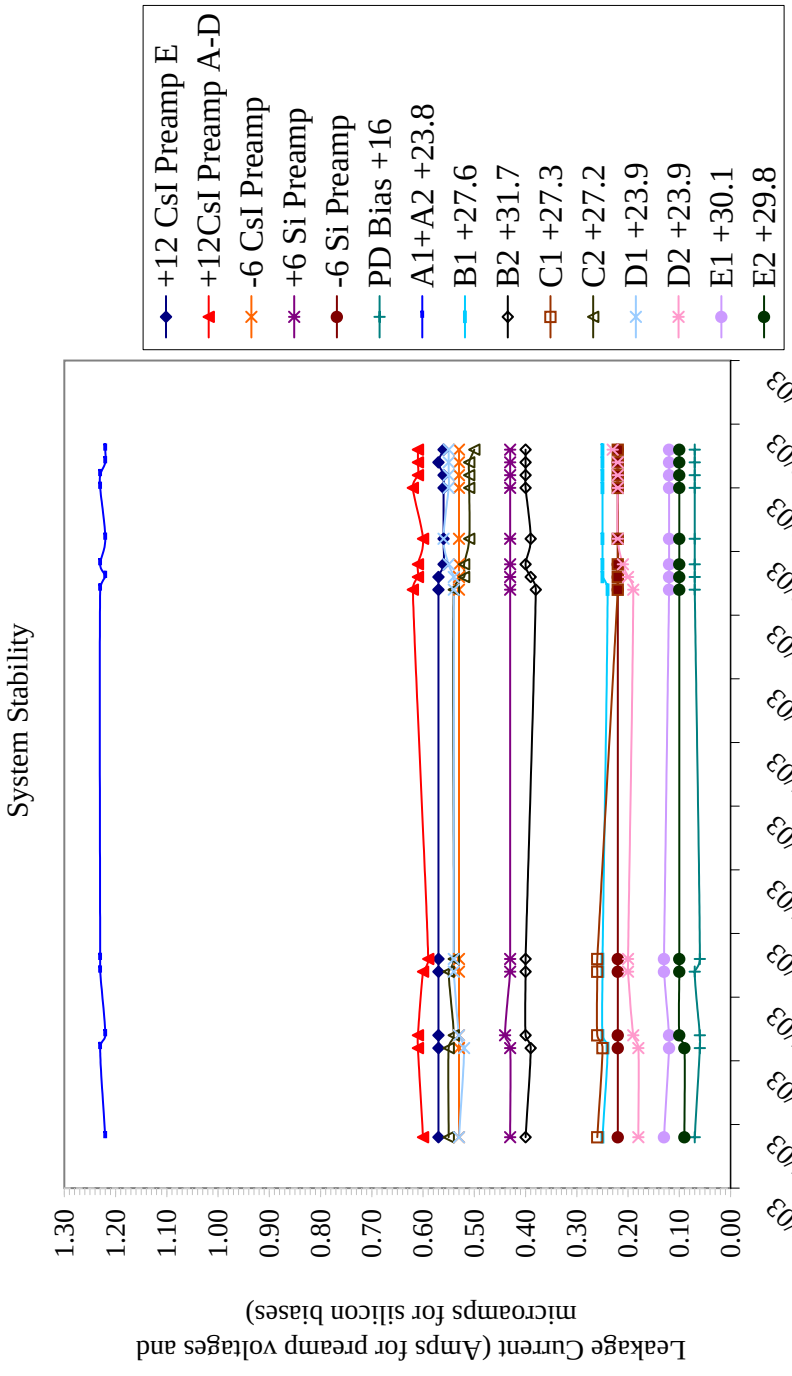


FIG. 9. (Color online) Leakage currents for all the power supplies used over the duration of the experiment.

beam line, to make sure the beam was centered through FAUST. Also the beam spot was small enough to not impinge on the target ladder.

## D. Electronics

A Topward 6302D power supply provided all of the CsI preamplifiers power of +12 V and -6 V with leakage currents of 1.13 A and 0.53 A, respectfully. Another Topward power supply provided all of the Si preamplifiers power of -6 V and +6 V with leakage currents of 0.20 A and 0.48 A, respectfully. Both the Si and CsI preamplifiers were located on the rings inside the FAUST array, which helped to maximize the signal to noise ratio.

The electronics diagram is shown in figure 10. The silicon signals go through an eight channel charge sensitive preamplifier chip (LeCroy Model HQV810), then a FAUST timing/shaping amplifier (FAUST main/timing amplifier built in-house). The fast timing signal then goes to a discriminator to be used as a trigger and the slow shaping signal to an Analog to Digital Converter (ADC) (Phillips Scientific Model 7164/7164H).

The CsI(Tl) signal goes to a low noise N-channel JFET IC charge sensitive preamplifier (InterFET N-JFET IFPA300). The signal then goes to the FAUST shaping amplifier with a shaping time of 0.5 ms. Unipolar output is sent to an ADC (Phillips Scientific Model 7164/7164H).

The trigger electronics use the fast silicon signal from the FAUST amplifier, which was first sent to a Constant Fraction Discriminator (CFD) (LeCroy Model 3420). Then the fast silicon signal was daisy chained through a Coincidence Register (CR) (LeCroy Model 4448), a Time to Digital Converter (TDC) (LeCroy Model 3377), and a scaler (LeCroy Model 4434). Two outputs were taken out of the CFD. The

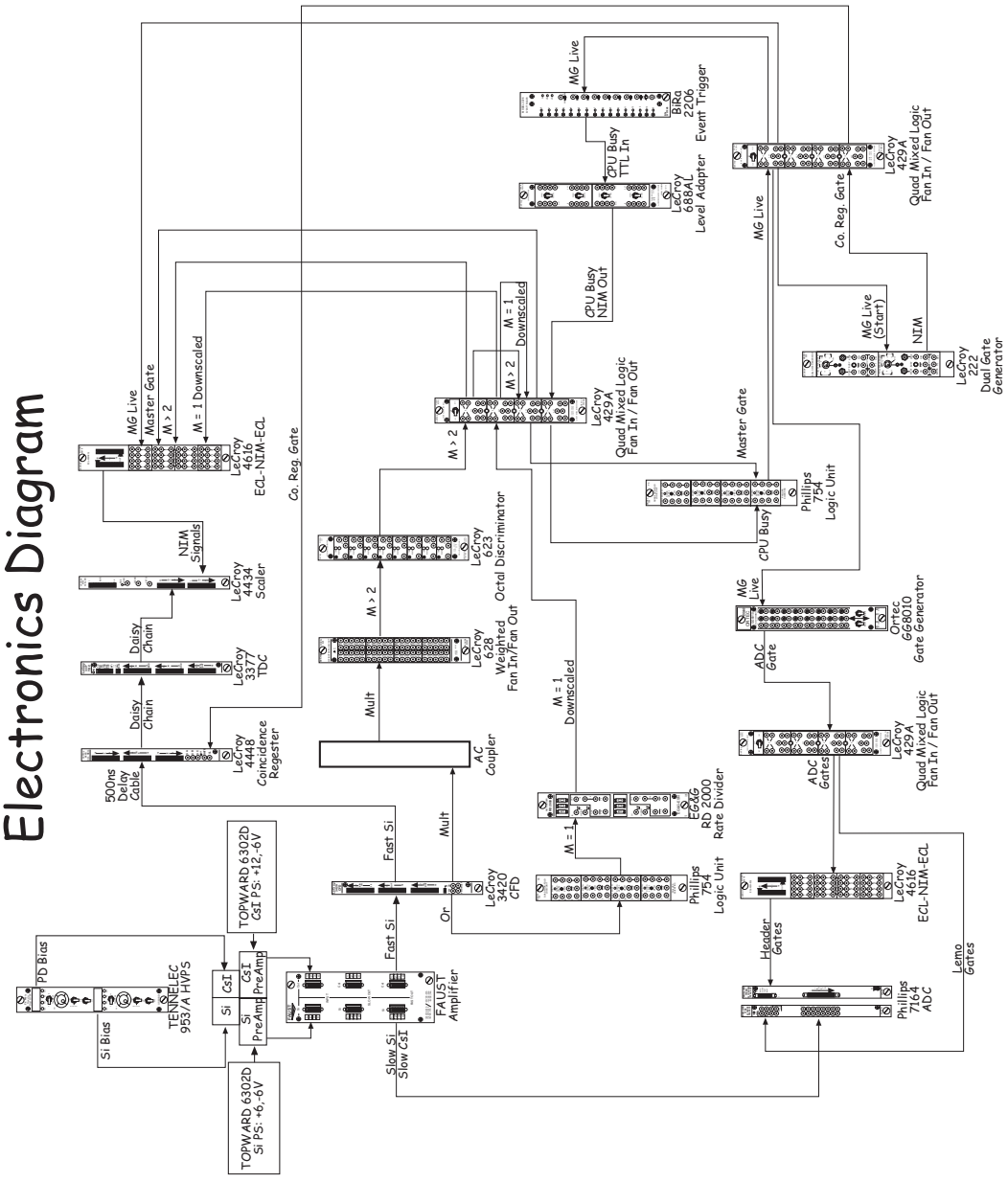


FIG. 10. The FAUST electronics diagram.

first output was the OR signal, which was sent to a Logic Unit (Phillips Scientific Model 754) to create the multiplicity 1 signal. The multiplicity 1 signal then went to a rate divider (EG&G Model RD2000) for downscaling. The second output from the CFD was the MULT signal. Each ring has one CFD, so all the CFD MULT signals pass through an AC-Coupler (Built In-House) to make sure they all have the same baseline and are then combined in a Fan-In/Fan-Out (FI-FO) (LeCroy Model 628). This total MULT signal was sent to an Octal Discriminator (LeCroy Model 623), where a multiplicity cut of greater than two was made. Then the multiplicity 1 and multiplicity greater than two signals were combined in a FI-FO (LeCroy Model 429A) creating the master gate.

To create the master gate live signal a computer busy signal is needed. The computer busy signal was created by the Event Trigger module (Bi Ra Model 2206) that then proceeds to a Level Adapter (LeCroy model 688AL) and then to a FI-FO (LeCroy Model 429A) to create multiple computer busy vetoes. Both the master gate and computer busy then were sent to a logic unit (Phillips Scientific Model 754), which created the master gate live signal. The master gate live signal then goes to a Gate Generator (Ortec Model GG8010) to create the gates for the ADCs (Phillips Scientific Model 7164/7164H). The ADC gate from the Gate Generator first goes to a FI-FO (LeCroy Model 429A) and the Lemo output sent to the Lemo ADCs (Phillips Scientific Model 7164), then one of the Lemo outputs from the FI-FO was sent to an ECL-NIM-ECL Converter (LeCroy Model 4616) to provide a header output, which goes to the Header ADCs (Phillips Scientific Model 7164H). The master gate live is also sent back to the event trigger to provide a busy signal during an acquisition event. The master gate live signal is also sent to another Gate Generator (LeCroy Model 222) to create the CR Gates.

The CR Gates go through a FI-FO (LeCroy Model 429A) and then to the CR.

The ADCs, CRs, TDCs, and Scalers are all read by the front end computer. The TDCs were incorrectly set to take a common stop instead of a common start, and so no useful TDC data entered the data stream. The scalers also received other signals from the NIM electronics, first being sent through an ECL-NIM-ECL Converter (LeCroy Model 4616). These signals include multiplicity 1, multiplicity greater than 2, master gate, and master gate live.

Two Bi Ra CAMAC (Computer Automated Measurement And Control) crates were used, each with a parallel crate controller (Bi Ra Model 1302 LM). The first CAMAC crate had the selector set to 1 and was connected to the VME (Versa Module Europa) and to the second crate with a Branch Highway Cable. The second CAMAC crate had the selector set at 2 and was terminated with a Branch Highway Terminator (Bi Ra Model 6601 BHT). The VME held the computer (SBS VMEbus to PCI Adapter with DMA Model 618) which provides the communication between the backend computer and the CAMAC crates. The back end computer and front end computer are discussed in the next section.

Some of the CAMAC modules, most notably the ADCs, draw enough power and can generate enough heat to cause crate failure and module failure. To advert these problem high powered crates from Bi Ra (Bi Ra Models 9700-SCB and 6700-SCB) were used and the CAMAC modules were divided among the two crates to optimize power requirements shown in figure 11. Also slots for the ADCs were selected to have empty slots on either side, to allow airflow from external fans to help dissipate the generated heat. Figure 11 also shows the slot positions of all modules in the two crates.

| CAMAC POWER REQUIREMENTS | Quantity | 25A | 25A | 6A | 6A |
|---|---|---|---|---|---|
| **Modules** | | **+6V** | **-6V** | **+24V** | **-24V** |
| Phillips 7164 ADC | 5 | 2.4A | 1.8A | 510mA | |
| Phillips 7164H ADC | 6 | 2.4A | 1.8A | 510mA | |
| LeCroy 4448 CR | 2 | 0.4A | 1.9A | | |
| LeCroy 3420 CFD | 5 | 1A | 1.75A | 50mA | 250mA |
| LeCroy 4434 Scaler | 3 | 3.1A | 0.4A | | |
| LeCroy 3377 TDC | 3 | 1.1A | 2A | 25mA | 170mA |
| Bi Ra 6601 BHT | 1 | | | | |
| Bi Ra 1302LM Crate Controller | 2 | | | | |

| Division | Crate 1 | Crate 2 |
|---|---|---|
| **ADCs** | 6 | 3 |
| **CRs** | 0 | 2 |
| **CFDs** | 5 | 0 |
| **Scalers** | 0 | 3 |
| **TDCs** | 0 | 3 |
| **BHT** | 0 | 1 |
| **1202LMs** | 1 | 1 |

| Voltage | Crate 1 A | Crate 2 A | Max A |
|---|---|---|---|
| **+6 V** | 19.4 | 20.6 | 25 |
| **-6 V** | 19.6 | 16.4 | 25 |
| **+24 V** | 3.3 | 1.6 | 6 |
| **-24 V** | 1.3 | 0.5 | 6 |

| Slot | Crate 1 | Crate 2 |
|---|---|---|
| **1** | 3420 CFD 1 B36614 | 4448 CR 1 05226 |
| **2** | 3420 CFD 2 B36612 | 4448 CR 2 B03303 |
| **3** | | |
| **4** | | |
| **5** | 3420 CFD 3 B25817 | 3377 TDC 1 B38711 |
| **6** | 3420 CFD 4 B258231 | 3377 TDC 2 B55127 |
| **7** | | 3377 TDC 3 B55113 |
| **8** | 7164 ADC 1 14565 | |
| **9** | | 4434 Scaler 1 B19771 |
| **10** | 7164 ADC 2 14563 | 4434 Scaler 2 A66233 |
| **11** | | 4434 Scaler 3 B51008 |
| **12** | 7164 ADC (BigSol) | |
| **13** | | 7164 ADC (BigSol) |
| **14** | 7164 ADC 3 19569 | |
| **15** | | 7164 ADC (Flash) |
| **16** | | |
| **17** | 3420 CFD 5 B52057 | 7164 ADC (BigSol) |
| **18** | | |
| **19** | | Clock (BigSol) |
| **20** | 7164 ADC 4 14561 | |
| **21** | | 7164 ADC (BigSol) |
| **22** | 7164 ADC 5 14564 | |
| **23** | | 6601 BHT |
| **24** | 1202LM | 1202LM |
| **25** | " | " |

FIG. 11. CAMAC power constraints and CAMAC module assignments from Excel spreadsheet.

## E. Data Acquisition and Online Analysis Software

The data acquisition and online analysis software (for checking spectra in real-time during the experiment), had switched from XSYS and VMS to ROOT, CycApps and Linux since the previous FAUST run. This new software was developed by Kris Hagel based on the transport manager and analysis manager used at the RHIC (Relativistic Heavy Ion Collider) experiment BRAHMS (Broad RAnge Hadron Magnetic Spectrometer). All the acquisition codes were modified and reduced from those of NIMROD (Neutron and Ion Multidetector for Reaction Oriented Dynamics) to work with the FAUST array. All new analysis codes were written and developed for the calibrations, gating, and analysis as discussed in chapter III. The transport manager is run on the back end computer and talks to the CAMAC crates and transfers the data to disk. Also when the transport manager is first launched a control panel allows thresholds of CAMAC modules to be set. The thresholds were chosen to be just above the noise for each channel by watching the scaler values as the thresholds were increased.

The analysis manager runs on the front end computer and reads the data stream created by the transport manager and fills spectra, such as Si, CsI and Si vs. CsI spectra, which is shown in figure 12, and displays various outputs, such as values from the scalers, such as event rate and detector hit rates. These spectra and values allow for real-time checks that the experiment is proceeding well.

To check for gain changes and other drift in detectors, two telescopes were chosen, 14 from ring B and 67 from ring E. They were zoomed to 1000 channels by 1000 channels and printed on transparency film. Then on subsequent runs the same scaled spectra were printed and transparencies overlaid to check. For these two detectors no drift occurred throughout all 12 systems collected, however several other detectors

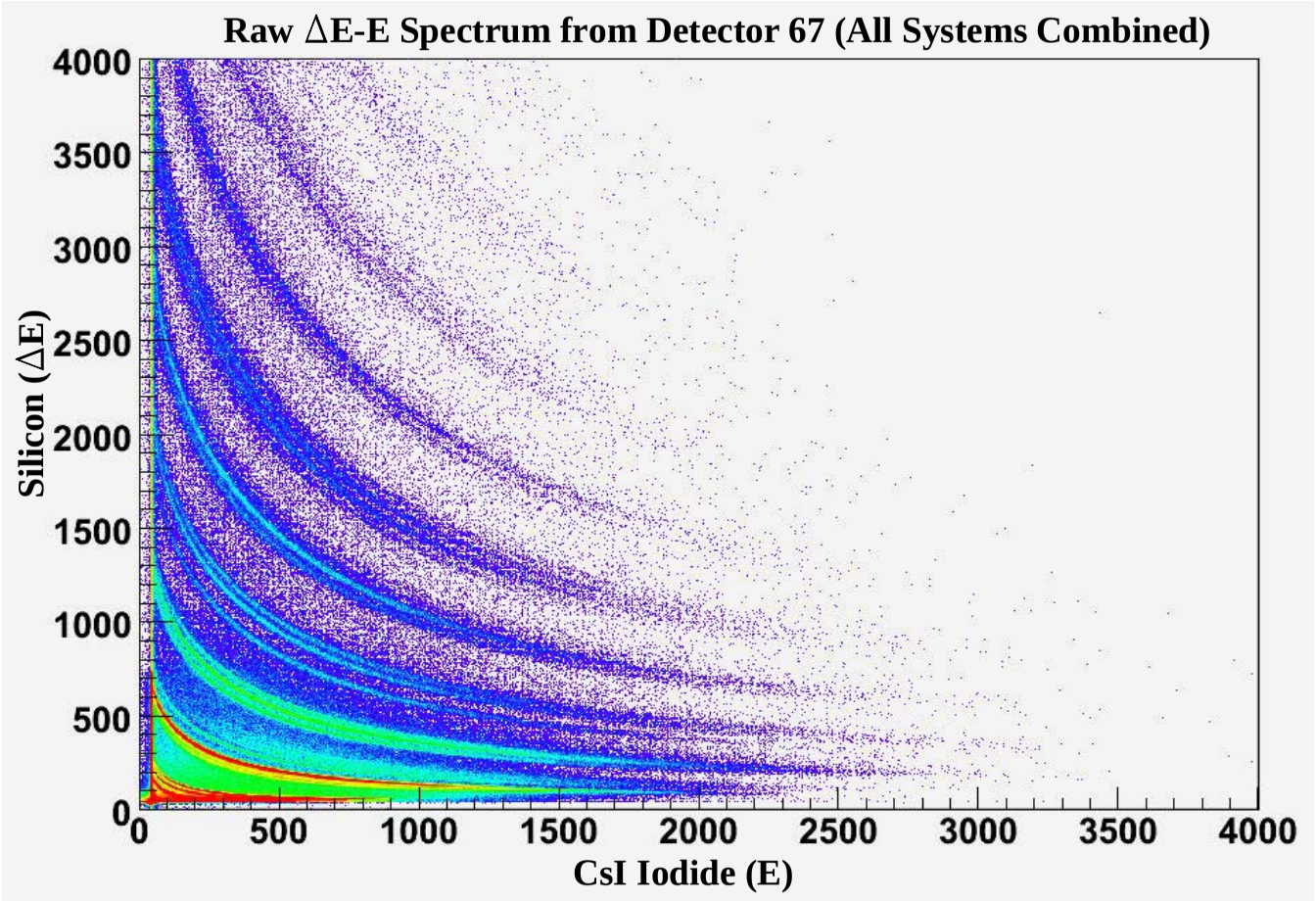


FIG. 12. (Color online) Silicon versus Cesium Iodide (ΔE-E) spectrum from detector 67 in ring E. This is the total raw spectrum, which combined all 12 systems for the best statistics used for gating and calibrations.

did experience drift between beam changes. These were identified during calibrations and were gated and calibrated separately for those systems, as discussed in chapter III.

# CHAPTER III

## CALIBRATIONS, GATES AND ANALYSIS

ROOT [55], version 2.25/03, was used for gating, calibrations and some of the analysis. During analysis ROOT was updated to version 4.04/02. This chapter discusses the calibrations, gates and analysis procedures. A flow chart overview of the analysis is shown in figure 13. The raw data files, which are created during the experiment, are the starting point of the analysis. The first section describes the generation of the raw spectra, which are used for calibrations and gates. The next sections discuss the calibration of the Si detectors, calibration of the CsI detectors, and then a description of several additional calibration techniques used for troublesome detectors [56, 57]. Then sections on the gating procedure will be described, followed by the analysis using all the calibrations and gates to create the Full Physics Tapes [58]. The final sections describe the cuts, which create the Modified Physics Tapes, assignment of unknown values, which create the Reduced Physics Tapes, and finally the reconstruction of the quasiprojectiles, which create the Reconstructed Physics Tapes.

The FAUST array had one non-operational silicon detector in ring D, detector number 37, caused by broken wire bonds. Several CsI detectors were also non-operational, these include detectors 9 and 15 in ring B, detector 36 in ring C, detectors 37, 40, and 47 in ring D and detector 65 in ring E. When the $^{48}$Ca systems were run at the end of the experimental campaign the CsI in ring C detector 23 stopped responding. During refurbishment of the FAUST array these detectors were found to have bad pre-amplifiers or the optical connections inside the wrapped telescopes had broken down. During the experiment detectors 33, 34, 63 and 64 experienced significant gain change. These detectors had their gates and calibrations done system by system and not globally as the other detectors. There were high thresholds in CsI

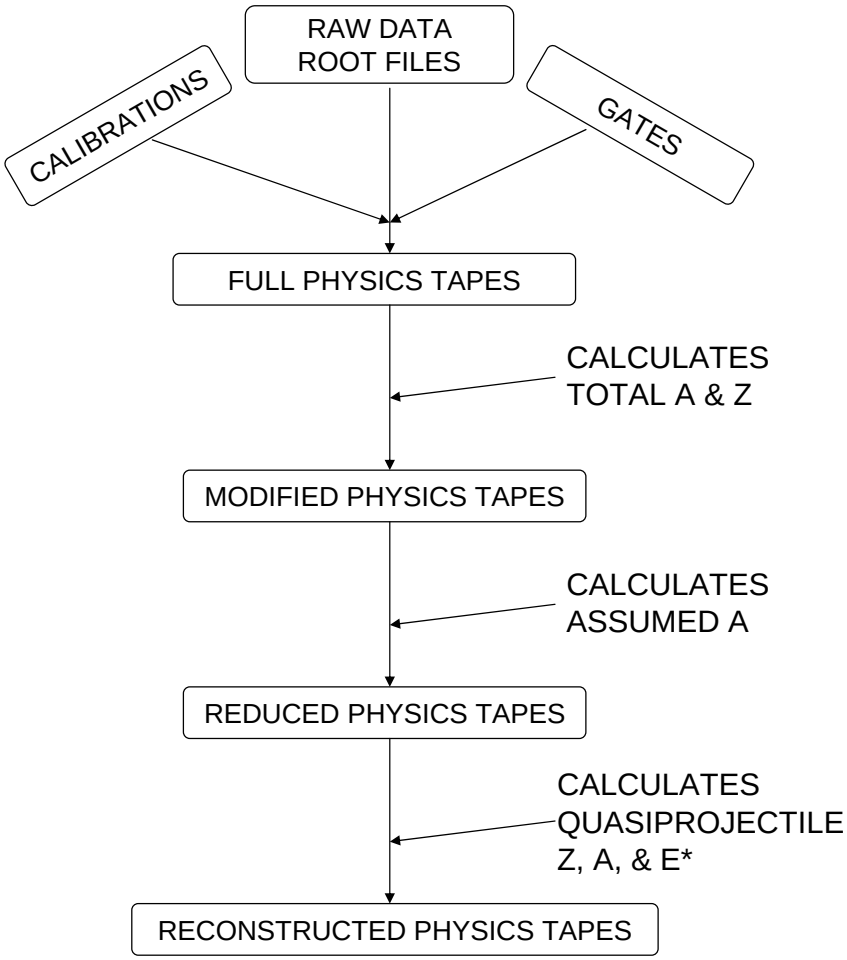


FIG. 13. A flowchart from raw data to reconstructed physics tapes.

detectors 27, 34, 35 and 43 and Si detector 12. When the yields are calculated by integrating the energy spectra, the area of integration is consistent between detectors at a given angle.

## A. Generating Raw Spectra

The raw experimental data are stored as ROOT files with a specific event structure. There are multiple ROOT files for each system. For each new run, which lasts roughly 4 hours, a new ROOT file is started. When the file reaches 100 MB the file closes and starts a new file with the same run number, but different file number. A file was created for each system, which contains the list of all ROOT files for that system. Then in ROOT the raw ROOT files were reduced for each system. This procedure reads in the raw ROOT files and compresses them to a few larger (1.2 GB) ROOT files. These reduced files are then read by ROOT to produce TTrees. The TTrees allow for the creation of the $\Delta$E versus E raw energy spectra, as shown in figure 12.

## B. Beam Spots and Punch Through Points

Rings A and B had scattered beam, however the beam is not a good calibration, because the detectors have charge leakage and noise around the beam spots. For example the $\Delta$E-E spectra for detector 2 is shown in figure 14. This figure has all 12 systems combined, creating the largest statistics, and shows the elemental lines from Helium to Scandium along with the beam spots numbered and corresponding systems listed. Note that the $^{48}$Ca at 45 MeV/nucleon is out of the range of the ADC and does not appear in the spectra. The silicon detectors experienced charge leakage and other problems from being hit by the beam, as is evident from the long strips above and below the beam spots and the terrible resolution in ring A. The difference

between the energy calculated using punch through points and beam points is about 100 MeV as shown in figure 15. The slope, intercept and $R^2$ value for the punch through points are 0.257, -15.244, and 0.998, respectfully, while those for the beam spots are 0.199, -41.109, and 0.999, respectfully.

Punch through points were calculated by extrapolation to 0 CsI channel. Using a previously alpha calibrated detector from ring B, the punch through points were calculated and calibration parameters determined (figure 15). Then the calibration from punch through points were compared to the alpha calibration, and found to be similar. For example using the punch through points the slope and intercept were found to be 0.0181 and -5.4881, respectively, which for a channel of 1000, corresponds to an energy of 12.56 MeV. The same detector calibrations using the alpha calibrations gives the slope and intercept ad 0.0163 and -5.347 and an energy of 10.95 MeV. If both alphas and punch throughs are used the slope and intercepts are 0.0183 and -6.2437 giving an energy of 12.10 MeV.

Since the thresholds of the detectors vary and the extrapolation to get the punch through points are not as exact, only the alpha calibrations will be used for calibrating the Si detectors. The fragments of interest are in the low energy range, so the alpha calibrations are more appropriate.

## C. Silicon Calibrations

The majority of the Si detectors were calibrated using a $^{228}$Th alpha source. Table V shows all the possible alpha energies, their decay intensity (with respect to the daughter decays), and the daughter (or emitting nuclide). With the FAUST experimental setup 6 different alphas were resolved in the Si detectors with energies 5.423, 5.686, 6.051, 6.288, 6.778, and 8.784 MeV. Other detectors, such as those in ring A,

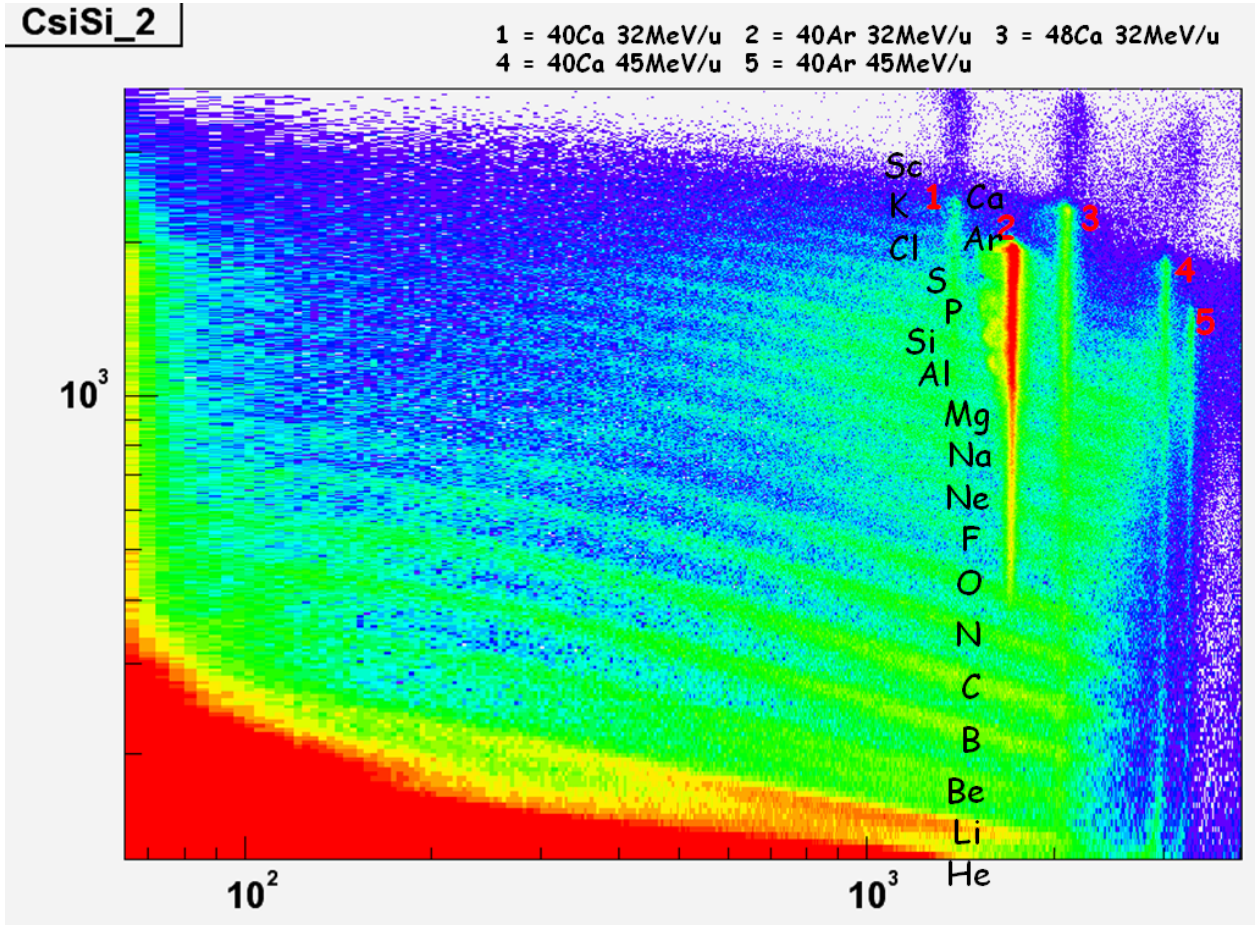


FIG. 14. (Color online) The beam spots for 5 of the 6 beams can be seen in this ΔE-E spectra from detector 2, which has all systems combined.

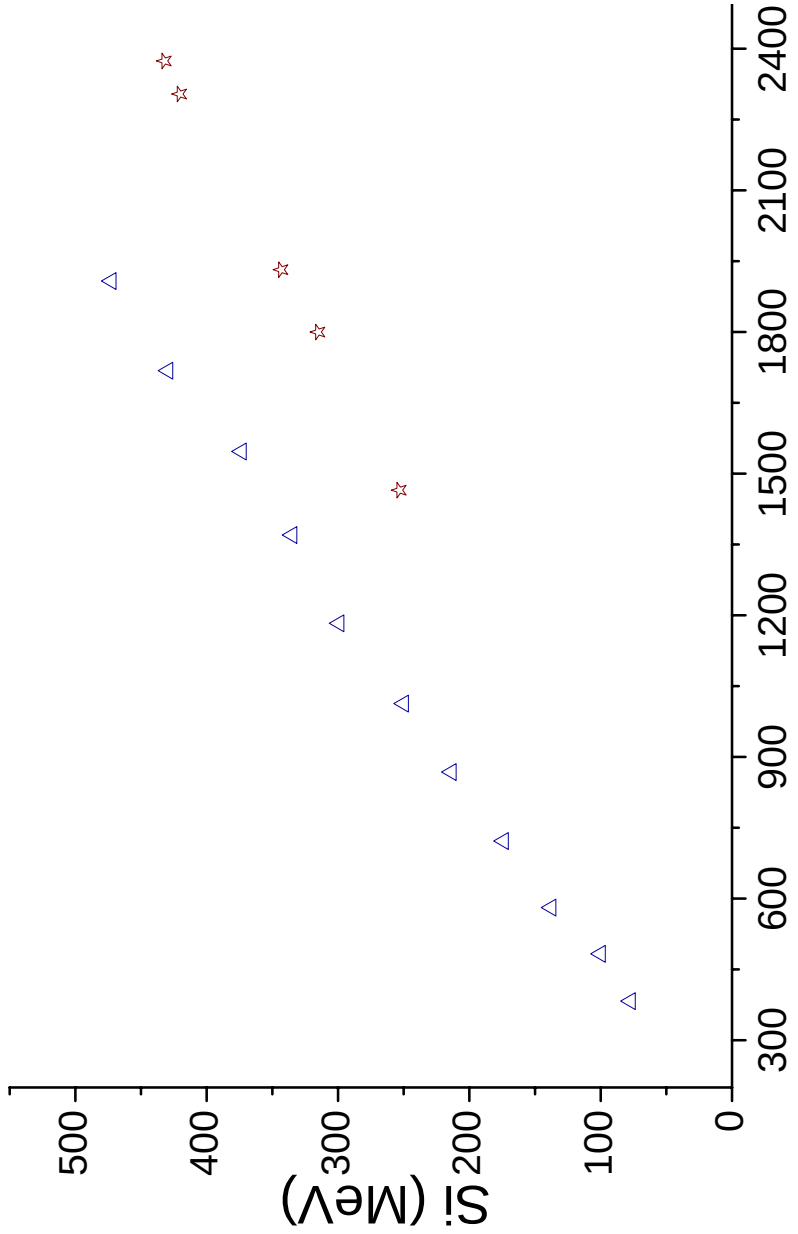


FIG. 15. The punch through points (triangles) and beam spots (stars) shown on a plot of Si energy versus CsI channel.

TABLE V. Table of alpha particles from the $^{228}$Th decay chain. The energy, decay intensity and emitting nuclide are listed.

| Energy (MeV) | Decay Intensity | Emitting Nuclide |
|---|---|---|
| 5.340 | 28% | $^{228}$Th |
| 5.423 | 71% | $^{228}$Th |
| 5.449 | 5% | $^{224}$Ra |
| 5.686 | 95% | $^{224}$Ra |
| 6.051 | 70% | $^{212}$Bi |
| 6.080 | 27% | $^{212}$Bi |
| 6.288 | 100% | $^{220}$Rn |
| 6.778 | 100% | $^{216}$Po |
| 8.784 | 100% | $^{212}$Po |

that did not detect the alphas due to the thick Mylar and high energy thresholds, were dealt with as discussed in the Additional Calibrations section.

### 1. Getting the Centroid

A raw alpha spectrum is shown in figure 16. To find the centroid a Gaussian fit function in ROOT was used. The centroid channel was assigned the corresponding alpha energy and a linear channel-energy relation can be found using equation 3.1, where Y is the energy, m is the slope parameter, X is the channel, and b is the Y intercept. The energy versus channel plots (figure 17) for each detector were created and the best-fit line was found. The $R^2$ value was near 0.99 for the majority of the detectors.

$$Y = mX + b \tag{3.1}$$

### 2. Double Alphas

Figures 18 to 22 show each of the 5 rings and the alpha spectra for each detector in the ring. Ring A has no alpha spectra and were calibrated by fitting to a detector in ring B, as described in the Additional Calibrations section. Ring B has a nice set of alpha peaks in each detector, there is a higher energy set that can just be seen above the background. The double peaking can be due to a slight misalignment of the Mylar, with the higher energy set not passing through the Mylar. The dominant peaks are typically lower energy (i.e. they passed through the Mylar) and they are selected for use. Ring B has 2.535 mg/cm$^2$ Mylar in front, the apparent thickness depends on the specific detector, but for example detector 12, shown in figure 23, has an apparent thickness of 2.569 mg/cm$^2$ which makes the 8 MeV alpha loose 1.680 MeV. The difference in energy between the double peaks, at channels 759 and 860, for detector 12 is 1.646 MeV. In this case the higher energy peak had missed the Mylar and in the calibrations the lower energy peaks (i.e. those that passed through the Mylar) are used.

Ring C has the worst alpha spectra of all the rings with double peaking at about the same yields, i.e. no dominant set of peaks. The higher energy set was aasumed to pass through the Mylar and were used in the calibrations. The reason for this choice is that the higher energy peaks are relatively constant around the ring, while the lower energy peaks rise and fall around the ring. This suggests that there could be something in the way of some of the fragments which is not centered about the beam axis. Ring D has a dominant peak that is consistent throughout the ring, which is

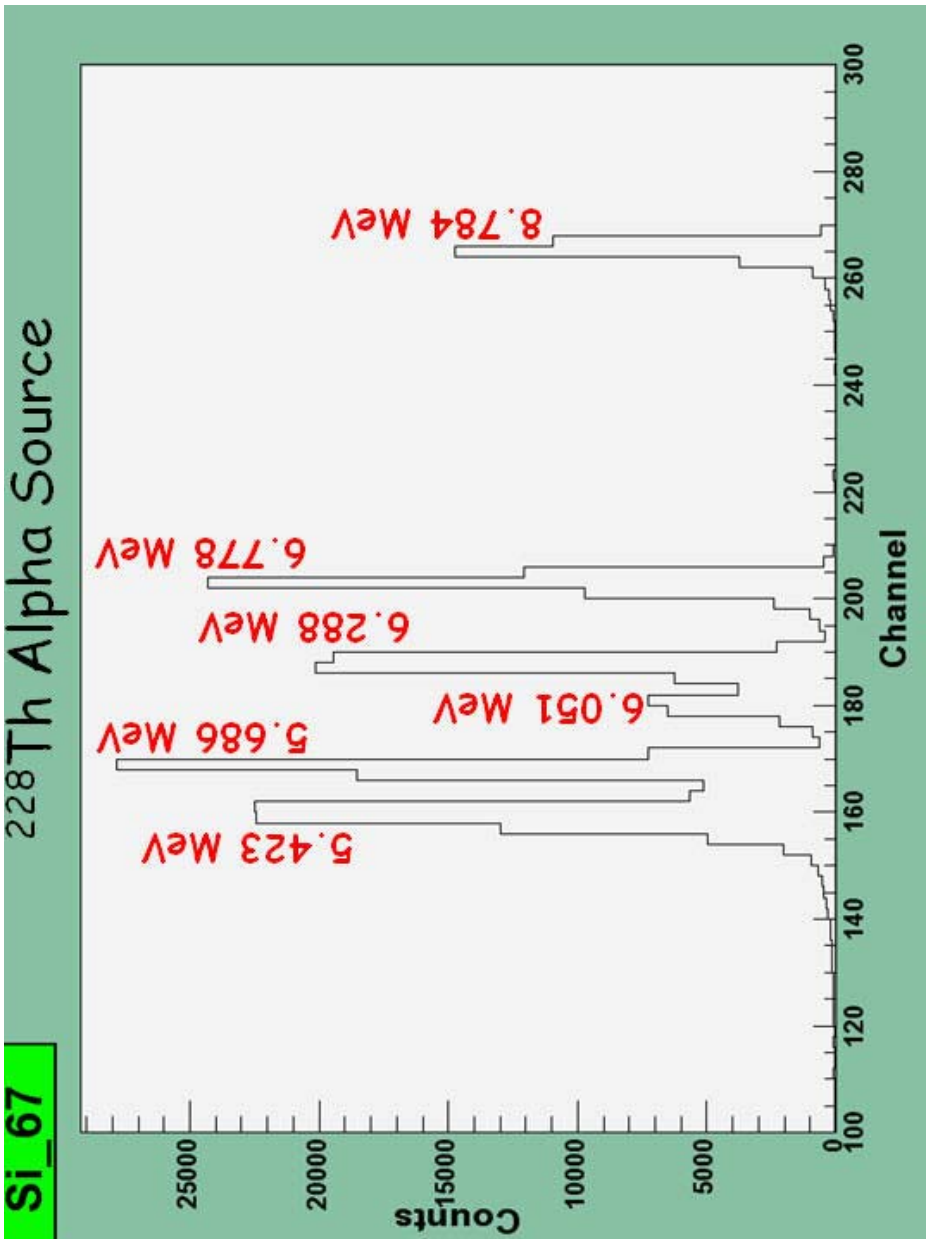


FIG. 16. An example $^{228}$Th spectra from ring E detector 67.

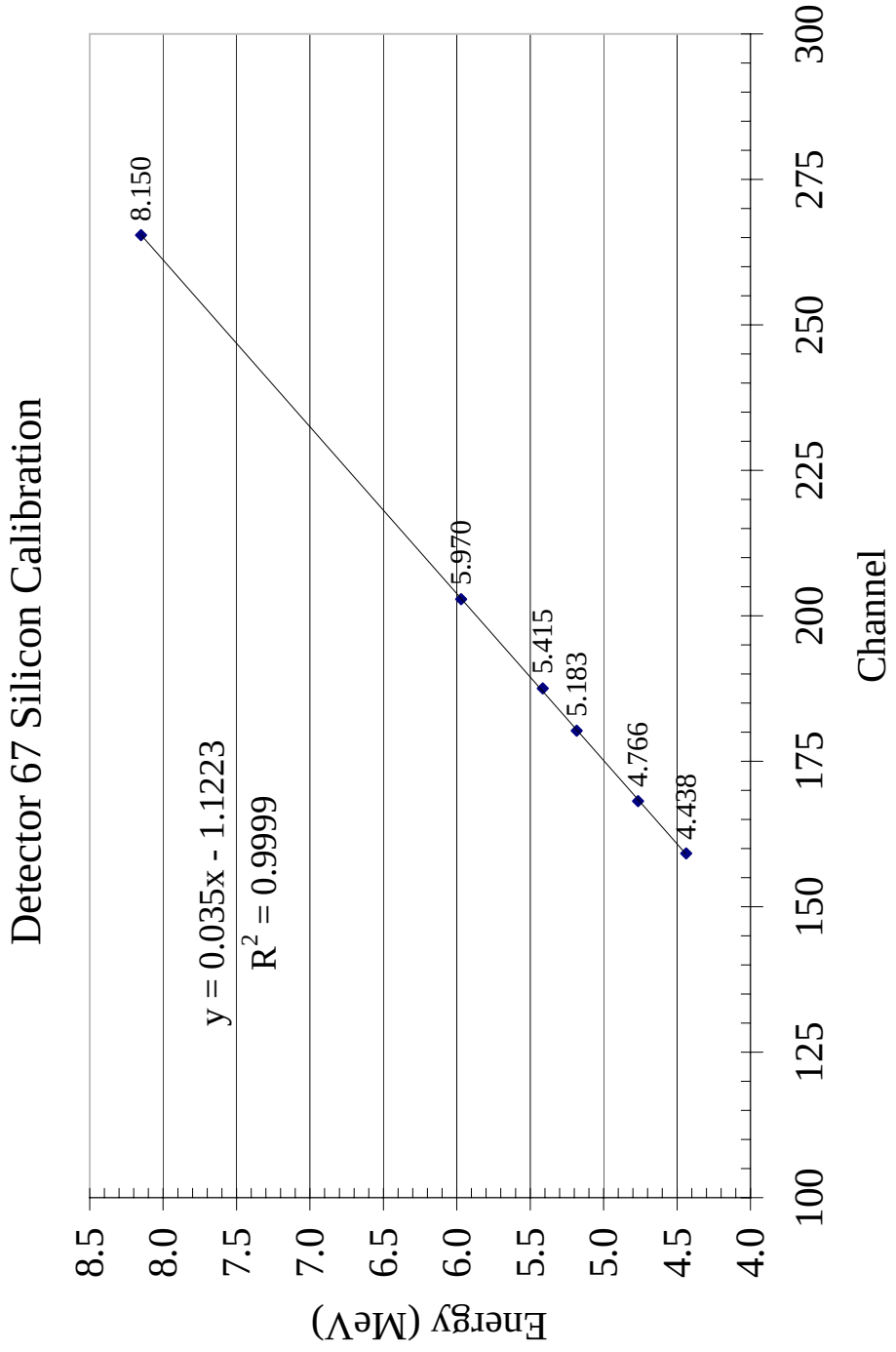


FIG. 17. Typical energy versus channel plot.

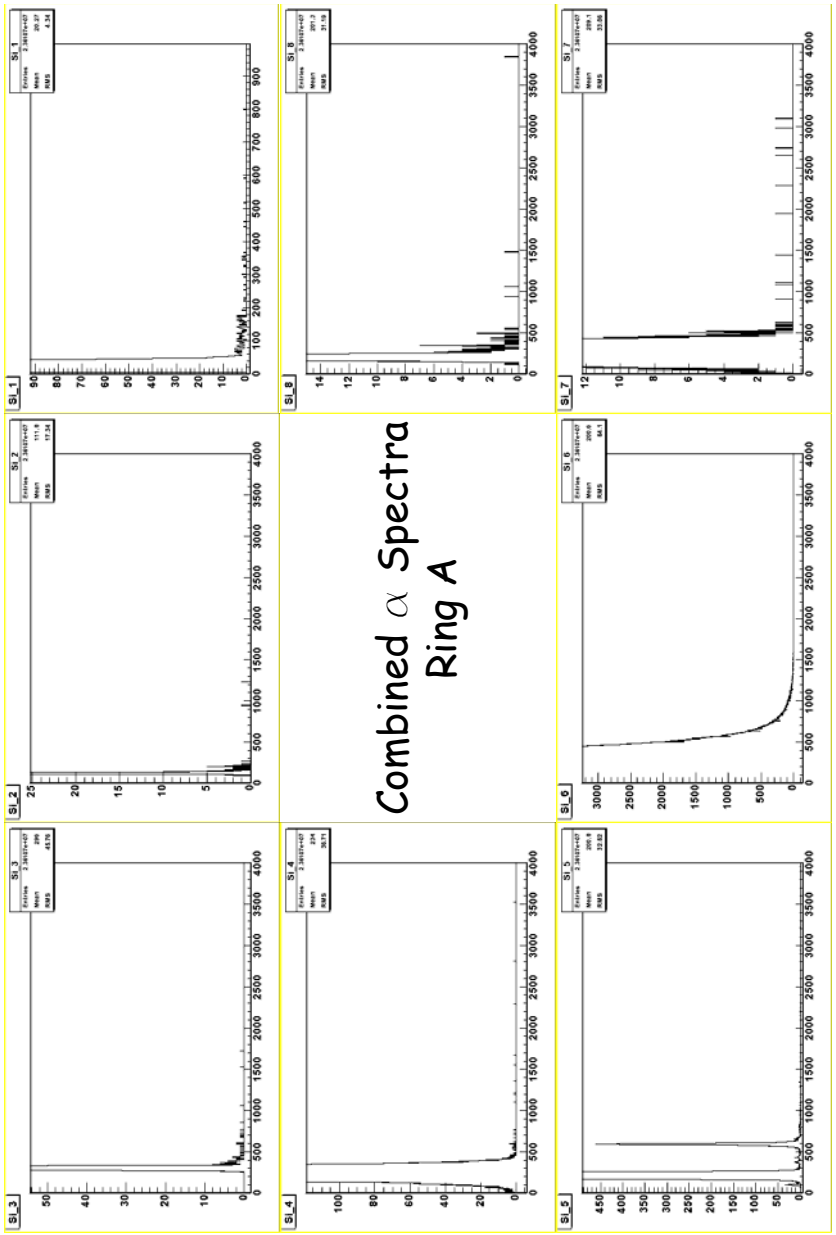


FIG. 18. Ring A alpha spectra.

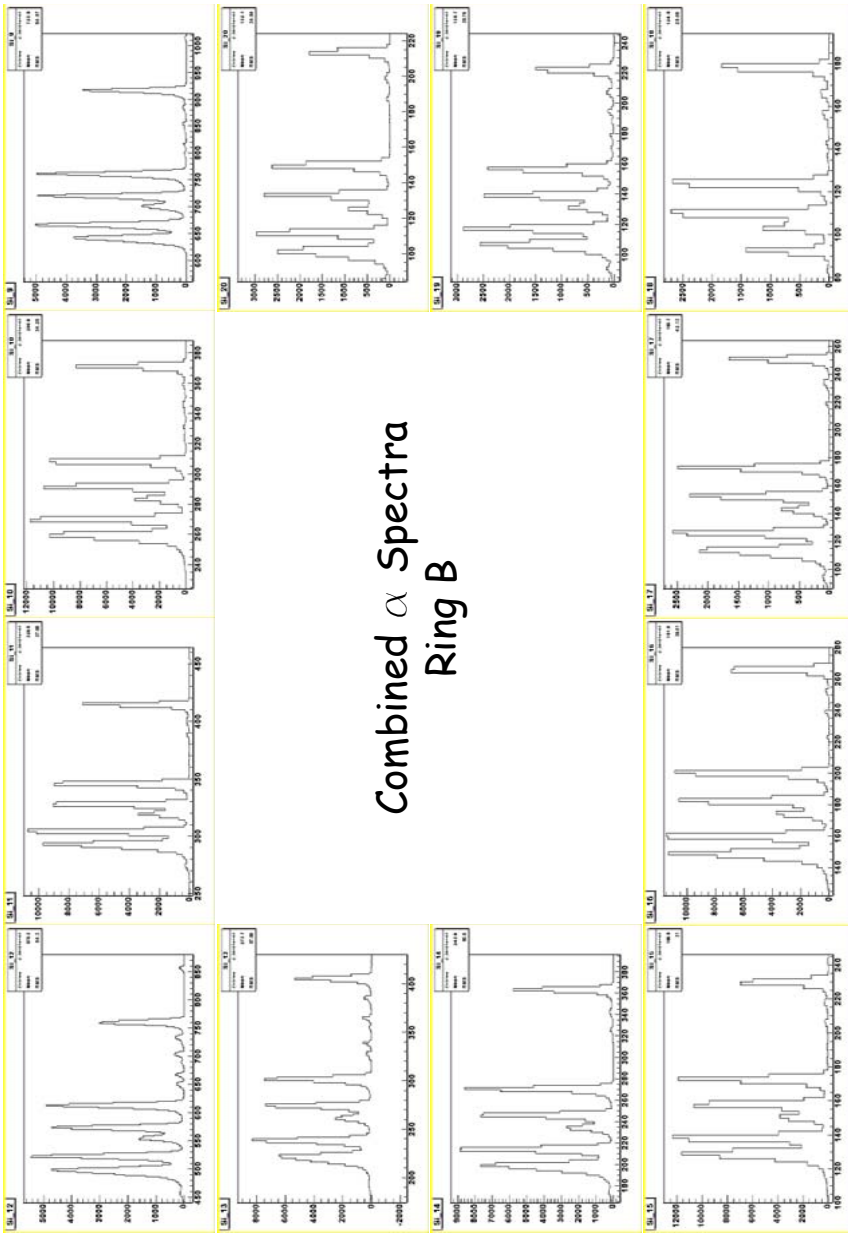


FIG. 19. Ring B alpha spectra.

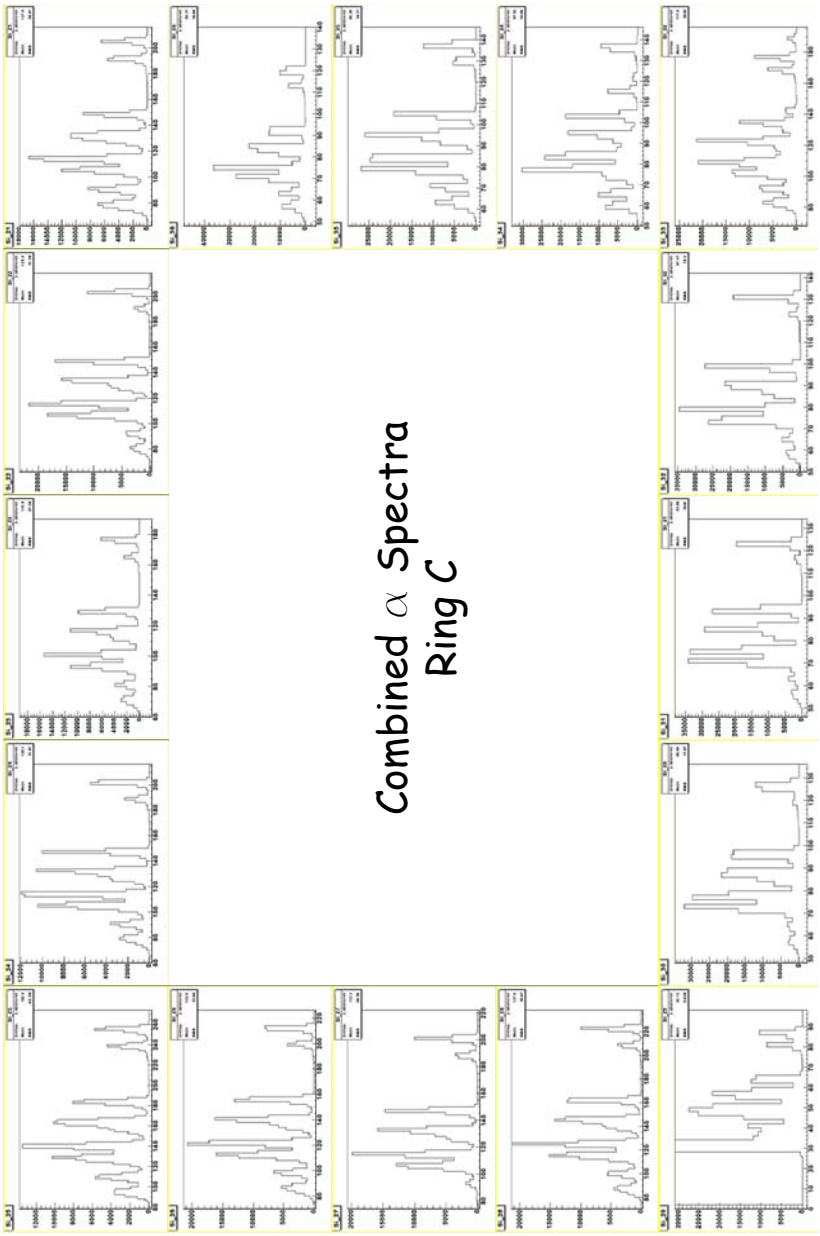


FIG. 20. Ring C alpha spectra.

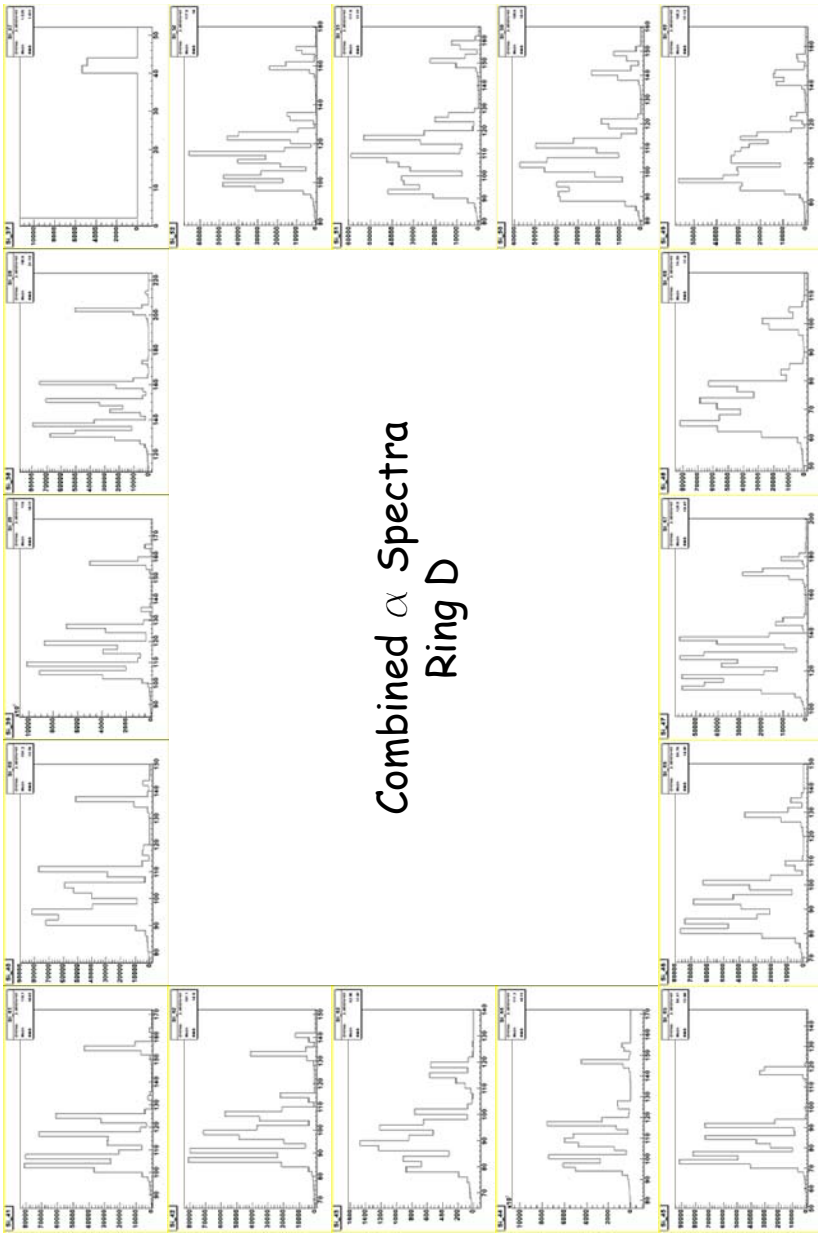


FIG. 21. Ring D alpha spectra.

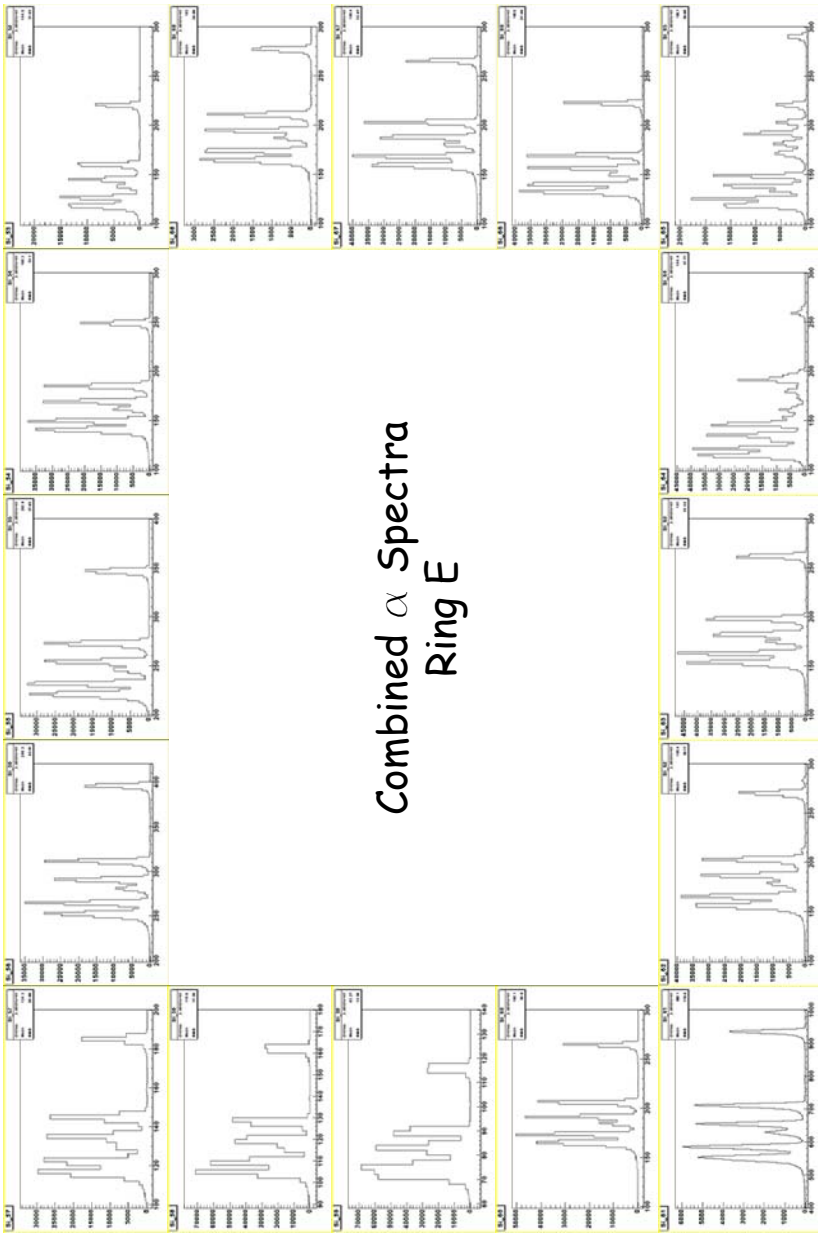


FIG. 22. Ring E alpha spectra.

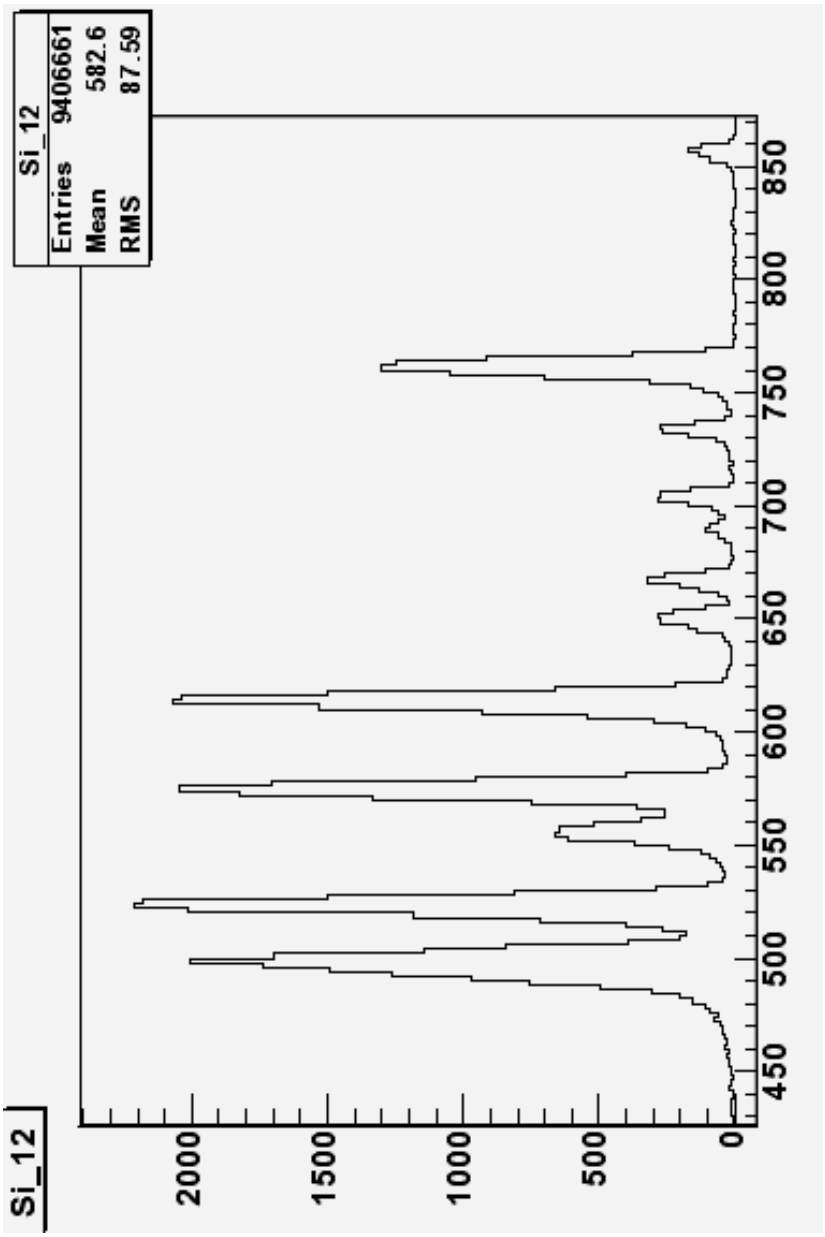


FIG. 23. The double alpha spectrum for detector 12 in ring B showing the higher energy set of alpha peaks, due to missing the Mylar.

used for the calibrations. There is a slight second set of alphas, as was seen in ring B. Ring E has a very clear set of dominant peaks, with the only contamination occurring in the corner.

### 3. Mylar Effects

During this experiment FAUST had Mylar thicknesses of 4.778 mg/cm$^2$ in front of ring A, 2.535 mg/cm$^2$ in front of rings B and C, and 0.833 mg/cm$^2$ in front of rings D and E. The Mylar helps reduce electron noise, but also slightly reduces the energies of particles passing through. This energy loss must be taken into account.

The fragments do not pass through the Mylar perpendicularly, but at an angle, dependent on the detector, so the energy loss is actually greater. An offline analysis was performed to account for these losses. A $^{228}$Th source was measured without any blocking material using an Ortec surface barrier silicon detector [59]. Then additional measurements were made by placing the same Mylar thicknesses that were in front of the FAUST rings in front of the Ortec detector [59]. From this data for each of the seven detected alphas the best fit lines were found as shown in figure 24. In this setup the noise and thresholds were lower and the 5.340 MeV alpha was able to be resolved. All linear fits had an $R^2$ value of 0.989 or better, which justifies using these linear equations to extrapolate the alpha energy from the apparent thickness of the Mylar for each detector in FAUST.

Each detector subtends an angular range, but there is no position sensitivity within a given detector, so only the central angle will be used to calculate the apparent thickness. The percent difference between apparent and perpendicular passage is roughly 1.5% for rings D and E having Mylar of thickness 0.883 mg/cm$^2$. Rings B and C have Mylar of thickness 2.535 mg/cm$^2$, which has a 1% difference. Ring A has a 0.2% difference for a Mylar thickness of 4.778 mg/cm$^2$. The best fit line was found

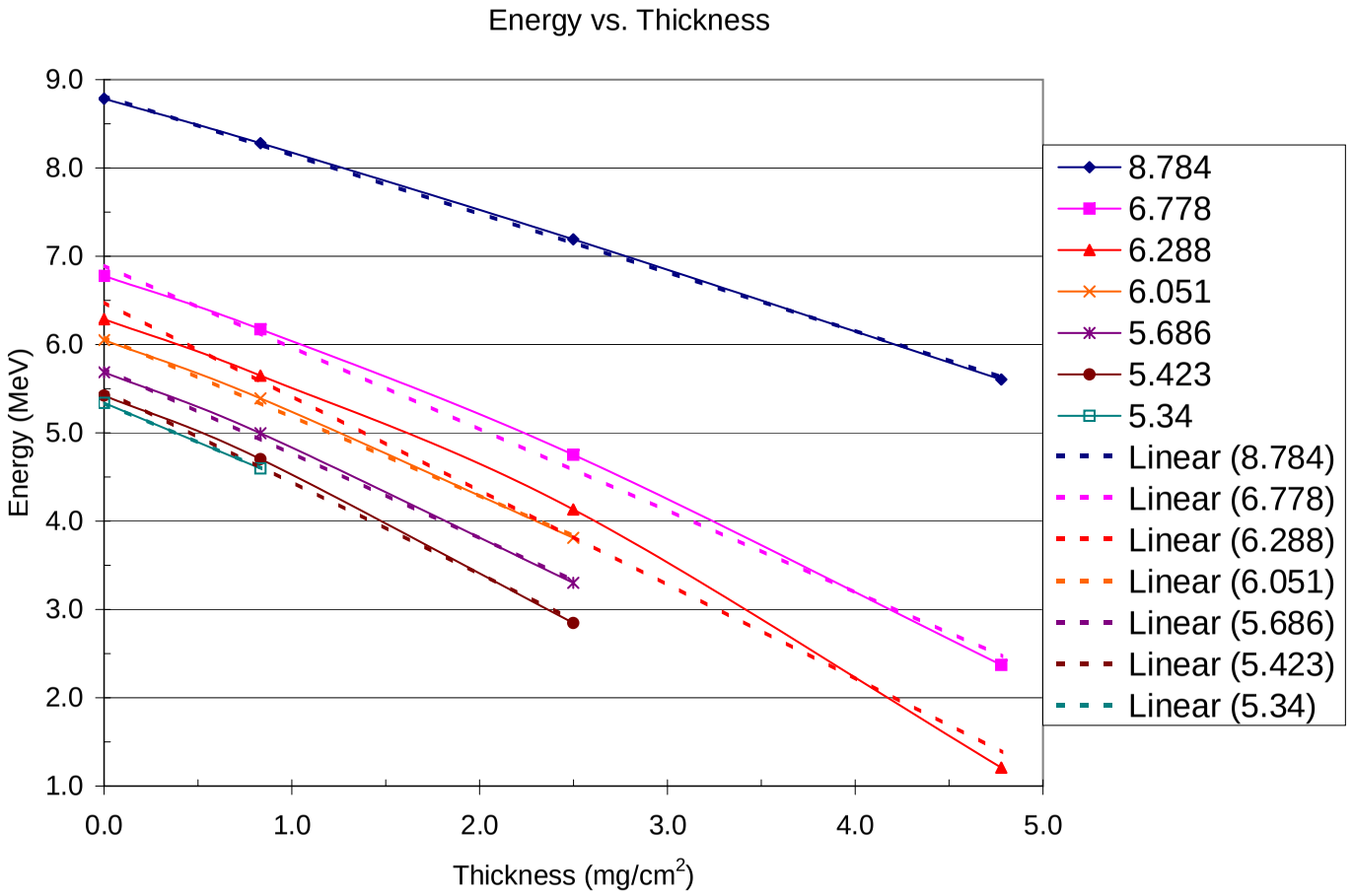


FIG. 24. (Color online) Alpha energy versus thickness for the 7 detected alphas. The best fit lines are used to find the alpha energy after passing through the apparent thickness of Mylar.

for each alpha energy in the energy versus thickness plot. Then using these equations the amount of energy loss can be calculated for each apparent thickness the alphas pass through. The effect of having no Mylar corrections is about 3% higher energies for 0.883 mg/cm$^2$, 5% for 2.535 mg/cm$^2$ and 63% for 4.778 mg/cm$^2$. Therefore this is an important correction for the alpha calibrations.

## D. Cesium Iodide Calibrations

Energy deposited in the CsI is related to the light output as described by the Birks equation given in equation 3.2, where L is the light variable and depends on two parameters: a pedestal (L-Parameter1) and a scaling parameter (L/Parameter2) [60]. The $\rho$ is proportional to $\eta Z^2 A$, where $\eta$ is Parameter3, Z is the charge and A the mass of the nuclide being used.

$$E = \sqrt{L^2 + 2\rho L(1 + log(1 + L/\rho))} \tag{3.2}$$

The Si calibration parameters and a three line minimization were used to calibrate the CsI detectors. Problem detectors will be discussed in the Additional Calibrations section. Using polyline in ROOT lines were drawn over the nuclides $^4$He, $^7$Li, and $^9$Be shown in figure 25. The lines are drawn on zoomed in spectra, so the lines were carefully drawn on top of the given nuclides. These three nuclides were chosen because they are identifiable in the majority of the detectors.

The x-y coordinates were then placed in an Excel file along with energies calculated by Donna, an energy loss code [61]. Then the experimental and theoretical lines were minimized by simultaneously changing the three parameters of the Birks equation for the best fit.

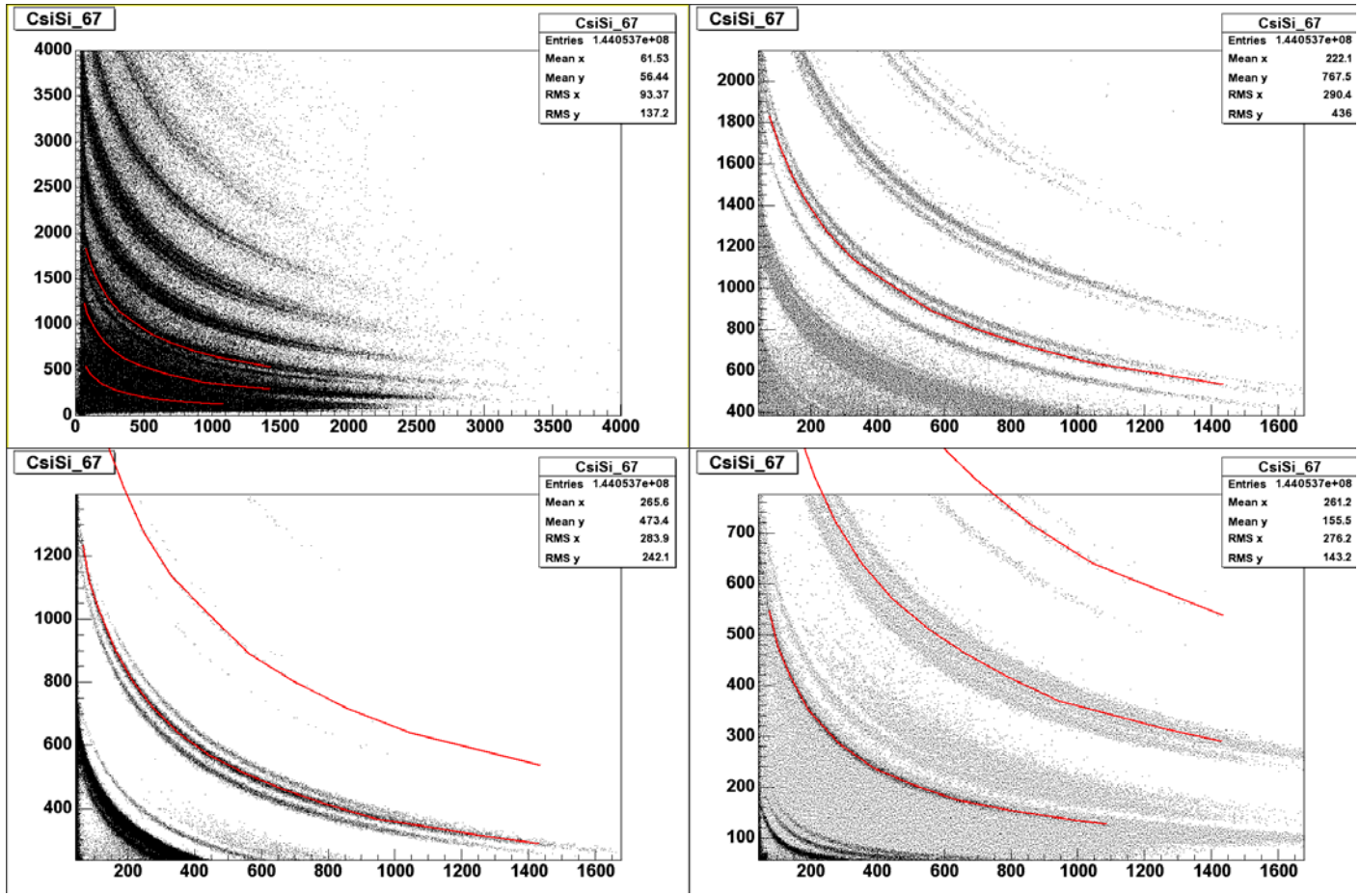


FIG. 25. The three-line calibration. From top left clockwise: full spectrum, zoomed for drawing $^{9}$Be, zoomed for drawing $^{7}$Li, zoomed for drawing $^{4}$He. Note that p, d, t can be discerned in the last panel.

## E. Additional Calibrations

After the Si and CsI calibrations were complete the calibrated energy spectra were created. Then detectors at similar angles were drawn together for comparison. Detectors that had inconsistent energy spectra had their calibrations revisited. The energy spectra were also compared to the energy spectra from Rowland shown in figure 26 [5, 62]. The energy spectra are very similar supporting the quality of the calibrations. The energy spectra are for $^4$He at each of the 13 angles in FAUST, with the smallest angle at the top working down to the largest angles. Note that the energy spectra have been scaled to show shape changes with increasing angle. In this data set there is no isotopic resolution in ring A, which causes the two smallest angle energy spectra to be different from those of Rowland.

The first technique used was the opposite/similar detector technique, which assumes that if two detectors have similar energy spectra (i.e. having the same shape and thresholds), then the calibrations should be similar. For Si detectors in ring A, all eight detectors were scaled to detector 1, so only one set of calibrations would be needed. Then the CsI energy spectra were also scaled to detector 1. Then the CsI spectrum of detector 1 was matched to a detector in ring B. Then several CsI energies were selected and then the Si energy was deduced from the 2D spectra. Donna was used to get the Si energy based on the CsI energy [61]. Finally new calibration constants were derived using the channel-energy relationship. The other detectors that needed to use the similar detector technique were: Si detectors 27 and 42 and CsI detectors 27, 34, 42 and 64.

The other technique used was the forcing technique, where the calibration parameters are changed manually to force the energy spectra to align with the energy spectra of good telescopes at the same angle. The detectors that used the forced

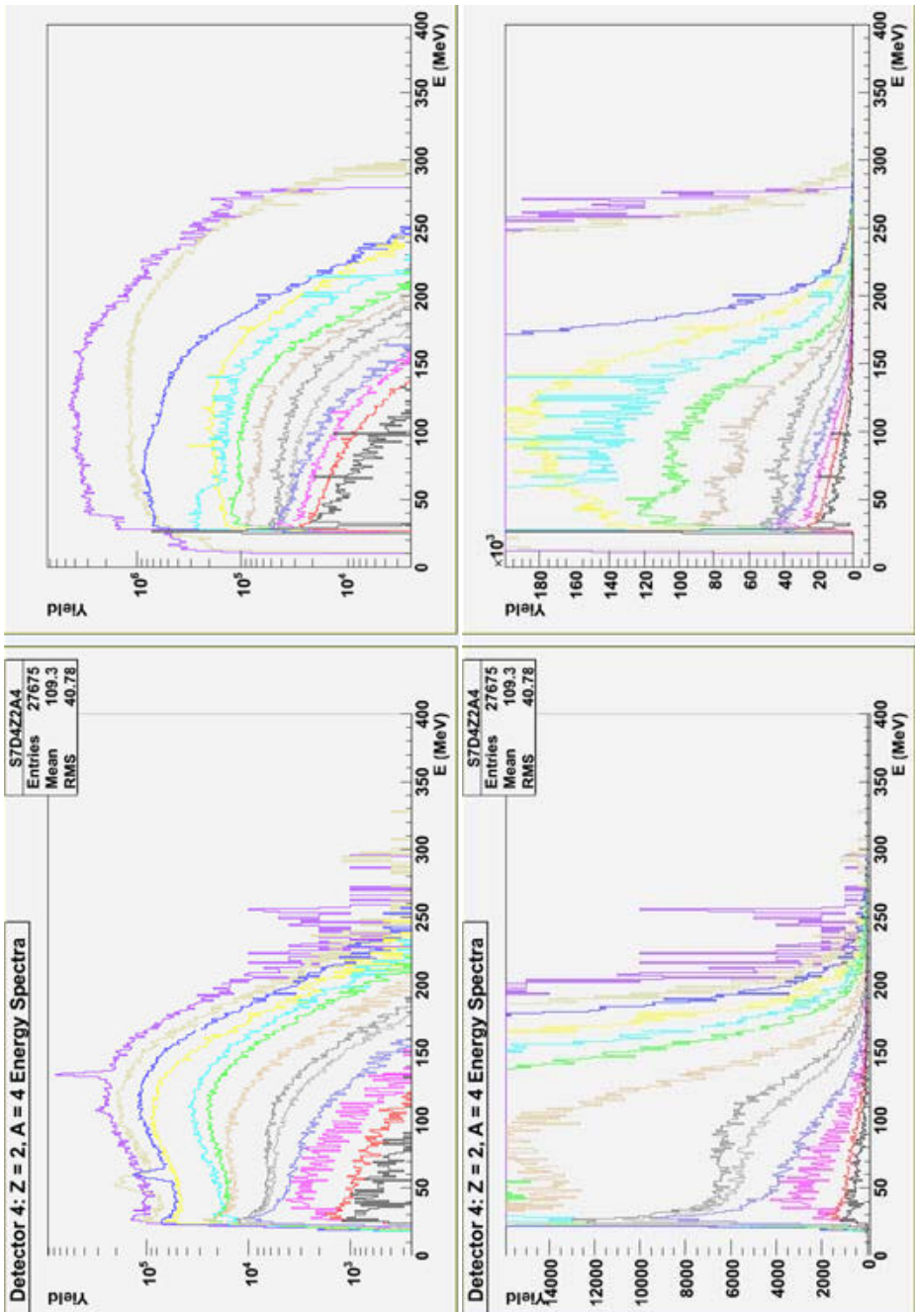


FIG. 26. (Color online) Energy spectra comparison between this data (right) and the mass 20 data of Rowland (left) [5]. The top is on a log scale, while the bottom is linear and expanded to show the tails of the distribution.

technique were: CsI detectors 3, 17, 31, and 35. The CsI energy spectra for ring A were very poor when compared to the other angles. This is due to the poor resolution in ring A, so to improve the calibrations the energy spectra were fitted to an energy spectra in ring B that was calibrated using the 3-line fit. Once all the energy spectra were fitted, the calibrations used in ring B then apply to ring A.

## F. Gating

Gates were drawn on the ΔE-E spectrum shown in figure 27 over elements and isotopes of the elements having sufficient resolution in a ROOT session. Gates were first drawn on the full data set, where all systems were combined, for the highest statistics to be able to extend the gates further and see higher Z and isotopic resolution. Then the gates were overlaid on each of the 12 systems and visually inspected to make sure each gate was good and changes were made when necessary system by system.

Ring B has saturation in elements with high Z, as shown in the ΔE-E spectrum of detector 29 in figure 28. The line in figure 28 is the cut off where the back bending starts occurring and gates were not extended into this region.

Detectors 33, 34, 62, 63 and 64, had a gain change between systems, as demonstrated by figure 29. Here there are distinctly two alpha peaks as well as many more isotopes for each element. The gain changed detectors had their gates drawn system by system.

## G. Full Physics Tapes

After the calibrations and gates were completed the Full Physics Tapes (FPTs) were created. The FPTs contain all experimental information, such that if a later analysis needs different assumptions, all the necessary information is available. The FPTs

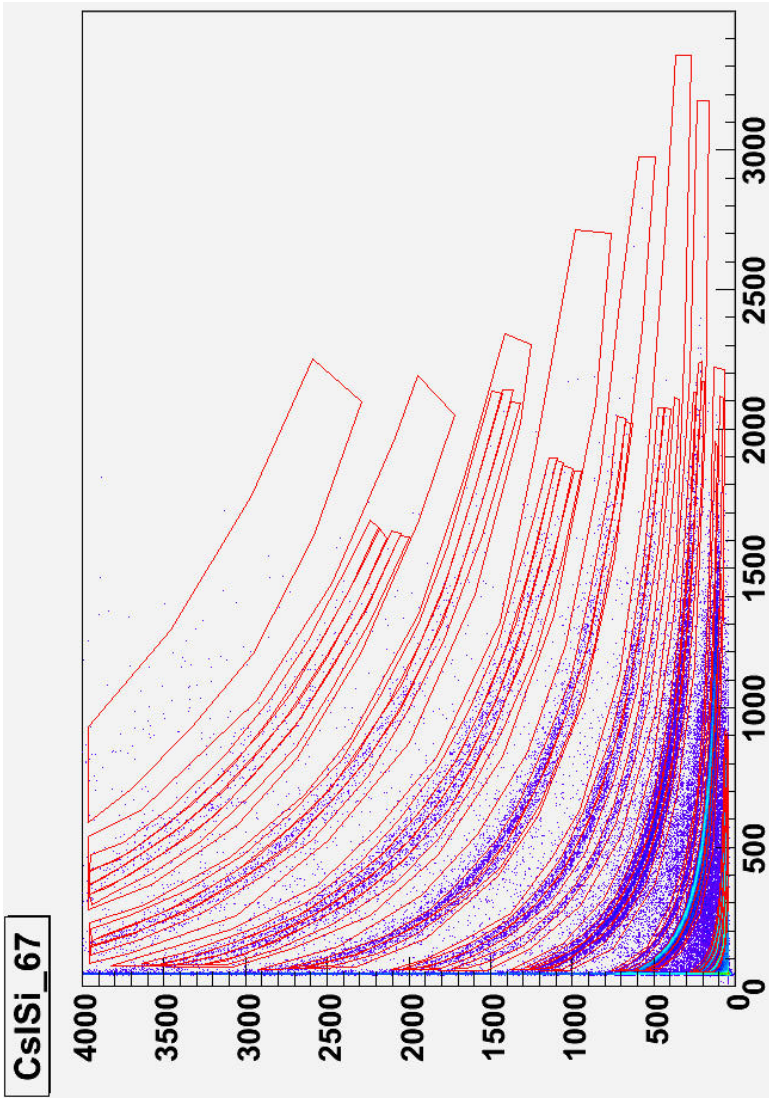


FIG. 27. (Color online) Example of gates. Si channel versus CsI channel spectra of detector 67 from a single system, with total system gates overlaid.

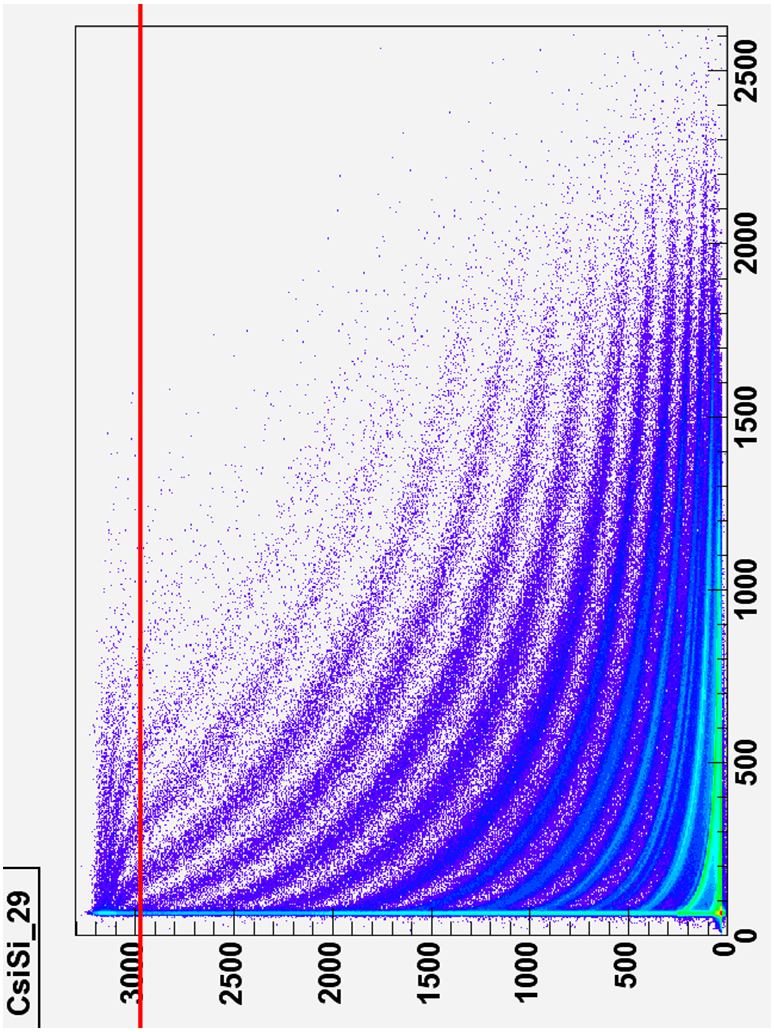


FIG. 28. (Color online) Si versus CsI channel spectrum showing the back bending for high Z (above line).

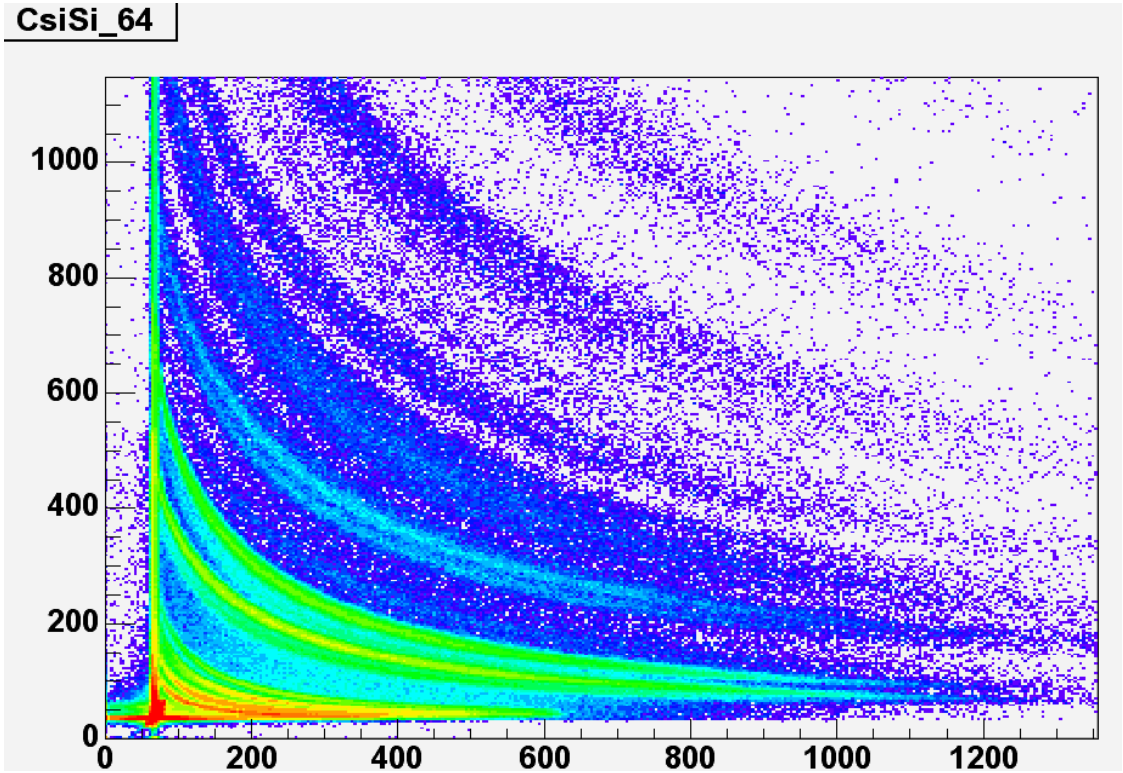


FIG. 29. (Color online) Si versus CsI channel spectrum showing that the gain changed for the detector by showing the double isotope lines.

contain the multiplicity of the event followed by the flag, Z, A, Si energy, CsI energy and detector number of each fragment. The flag for a given fragment is created by calculating the total score of the fragment, where the scores are as follows:

1 point: Elementally identified fragment (i.e. fragment falls within an elemental gate (Z))

2 points: Isotopically identified fragment (i.e. fragment falls within an isotopic gate (A, Z))

4 points: Second isotopic gate (i.e. fragment falls within a second isotopic gate (A+1, Z))

16 points: Second element gate (i.e. fragment falls within a second elemental gate (Z+1))

The reason for the second isotopic and element gate scores, is that the isotopic gates are drawn in a ROOT session from a series of hand picked points, and when the points are connected, slight overlap may occur. Adding the fragment points together provides the fragment flag value. Here is the list of the possible flags, what they mean, and how many fragments fall into that flag in parentheses:

1: Elementally identified fragment (i.e. the fragment falls within a single elemental gate, but not in an isotopic gate ($10^5$))

2: Isotopically identified fragment (i.e. the fragment falls within a single isotopic gate, but not in an elemental gate ($10^2$))

3: Both isotopically and elementally identified fragment (i.e. the fragment falls within an elemental gate and an isotopic gate ($10^6$))

6: Two isotopic gates (i.e. the fragment falls within two isotopic gates, but outside the Z gate ($10^0$))

7: Two isotopic gates and an element gate (i.e. they fall within two isotopic gates and a Z gate ($10^3$))

17: Double elemental gates (i.e. they fall within two Z gates ($10^0$))

A few flags require further explanation as to their occurence. The flag 2 case occurs from some isotopic gates extending further than the elemental gate. For these fragments the element is known from the isotopic gate. Flag 6 is a very rare occurrence (one in a million) where two isotopic gates overlap and extend further than the elemental gate. Isotopic gates are drawn very close to one another, so some overlap occurs. On the other hand elemental gates are separated by large space in the spectrum, however at low CsI energy, where all the elemental gates curve upwards, there is a rare case (again one in a million) where two elemental gates could overlap. However there are no cases where a fragment has an isotopic gate and two elemental gates or two isotopic gates and two elemental gates.

The flag is used to identify what assumptions need to be made. For example a fragment in a double gate is not uniquely identified, so an assumption must be made to determine what the fragment will be during analysis. In this case the ratios between isotopes and elements are found using only the uniquely identified fragments (flags 2 and 3) and a random number generator is used to select between the two choices. This keeps the same ratios throughout the data when all flags are used. Similarly for non-isotopically identified fragments, one must assume an A, which again is based on the fractional yields of uniquely identified fragments (flags 2 and 3). However, the CsI calibration requires knowledge of the A before the distribution from isotopically identified fragments is known, so the most stable A is used. The error involved in using a different A can be seen by an example. Lithium has 3 isotopes seen in the data, 6, 7 and 8. For example the CsI energy based on a fragment in detector 68 gives 56.52 MeV for $^6$Li, 57.67 MeV for $^7$Li and 58.75 MeV for $^8$Li. Compared to $^6$Li, $^7$Li has 2.04% error and $^8$Li has 3.94% error. These assumed A fragments, however will not be used in the yield calculations, and the energies can be recalculated using

the assigned A in later analyses.

The fractional yields of Z $\leq$ 8 are known for each system from uniquely identified fragments, after the FPTs have been produced. For fragments with Z greater than 8 the assumption was to use the most stable A. The flags are kept throughout the analysis, so analysis can be done on all fragments or just isotopically identified fragments. For double isotopic gates the fractional yields of the two isotopes involved are used along with a random number generator to select between the choices. For double Z gates the fractional yields of the two element gates are used along with a random number generator to select between the choices. Note that all the ratios and fractional yields used, were calculated from all detectors (i.e. all angles). So angular distributions are not taken into account, but none of the fragments that get an assigned A are used in the yield calculations later on, so this bulk assumption is fine and can be changed in later analyses.

## H. Modified Physics Tapes

From the FPT the Modified Physics Tapes (MPTs) were produced. Cuts, such as multiplicity, total A or Z and Flags, could be applied at this stage if needed, by applying cuts at this early stage the analysis at later stages proceeds much faster. These cuts were used in the developmental stages of the analysis codes. Once the codes were finalized the MPTs were calculated without cuts. The only difference between the FPT and MPT is the addition of the total A and total Z of each event, which uses all flags.

## I. Reduced Physics Tapes

The MPTs need several assumptions to create Reduced Physics Tapes (RPTs). The first assumption is how to assign an unknown mass. Using isotopically identified fragments (flags 2 and 3) the mass distribution of each element was determined. Then using this distribution and a random number generator the unknown masses were assigned. This way the distributions remain unchanged. Since the highest isotopically resolved element is Oxygen, the heavier elements use the most stable mass.

The next assumption is how to handle the double Z gates. Using the known Z distributions, the ratio of each element with its neighbors is calculated. Then these ratios and a random number generator are used to assign a single gate to that fragment. The final assumption is how to handle double isotope gates. Using the isotopically identified fragment yields, the isotopic ratios are calculated. Then these ratios are used along with a random number generator to assign a single isotopic gate.

## J. Reconstructed Physics Tapes

Here a brief description of the reconstruction is given, a full step by step reconstruction of an event is given in appendix A. To reconstruct an event the quasiprojectile charge, $Z_{qp}$, and apparent quasiprojectile mass number, $A_{qp}$, are calculated using equations 3.3 and 3.4, where the summations are over the charge of the fragment, $Z_f$, and the mass number of the fragment, $A_f$, respectfully.

$$Z_{qp} = \sum Z_f \tag{3.3}$$

$$A_{qp} = \sum A_f \tag{3.4}$$

The apparent quasiprojectile excitation energy is calculated using the balance of energy given by equation 3.5, where the masses can be calculated from the mass number and the mass excesses, which are known from the mass tables of Audi & Wapstra [22, 21, 20]. The energy of the fragment in the center of mass frame is given by equation 3.6, where the velocity of the fragment in the center of mass is given by equation 3.7. Then the velocity of the fragment defined by equation 3.8 and the velocity of the quasiprojectile defined by equation 3.9. The total momentum is given by equation 3.10 and the total mass is given by equation 3.11

$$E^*_{qp_{Apparent}} = \sum(m_f + E_{f_{com}}) - m_{qp} \tag{3.5}$$

$$E_{f_{com}} = 1/2 m_f v^2_{f_{com}} \tag{3.6}$$

$$v^2_{f_{com}} = v_f - v_{qp} \tag{3.7}$$

$$v_f = \sqrt{2E_f/m_f} \tag{3.8}$$

$$v_{qp} = p_{total_f}/m_{total_f} \tag{3.9}$$

$$p_{total_f} = \sum v_f m_f \tag{3.10}$$

$$m_{total_f} = \sum m_f \tag{3.11}$$

To check that the reconstructed source is projectile-like, the velocity spectra, shown in figure 30, can be used. Quasitarget sources would peak around 0.00 c ,

while mid-velocity (neck) sources would peak around 0.13 c. Quasiprojectile source would peak around beam velocity 0.26 c, shown by the arrow. These sources were reconstructed only using isotopically identified fragments. This spectrum shows that the distribution is sharply peaked near the beam velocity and there is little contamination from quasitarget or mid-velocity sources. The multiplicity distribution is shown in figure 31 and shows that the quasiprojectile sources undergo multifragmentation, from the large number of fragments that they break into.

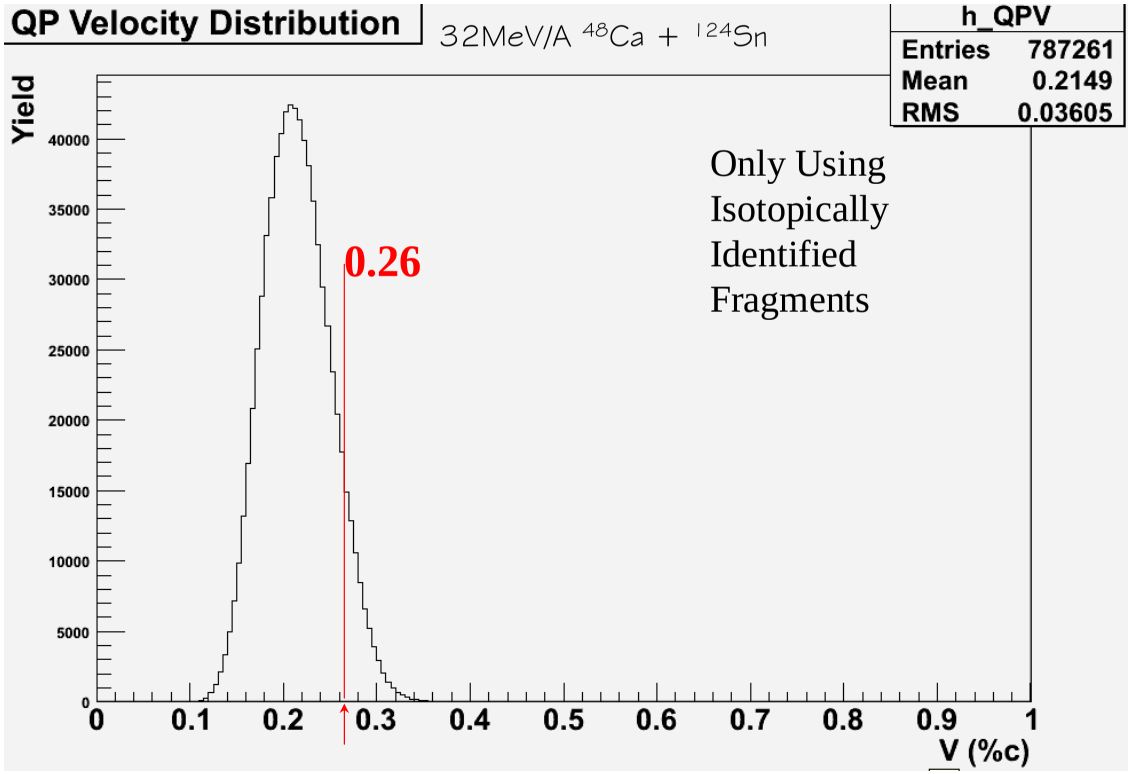


FIG. 30. Velocity spectrum of reconstructed sources from the reaction 32 MeV/nucleon $^{48}$Ca + $^{124}$Sn. The arrow shows the beam velocity at 0.26c.

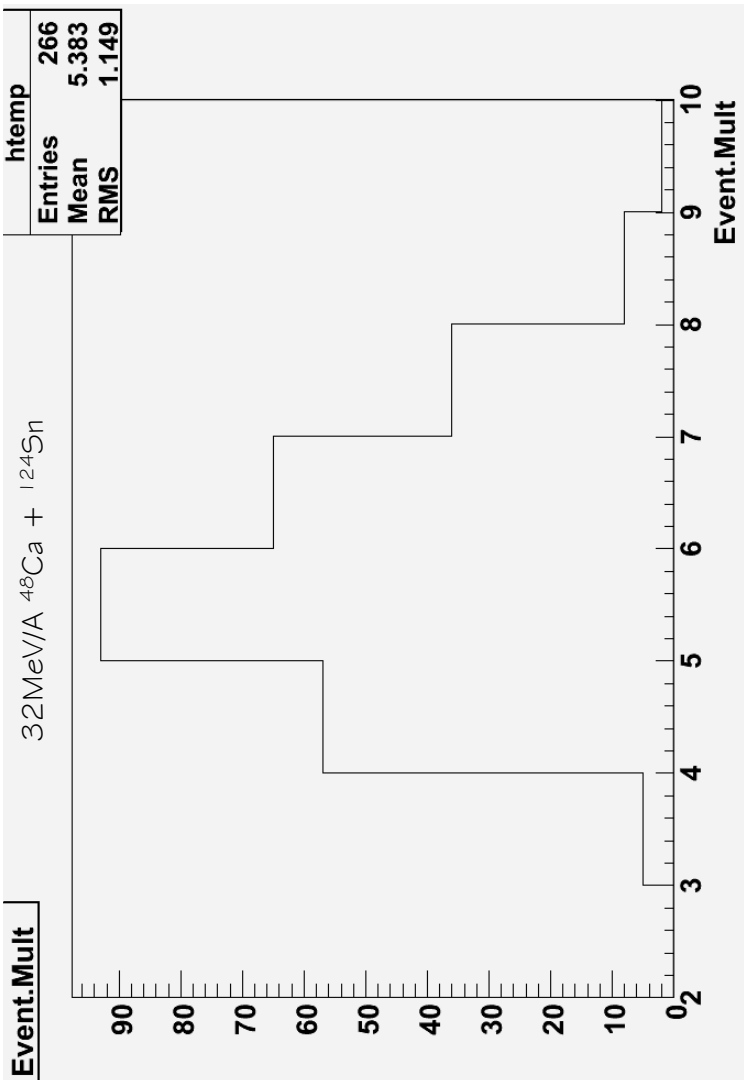


FIG. 31. Multiplicity spectrum of reconstructed sources from the reaction 32 MeV/nucleon $^{48}$Ca + $^{124}$Sn.

# CHAPTER IV

## EXPERIMENTAL RESULTS

This chapter begins with a discussion of the energy spectra of uniquely isotopically identified fragments (these are fragments that have a flag 2 or 3). The energy spectra are used to find the energy thresholds needed to calculate the fragment yields. Next the systems are compared using bulk results, meaning all uniquely isotopically identified fragments will be used regardless of the source that they may have originated from. This allows a general comparison between systems to study the effect of neutron richness on fractional yield ratios, isotopic yield ratios, isobaric yield ratios, and mean N/Z values [63].

Then events that only contain isotopically identified fragments are reconstructed. From this subset of data the requirement that the charge of the quasiprojectile source must be equal to the charge of the beam plus or minus 2 is imposed. The inhomogeneous distribution of N/Z will be discussed in sections on multiplicity of LCPs and IMFs, average N/Z IMF divided by the average N/Z LCP and the isobaric mirror ratios. Finally the mass distributions from reconstruction will be used to find the mean N/Z of the quasiprojectile source and a new technique will be discussed using the isobaric yield ratios to calculate the N/Z of the quasiprojectile source. These results will be compared to the theoretical results in chapter VI to explain the discrepancy between the reconstruction and isobaric yield techniques, as well as determining what symmetry energy best describes the experimental data.

### A. Energy Spectra

Energy spectra were created for every nuclide of every detector for every system. There is a maximum of 25 nuclides ($^{1,2,3}$H, $^{3,4,6}$He, $^{6,7,8}$Li, $^{7,9,10}$Be, $^{10,11}$B, $^{11,12,13,14}$C,

$^{14,15,16}$N, and $^{15,16,17,18}$O), 68 detectors and 12 systems, which would be 20,400 energy spectra (40,800 thresholds: low and high). There were some dead detectors and detectors with fewer identified nuclides, as discussed in chapter III, which decreases the number of energy spectra slightly. There are 13 laboratory angles (3.07, 4.34, 7.01, 9.32, 11.47, 12.81, 16.17, 18.32, 20.06, 25.09, 28.13, 30.62, and 37.09 degrees) in the FAUST array, so all detectors at a given angle have their energy spectra overlaid for each nuclide. If the calibrations and gates are good, then these energy spectra should overlap. Roughly 2,600 energy spectra comparisons were generated and individually studied. An example of the comparison energy spectra is shown in figure 32. In the figure all detectors at 20 degrees have their alpha energy spectra overlaid. Detector 42 shows a high energy threshold, which must be taken into account.

The thresholds were first calculated by visual inspection of the energy spectra for one system, then a ROOT macro was created to automatically find the minimum and maximum thresholds over all detectors at a given angle. The results were compared to the visual results to verify that the code was functioning properly. There was an issue of false thresholds if an energy spectra had fewer than 100 counts. These spectra were not used during the calculation of the thresholds because they do not have distinct high and low thresholds, for example figure 33. Also there was a sharp low energy noise peak in a few of the detectors, and these peaks were also excluded when calculating the thresholds, for example figure 34. Note that the thresholds cannot be collapsed further by angle, because the integration regions becomes too small and statistics are lost.

Another ROOT macro was developed to select the highest low and lowest high threshold at each angle for all systems. When comparing systems the yields must be integrated over the same region. This gives 208 threshold values for the isotopic thresholds and another 208 threshold values for the isobaric thresholds. Note that

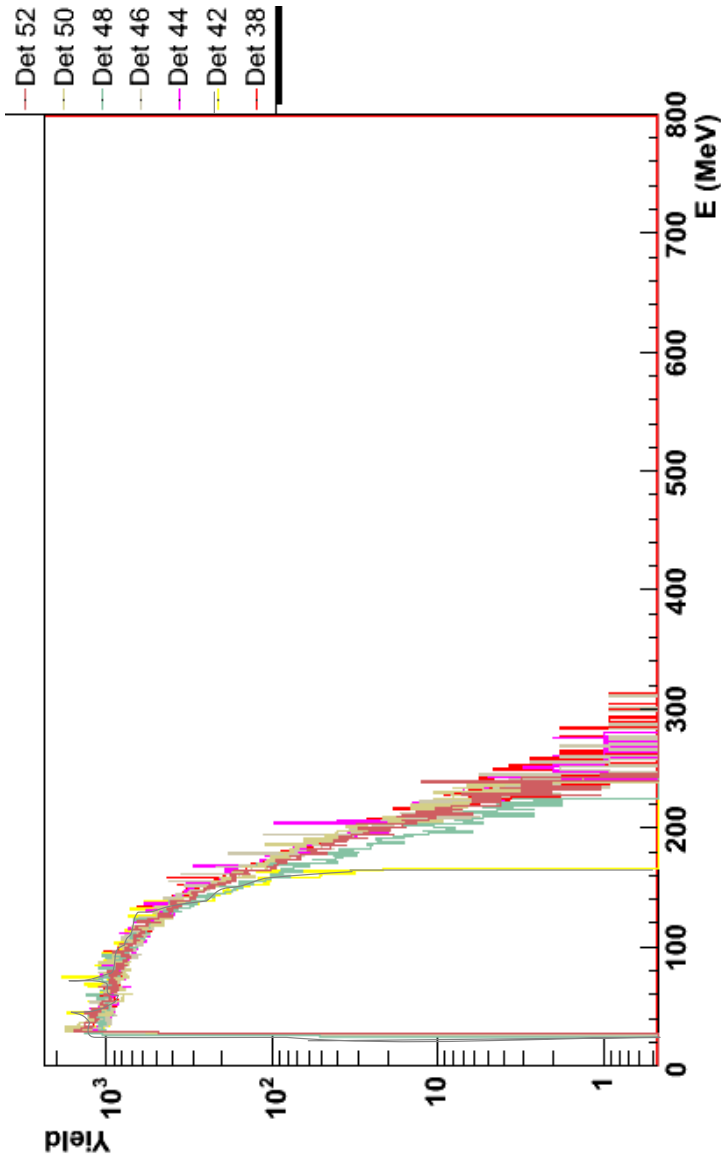


FIG. 32. (Color online) A comparison between $^4$He energy spectra for detectors at 20 degrees.

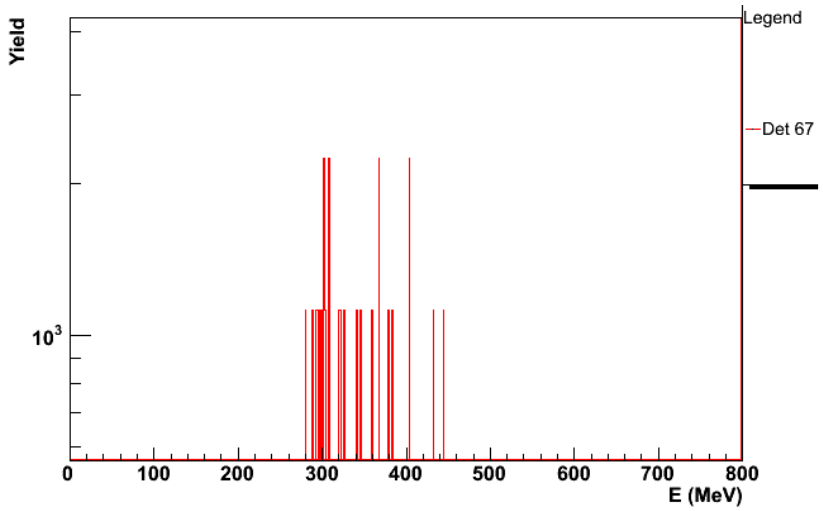


FIG. 33. $^{18}$O energy spectra at 28.13 degrees showing a low statistics energy spectra.

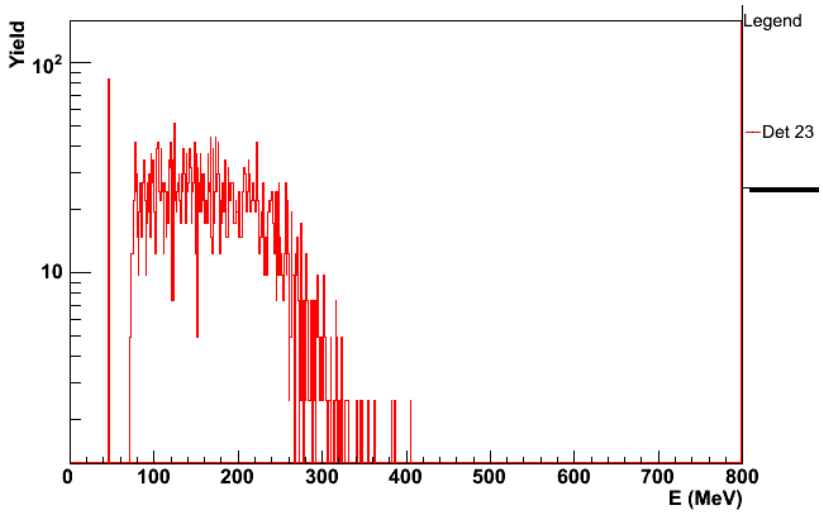


FIG. 34. $^{7}$Be energy spectra at 11.47 degrees showing a low energy noise peak.

only the isobars have consistent integration regions in the isobaric thresholds (table VII), for isotopic comparisons the isotopic thresholds must be used (table VI).

Using these thresholds another ROOT macro was developed to integrate the region between the thresholds of the energy spectra. This was done for both isotopic comparisons and isobaric comparisons. In the next section the bulk yields are discussed, then the last section discusses the exclusive yields.

## B. Bulk Results

For simplicity, only results from the angle at 7 degrees will be shown, the other angles exhibit similar trends and are shown in the appendices. The reason for selecting 7 degrees is this angle has high statistics for all 25 nuclides. In the following subsections there is a general comparison between systems to study the effect of neutron richness on fractional yield ratios, isotopic yield ratios, isobaric yield ratios, and mean N/Z values. The last subsection reviews the general trends observed throughout the various comparisons.

### 1. Fractional Yield Ratios

Using the isotopic yields the fractional yields of a given element can be calculated using equation 4.1 where the yield of a given isotope, $Y(^{A}X_{Z})$, is divided by the yields of all the isotopes of that element, which is independent of the number of events and the systems can be compared. Figures 35 to 42 show the Hydrogen fractional yields to Oxygen fractional yields for all 12 systems at 7.01 degrees. The fractional yields for the other 12 angles are shown in appendix B.

In the Ar systems the more neutron-rich system ($^{124}$Sn) preferentially populates the more neutron-rich fragments, while the neutron-poor system ($^{112}$Sn) preferen-

TABLE VI. The low (top), and high (bottom) thresholds for each element at each angle for isotopic comparisons.

| Z | 3.07 | 4.34 | 7.01 | 9.32 | 11.47 | 12.81 | 16.17 | 18.32 | 20.06 | 25.09 | 28.13 | 30.62 | 37.09 |
|---|---|---|---|---|---|---|---|---|---|---|---|---|---|
| H | NA | 3 | 16 | 15 | 14 | 16 | 15 | 13 | 15 | 12 | 14 | 21 | 65 |
| He | 59 | 52 | 34 | 33 | 34 | 38 | 37 | 32 | 34 | 32 | 47 | 38 | 36 |
| Li | NA | NA | 70 | 56 | 60 | 72 | 60 | 54 | 57 | 55 | 60 | 62 | 66 |
| Be | 78 | 108 | 88 | 83 | 93 | 93 | 91 | 83 | 84 | 82 | 86 | 85 | NA |
| B | NA | NA | 114 | 137 | 124 | 122 | 122 | 109 | 111 | 111 | 119 | 112 | NA |
| C | NA | NA | 174 | 249 | 158 | 152 | 167 | 150 | 155 | 152 | 151 | 154 | NA |
| N | NA | NA | 198 | 368 | NA | 174 | 191 | 190 | 195 | 191 | 200 | 197 | NA |
| O | NA | NA | 250 | NA | NA | 229 | 256 | NA | 238 | NA | 282 | NA | NA |
| H | NA | 73 | 77 | 81 | 65 | 59 | 64 | 63 | 61 | 58 | 34 | 52 | 59 |
| He | 196 | 259 | 173 | 177 | 215 | 171 | 206 | 217 | 166 | 192 | 46 | 124 | 119 |
| Li | NA | NA | 296 | 284 | 325 | 271 | 298 | 340 | 276 | 287 | 254 | 132 | 184 |
| Be | 578 | 366 | 306 | 300 | 372 | 314 | 336 | 366 | 241 | 283 | 206 | 218 | NA |
| B | NA | NA | 412 | 340 | 428 | 406 | 365 | 389 | 381 | 312 | 117 | 244 | NA |
| C | NA | NA | 417 | 471 | 466 | 404 | 375 | 391 | 390 | 267 | 332 | 270 | NA |
| N | NA | NA | 522 | 552 | NA | 460 | 489 | 439 | 393 | 292 | 354 | 330 | NA |
| O | NA | NA | 522 | NA | NA | 497 | 606 | NA | 416 | NA | 425 | NA | NA |

TABLE VII. The low (top), and high (bottom) thresholds for each element at each angle for isobaric comparisons.

| Z | 3.07 | 4.34 | 7.01 | 9.32 | 11.47 | 12.81 | 16.17 | 18.32 | 20.06 | 25.09 | 28.13 | 30.62 | 37.09 |
|---|---|---|---|---|---|---|---|---|---|---|---|---|---|
| H | NA | 3 | 26 | 26 | 26 | 28 | 27 | 25 | 26 | 25 | 26 | 32 | 30 |
| He | NA | NA | 61 | 51 | 52 | 63 | 53 | 48 | 50 | 50 | 51 | 56 | 54 |
| Li | 78 | 108 | 88 | 74 | 88 | 80 | 80 | 72 | 72 | 71 | 75 | 77 | NA |
| Be | NA | NA | 108 | 126 | 116 | 115 | 115 | 105 | 106 | 106 | 111 | 108 | NA |
| B | NA | NA | 149 | 204 | 141 | 135 | 149 | 132 | 137 | 136 | 135 | 140 | NA |
| C | NA | NA | 181 | 349 | 154 | 174 | 162 | 176 | 181 | 176 | 184 | 183 | NA |
| N | NA | NA | 186 | 368 | 158 | 168 | 183 | 184 | 187 | 184 | 194 | 192 | NA |
| O | NA | NA | 198 | 95 | NA | 215 | 223 | 190 | 195 | 191 | 241 | 197 | NA |
| H | NA | 152 | 134 | 136 | 144 | 109 | 131 | 148 | 132 | 129 | 44 | 93 | 103 |
| He | NA | NA | 296 | 268 | 323 | 248 | 272 | 302 | 273 | 246 | 55 | 132 | 195 |
| Li | 578 | 366 | 305 | 288 | 372 | 314 | 336 | 366 | 241 | 283 | 206 | 141 | 205 |
| Be | NA | NA | 398 | 317 | 428 | 406 | 365 | 389 | 284 | 312 | 117 | 234 | NA |
| B | NA | NA | 417 | 346 | 466 | 404 | 375 | 391 | 390 | 285 | 134 | 244 | NA |
| C | NA | NA | 482 | 499 | 510 | 418 | 150 | 439 | 391 | 292 | 354 | 285 | NA |
| N | NA | NA | 482 | 518 | 502 | 428 | 431 | 419 | 419 | 267 | 381 | 306 | NA |
| O | NA | NA | 522 | 578 | NA | 496 | 506 | 473 | 393 | 311 | 432 | 361 | NA |

tially populates the more neutron-poor fragments. Similar behavior is seen in the Ca systems. This trend shows the importance of neutron richness in the system on the neutron content of the fragments produced, which is consistent with other data [64]. Looking at both the Ar and Ca systems together, this trend does not hold, and is due to the projectile charge effect. For example looking at the systems based on the composite system N/Z (shown in parentheses) the order is $^{40}$Ca + $^{112}$Sn (N/Z = 1.17), $^{40}$Ar + $^{112}$Sn (N/Z = 1.24), $^{48}$Ca + $^{112}$Sn (N/Z = 1.29), $^{40}$Ca + $^{124}$Sn (N/Z = 1.34), $^{40}$Ar + $^{124}$Sn (N/Z = 1.41) and $^{48}$Ca + $^{124}$Sn (N/Z = 1.46). The order in the yield plots however is changed with the $^{40}$Ca + $^{124}$Sn moving down two spots in the sequence.

Comparing the energy effect, the higher energy has reduced difference between the neutron-rich and proton-rich systems. This is possibly caused by reduced interaction time between the projectile and target, so less nucleon transfer can occur. The other possible cause is that the higher energy systems populate a different excitation energy distribution, leading to different multifragmentation processes.

$$FractionalYield = \frac{Y(^{A}X_{Z})}{\sum Y(^{A}X_{Z})} \tag{4.1}$$

### 2. Isotopic Yield Ratios

Using the isotopic yields, the isotope ratios were calculated. Figure 43 shows the isotopic ratios for all systems at 7.01 degrees. The isotopic yield ratios for the other 12 angles are shown in appendix C. The trends observed in the fractional yields are the same for the isotopic yields. The more neutron-rich systems populate more neutron-rich nuclides and the difference between the extreme systems decreases with increasing energy.

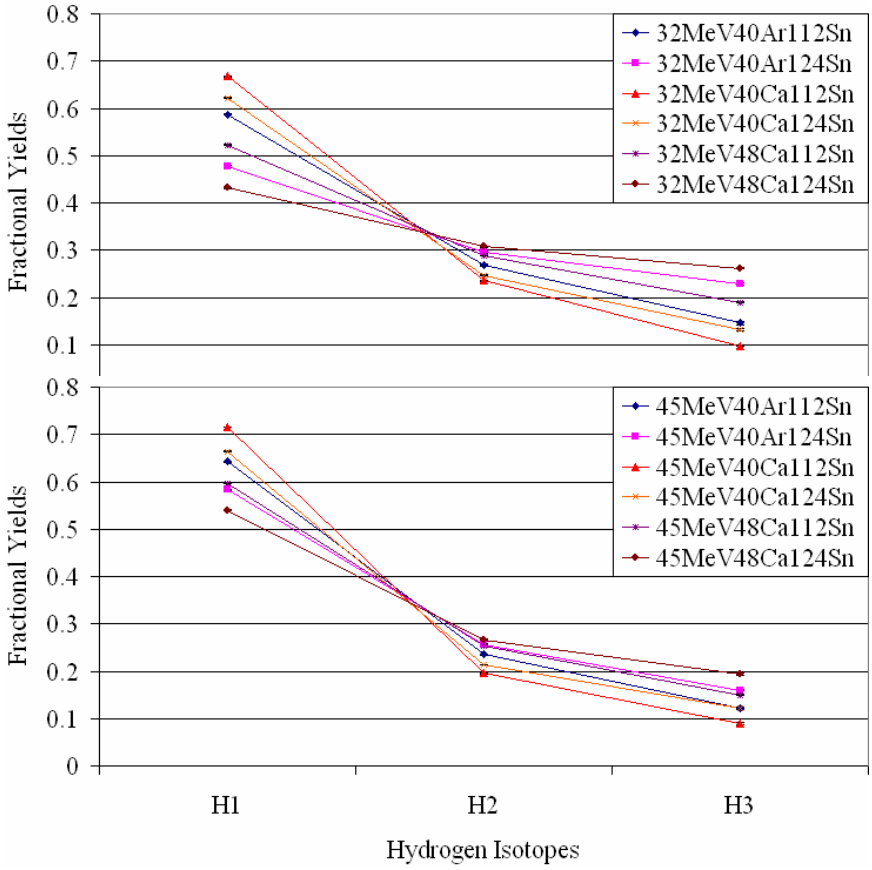


FIG. 35. (Color online) Hydrogen fractional yields at 7.01 degrees.

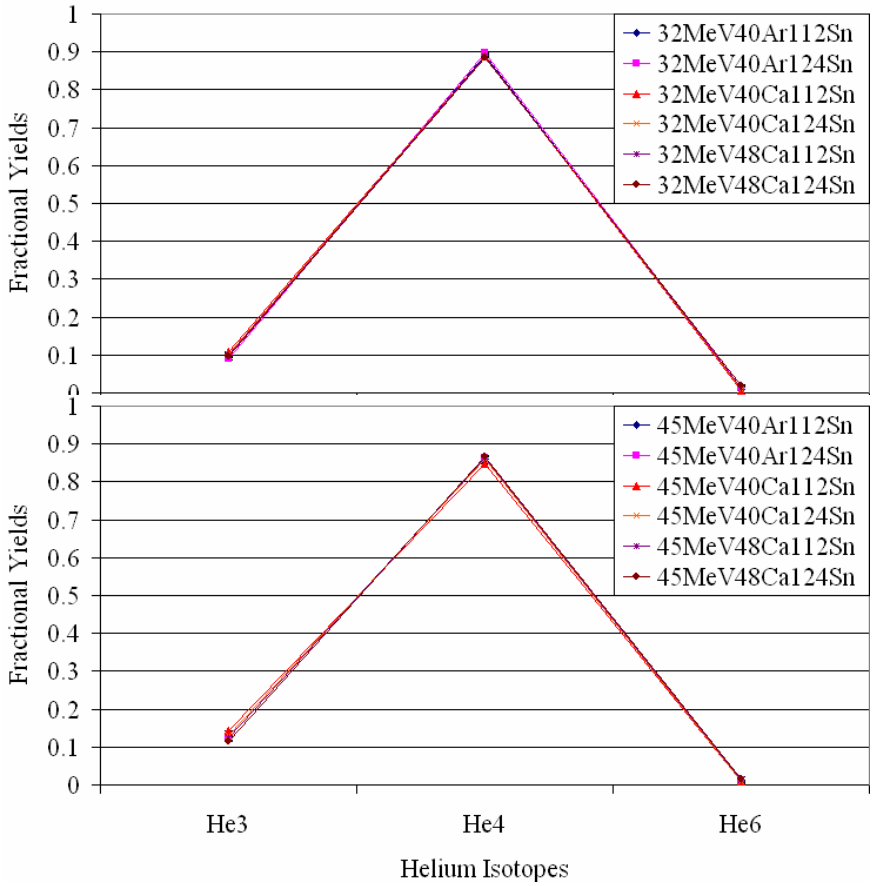


FIG. 36. (Color online) Helium fractional yields at 7.01 degrees.

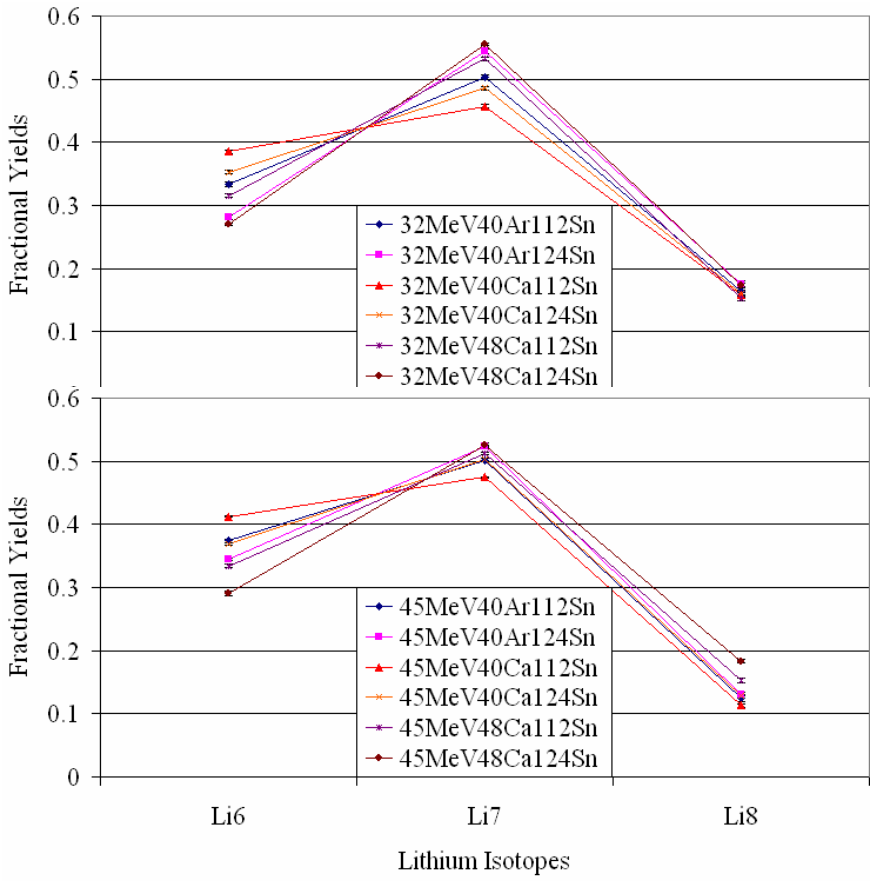


FIG. 37. (Color online) Lithium fractional yields at 7.01 degrees.

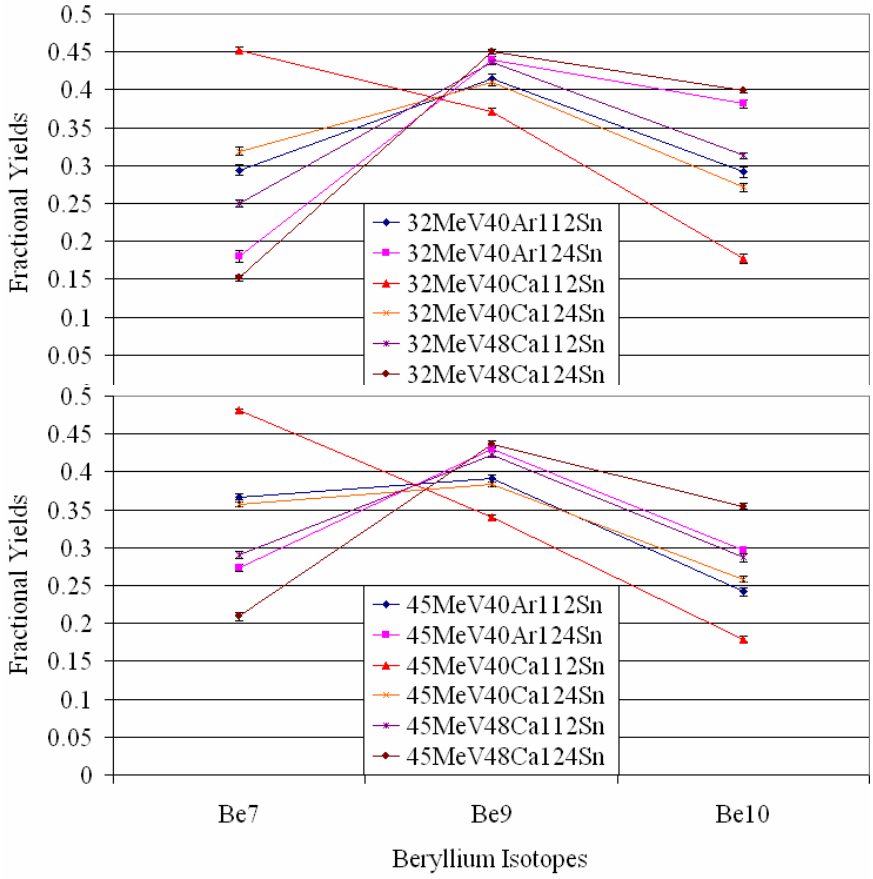


FIG. 38. (Color online) Beryllium fractional yields at 7.01 degrees.

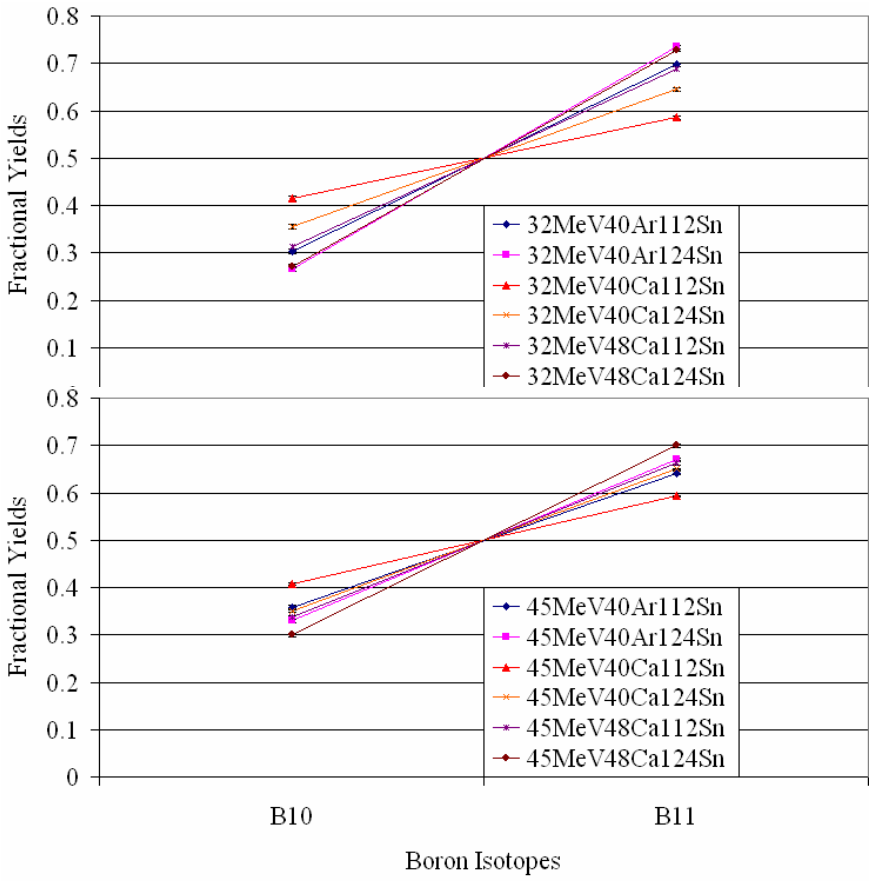


FIG. 39. (Color online) Boron fractional yields at 7.01 degrees.

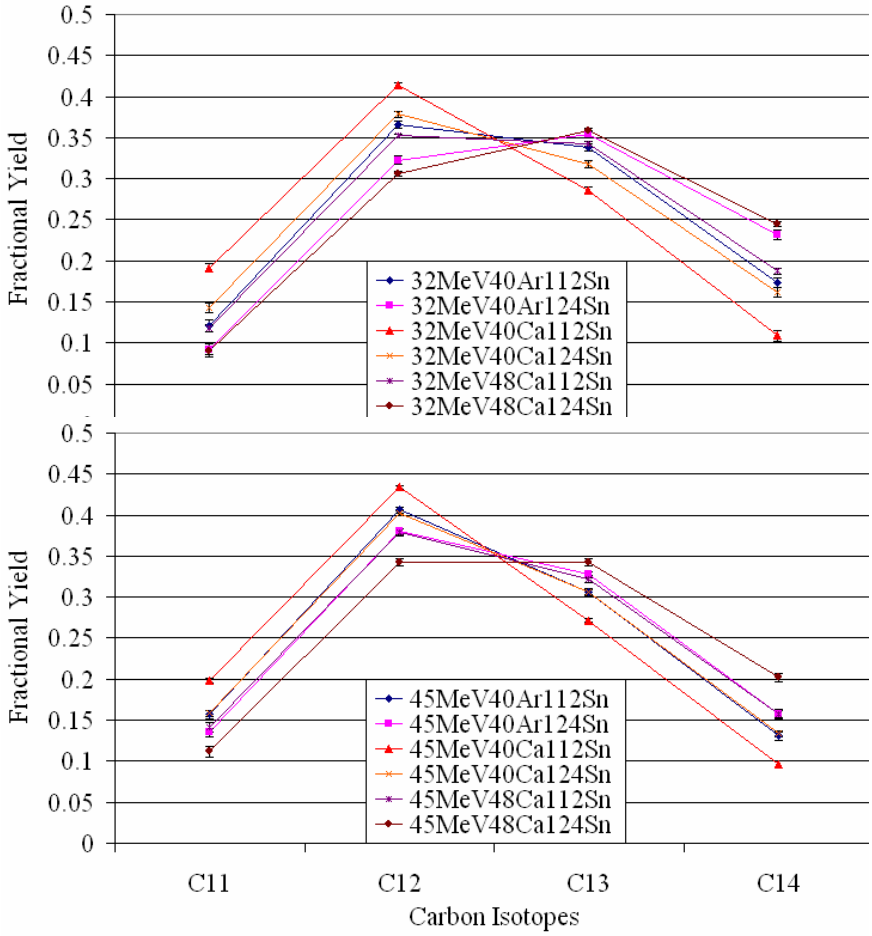


FIG. 40. (Color online) Carbon fractional yields at 7.01 degrees.

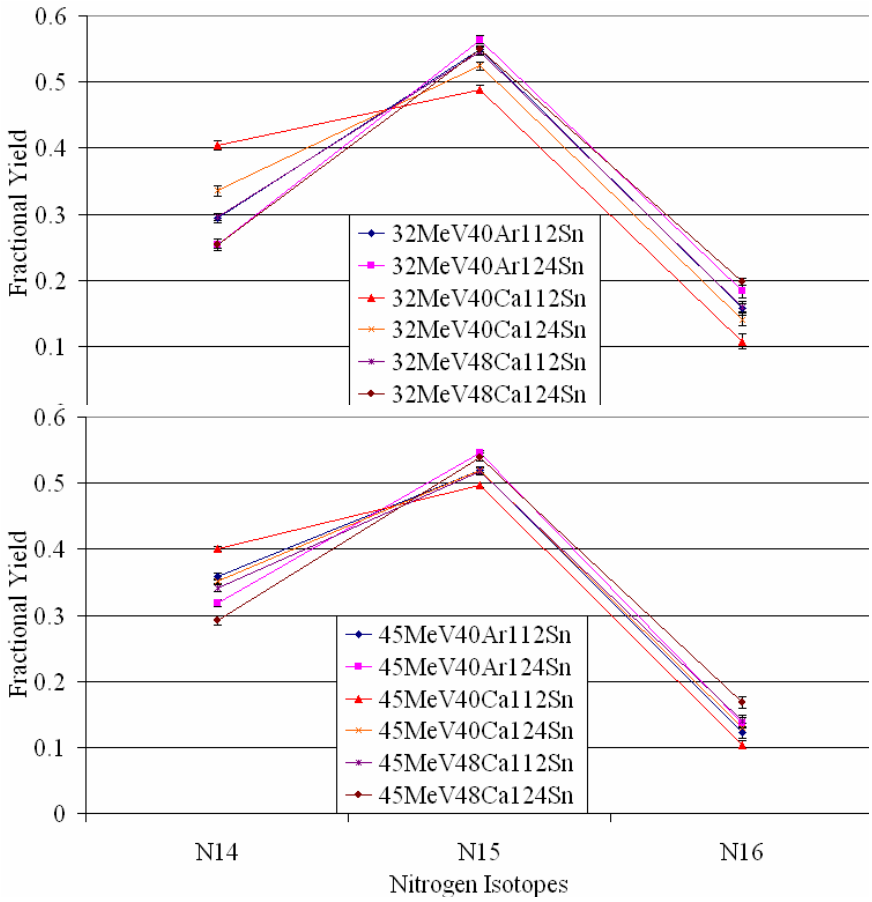


FIG. 41. (Color online) Nitrogen fractional yields at 7.01 degrees.

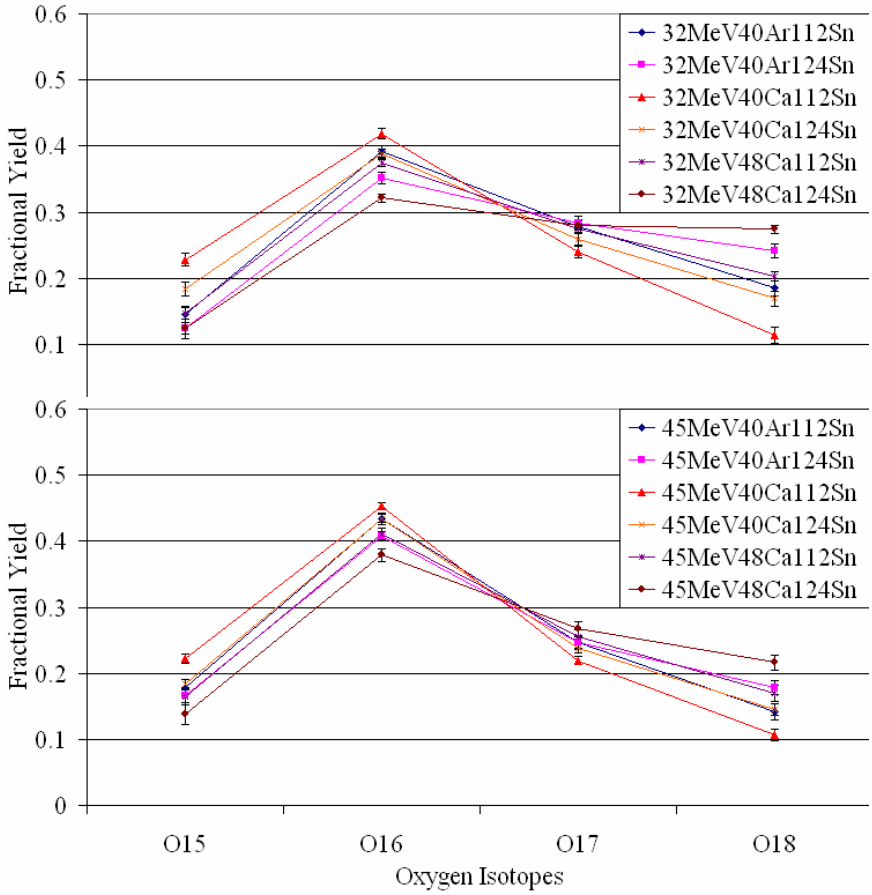


FIG. 42. (Color online) Oxygen fractional yields at 7.01 degrees.

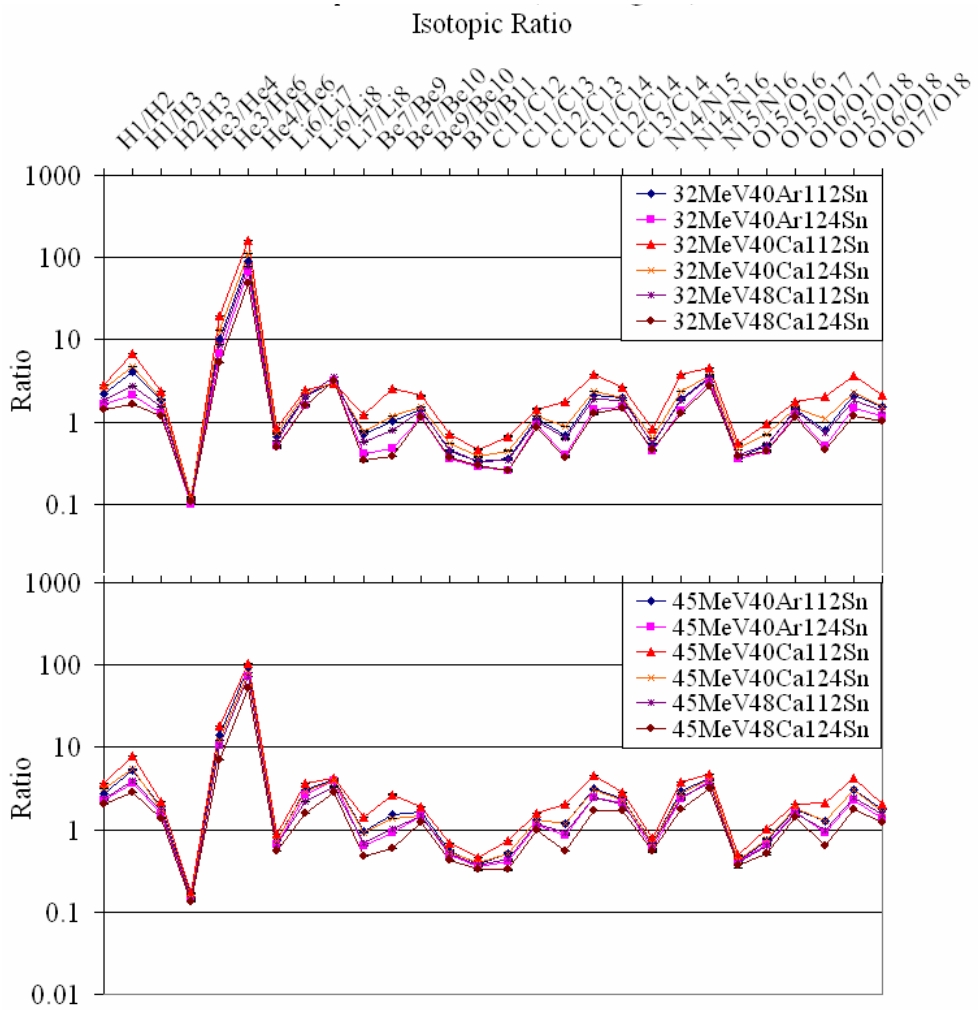


FIG. 43. (Color online) Isotopic ratios at 7.01 degrees.

### 3. Isobaric Yield Ratios

The isobaric yield ratios for all systems at 7.01 degrees are shown in figure 44. The isobaric yield ratios for the other 12 angles are shown in appendix D. Again the same trends as seen in the fractional and isotopic yield ratios are seen in the isobaric yield ratios. Here there is an interesting odd-even effect where the odd masses exhibit a higher production of neutron-rich fragments relative to the even masses. This means that even masses favor more neutron-poor nuclides than odd masses. This effect has been observed in other studies as well [65] and references therein.

### 4. Average N/Z Plots

Using equation 4.2 where the summation is over all detected isotopes and the yield of a given isotope, $Y_{A}X_{Z}$, is multiplied by its neutron number in the numerator, while the denominator is the charge multiplied by the sum of yields of each isotope of the element [10]. Figure 45 shows the average N/Z versus charge for all twelve systems with 32 MeV systems on top and 45 MeV systems on bottom at 7.01°. The average N/Z plots for the other 12 angles are shown in appendix E.

The trends remain consistent as shown in the previous sections. Here the first hint of the inhomogeneous distribution of N/Z can be seen. A phase transition with distillation would result in the light fragments having a large N/Z and the heavy fragments having a more symmetric N/Z, and indeed this is the trend observed in this figure. This has also been observed and discussed in [10] and references therein.

$$< N/Z >= \frac{\sum Y_{A}X_{Z}(A-Z)}{Z\sum Y_{A}X_{Z}} \tag{4.2}$$

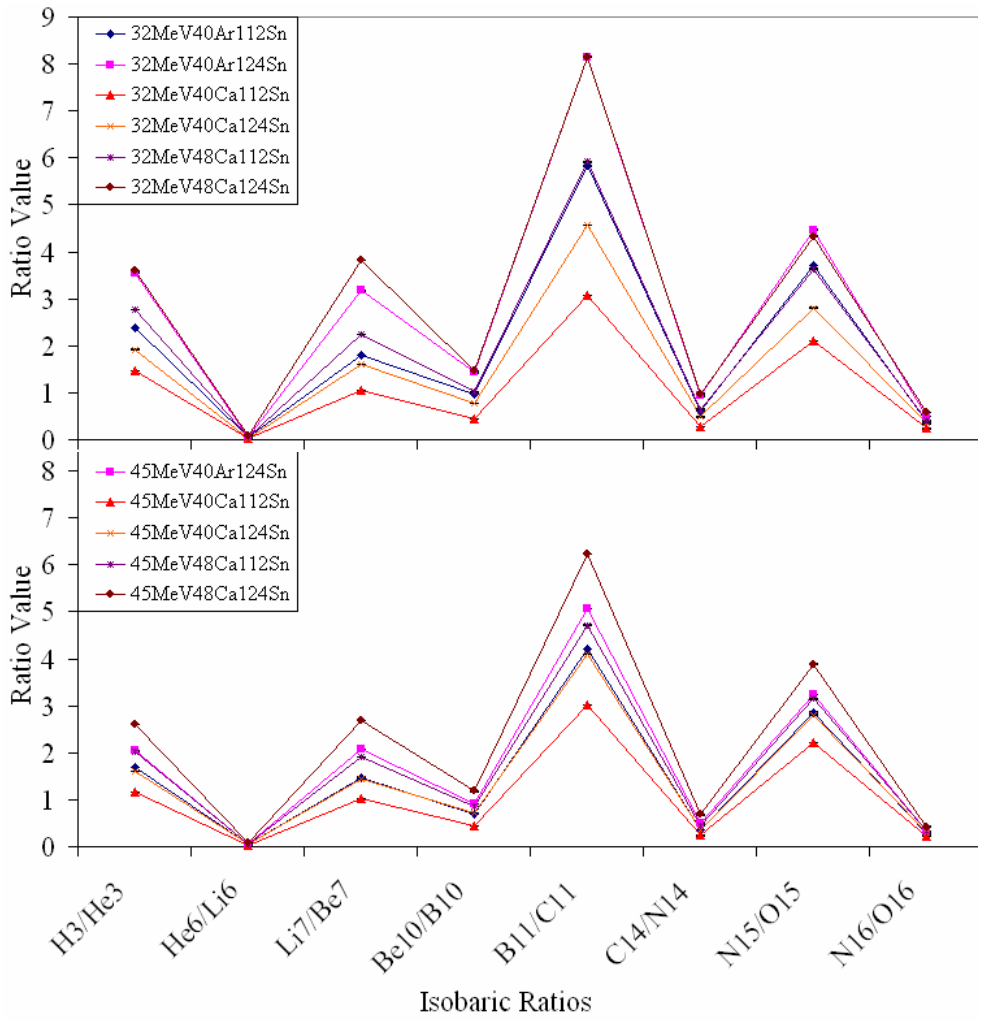


FIG. 44. (Color online) Isobaric ratios at 7.01 degrees.

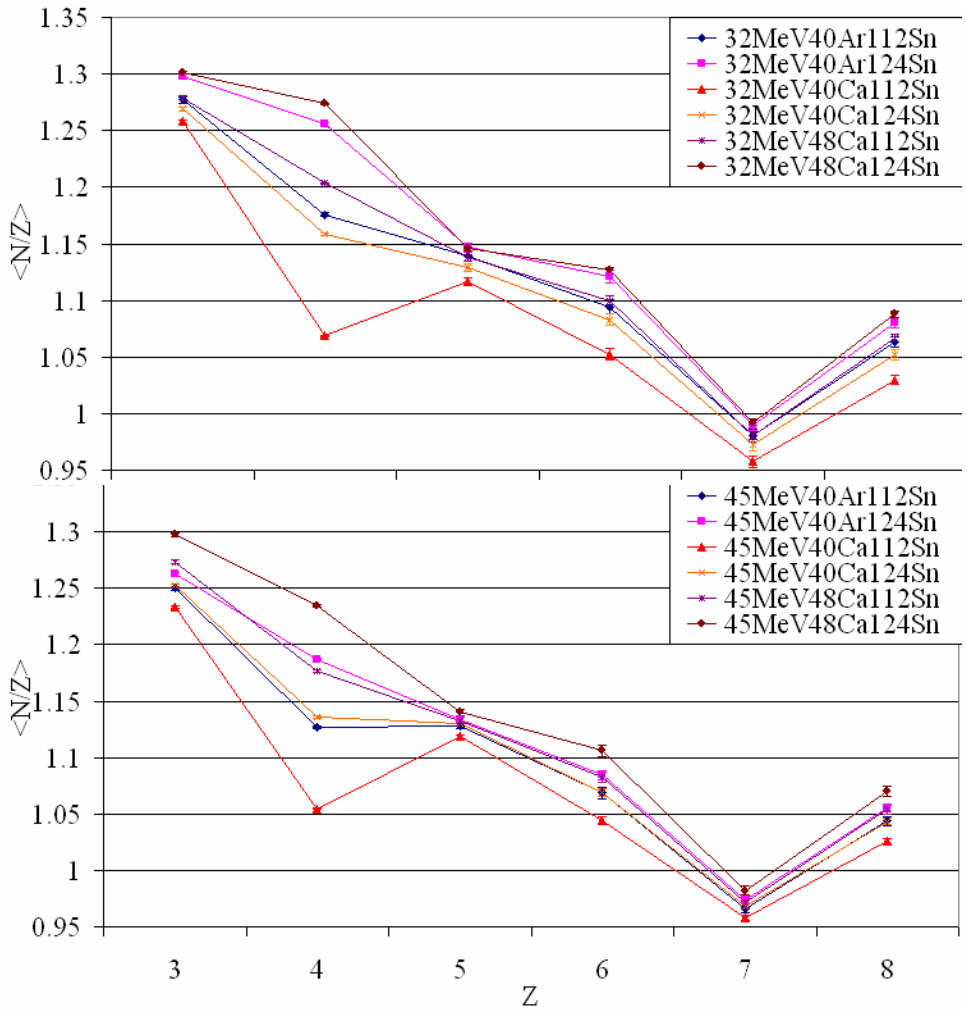


FIG. 45. (Color online) Mean N/Z versus Z plot of the 32 MeV/nucleon systems (top) and 45 MeV/nucleon systems (bottom) at 7.01 degrees.

### 5. Bulk Results Summary

Isobaric, isotopic, fractional and mean N/Z yield comparisons between systems were calculated. The comparisons indicate that the neutron richness of the system affects the fragment yields, with the neutron-rich systems preferentially populating the neutron-rich fragments and similarly the neutron-poor systems preferentially populating the neutron-poor fragments. Odd-even affects were observed, where even masses favor more neutron-poor nuclides than odd masses. The first glimpse at an inhomogeneous distribution of N/Z was observed with the light fragments having a large N/Z and the heavy fragments having a more symmetric N/Z.

## C. Exclusive Results

In this section events that contain only isotopically identified fragments are reconstructed (Reconstruction is discussed in chapter III and appendix A). From this subset of data the requirement that the charge of the quasiprojectile source must be within plus or minus 2 to the charge of the beam, creates an exclusive data set for further study. There is a subsection on inhomogeneous distribution of N/Z that will discuss multiplicity of LCPs and IMFs, average N/Z IMF divided by the average N/Z LCP and the mirror nuclei ratios. Then a subsection discusses the calculation of the N/Z of the quasiprojectile source to look at N/Z equilibration using two techniques.

The statistics for each system are given in table VIII. The higher energy has more statistics and therefore will demonstrate the trends that will be discussed in this section the best. The lower energy systems will still be shown, although the large error bars can hide the trends.

TABLE VIII. List of systems with the number of reconstructed events for each beam energy.

| System | 32 MeV | 45 MeV |
|---|---|---|
| $^{40}$Ar + $^{112}$Sn | 316 | 1271 |
| $^{40}$Ar + $^{124}$Sn | 208 | 1122 |
| $^{40}$Ca + $^{112}$Sn | 41 | 444 |
| $^{40}$Ca + $^{124}$Sn | 35 | 300 |
| $^{48}$Ca + $^{112}$Sn | 334 | 454 |
| $^{48}$Ca + $^{124}$Sn | 266 | 386 |

### 1. Inhomogeneous Distribution of N/Z

The first observable studied was the total, LCP and IMF multiplicities. Figures 46 to 51 show the total multiplicity, LCP multiplicity and IMF multiplicity as a function of N/Z of the quasiprojectile source for all 12 systems. The error bars shown are statistical. This work is in agreement with previous studies that have shown that with increased proton richness the LCP multiplicity increases dramatically, while the IMF multiplicity remains nearly constant [16]. However the neutron-rich side has been extended further than the previous studies and shows the opposite trend, the IMF multiplicity increases, while the LCP multiplicity levels off. Another interesting trend is the comparison of energies, 32 and 45 MeV. The higher energy results in a greater LCP multiplicity level, which pushes the crossing point to higher quasiprojectile N/Z. Figure 52 shows the effect of neutron uncertainty, which effects the N/Z calculated. Using the simulations described in chapter V the neutron loss was determined, which shifts the larger N/Z values of the quasiprojectile further to the right and creates

some statistical error in the N/Z value, shown by the X-axis error bars. The trend does not change, only the distribution is stretched on the X-axis.

The next observable studied was the mean N/Z of the IMF divided by the mean N/Z of the LCP. Figure 53 shows the 32 MeV data on top and 45 MeV data on bottom. The ratio is large for proton-rich quasiprojectiles and decrease towards unity with increasing N/Z of the quasiprojectile, in agreement with other studies [16]. The energy effect is negligible. The error bars shown are statistical. Then taking a step further to see if the mean N/Z of the IMF has dependence on the N/Z of the quasiprojectile source, the 45 MeV/nucleon $^{40}$Ar on $^{112}$Sn system was used. Figure 54 shows the mean values of the IMF and the LCP as well as the ratio. These results show that a more neutron-rich system has more neutrons entering the LCPs than the IMFs, but both LCPs and IMFs have dependence on the neutron richness of the system.

The last observable studied were the mirror nuclei ratios t/$^3$He, $^7$Li/$^7$Be, $^{11}$B/$^{11}$C and $^{15}$N/$^{15}$O. Figures 55 to 58 show the 32 MeV data on top and 45 MeV data on bottom for the 4 mirror nuclei ratios. The error bars shown are statistical. With increasing neutron richness of the quasiprojectile more neutron-rich isobars are created, as shown by the increasing ratios. This is in agreement with prior work [16], which had only used the t/$^3$He ratio.

### 2. Source N/Z

When target and projectile nuclei have a difference in N/Z, the quasiprojectiles formed in a DIC should have a mean N/Z between that of the N/Z of the target and the N/Z of the projectile, depending on the amount of N/Z equilibration that occurred. If full N/Z equilibration occurred then the N/Z of the quasiprojectile should be identical to the N/Z of the composite system. Table IX summarizes the absolute difference in N/Z between target and projectile. Two techniques will be presented to calculate the

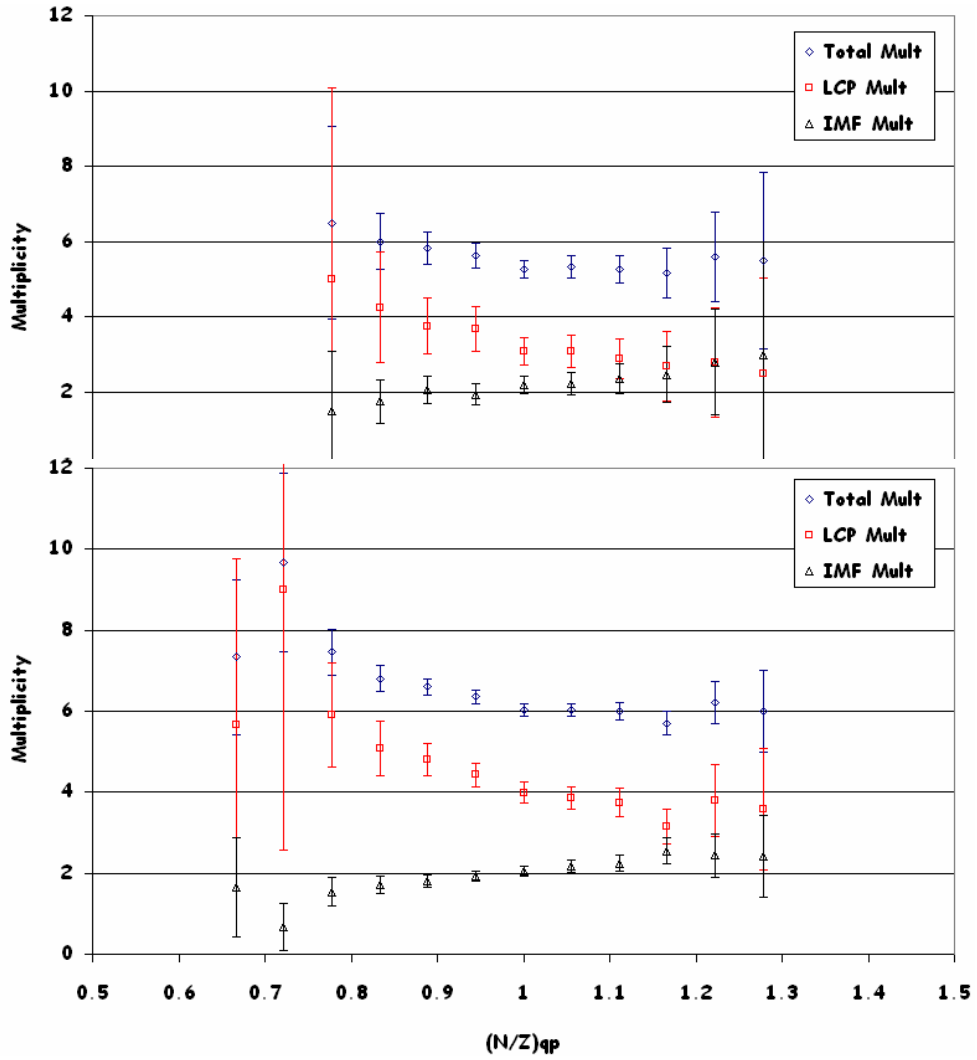


FIG. 46. (Color online) $^{40}$Ar on $^{112}$Sn multiplicity distributions of total, LCP and IMF as a function of N/Z of the quasiprojectile source. 32 MeV/nucleon system on top and 45 MeV/nucleon system on bottom.

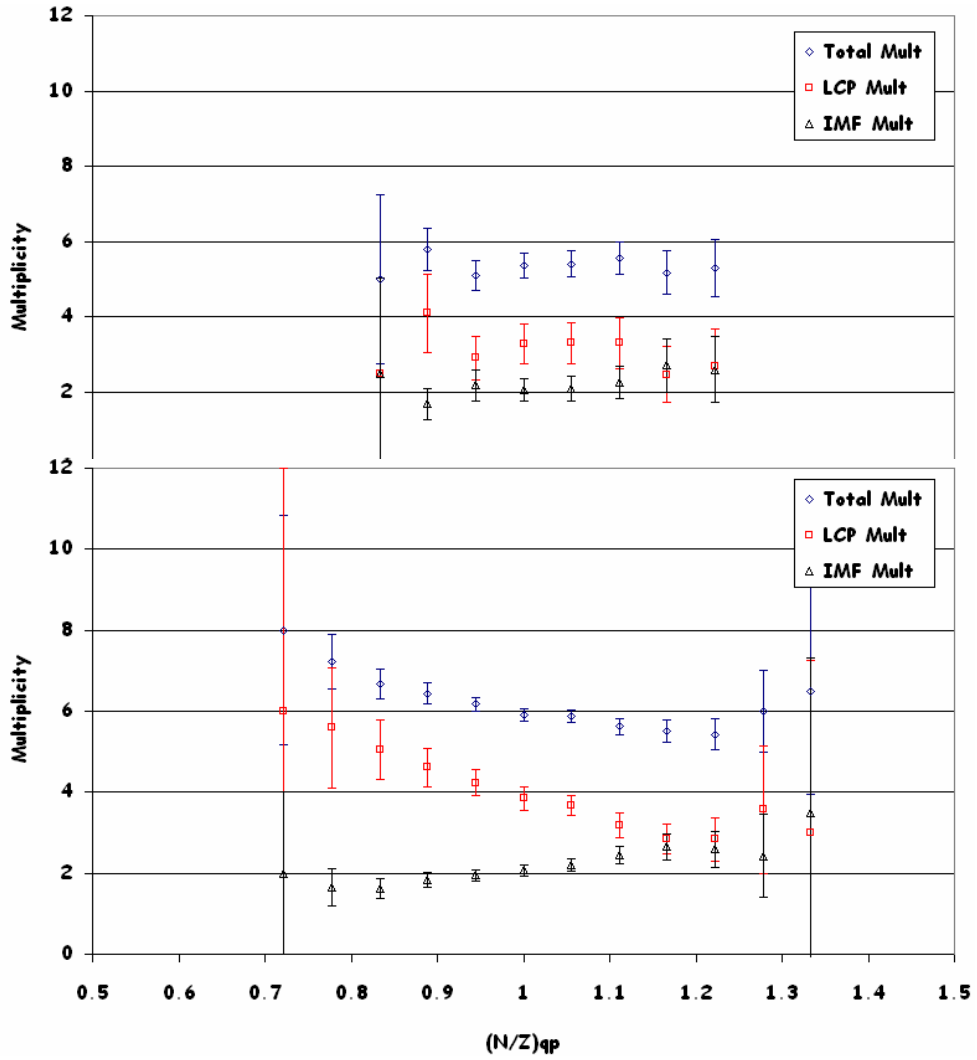


FIG. 47. (Color online) $^{40}$Ar on $^{124}$Sn multiplicity distributions of total, LCP and IMF as a function of N/Z of the quasiprojectile source. 32 MeV/nucleon system on top and 45 MeV/nucleon system on bottom.

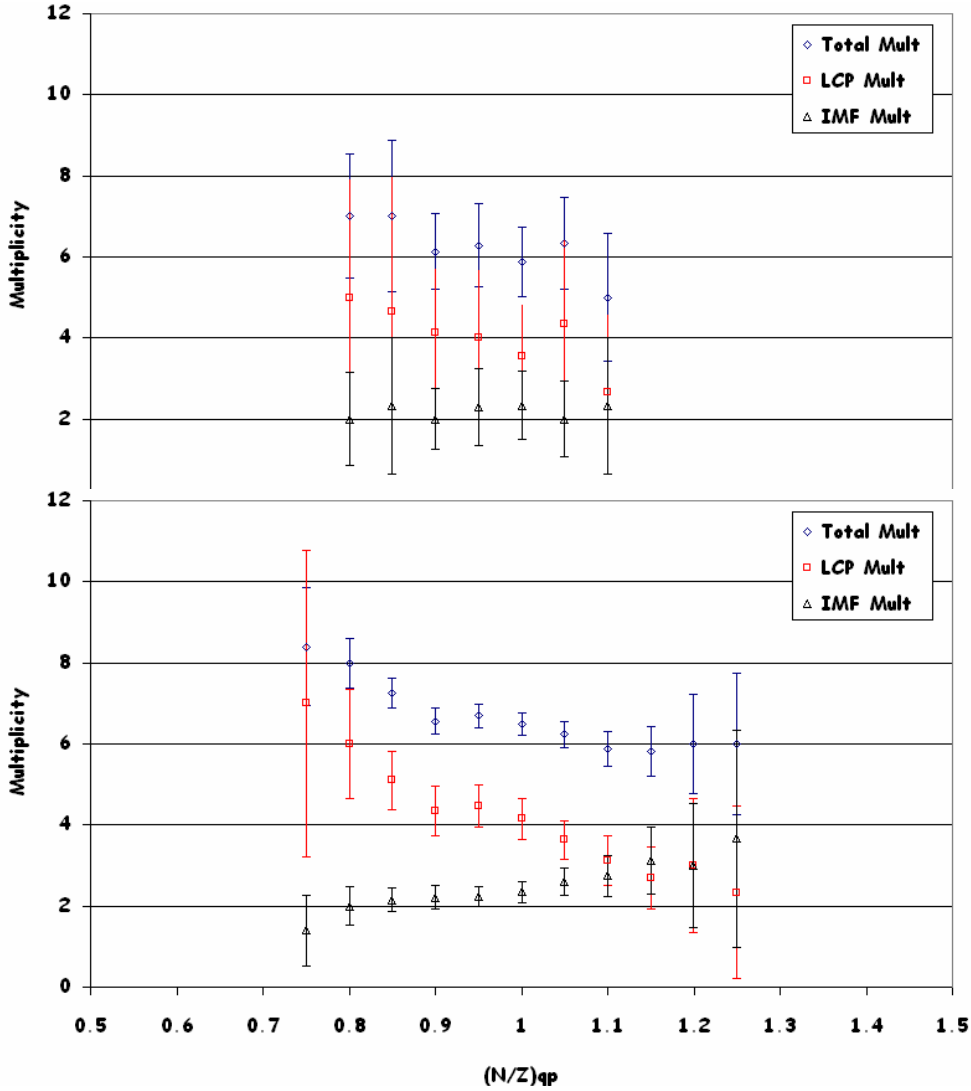


FIG. 48. (Color online) $^{40}$Ca on $^{112}$Sn multiplicity distributions of total, LCP and IMF as a function of N/Z of the quasiprojectile source. 32 MeV/nucleon system on top and 45 MeV/nucleon system on bottom.

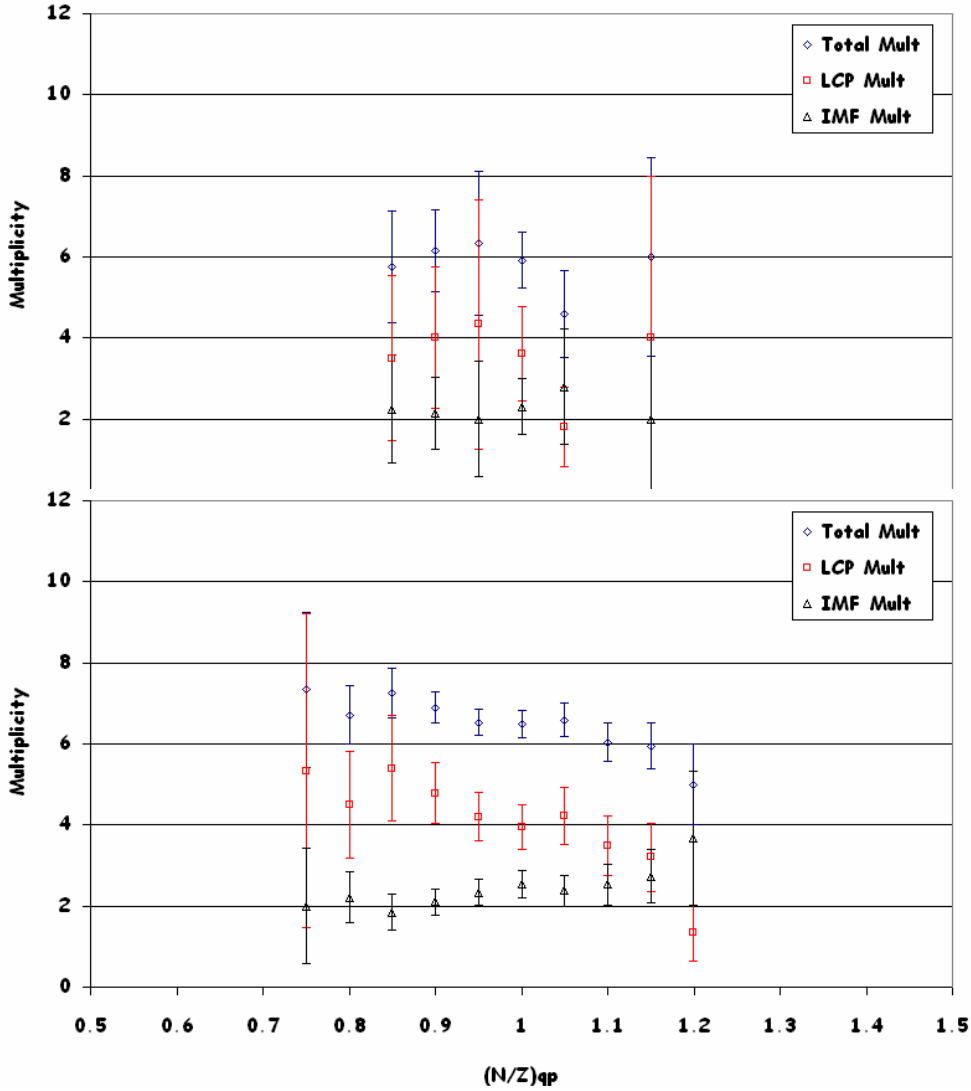


FIG. 49. (Color online) $^{40}$Ca on $^{124}$Sn multiplicity distributions of total, LCP and IMF as a function of N/Z of the quasiprojectile source. 32 MeV/nucleon system on top and 45 MeV/nucleon system on bottom.

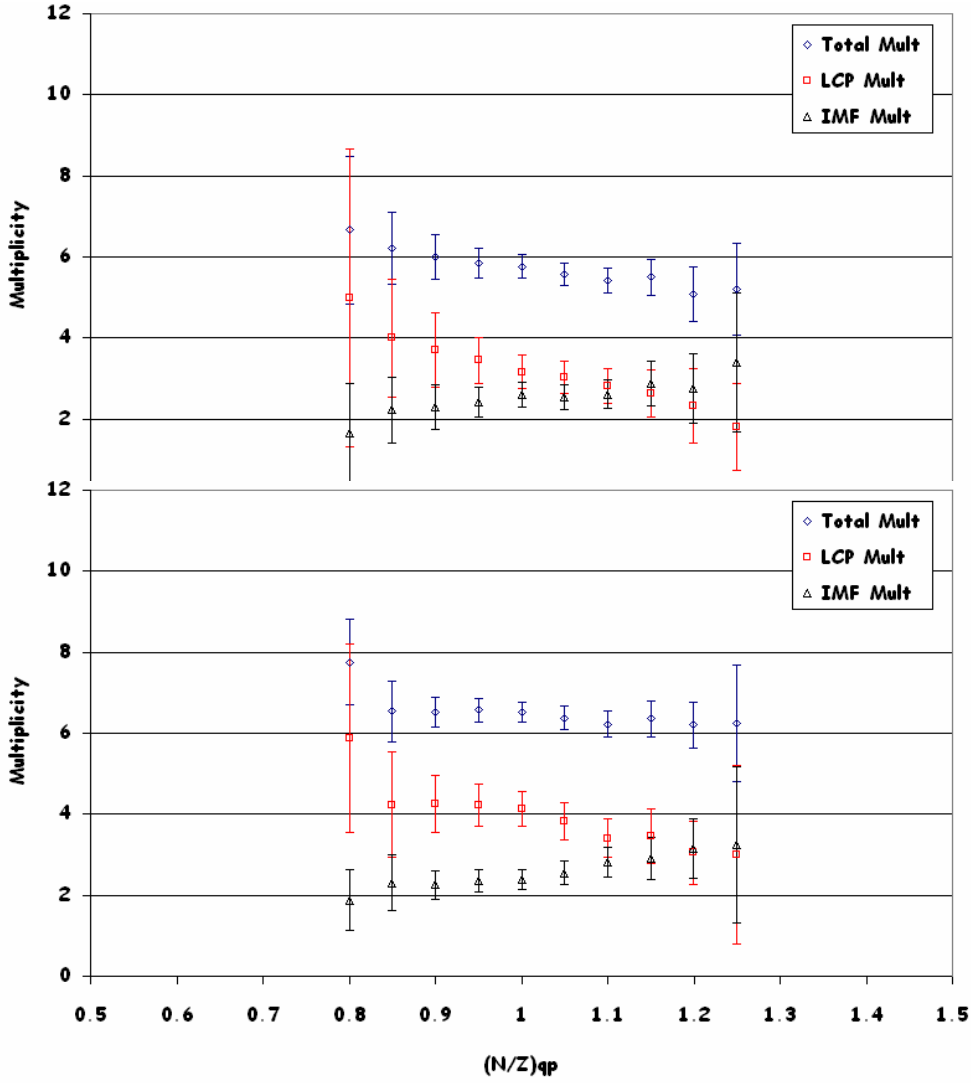


FIG. 50. (Color online) $^{48}$Ca on $^{112}$Sn multiplicity distributions of total, LCP and IMF as a function of N/Z of the quasiprojectile source. 32 MeV/nucleon system on top and 45 MeV/nucleon system on bottom.

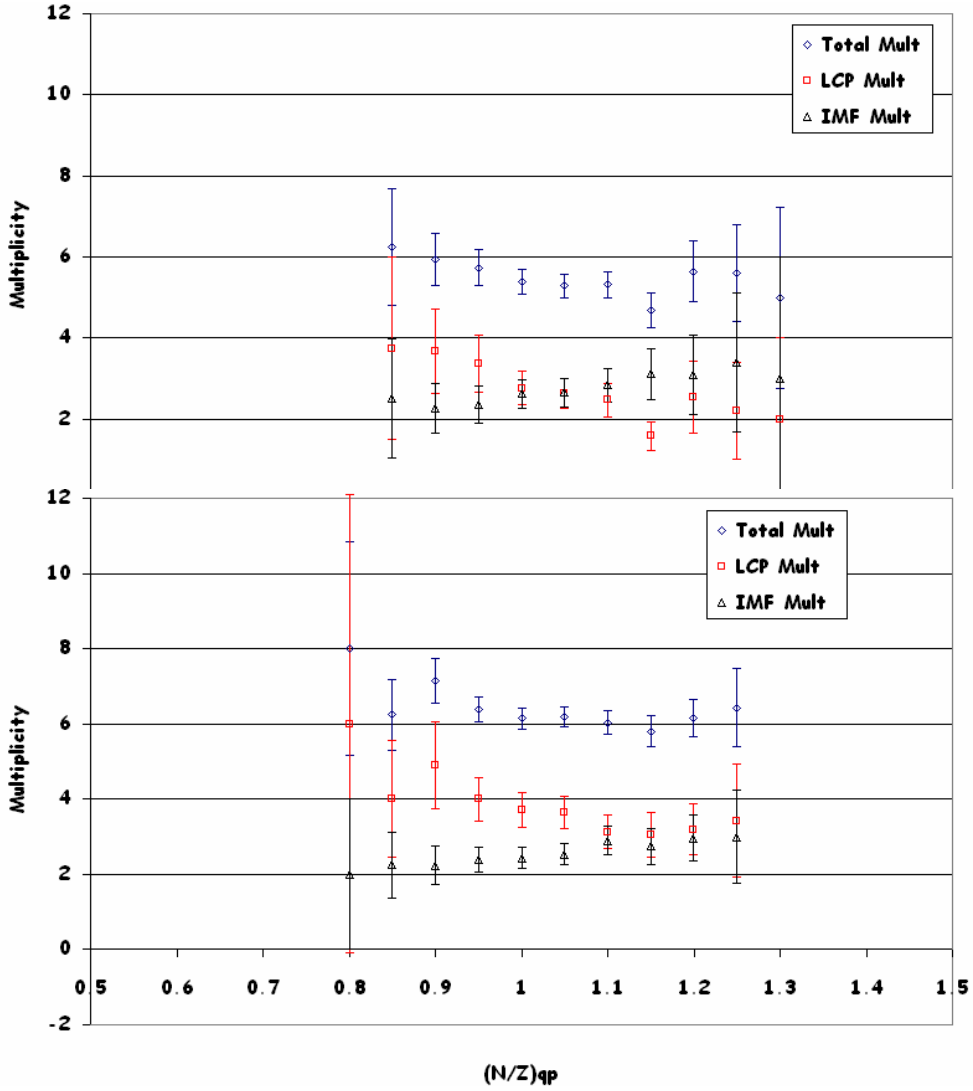


FIG. 51. (Color online) $^{48}$Ca on $^{124}$Sn multiplicity distributions of total, LCP and IMF as a function of N/Z of the quasiprojectile source. 32 MeV/nucleon system on top and 45 MeV/nucleon system on bottom.

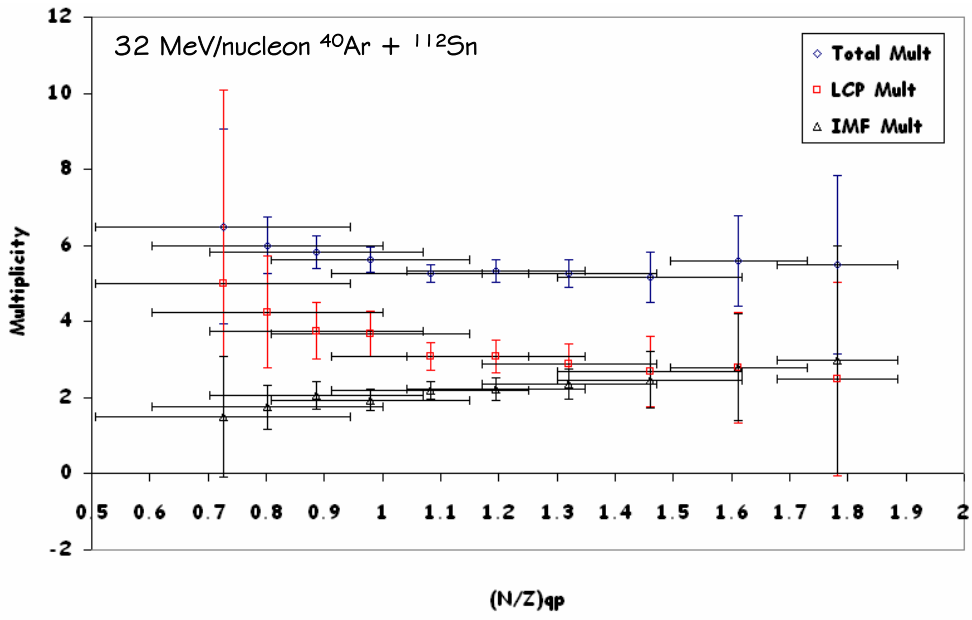


FIG. 52. (Color online) 32 MeV/nucleon $^{40}$Ar on $^{112}$Sn multiplicity distributions of total, LCP and IMF as a function of N/Z of the quasiprojectile source with neutron error bars.

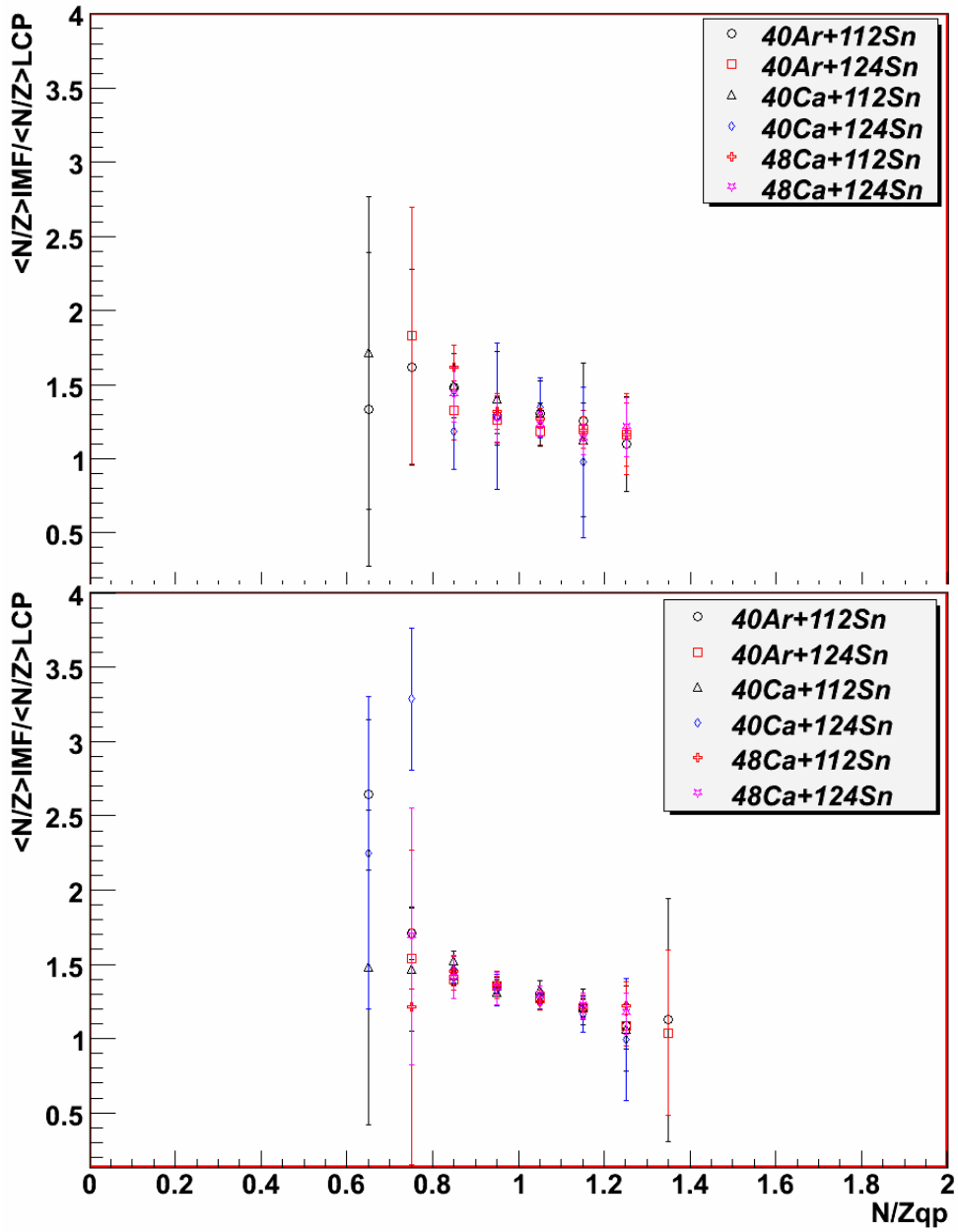


FIG. 53. (Color online) The mean N/Z of the IMF divided by the mean N/Z of the LCP as a function of the N/Z of the quasiprojectile source. 32 MeV/nucleon systems on top and 45 MeV/nucleon systems on bottom at 7.01 degrees.

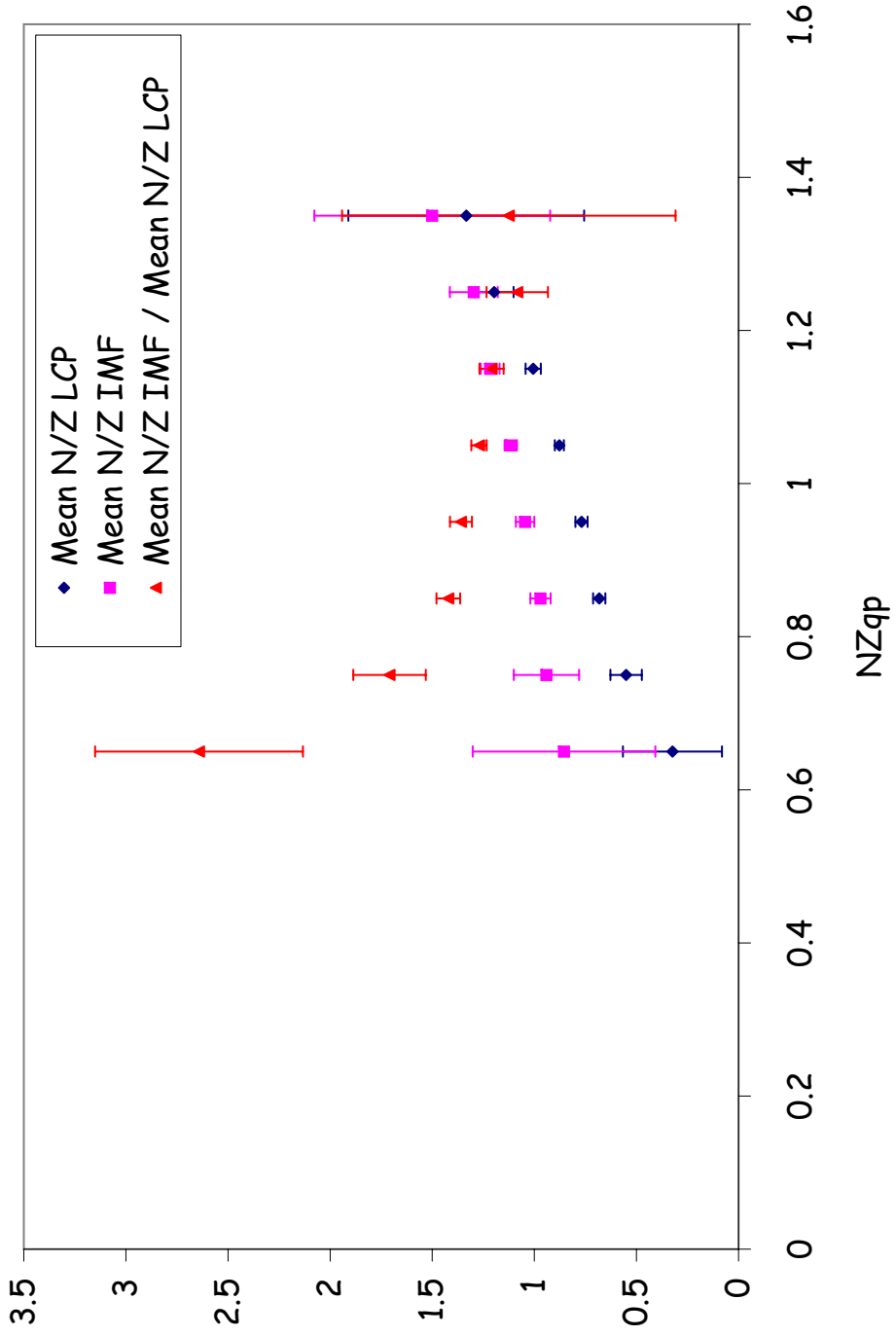


FIG. 54. (Color online) The mean N/Z of the IMF and the mean N/Z of the LCP as well as their ratio plotted as a function of the N/Z of the quasiprojectile source for the system 45 MeV/nucleon $^{40}$Ar on $^{112}$Sn.

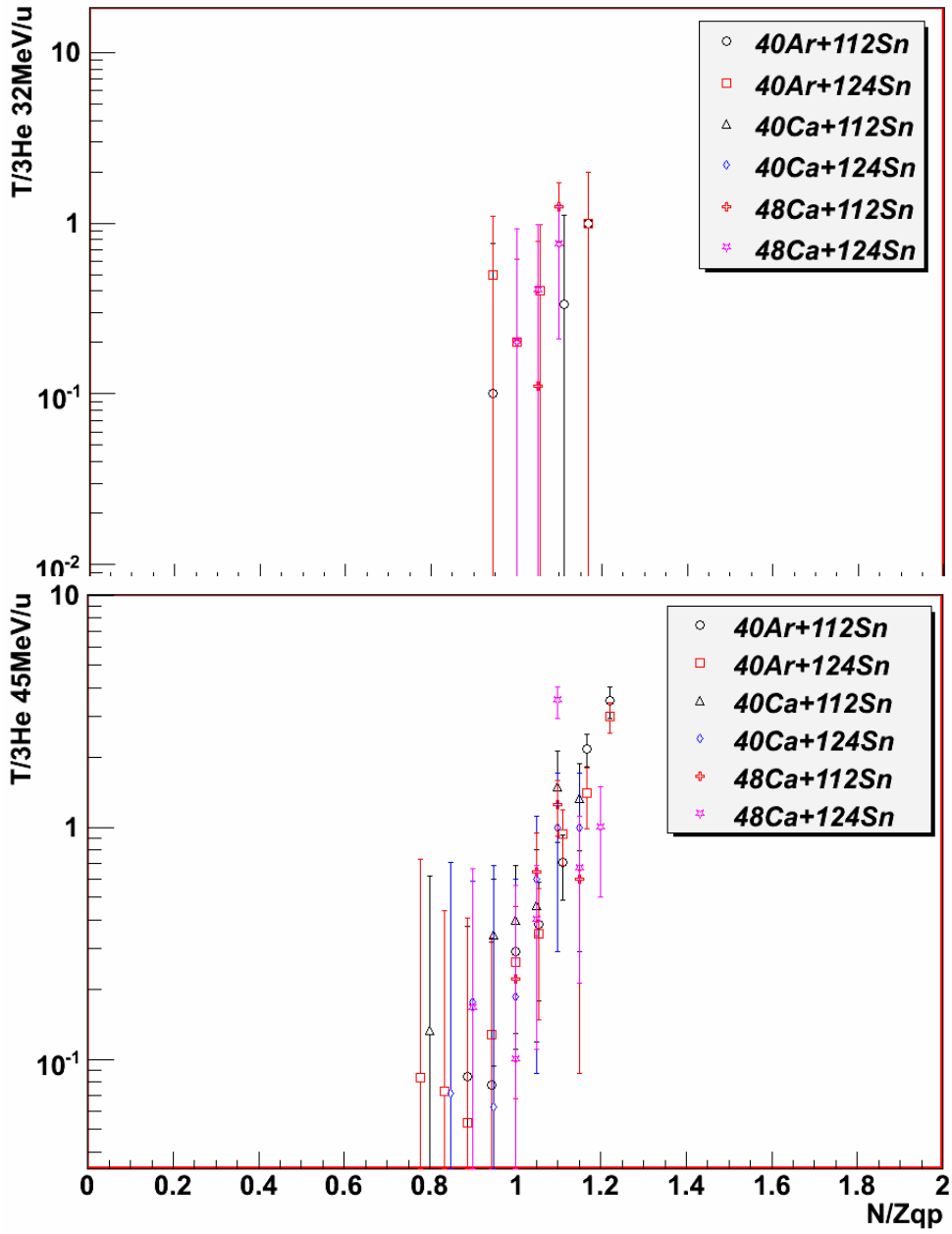


FIG. 55. (Color online) The t/$^3$He ratio versus the N/Z of the quasiprojectile source. 32 MeV/nucleon systems on top and 45 MeV/nucleon systems on bottom.

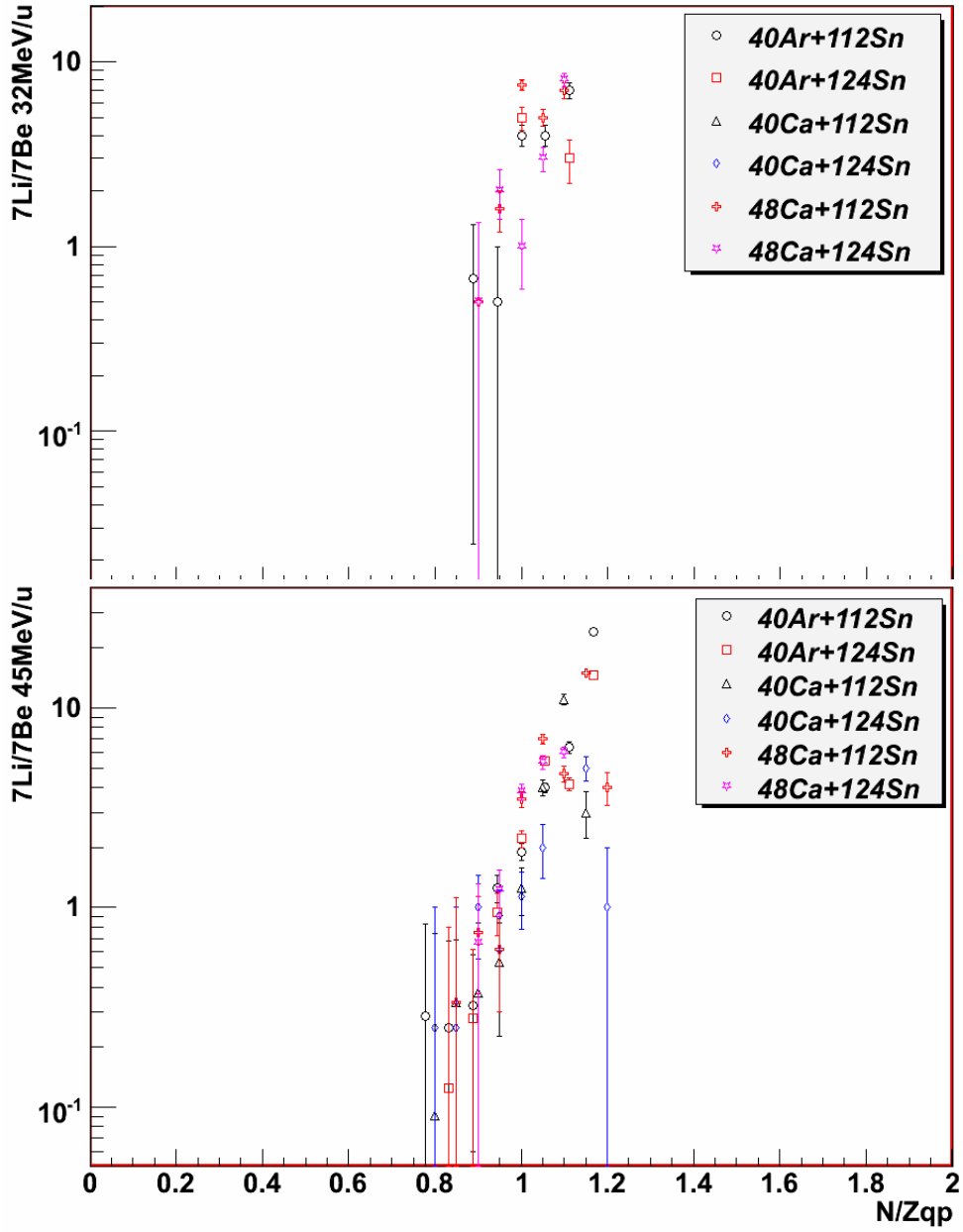


FIG. 56. (Color online) The $^{7}$Li/$^{7}$Be ratio versus the N/Z of the quasiprojectile source. 32 MeV/nucleon systems on top and 45 MeV/nucleon systems on bottom.

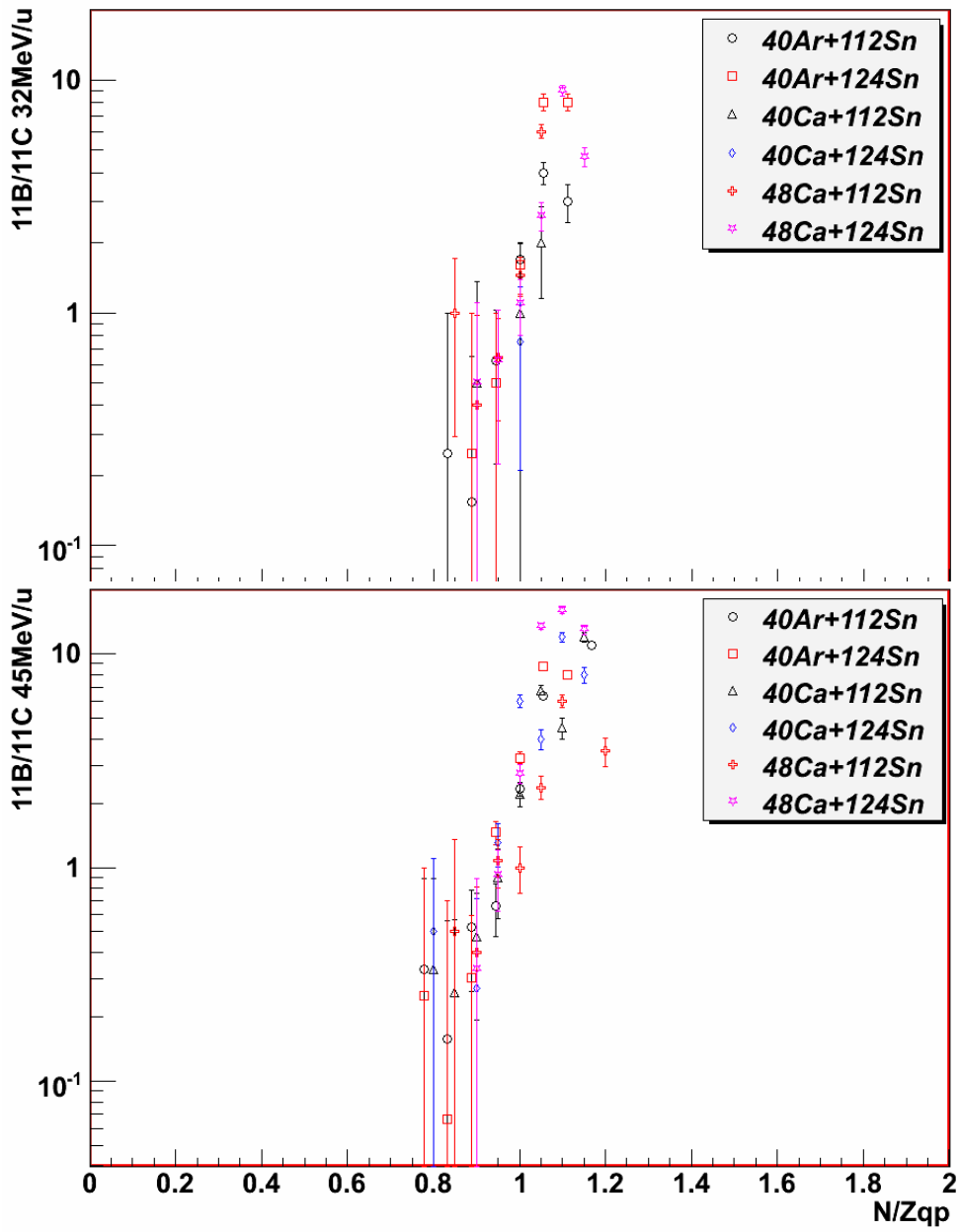


FIG. 57. (Color online) The $^{11}B/^{11}C$ ratio versus the N/Z of the quasiprojectile source. 32 MeV/nucleon systems on top and 45 MeV/nucleon systems on bottom.

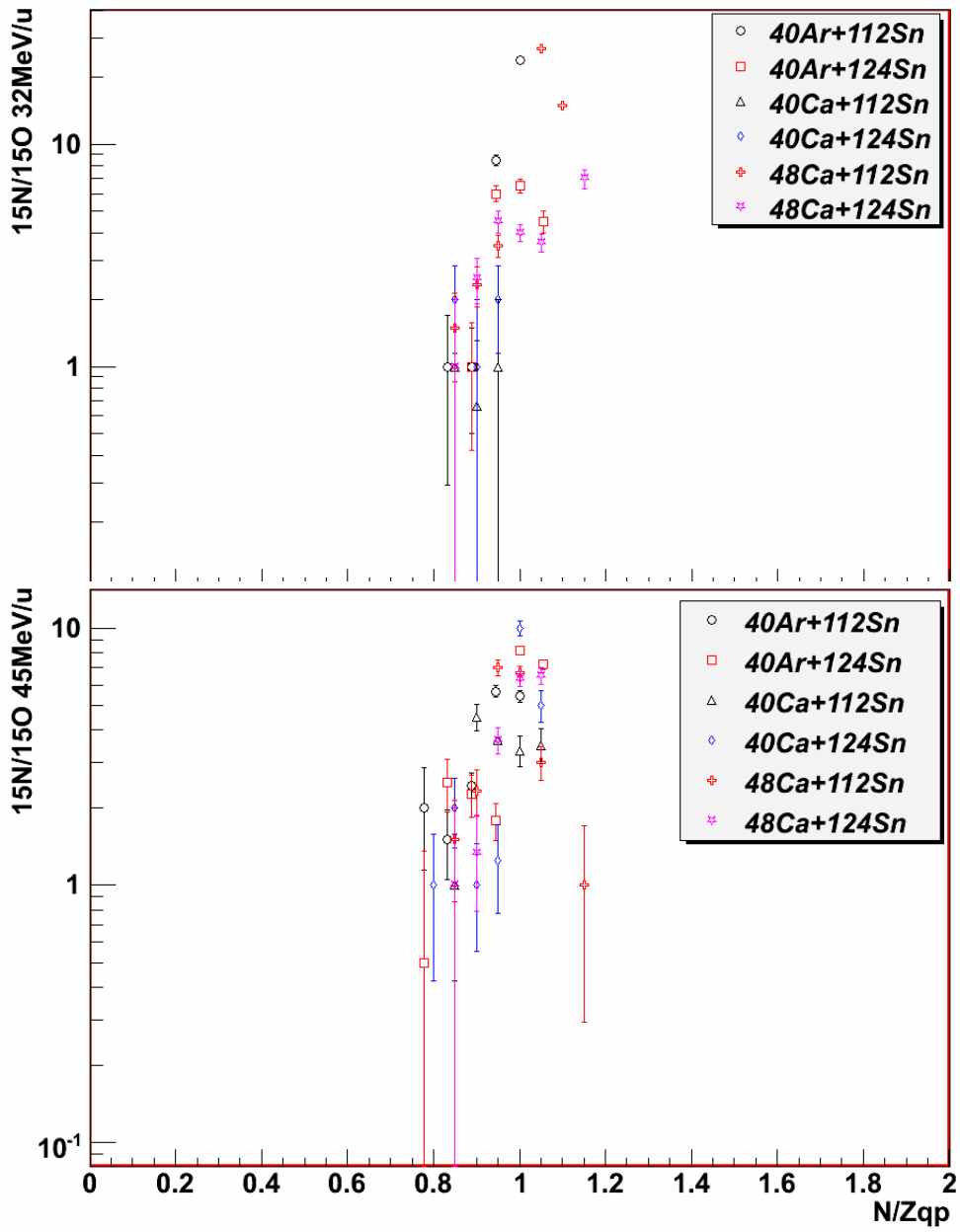


FIG. 58. (Color online) The $^{15}N/^{15}O$ ratio versus the N/Z of the quasiprojectile source. 32 MeV/nucleon systems on top and 45 MeV/nucleon systems on bottom.

TABLE IX. List of systems and their absolute difference between target and projectile N/Z.

| System | ΔN/Z |
|---|---|
| $^{40}$Ar + $^{112}$Sn | 0.0178 |
| $^{48}$Ca + $^{124}$Sn | 0.0800 |
| $^{48}$Ca + $^{112}$Sn | 0.1600 |
| $^{40}$Ca + $^{112}$Sn | 0.2400 |
| $^{40}$Ar + $^{124}$Sn | 0.2578 |
| $^{40}$Ca + $^{124}$Sn | 0.4800 |

N/Z of the source.

The first method is reconstruction, which has been discussed in chapter III and in great detail in appendix A. The mean mass from the mass distributions from the reconstruction are summarized in table X along with the N/Z of the target, projectile and composite system. All of the systems have moved toward stability (i.e. N/Z roughly 1.0). The reconstructed N/Z is not between the N/Z of the target and the N/Z of the projectile, so no information about the amount of N/Z equilibration can be stated. This is most likely caused by not detecting free neutrons. The effect of neutron loss will be studied in the simulations and compared with experimental results in chapter VI.

Since the missing neutrons may be the problem another method that was not dependent on detecting neutrons was developed. The fragment yields are determined by the quasiprojectile N/Z, while reconstruction requires all fragments, including neutrons be detected. The fragment yields were used to calculate the N/Z of the source that they originated in. The fractional yields, isotopic yield, and isobaric

TABLE X. List of systems with their reconstructed N/Z, target N/Z, projectile N/Z and composite system N/Z.

| System | N/Z Source | N/Z Tar. | N/Z Proj. | N/Z Comp. Sys. |
|---|---|---|---|---|
| $^{40}$Ar + $^{112}$Sn | 1.00 | 1.24 | 1.22 | 1.24 |
| $^{40}$Ar + $^{124}$Sn | 1.02 | 1.48 | 1.22 | 1.41 |
| $^{40}$Ca + $^{112}$Sn | 0.98 | 1.24 | 1.00 | 1.17 |
| $^{40}$Ca + $^{124}$Sn | 0.99 | 1.48 | 1.00 | 1.34 |
| $^{48}$Ca + $^{112}$Sn | 1.03 | 1.24 | 1.40 | 1.29 |
| $^{48}$Ca + $^{124}$Sn | 1.05 | 1.48 | 1.40 | 1.46 |

yields were used to calculate the quasiprojectile N/Z, and give consistent results. Here only the isobaric yields will be used as an example.

When the isobaric yield ratios are plotted as a function of composite system N/Z, shown in figure 59, the ratios increase with increasing neutron richness of the projectile and with the target. There are two distinct sections of this plot one for the $^{112}$Sn and the other for the $^{124}$Sn target. The slope of the heavier target is slightly steeper than the slope of the lighter target, caused by the target neutron-richness. The projectile neutron-richness, however is more important, with a greater increase of both slopes. The $^{48}$Ca systems do not have $^{15}$O/$^{15}$N points because of low statistics in gates near high statistics isotopes, where a little contamination could cause large effects. This data demonstrates that the colliding system has most likely not achieved full N/Z equilibration and led to the development of the quasiprojectile N/Z source determination method discussed below.

The data is fit using equation 4.3, which is a simple equation that says some fraction of the quasiprojectile N/Z comes from the target and the rest comes from

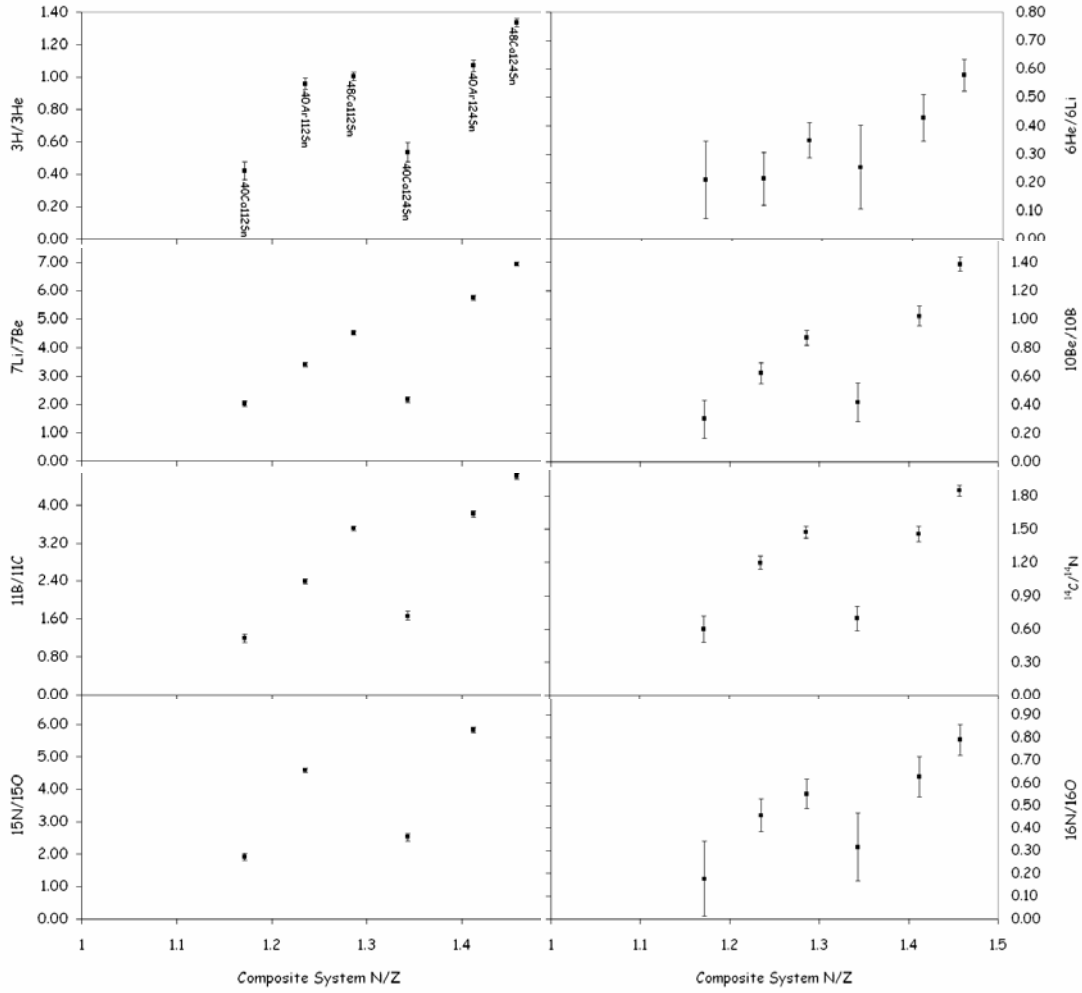


FIG. 59. Isobaric yield ratio plotted as a function of the composite system N/Z.

the projectile. First each isobaric yield ratio was used individually to calculate the quasiprojectile N/Z shown in figure 60. There are slight differences between the calculated quasiprojectile N/Z using the different isobaric ratios. To investigate the mass dependence the X and Y fractions were plotted as a function of ratio mass, shown in figure 61. This figure shows that indeed there is a mass dependence with larger mass having greater projectile contribution.

$$\frac{N_{Source}}{Z_{Source}} = X\frac{N_T}{Z_T} + Y\frac{N_P}{Z_P} \tag{4.3}$$

Then a global fitting of all systems simultaneously maximizing the R-squared value between the isobaric yield ratios and the N/Z of the quasiprojectile source, which should have a linear behavior. From the global fitting the X-value, or target contribution, is 39 percent and the Y-value, or projectile contribution, is 61 percent. Figure 62 shows an example plot of the isobaric yield fit of the six systems to a source N/Z. This plot averages the mass dependent spread that was seen in figure 60.

The calculated mean N/Z of the quasiprojectile source for each system is given in table XI along with the reconstructed quasiprojectile, target, projectile and composite system N/Z. Now with this method the N/Z value is between that of the target and projectile N/Z, but is not fully N/Z equilibrated. Because all six systems were globally fit, they all have the same amount of equilibration, which is roughly 54% as calculated using equation 1.6.

The two methods will be compared to DIT/SMM results to determine if the undetected neutrons account for the difference between the two methods and also to allow for a test of how good the isobaric yield ratio fitting is, by comparing with the known N/Z of the simulated quasiprojectile. These results are discussed in chapter VI.

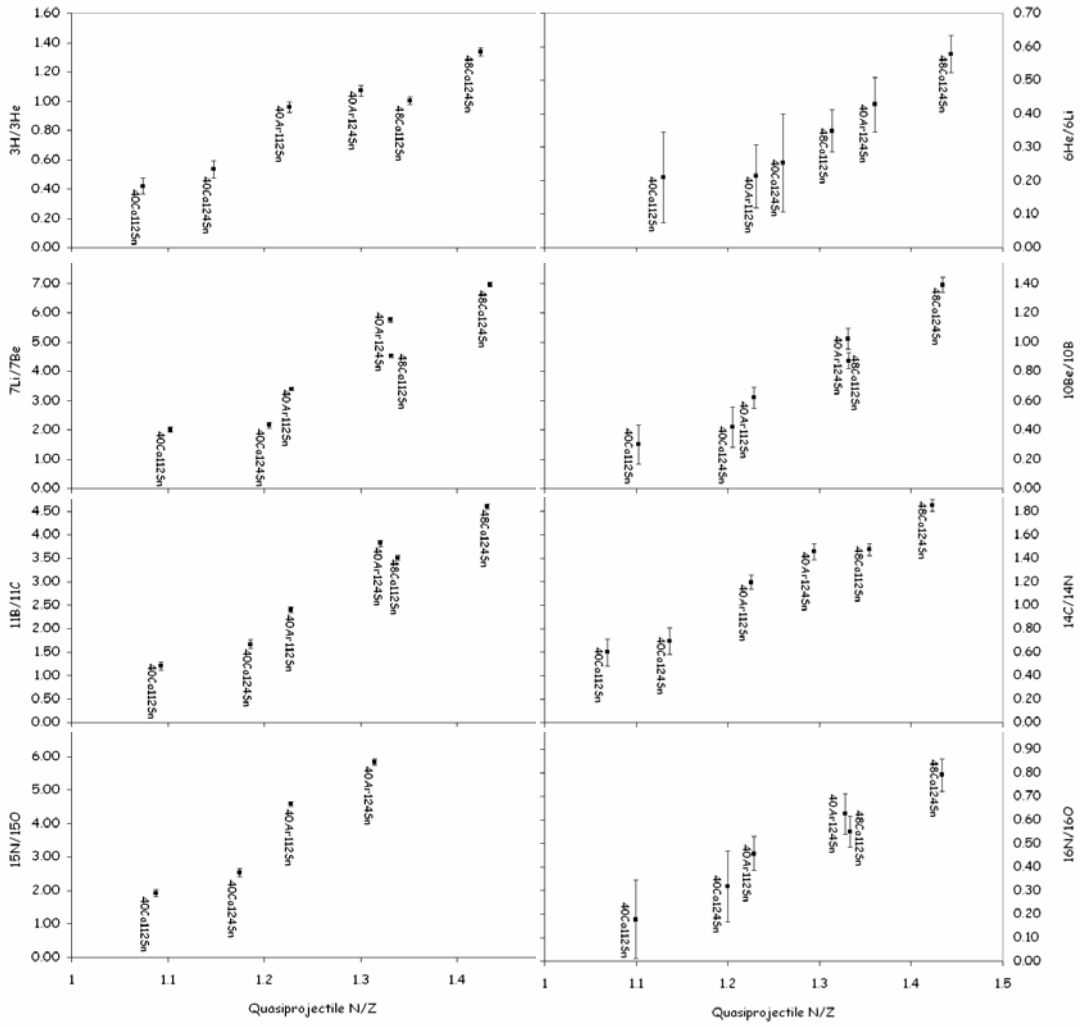


FIG. 60. Example of individual fitting the isobaric yield ratios of all six systems to the N/Z source using equation 4.3.

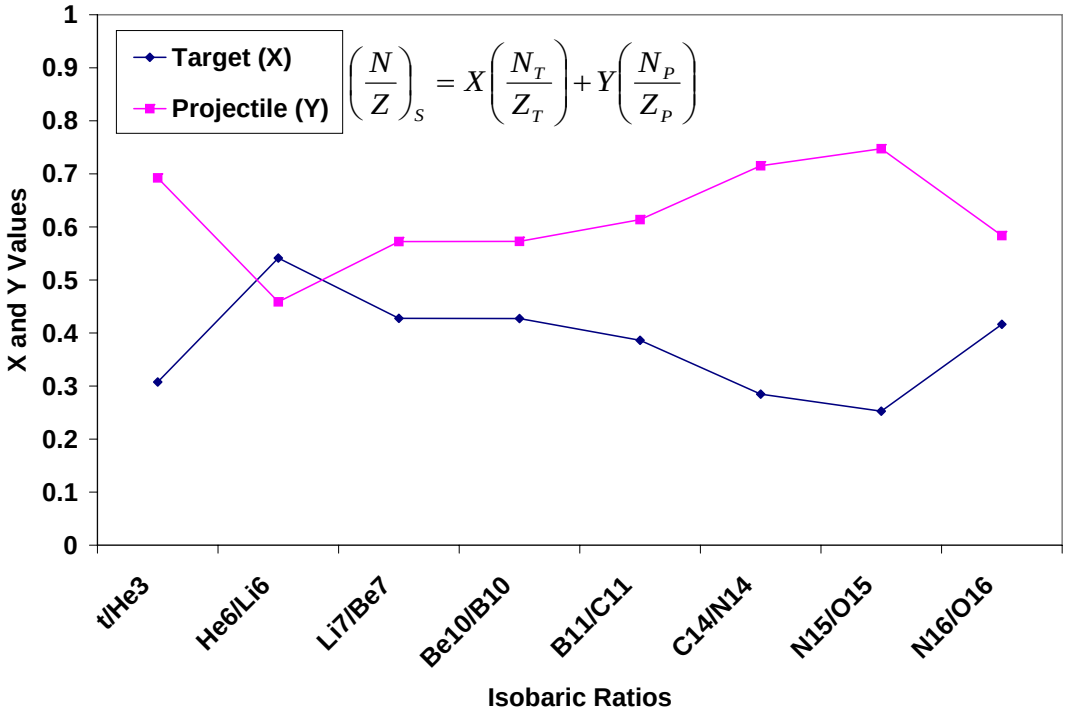


FIG. 61. The mass dependence of the isobaric ratio fitting technique. X and Y are parameters in equation that are extracted for each ratio fit.

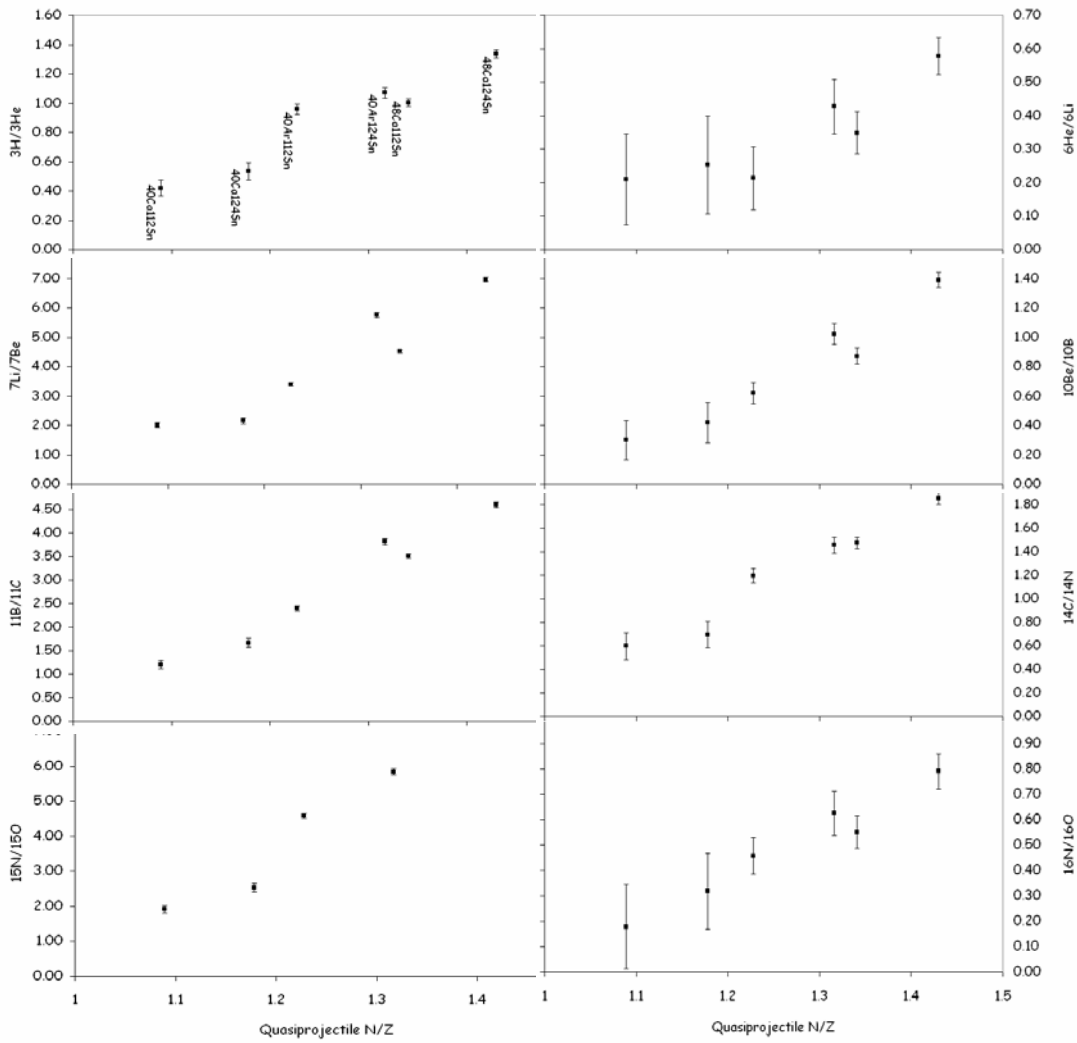


FIG. 62. Example of the global fitting the isobaric yield ratios of all six systems to extract the N/Z source.

TABLE XI. List of systems with their source N/Z from the isobaric ratio method, reconstruction method, as well as target N/Z, projectile N/Z and composite system N/Z.

| System | N/Z Isobaric | N/Z Reconstruction | N/Z Target | N/Z Projectile | N/Z Composite |
|---|---|---|---|---|---|
| $^{40}$Ar + $^{112}$Sn | 1.23 | 1.00 | 1.24 | 1.22 | 1.24 |
| $^{40}$Ar + $^{124}$Sn | 1.32 | 1.02 | 1.48 | 1.22 | 1.41 |
| $^{40}$Ca + $^{112}$Sn | 1.09 | 0.98 | 1.24 | 1.00 | 1.17 |
| $^{40}$Ca + $^{124}$Sn | 1.18 | 0.99 | 1.48 | 1.00 | 1.34 |
| $^{48}$Ca + $^{112}$Sn | 1.33 | 1.03 | 1.24 | 1.40 | 1.29 |
| $^{48}$Ca + $^{124}$Sn | 1.43 | 1.05 | 1.48 | 1.40 | 1.46 |

### 3. Exclusive Results Summary

An inhomogeneous distribution of N/Z between LCPs and IMFs was observed in this data set. The multiplicity of LCPs and IMFs showed a new trend that the IMF multiplicity increases, while the LCP multiplicity stays nearly constant for neutron-rich quasiprojectile sources. The mean N/Z of the IMF divided by the mean N/Z of the LCP also demonstrated that the mean N/Z of the IMF does have dependence on the N/Z of the quasiprojectile source. The mirror nuclei ratios t/$^3$He, $^7$Li/$^7$Be, $^{11}$B/$^{11}$C and $^{15}$N/$^{15}$O all show an increase with increasing N/Z of the quasiprojectile source.

The reconstruction is sensitive to neutron loss, so the N/Z of the quasiprojectile determined is a lower value than the true value, and indeed the N/Z value is lower than the N/Z of both the target and projectile. The yield ratio technique is not sensitive to neutron loss, and provides a larger N/Z value, which is between the target and

projectile N/Z values. To determine if the difference between the two techniques is purely due to neutron loss, simulations were run to create quasiprojectiles and de-excite them and then the fragments were filtered using a software replica of the FAUST array. Then using the same techniques as the experimental data the theoretical data was analyzed, but here the N/Z of the quasiprojectile source is known and the results can be checked for agreement. These results will be discussed in chapter VI.

# CHAPTER V

# SIMULATIONS

Several theoretical models were used to compare with experiment. The interaction stage was simulated using DIT, HIPSE, BNV, and iBUU. BNV and iBUU allow for different settings of the nuclear equation of state. The primary quasiprojectiles formed were compared to experimentally reconstructed results. Then all the primary simulation results were de-excited using SMM, having four different settings for the symmetry energy. The HIPSE results were also de-excited using SIMON, which is built into HIPSE. These de-excited cold fragments are then filtered using a FAUST filter, a software version of the FAUST array. Then the theoretical fragments were analyzed the same as the experimental fragments. In this chapter each of the simulations will be discussed with sections on input parameters, selecting the quasiprojectile source, and hot results. The cold results will be compared to the experimental data in chapter VI.

## A. D.I.T.

DIT is the Deep Inelastic Transfer model of Tassan-Got [66, 17]. DIT uses a Monte Carlo simulation to exchange nucleons through a window using classical trajectories. Energy is dissipated by the successive transfer of nucleons. When the two nuclei are within a given distance, a window opens for the transfer between the two systems based on potential barriers. The transfer probability is calculated taking into account Pauli blocking. This simulation is used to interact the projectile and target and form an excited quasiprojectile source. DIT was written specifically for the Fermi energy domain, 27 to 44 MeV/nucleon, and includes angular momentum in the transfer probabilities and cross-sections.

TABLE XII. Relationship between fn and lstep for finding the number of generated events for 32 MeV/nucleon $^{40}$Ar on $^{112}$Sn in the DIT simulation.

| fn | lstep | Events |
|---|---|---|
| 0.01 | 1 | 520 |
| 0.01 | 10 | 50 |
| 0.01 | 100 | 5 |
| 0.01 | 1 | 520 |
| 0.1 | 1 | 5254 |
| 1.0 | 1 | 52278 |
| 20.0 | 1 | 1045932 |

### 1. Input Parameters

The input parameters include the Z and A of the target and projectile and the beam energy. The Randrup equivalent was used in the type of interaction. This means that both nucleons directed toward and away from the window can be transferred. This takes into account orbiting and has a quadratic dependence of dissipation with velocity. The minimum angular momentum is 10 and the maximum of 1000, the number of events was determined by setting fn to 0.1 and lstep to 10 for about 15,000 events, and set the maximum excitation cut-off to 1000, to keep all fragments. Several fn and lstep settings were initially run to find the optimal setting that were used for all systems. Table XII shows the relationship of fn and lstep to the number of events generated, so one can extrapolate these values to achieve their desired number of events.

### 2. Selecting the Quasiprojectile Source

This code was written specifically for deep inelastic transfers and the quasiprojectile source is written out automatically.

### 3. Results

Figure 63 shows an example of the mass and charge distributions. This shows that the source is projectile like. Table XIII shows the actual number of events calculated along with the mean values of the excitation energy (E*), mass (A), charge (Z), neutron number (N), and neutron to proton ratio (N/Z). There is not much difference in the mean A, Z, or N/Z between the two energy sets, but the mean excitation energy is about 50 MeV greater in the higher energy set of systems. DIT was initially run with 40 times more events, because only a single de-excitation per primary event was going to be used in the SMM afterburner. These results are summarized in Table XIV. Comparison between Table 6 and Table 7 show that the mean values do not require a large number of events to stabilize. At the time the disk filled up with the millions of events and they had to be deleted due to space constraints.

## B. H.I.P.S.E.

HIPSE is the Heavy-Ion Phase-Space Exploration event generator by Denis Lacroix [67]. This generator uses a Thomas-Fermi approximation using a Seyler-Blanchard force to sample nucleons inside the target and projectile. This code is applicable to intermediate energies, 10 to 80 MeV/nucleon. Also integrated with this code is a SIMON routine that generates a cold fragment output file.

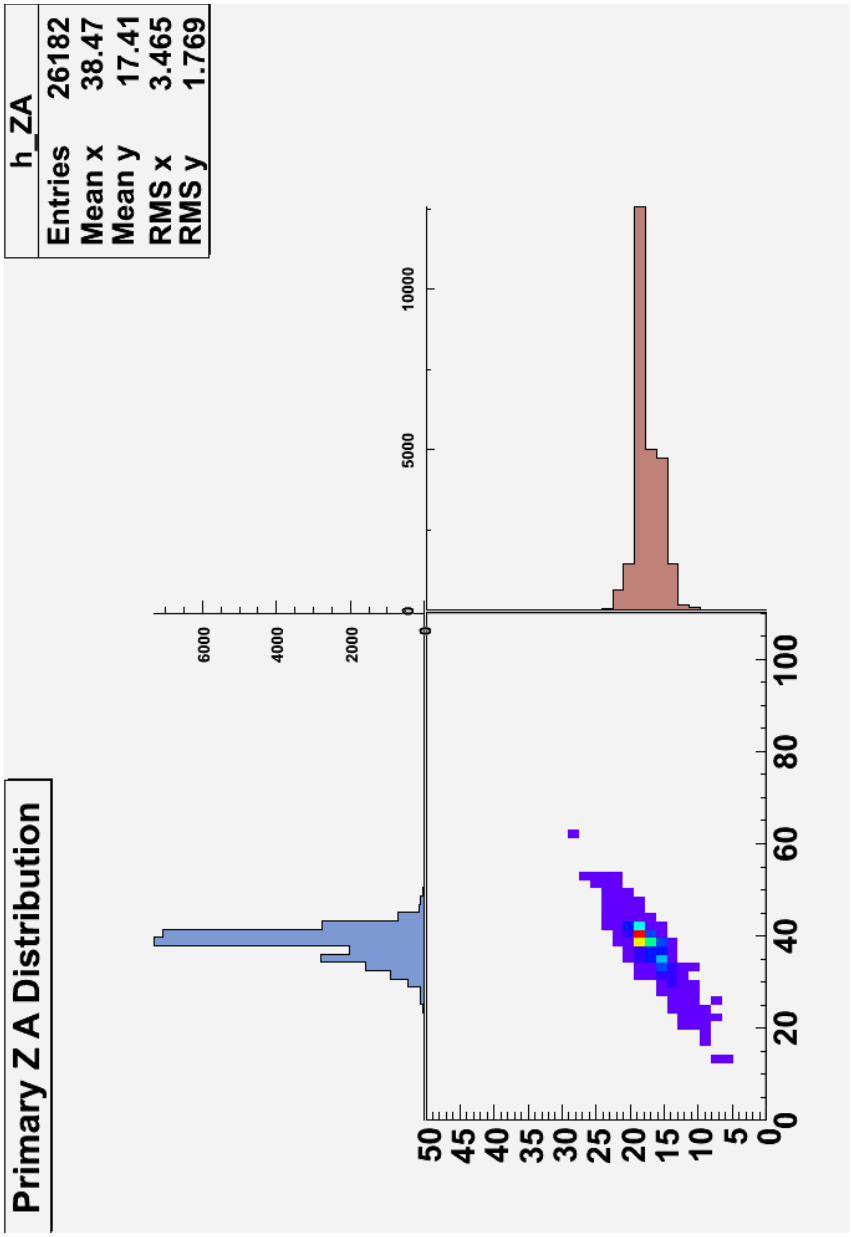


FIG. 63. (Color online) Example charge and mass distributions from DIT using the reaction 32 MeV/nucleon $^{40}$Ar on $^{112}$Sn.

TABLE XIII. List of systems with their total number of events, mean excitation energy, mean mass, mean charge, mean neutron number, and mean N/Z from the DIT simulation.

| System | Events | Mean E* | Mean A | Mean Z | Mean N | Mean N/Z |
|---|---|---|---|---|---|---|
| 32Ar40Sn112 | 26182 | 110.7 | 38.47 | 17.41 | 21.06 | 1.21 |
| 32Ar40Sn124 | 28885 | 113.9 | 38.37 | 16.71 | 21.66 | 1.30 |
| 32Ca40Sn112 | 25106 | 111.2 | 38.57 | 18.66 | 19.91 | 1.07 |
| 32Ca40Sn124 | 27852 | 116.4 | 38.48 | 17.96 | 20.52 | 1.14 |
| 32Ca48Sn112 | 35364 | 127.1 | 46.60 | 19.98 | 26.62 | 1.33 |
| 32Ca48Sn124 | 39257 | 130.2 | 46.54 | 19.25 | 27.29 | 1.42 |
| 45Ar40Sn112 | 37619 | 151.5 | 38.52 | 17.42 | 21.10 | 1.21 |
| 45Ar40Sn124 | 41421 | 156.7 | 38.43 | 16.79 | 21.64 | 1.29 |
| 45Ca40Sn112 | 36133 | 153.1 | 38.63 | 18.74 | 19.89 | 1.06 |
| 45Ca40Sn124 | 40170 | 160.0 | 38.54 | 18.08 | 20.46 | 1.13 |
| 45Ca48Sn112 | 50429 | 172.7 | 46.64 | 19.95 | 26.69 | 1.34 |
| 45Ca48Sn124 | 55933 | 176.8 | 46.59 | 19.28 | 27.31 | 1.42 |

TABLE XIV. List of systems with their total number of events, mean excitation energy, mean mass, mean charge, mean neutron number, and mean N/Z from the DIT simulation with 40 times more events.

| System | Events | Mean E* | Mean A | Mean Z | Mean N | Mean N/Z |
|---|---|---|---|---|---|---|
| 32Ar40Sn112 | 1045475 | 110.5 | 38.47 | 17.41 | 21.06 | 1.21 |
| 32Ar40Sn124 | 1155071 | 113.7 | 38.38 | 16.72 | 21.66 | 1.30 |
| 32Ca40Sn112 | 1000794 | 111.2 | 38.58 | 18.67 | 19.91 | 1.07 |
| 32Ca40Sn124 | 1110481 | 116.8 | 38.48 | 17.94 | 20.53 | 1.14 |
| 32Ca48Sn112 | 1410436 | 127.5 | 46.61 | 19.99 | 26.62 | 1.33 |
| 32Ca48Sn124 | 1568410 | 129.8 | 46.52 | 19.25 | 27.28 | 1.42 |
| 45Ar40Sn112 | 1498789 | 151.4 | 38.52 | 17.42 | 21.10 | 1.21 |
| 45Ar40Sn124 | 1652036 | 156.0 | 38.44 | 16.80 | 21.64 | 1.29 |
| 45Ca40Sn112 | 1442199 | 153.1 | 38.63 | 18.75 | 19.89 | 1.06 |
| 45Ca40Sn124 | 1599998 | 159.8 | 38.55 | 18.11 | 20.44 | 1.13 |
| 45Ca48Sn112 | 2014270 | 171.6 | 46.65 | 19.96 | 26.89 | 1.35 |
| 45Ca48Sn124 | 2234576 | 174.9 | 46.57 | 19.27 | 27.29 | 1.42 |

### 1. Input Parameters

The input file requires the Z and A of the projectile and target and the beam energy in MeV/nucleon. The impact parameter range must also be specified, and the range 0-11 fm was used for all systems. The maximum impact parameter was approximated using the relation

$$r = r_0 A^{1/3} \tag{5.1}$$

with $r_0$ equal to 1.2 fm, for mass 40, 48, 112, and 124 the radii are 4.104 fm, 4.361 fm, 5.784 fm and 5.984 fm, respectively. The largest system ($^{48}$Ca + $^{124}$Sn) has the maximum impact parameter of 10.345 fm, so 11 fm was chosen for the upper limit. The impact parameters are randomly distributed in this interval with the probability:

$$2\pi b db \tag{5.2}$$

Several modifications were made from the standard use of the code. First the meanaz.data file, which contains the mean A for each Z, had K and Ca changed from 41 and 42 to 39 and 40, respectively, because these are the most abundant mass for these elements. Second the standard input parameters had to be adjusted for the two beam energies of 32 and 45 MeV/nucleon. Given the standard values at 10, 25, 50, and 80 MeV/nucleon (Table XV), a best fit equation was used to extrapolate the parameters at 32 and 45 MeV/nucleon.

The percent of nucleon-nucleon collisions, which is the percent of collisions occurring in the overlap region, was fitted using a second degree polynomial of the form:

TABLE XV. Table of the standard values used in HIPSE at 10, 25, 50, and 80 MeV/nucleon along with the extrapolated values for the two energies used in this work.

| Beam Energy | Hardness of Potential | Percent Exchange | Percent NN Collisions |
|---|---|---|---|
| 10 MeV/A | -0.10 | 0.60 | 0.00 |
| 25 MeV/A | 0.10 | 0.45 | 0.02 |
| 50 MeV/A | 0.20 | 0.30 | 0.05 |
| 80 MeV/A | 0.25 | 0.25 | 0.10 |
| 32 MeV/A | 0.140 | 0.399 | 0.027 |
| 45 MeV/A | 0.187 | 0.320 | 0.044 |

$$PercentNNCollision = 0.000005E_{Beam}^2 + 0.000960E_{Beam} - 0.009124 \quad (5.3)$$

with an $R^2$ value of 0.9988. The percent exchange, which is the fraction of nucleons exchanged, was also fitted using a second degree polynomial of the form:

$$PercentExchange = 0.000085E_{Beam}^2 - 0.012621E_{Beam} + 0.715948 \quad (5.4)$$

with an $R^2$ value of 0.9997. Finally the hardness of the potential, which determines the amount of transparency, was fitted using a second order exponential decay of the form:

$$Hardness = -0.33554e^{-E_{Beam}/38.39901} - 0.5294e^{-E_{Beam}/7.24587} + 0.29179 \quad (5.5)$$

with an $R^2$ of 1. With the beam energy of 32 MeV/nucleon the hardness of the

potential was 0.140, the percent exchange was 0.399, and the percent nucleus-nucleus collision was 0.027. For the 45 MeV/nucleon the hardness of the potential was 0.187, the percent exchange was 0.320, and the percent nucleus-nucleus collision was 0.044. Roughly 50,000 events were generated for each of the 12 systems.

### 2. Selecting the Quasiprojectile Source

The output files from HIPSE have flags, which label the target, projectile and neck regions. However the flags should not be used and another method is needed to find the quasiprojectile source [68]. To select the quasiprojectile sources the results were cut on percent beam velocity. Figure 64 shows plots of mass versus impact parameter using different momentum cuts from 0% to 50%. The 50% cut is the cleanest and was used to feed into SMM. There are low mass fragments, which could have also been cut, but they were also fed to SMM, and were essentially filtered out (as they should be) from having low excitation energies and non-quasiprojectile-like masses. Any leftover events will be filtered during the reconstruction, which requires the charge of the quasiprojectile to be the charge of the beam plus or minus 2.

### 3. Results

There are two output files: a cold, or after de-excitation, and a hot, or before de-excitation, file. Table XVI summarizes the mean A, Z and N/Z from the hot and cold output from HIPSE (The cold file was created by a SIMON routine inside HIPSE). The code does not write out neutrons in the cold file, however the hot file contains this information, so the means are more realistic. The neutrons can be determined in the cold file by subtracting the charged particle multiplicity from the total multiplicity.

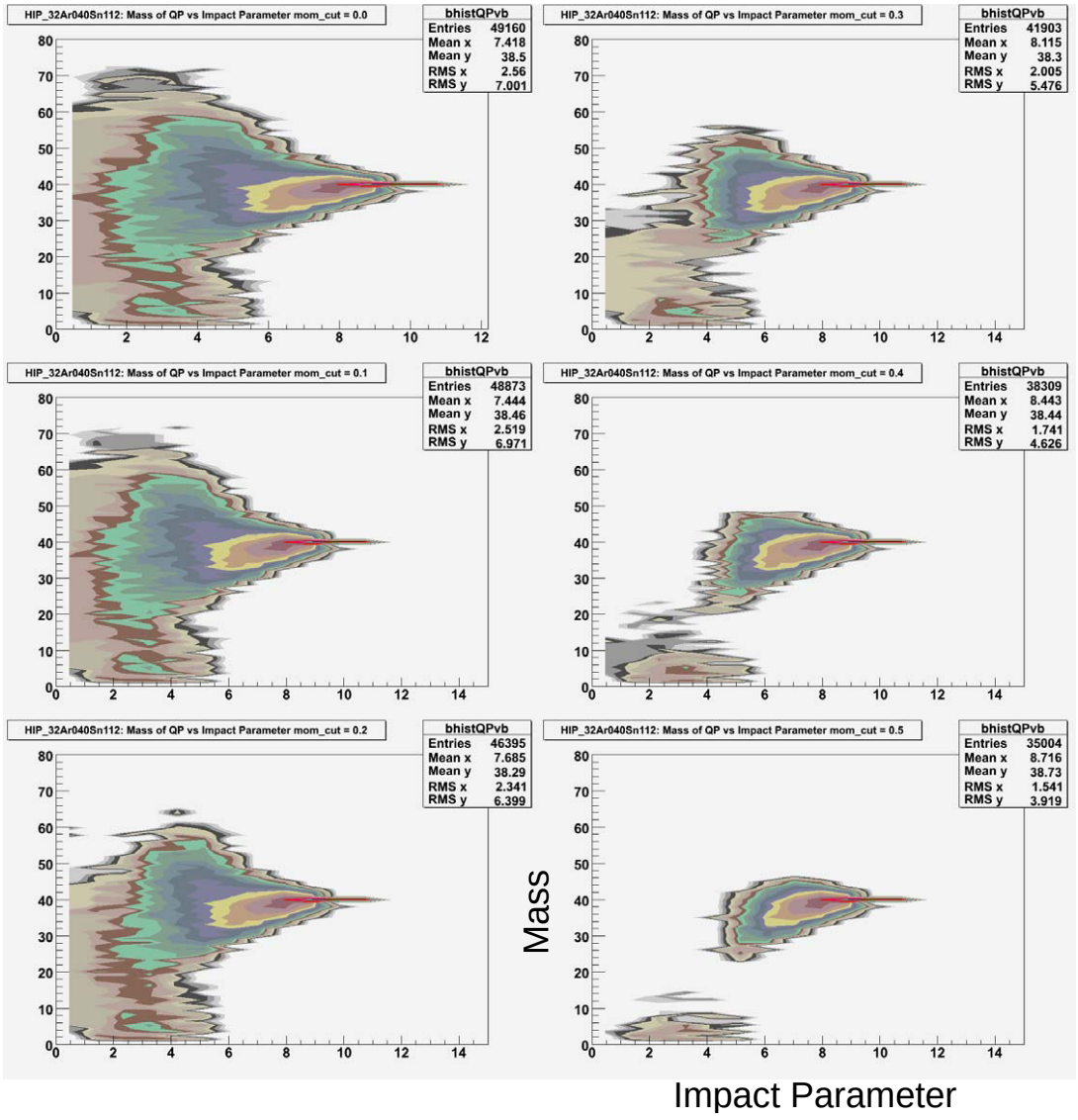


FIG. 64. (Color online) HIPSE mass versus impact parameter plots with cuts of 0, 10, 20, 30, 40 and 50 percent beam momentum.

TABLE XVI. List of systems with their mean mass, mean charge, and mean N/Z for the cold and hot output from HIPSE.

| System | Cold A | Cold Z | Cold N/Z | Hot A | Hot Z | Hot N/Z |
|---|---|---|---|---|---|---|
| 32Ar40Sn112 | 37.40 | 17.52 | 1.135 | 38.54 | 17.56 | 1.195 |
| 32Ar40Sn124 | 37.20 | 17.28 | 1.153 | 38.57 | 17.28 | 1.232 |
| 32Ca40Sn112 | 37.95 | 19.19 | 0.978 | 38.69 | 19.19 | 1.016 |
| 32Ca40Sn124 | 37.73 | 18.86 | 1.001 | 38.62 | 18.86 | 1.048 |
| 32Ca48Sn112 | 44.25 | 19.69 | 1.247 | 45.97 | 19.69 | 1.335 |
| 32Ca48Sn124 | 43.88 | 19.37 | 1.265 | 45.89 | 19.39 | 1.367 |
| 45Ar40Sn112 | 36.38 | 17.12 | 1.125 | 37.64 | 17.17 | 1.192 |
| 45Ar40Sn124 | 36.10 | 16.86 | 1.141 | 37.56 | 16.86 | 1.228 |
| 45Ca40Sn112 | 36.79 | 18.68 | 0.969 | 37.62 | 18.68 | 1.014 |
| 45Ca40Sn124 | 36.57 | 18.40 | 0.988 | 37.60 | 18.40 | 1.043 |
| 45Ca48Sn112 | 42.89 | 19.17 | 1.237 | 44.82 | 19.17 | 1.338 |
| 45Ca48Sn124 | 42.47 | 18.89 | 1.248 | 44.65 | 18.89 | 1.364 |

TABLE XVII. Mean values of mass, charge, excitation energy per nucleon at time 180 fm/c from different number of events along with the time it took to run in BNV in the test code setup.

| Number | A | Z | $E^*$ | Time |
|---|---|---|---|---|
| 2 | 34.5 | 14.5 | 3.86 | 00:32:00 |
| 10 | 35.5 | 15.5 | 3.67 | 02:14:04 |
| 100 | 36.5 | 15.5 | 3.60 | 20:35:22 |
| 518 | 36.5 | 15.5 | 3.60 | 280:07:53 |

## C. B.N.V.

BNV is the Boltzmann-Nordheim-Vlasov code. This code has been developed by the Catania group. The base BNV code used is TWINGO [69]. One event takes about 15 minutes to calculate on a single processor in the Cyclotron Institute cluster. To optimize the number of events required to achieve a stabilized mean A, Z and excitation energy per nucleon a single system, 32 MeV/nucleon $^{48}$Ca on $^{124}$Sn using a soft EOS and impact parameter of 8, was run for 2, 10, 100 and 518 events. Table XVII show the mean values of A, Z, excitation energy and how long it took to run. The mean values have stabilized by 100 events. Based on the triangular distribution of impact parameters used, described in the next section, roughly 1000 total events were run for each systems and two different nEOS to compare with the experimental data.

### 1. Input Parameters

The parameters that were user defined will be discussed next, followed by the parameters that were left at default values. The first parameter is the impact parameter,

which varied from 0 to 12 by integer values using a triangular distribution. The maximum impact parameter was chosen at touching spheres for the largest system, $^{48}$Ca on $^{124}$Sn. Then the beam energy and neutron and proton numbers for the target and projectile were specified. The strength of the nEOS was chosen to be either stiff or soft. Every combination was used, creating a total of 312 distinct simulations.

The parameters that were unchanged from default are discussed here. The number of test particles per nucleon was set at 50. The maximum time to run was set at 300 fm/c. GR is the full width at half max of the Gaussian in fm and was set to 1.444. GK is the full width at half max of the Gaussian in 1/fm and was set to 0.346. ZREL is the starting distance between the projectile and target in fm and was set to 16. DT is the time interval in fm/c and was set to 0.5. TDEN is the time interval for file output in fm/c and was set to 20. DTDEN is also a time interval for file output in fm/c and was set to 20. ICT is the number of individual collisions within a time interval DT and was set to 2. IDP is the compressibility constant and was set to 200. ISIG was 1 to turn on the angular dependence of the collision. IFULL was 1 to use a full ensemble. ICOUL was 1 to turn on the Coulomb term. ISY was 1 to turn on the symmetry term. V1 is the B parameter from the soft mean field potential for K = 200 and was set to 303. SG is the sigma parameter from the soft mean field potential for K = 200 and was set to 1.16666666667. aaa is the A parameter from the soft mean field potential for K = 200 and was set to -356. surf is the surface coefficient and was set to 6. ITMAX is twice the final time in fm/c and was set to 600.

To get a distribution similar to the experimental distribution a triangular distribution was used. The triangular distribution is based on equation 5.2, so at 0 impact parameter there are 0 events, then 25, 50, 75, 100, 125, 150, 175, 200, 225, 250, 275, and 300 events for 1, 2, 3, 4, 5, 6, 7, 8, 9, 10, 11, 12 impact parameter. Since there are 312 BNV simulations that need to run, since each system must be run at each

of 13 impact parameters and there are two equation-of-states being used. A code, CondorScriptCreator.f, was created, to create all 312 directories, copy the simulations into them, generate the input files, generate the Condor job files and finally create a script that launches all the Condor jobs.

### 2. Selecting the Quasiprojectile Source

BNV writes output at specific time steps. Figure 65 shows the interaction between projectile and target for the 32 MeV/nucleon $^{48}$Ca on $^{124}$Sn using a soft equation of state for impact parameters 1, 5 and 8. The plots show the density contours of the reacting system from t = 0 fm/c to t = 300 fm/c (roughly $10^{-22}$ seconds) in time steps of 20 fm/c. At an impact parameter of 1 there is a fusion reaction forming a compound system. At an impact parameter of 5 there is a mid peripheral reaction with a slight neck region produced. Then at an impact parameter of 8 there is a peripheral reaction leaving a quasiprojectile and a quasitarget.

The time step chosen for input into SMM was 160 fm/c. This is when the target and projectile have separated. The excitation energy versus time is shown in figure 66. The gap from 40 to 120 fm/c is when the target and projectile are interacting and the excitation energy of the projectile cannot be calculated. Then after the peak is reached shortly after separation, the excitation energy decreases.

BNV was run with distinct impact parameters, so there are multiple output files for each impact parameter. A code, CatBNV.f, was written, which reads in each of the impact parameter output files at 160 fm/c and combines them into a single file. Then to convert the BNV output into SMM input a code, bnv2smm.f, was written. This code also filters out fusion events and selects the quasiprojectile source from target and projectile events, as well as from events with a mid velocity source. To select the quasiprojectile source a cut on charge is used. Figure 67 shows three plots. The top

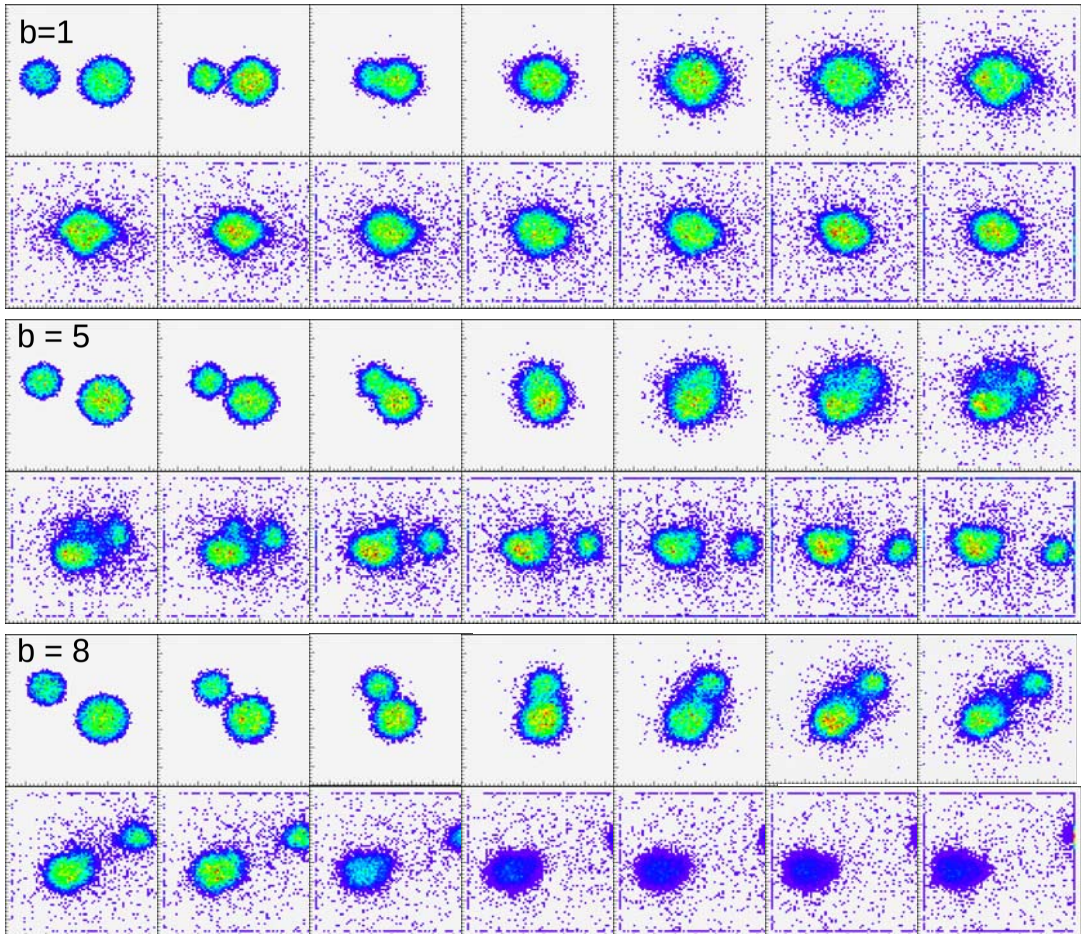


FIG. 65. (Color online) BNV density profiles for 32 MeV/nucleon $^{48}$Ca on $^{124}$Sn using a soft equation of state with time steps of 20 fm/c for impact parameters 1 (top), 5 (middle) and 8 (bottom).

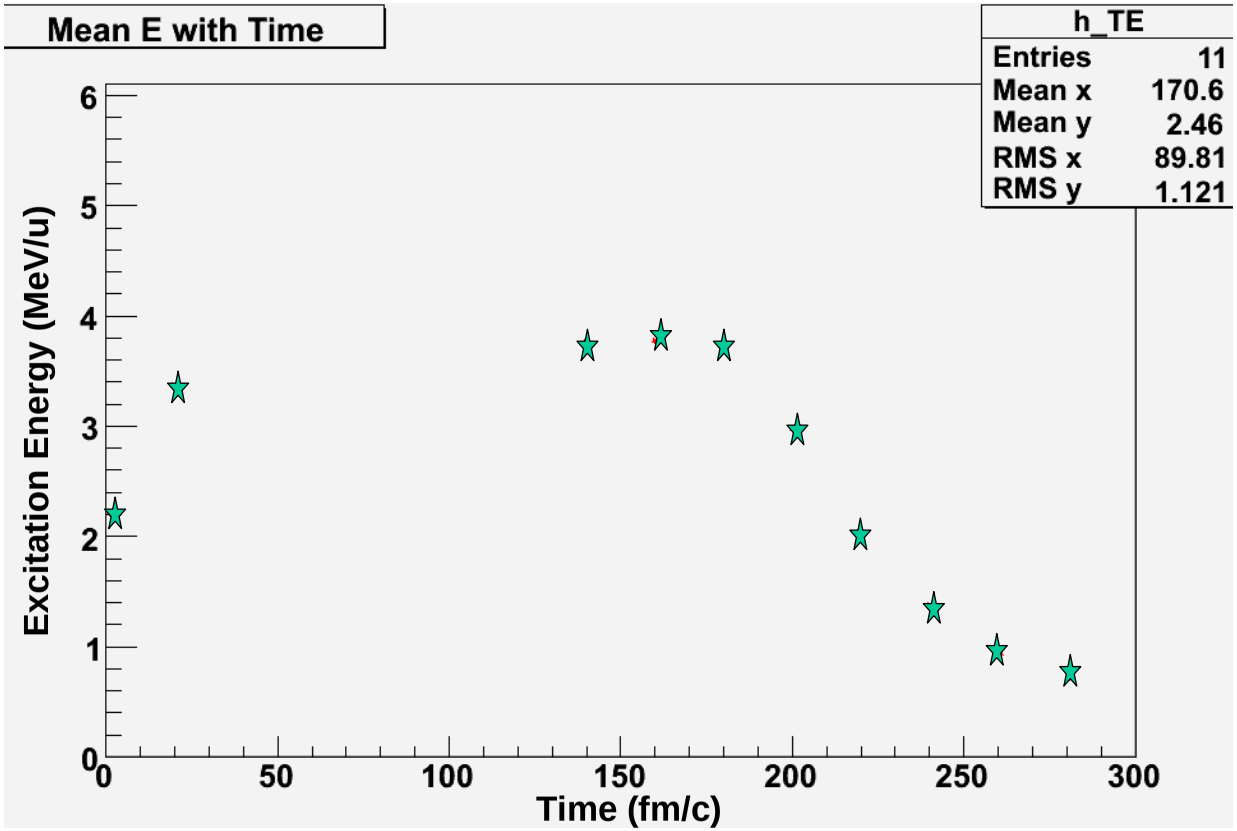


FIG. 66. Excitation energy versus time in fm/c from BNV used to select time of maximum excitation energy after separation of the projectile and target.

left is the mass versus charge plot having three distinct regions, the projectile, target and composite system. The top right and bottom left plots show the mass and charge projections, respectfully, which better illustrate the separation of the three sources. Using the requirement that the charge must be between 10 and 30 provides a good cut on the quasiprojectile source.

Once the SMM input files were ready a code, CondorScriptCreatorSMM.f, was created, which sets up directories for all systems at both soft and stiff nEOS and then creates four sub-directories for each of the four symmetry energy parameterizations of SMM. Then the necessary SMM files and input files are moved to the respective directories. Then the code generates condor job files, which allows the simulations to run using a cluster of computers. Finally a script is created, which launches all the condor jobs.

### 3. Results

The mean A, Z and excitation energy per nucleon for the hot quasiprojectile source are given in table XVIII for the 32 and 45 MeV/nucleon systems. The lower energy has larger mean A, Z, and excitation energy per nucleon than the higher energy. At a given energy there is not much difference between the soft and stiff nEOS used.

## D. i.B.U.U.

iBUU (2004 version) is the isospin (here referring to N/Z) and momentum dependent Boltzmann-Uheling-Uhlenbeck code by Boa-An Li [70]. This code was also modified by Lie-Wen Chen to use a specific input file and parameters contained therein. The N/Z dependence of the code is from the nucleon-nucleon cross sections, which are different for n-n, n-p, and p-p interactions. There is also a symmetry energy

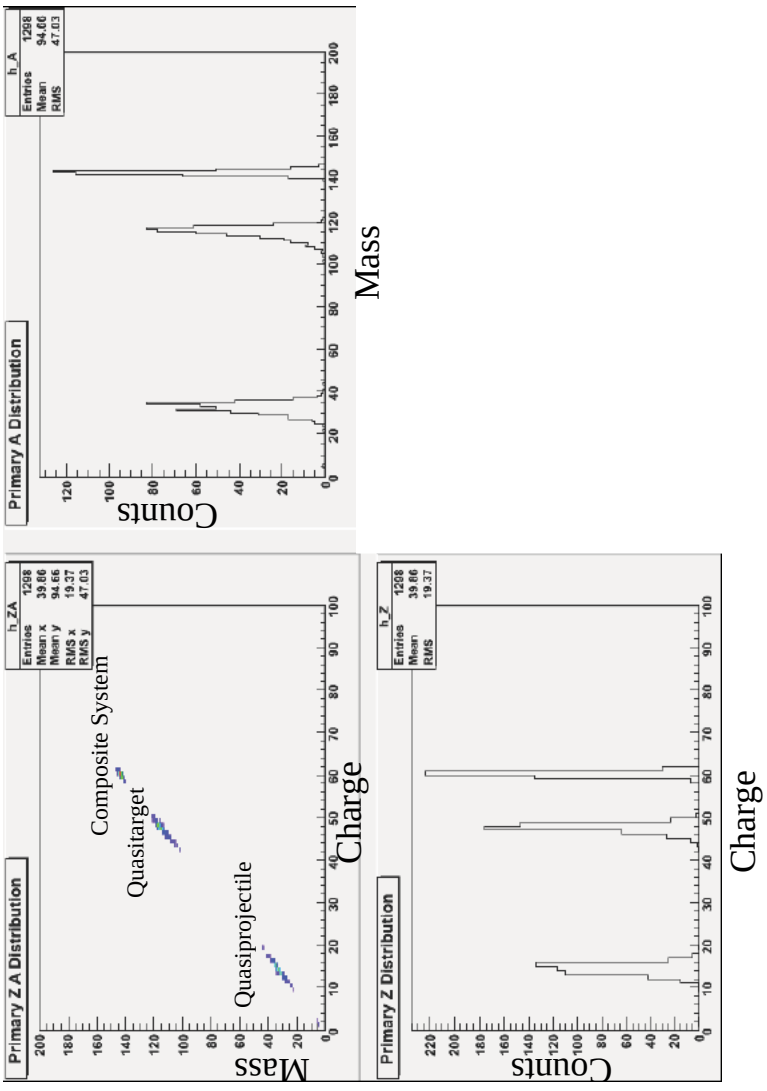


FIG. 67. (Color online) Selecting the quasiprojectile from BNV hot output at 160 fm/c. Top left: mass versus charge, top right: mass distribution, bottom left: charge distribution.

TABLE XVIII. Summary of mean results from BNV quasiprojectiles for 32 MeV/nucleon systems (top) and 45 MeV/nucleon systems (bottom).

| | Soft nEOS | | | Stiff nEOS | | |
|---|---|---|---|---|---|---|
| System | A | Z | $E^*$ | A | Z | $E^*$ |
| 40Ar112Sn | 32.51 | 14.91 | 3.10 | 32.55 | 14.93 | 3.11 |
| 40Ar124Sn | 32.36 | 14.32 | 3.01 | 32.42 | 14.40 | 2.99 |
| 40Ca112Sn | 32.94 | 15.78 | 3.06 | 32.80 | 15.72 | 3.05 |
| 40Ca124Sn | 32.57 | 15.10 | 3.05 | 32.38 | 14.97 | 3.17 |
| 48Ca112Sn | 39.39 | 17.39 | 3.08 | 39.79 | 17.56 | 3.01 |
| 48Ca124Sn | 39.32 | 16.82 | 2.92 | 39.13 | 16.73 | 2.94 |
| 40Ar112Sn | 29.17 | 13.37 | 2.08 | 28.89 | 13.29 | 2.14 |
| 40Ar124Sn | 28.80 | 12.81 | 1.92 | 29.04 | 12.89 | 1.92 |
| 40Ca112Sn | 28.84 | 13.88 | 2.18 | 29.51 | 14.16 | 2.22 |
| 40Ca124Sn | 28.99 | 13.51 | 2.02 | 28.98 | 13.51 | 1.94 |
| 48Ca112Sn | 34.70 | 15.39 | 2.28 | 34.80 | 15.43 | 2.27 |
| 48Ca124Sn | 34.58 | 14.85 | 2.13 | 34.67 | 14.88 | 2.07 |

incorporated that allows the user to select different values.

### 1. Input Parameters

One event takes about 10 hours on a single processor of the Cyclotron Institute cluster, since this is time intensive only 100 events were ran for each system. As in BNV the triangular distribution is used. To run the code the neutron and proton density profiles of the target and projectile are needed. These were calculated by Lie-Wen Chen using an RMF model [71]. The input file requires the mass and charge of the projectile and target as well as the beam energy. Single impact parameters were run, and later combined, using the triangular distribution setting the number of runs in manyb. ISEED, used for the random number generator was 5104971, then when more statistics were needed the date was used as the iseed in month day year format (MMDDYYYY).

Here are the values of the other parameters that were kept at the default values. ZEROPT, the initial Z-displacement of the system in fm, is 0. Zsurf in fm, is 1. The time intervals used were 0.5 fm/c, which should be small enough to only have a nucleon scattered once in that time interval. The maximum number of time steps is 400. ICOLL was selected to run the calculation as BUU. The number of test particles per nucleon was 200. The calculation was done in the center of mass frame, INSYS equal to 1. IPOT is 6, which selects a mean field. Interpolation of the Pauli-Blocking was used. isoPAU, the Pauli blocking flag was 1 for interpolated Pauli blocking. The dx, dy, dz in Fermi for the Pauli lattice were 2.73, 2.73 and 2.73, respectively. The dpx, dpy, dpz of the Pauli lattice were 0.18, 0.18 and 0.18, respectively. The first collision in one nucleus was avoided. The option for momentum distribution was set as usually. The output selected was final momenta, coordinates and px, pz of the nucleons. The time step interval for output was 10 fm/c. The pion production variables N*, direct

and indirect were 0 (only use delta resonances), 0 (no direct processes), and 0.2 (percentage of direct pion production in the n-n inelastic collision), respectfully. icoul had 1, 8, 0.038, 1, and 3. The x-parameter was -1 and Igogny was 1. IRNUMT and IRNUMP were both 100.

### 2. Selecting the Quasiprojectile Source

The density profiles were drawn and then the quasiprojectile source can be identified and velocity cuts can be made. However the density plots that were generated had a strange problem of both the projectile and target bursting as shown in figure 68. Discussing with Bao-An Li, had the possibility that these results were actually ring nuclei, however with additional discussions with Lie-Wen Chen, found that the compiler is most likely the culprit, therefore no results from iBUU will be discussed.

## E. S.M.M.

SMM is the Statistical Multifragmentation Model of Alexander Botvina [72, 73, 74, 75]. SMM assumes that the temperature and composition are homogeneous at freeze-out. The version used was SMM '05, which allows for variation of the symmetry energy coefficient to see what value best matches experiment.

### 1. Input Parameters

The four values of the symmetry energy chosen were 10, 15, 20 and 25 MeV. For each primary event, SMM will de-excite 10 times. The other input parameters used were full multifragmentation IMULF equal to 1. IMETR is 1 for Metropolis sampling. IMECH is 4 for (A,Z) Space with METR-4. FKACOL is 5 for kappa, where the total volume is 1 + kappa times initial volume. EPSIL0 is 16, so cold fragments are not

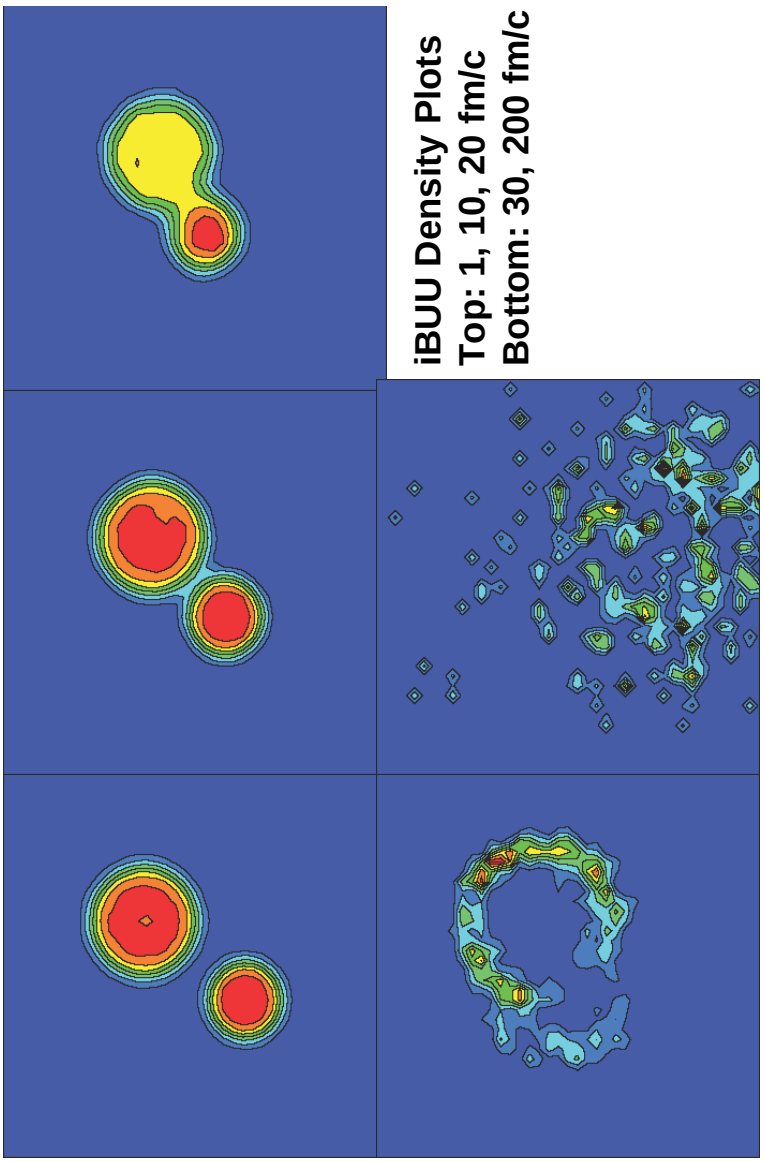


FIG. 68. (Color online) Density plots from iBUU showing the bursting bubble effect.

mass dependent. ILIDR is 1, so the liquid drop masses are used. The excitation energy parameters were set to have no lower limit and an upper limit of 15 MeV/nucleon, and the limit for multifragmentation to be 1.5 MeV/nucleon. I2S is 1, so both proximity and angular momentum are considered. iprox is 1, so the proximity of the second source is used. XRNO is 1 for the fragment overlap. IQUAN is 0, so the p, n, t and He are not treated quantum mechanically. IKAPPA is 0, so the free volume is multiplicity dependent. IMIC2 is 0, so the Metropolis partition is used. RR00 is 1.17 for the radius parameter used in METR4.

Souliotis has tried various parameterizations of the code to see if other parameters could effect the difference seen with changing the symmetry energy parameter. Changing the proximity (on/off), radius, breakup volume do not account for the changes seen when the symmetry energy parameter is changed from 15 to 25 [76].

The cold fragments will be analyzed like the experimental data to reconstruct the N/Z of the quasiprojectile source using both the reconstruction and fitting techniques. The results are discussed in chapter VI.

### F. F.A.U.S.T. Filter

The FAUST Filter is a software representation of the acceptance of FAUST. The simulation data is filtered leaving only what would be seen experimentally. This can help in understanding the effect of undetected particles. The filter also allows for dead detectors and setting thresholds as well. In this analysis no thresholds or dead detectors were removed by the filter. These are removed during the analysis, by the thresholds calculated from the experimental data.

The FAUST Filter was developed by Richard Laforest in VAX Fortran. The filter was then re-written by Marian Jandel and modified by Brian Stein and August Keksis.

This code was written in a ROOT macro that was compiled into an executable. The code uses two main input files a filter.data, which contains the X, Y, and Z coordinates for each of the four edges of all 68 silicon detectors, and a filter.input file, which allows for specifying thresholds and dead detectors. The filter takes the simulated fragments and determines their incident angle and see if the fragment would impinge on the detector. The fragments that would be detected are then written out in reduced physics tape format, and ready for the reconstruction stage.

# CHAPTER VI

## COMPARISON OF THEORY AND EXPERIMENT

The first section of this chapter describes the DIT/SMM study to determine the affect of undetected neutrons on the differences between the reconstruction and isobaric yield fitting methods for calculating the N/Z of the quasiprojectile. Then the simulation, which has a known N/Z of the quasiprojectile source, can be compared to the N/Z of the simulated source reconstructed using the newly developed technique, which can provide a means of validation of this procedure. The second section looks at the fractional yields, isobaric yields, isotopic yields and the mean N/Z of the experiment versus DIT/SMM results, with different values of the symmetry energy in the SMM calculation. Then there is a section on the mass distributions for reconstructed sources compared with the mass distributions from HIPSE, DIT, and BNV, which has two parameterizations of the nuclear equation-of-state. Finally a summary is given in the last section.

### A. D.I.T./S.M.M. Neutron Loss and Isobaric Ratio Fitting Method Testing

DIT/SMM was used to determine the effect of undetected neutrons on the differences between the reconstruction and isobaric yield fitting methods. Quasiprojectile sources generated in DIT were fed into SMM, which was run at the standard symmetry energy value of 25 MeV, for deexcitation. The results from SMM were then fed through the FAUST Filter and the fragments had their N/Z of the quasiprojectile source calculated both by reconstruction and the isobaric yield ratio fitting the same as was done in the experimental data. All the experimental results are shown in table XIX. For each system the target, projectile, and composite system N/Z values are given, the quasiprojectile N/Z values based on reconstruction and on the isobaric yield method

are given. The two methods yield a large difference, as was seen in the experimental data.

The quasiprojectile source N/Z is know from DIT and the results from the isobaric yield fitting method are in reasonable agreement, validating this procedure. The neutron loss was also determined and is show in the last column of table XIX. These results are in agreement with what is seen experimentally. At the higher energy there is a slight decrease in the N/Z calculated by the reconstruction, while the isobaric yield fitting is similar. There seems to be slightly more neutron loss at the higher energy, which is most likely caused by the greater mean excitation attained at the higher energy.

There is also an increased neutron loss with increasing N/Z of the quasiprojectile. Figures 69 to 80 show the N/Z of the quasiprojectile sources from DIT versus the N/Z of the quasiprojectile source reconstructed from SMM, using the standard symmetry energy of 25 MeV. If there were no neutron loss the reconstruction should yield the quasiprojectile N/Z of DIT, which is shown by the straight line. However when neutrons are not detected the N/Z reconstruction is increasingly deviating from the correct value with increasing neutron richness of the source, which is shown by the curved line. With higher energy the deviation starts earlier.

## B. Symmetry Energy Comparisons

In this section there are subsections for fractional yields, isobaric yields, isotopic yields and the mean N/Z comparisons of the experiment and DIT/SMM results. SMM was run four times using 10, 15, 20 and 25 MeV as the value of the symmetry energy. The experimental data appear to trend best with a lower value of the symmetry energy, however the results are not conclusive and further investigation is required.

TABLE XIX. Summary of results from DIT/SMM comparison with experiment. 32 MeV/nucleon systems top half, 45 MeV/nucleon systems bottom half.

| System | N/Z Tar. | N/Z Proj. | N/Z Comp. Sys. | N/Z Exp. Recon. | N/Z Exp. Fit. | N/Z Sim. Recon. | N/Z Sim. Fit. | N/Z DIT Back Track | Neutron Loss |
|---|---|---|---|---|---|---|---|---|---|
| $^{40}$Ar + $^{112}$Sn | 1.24 | 1.22 | 1.24 | 1.00 | 1.23 | 1.03 | 1.23 | 1.17 | 3.36 |
| $^{40}$Ar + $^{124}$Sn | 1.48 | 1.22 | 1.41 | 1.02 | 1.32 | 1.08 | 1.34 | 1.27 | 4.08 |
| $^{40}$Ca + $^{112}$Sn | 1.24 | 1.00 | 1.17 | 0.98 | 1.09 | 0.97 | 1.11 | 1.04 | 2.31 |
| $^{40}$Ca + $^{124}$Sn | 1.48 | 1.00 | 1.34 | 0.99 | 1.19 | 1.00 | 1.22 | 1.12 | 2.86 |
| $^{48}$Ca + $^{112}$Sn | 1.24 | 1.40 | 1.29 | 1.03 | 1.34 | 1.08 | 1.33 | 1.27 | 5.19 |
| $^{48}$Ca + $^{124}$Sn | 1.48 | 1.40 | 1.46 | 1.05 | 1.43 | 1.13 | 1.44 | 1.39 | 6.10 |
| $^{40}$Ar + $^{112}$Sn | 1.24 | 1.22 | 1.24 | 0.99 | 1.23 | 1.02 | 1.23 | 1.17 | 3.73 |
| $^{40}$Ar + $^{124}$Sn | 1.48 | 1.22 | 1.41 | 1.01 | 1.32 | 1.06 | 1.30 | 1.25 | 4.21 |
| $^{40}$Ca + $^{112}$Sn | 1.24 | 1.00 | 1.17 | 0.95 | 1.09 | 0.94 | 1.08 | 1.03 | 2.59 |
| $^{40}$Ca + $^{124}$Sn | 1.48 | 1.00 | 1.34 | 0.96 | 1.18 | 0.98 | 1.15 | 1.10 | 2.97 |
| $^{48}$Ca + $^{112}$Sn | 1.24 | 1.40 | 1.29 | 0.91 | 1.34 | 1.07 | 1.35 | 1.27 | 5.57 |
| $^{48}$Ca + $^{124}$Sn | 1.48 | 1.40 | 1.46 | 0.89 | 1.43 | 1.12 | 1.43 | 1.38 | 6.20 |

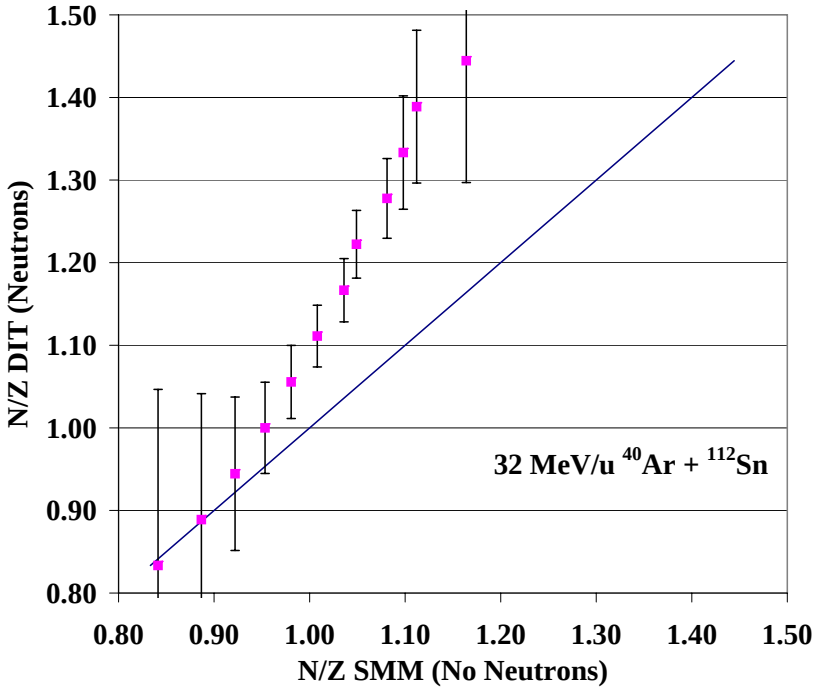


FIG. 69. (Color online) Comparison of the N/Z of the DIT quasiprojectile and the reconstructed SMM quasiprojectile, which has no neutrons, for the 32 MeV/nucleon $^{40}$Ar + $^{112}$Sn system. The straight line represents the N/Z of the quasiprojectile if no neutrons were lost, while the curved line represents the N/Z of the quasiprojectile with neutron loss.

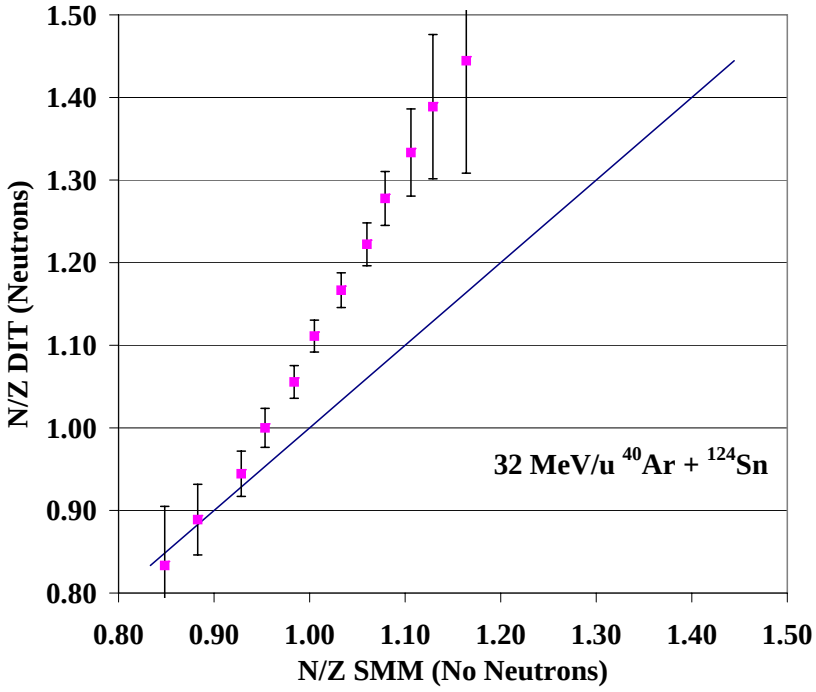


FIG. 70. (Color online) Comparison of the N/Z of the DIT quasiprojectile and the reconstructed SMM quasiprojectile, which has no neutrons, for the 32 MeV/nucleon $^{40}$Ar + $^{124}$Sn system. The straight line represents the N/Z of the quasiprojectile if no neutrons were lost, while the curved line represents the N/Z of the quasiprojectile with neutron loss.

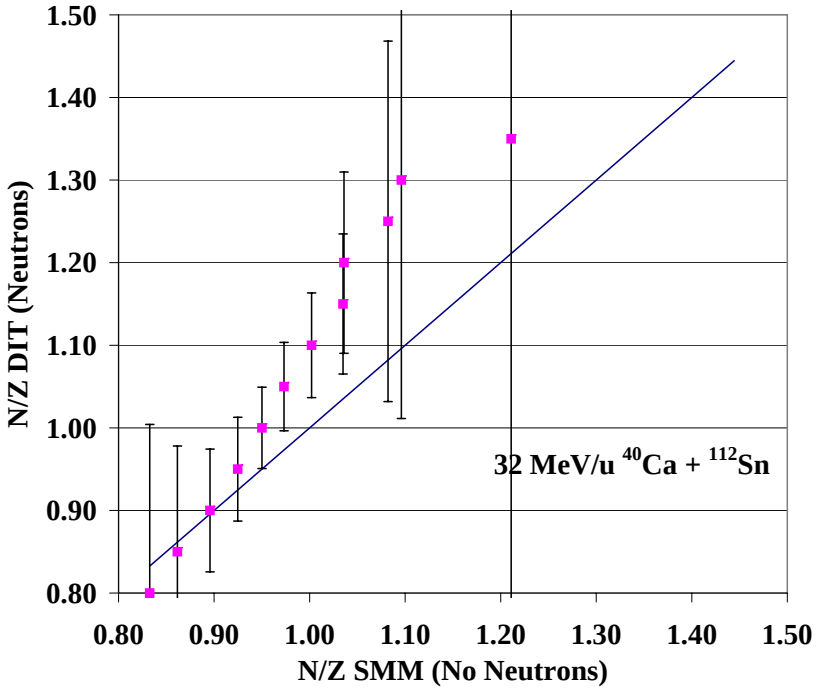


FIG. 71. (Color online) Comparison of the N/Z of the DIT quasiprojectile and the reconstructed SMM quasiprojectile, which has no neutrons, for the 32 MeV/nucleon $^{40}$Ca + $^{112}$Sn system. The straight line represents the N/Z of the quasiprojectile if no neutrons were lost, while the curved line represents the N/Z of the quasiprojectile with neutron loss.

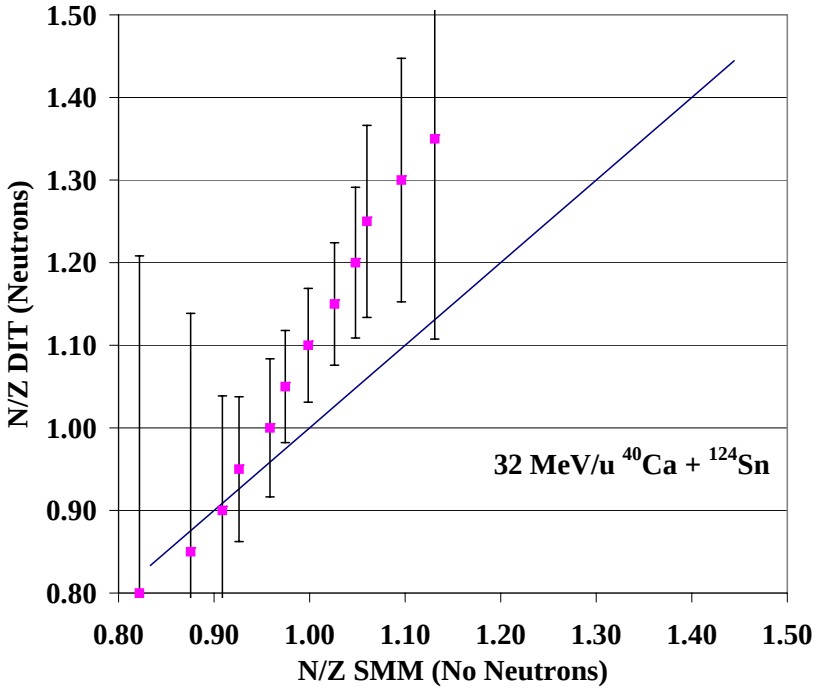


FIG. 72. (Color online) Comparison of the N/Z of the DIT quasiprojectile and the reconstructed SMM quasiprojectile, which has no neutrons, for the 32 MeV/nucleon $^{40}$Ca + $^{124}$Sn system. The straight line represents the N/Z of the quasiprojectile if no neutrons were lost, while the curved line represents the N/Z of the quasiprojectile with neutron loss.

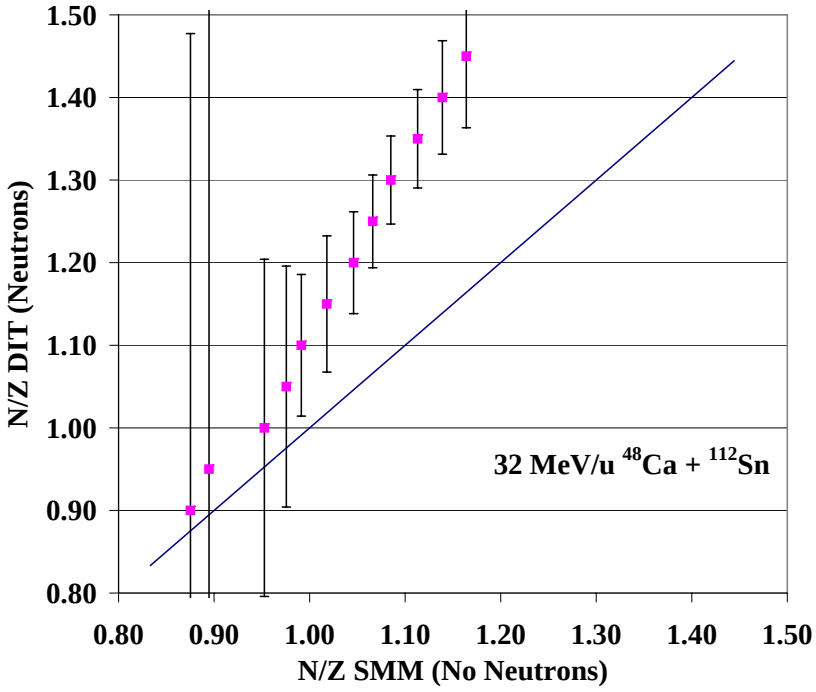


FIG. 73. (Color online) Comparison of the N/Z of the DIT quasiprojectile and the reconstructed SMM quasiprojectile, which has no neutrons, for the 32 MeV/nucleon $^{48}$Ca + $^{112}$Sn system. The straight line represents the N/Z of the quasiprojectile if no neutrons were lost, while the curved line represents the N/Z of the quasiprojectile with neutron loss.

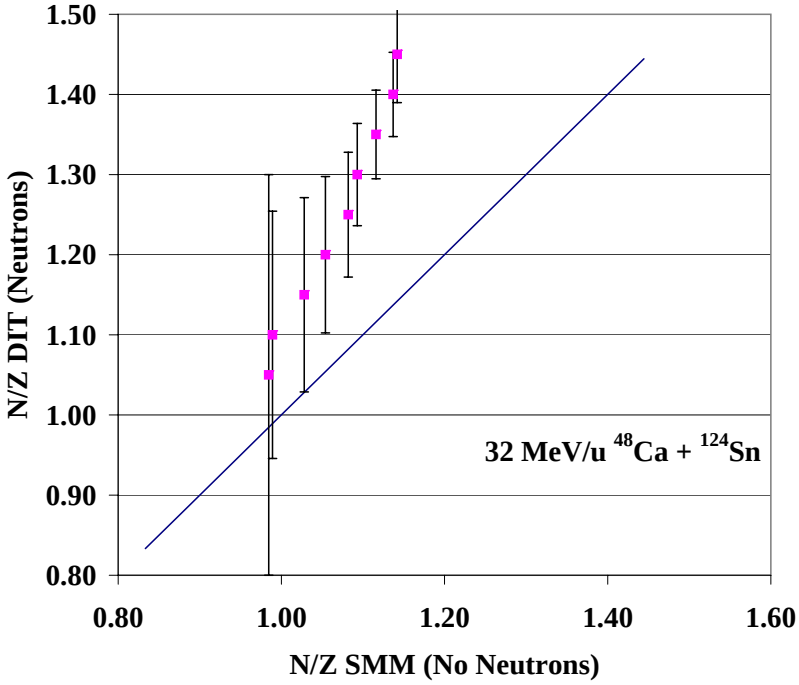


FIG. 74. (Color online) Comparison of the N/Z of the DIT quasiprojectile and the reconstructed SMM quasiprojectile, which has no neutrons, for the 32 MeV/nucleon $^{48}$Ca + $^{124}$Sn system. The straight line represents the N/Z of the quasiprojectile if no neutrons were lost, while the curved line represents the N/Z of the quasiprojectile with neutron loss.

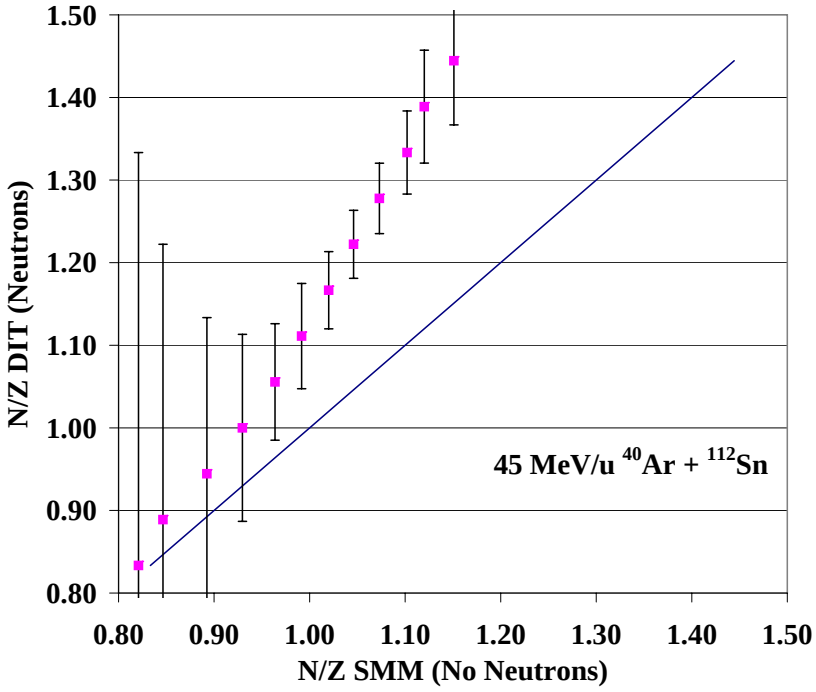


FIG. 75. (Color online) Comparison of the N/Z of the DIT quasiprojectile and the reconstructed SMM quasiprojectile, which has no neutrons, for the 45 MeV/nucleon $^{40}$Ar + $^{112}$Sn system. The straight line represents the N/Z of the quasiprojectile if no neutrons were lost, while the curved line represents the N/Z of the quasiprojectile with neutron loss.

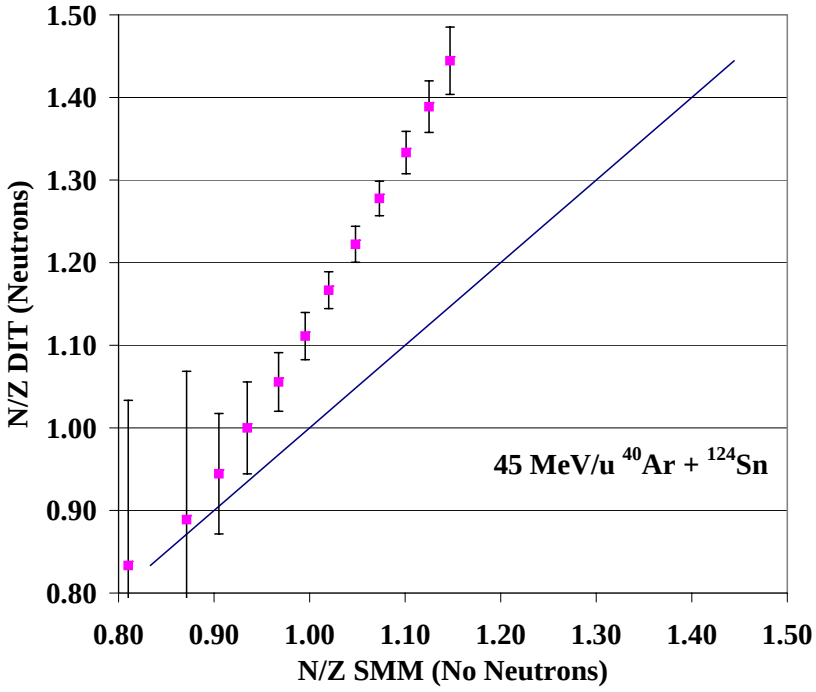


FIG. 76. (Color online) Comparison of the N/Z of the DIT quasiprojectile and the reconstructed SMM quasiprojectile, which has no neutrons, for the 45 MeV/nucleon $^{40}$Ar + $^{124}$Sn system. The straight line represents the N/Z of the quasiprojectile if no neutrons were lost, while the curved line represents the N/Z of the quasiprojectile with neutron loss.

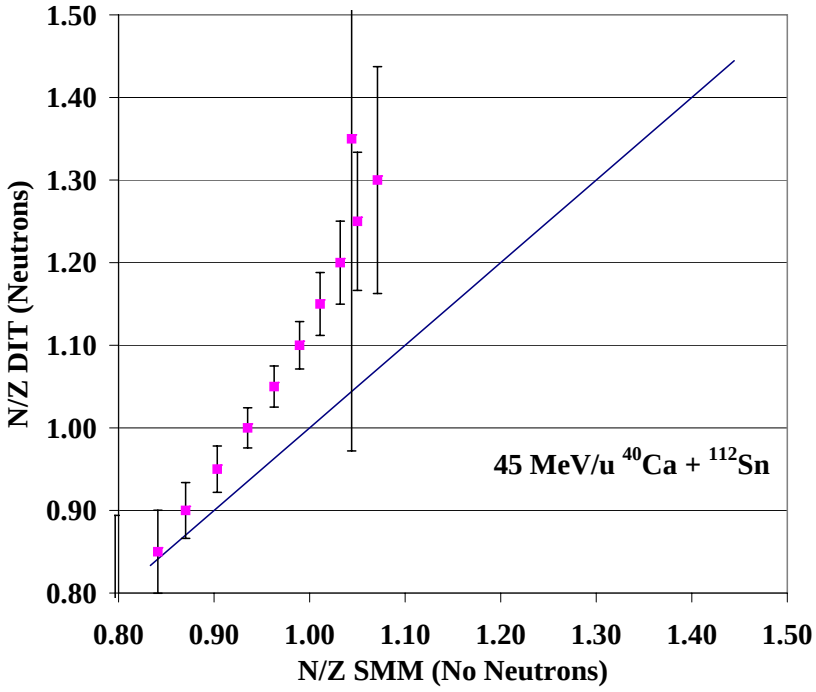


FIG. 77. (Color online) Comparison of the N/Z of the DIT quasiprojectile and the reconstructed SMM quasiprojectile, which has no neutrons, for the 45 MeV/nucleon $^{40}$Ca + $^{112}$Sn system. The straight line represents the N/Z of the quasiprojectile if no neutrons were lost, while the curved line represents the N/Z of the quasiprojectile with neutron loss.

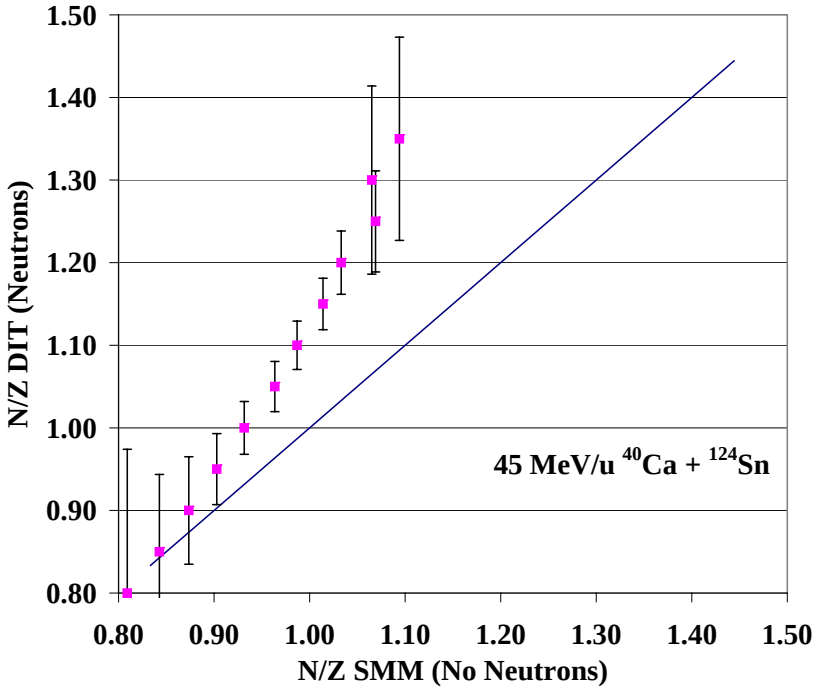


FIG. 78. (Color online) Comparison of the N/Z of the DIT quasiprojectile and the reconstructed SMM quasiprojectile, which has no neutrons, for the 45 MeV/nucleon $^{40}$Ca + $^{124}$Sn system. The straight line represents the N/Z of the quasiprojectile if no neutrons were lost, while the curved line represents the N/Z of the quasiprojectile with neutron loss.

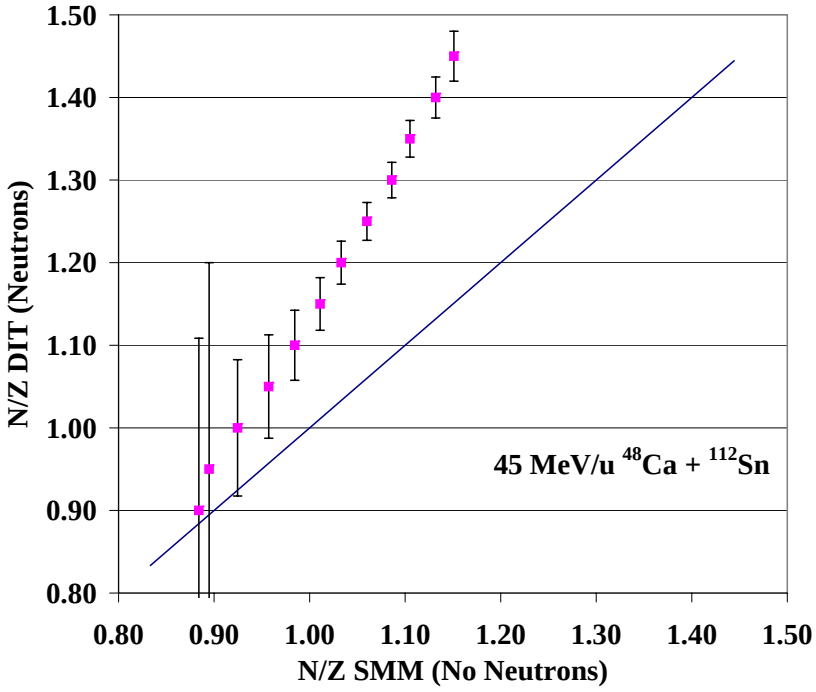


FIG. 79. (Color online) Comparison of the N/Z of the DIT quasiprojectile and the reconstructed SMM quasiprojectile, which has no neutrons, for the 45 MeV/nucleon $^{48}$Ca + $^{112}$Sn system. The straight line represents the N/Z of the quasiprojectile if no neutrons were lost, while the curved line represents the N/Z of the quasiprojectile with neutron loss.

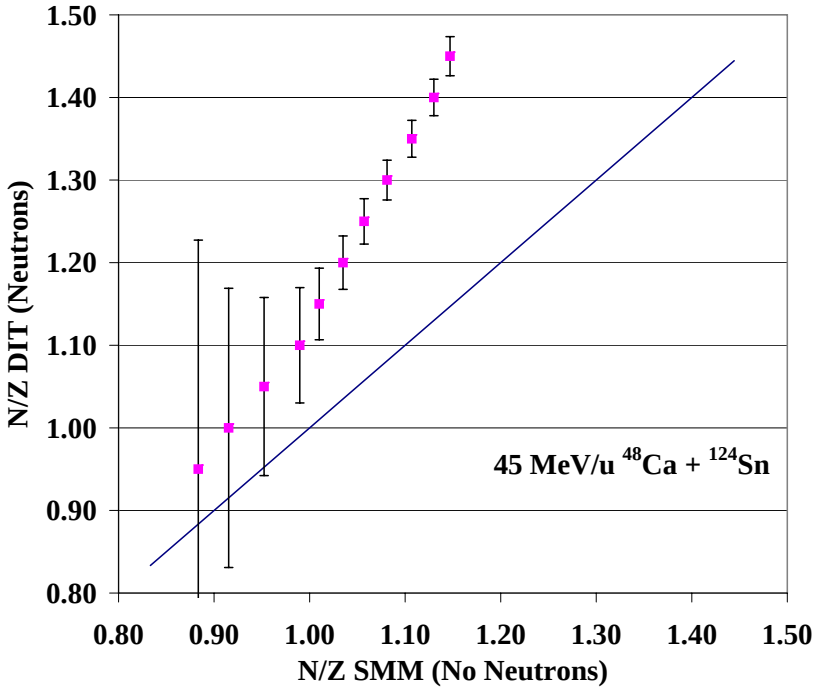


FIG. 80. (Color online) Comparison of the N/Z of the DIT quasiprojectile and the reconstructed SMM quasiprojectile, which has no neutrons, for the 45 MeV/nucleon $^{48}$Ca + $^{124}$Sn system. The straight line represents the N/Z of the quasiprojectile if no neutrons were lost, while the curved line represents the N/Z of the quasiprojectile with neutron loss.

### 1. Fractional Yield Comparisons

All the systems and angles exhibit similar trends, so only the 32 MeV/nucleon $^{40}$Ar on $^{112}$Sn at 7.01 degrees will be presented here. Figures 81 to 88 show the fractional yield plots for Hydrogen to Oxygen with the experimental data represented by a star, the symmetry energy of 25 with a cross, 20 with a triangle, 15 with a square and 10 with a diamond. Since the fractional yields for a given element depend on all of the isotopes and sum to one, a change in a single isotope effects all the other isotopes.

Starting with the Hydrogen fractional yields the proton is most abundant at the lowest symmetry energy and decreases with increasing symmetry energy. Both the deuteron and triton have this trend inverted, so the lowest symmetry energy has the smallest yield and increases in yield with increasing symmetry energy. Many of the points are very close together and have overlap in their error bars. This is very noticeable in the Helium fractional yields. Since alpha dominates in the helium yields it is difficult to differentiate amongst the different symmetry energies. Looking closely the values follow the same trend as the Hydrogen fractional yields.

Now looking at the IMFs there is a change observed, where now the largest symmetry energy populates the neutron-poor nuclides the least and the yields increase with decreasing symmetry energy. These differences most likely arise from the inhomogeneous distribution of N/Z between LCPs and IMFs. Now the Lithium fractional yields are the clearest yet, showing this trend in the IMFs. In the Beryllium yields this is still the trend, but the 20 and 25 symmetry energies are flipped in their mean values, but their error bars do overlap. The Beryllium trend also occurs in the Boron fractional yields. Then the Carbon, Nitrogen and Oxygen fractional yields also have the same trends. The experimental points are mixed throughout the various symmetry energies, but looking at the whole picture with all the elements there tends to be

greater agreement with the lower values of the symmetry energy.

### 2. Isotopic Yield Comparisons

All the systems and angles exhibit similar trends, so only the 32 MeV/nucleon $^{40}$Ar on $^{112}$Sn at 7.01 degrees will be presented here. Figure 89 shows all the isotopic yield ratios with the experimental data represented by a star, the symmetry energy of 25 with a cross, 20 with a triangle, 15 with a square and 10 with a diamond. There are two trends seen, the first is that for neutron-poor isotopes divided by neutron-poor isotopes, the ratio is greatest for the lowest symmetry energy. While for neutron-poor isotopes divided by neutron-rich isotopes this trend is reversed. These findings demonstrate that the symmetry energy does effect the fragment yields. The experimental points are mixed throughout the various symmetry energies, but looking at the whole picture there tends to be greater agreement with the lower values of the symmetry energy than the higher values.

### 3. Isobaric Yield Comparisons

All the systems and angles exhibit similar trends, so only the 32 MeV/nucleon $^{40}$Ar on $^{112}$Sn at 7.01 degrees will be presented here. Figure 90 shows all of the possible isobaric yield ratios with the experimental data represented by a star, the symmetry energy of 25 with a cross, 20 with a triangle, 15 with a square and 10 with a diamond. Here the larger symmetry energies typically have larger ratios than the smaller symmetry energies. The experimental data trend with the lower values. The $^{15}$N/$^{15}$O experimental point is much smaller than any of the theoretical points. This could be due to the $^{15}$O being on the fringe of the much more abundant $^{16}$O and the gates may have incorporated some additional $^{16}$O in the $^{15}$O yields.

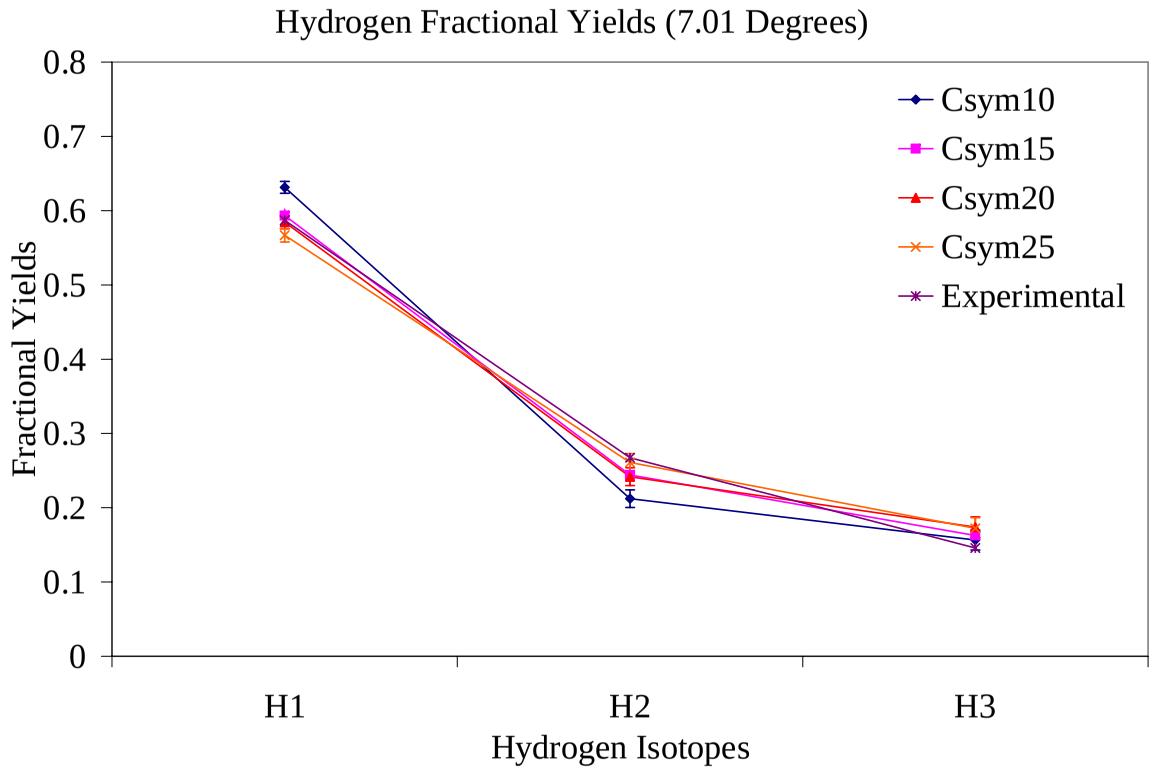


FIG. 81. (Color online) Hydrogen fractional yield comparisons between experiment and DIT/SMM using 10, 15, 20 and 25 MeV for the symmetry energy. This is from 32 MeV/nucleon $^{40}$Ar on $^{112}$Sn system at 7.01 degrees.

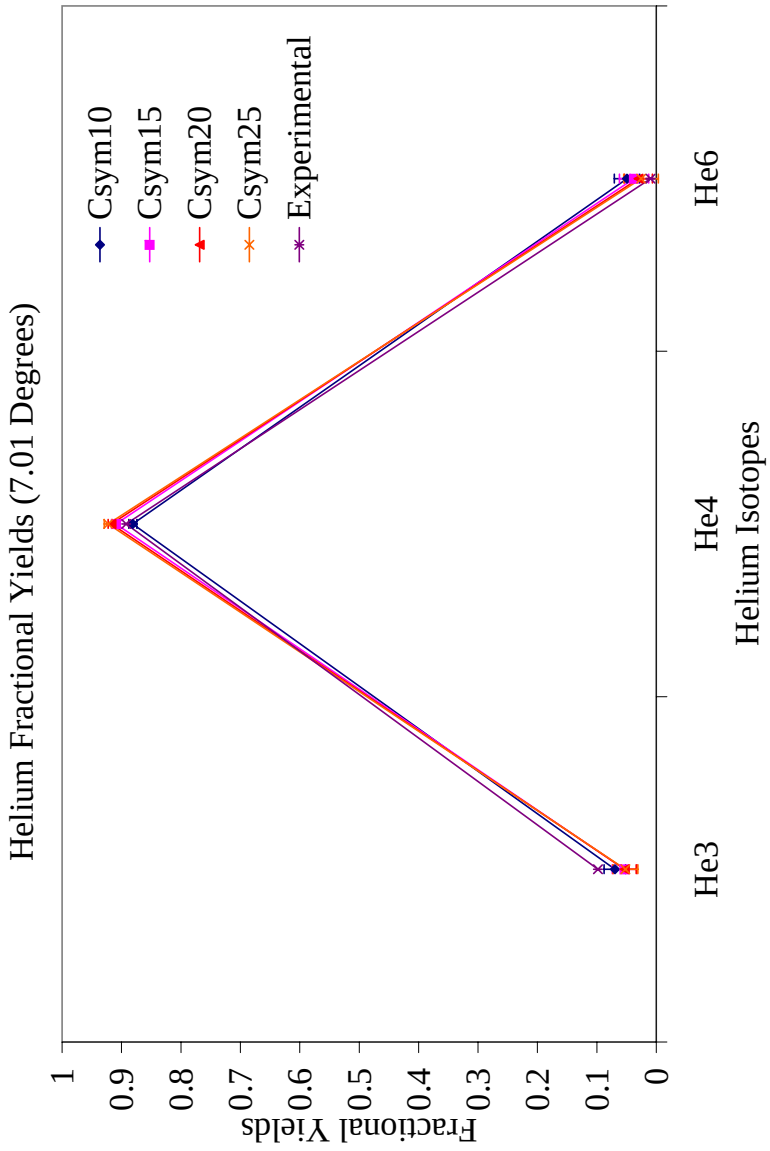


FIG. 82. (Color online) Helium fractional yield comparisons between experiment and DIT/SMM using 10, 15, 20 and 25 MeV for the symmetry energy. This is from 32 MeV/nucleon $^{40}$Ar on $^{112}$Sn system at 7.01 degrees.

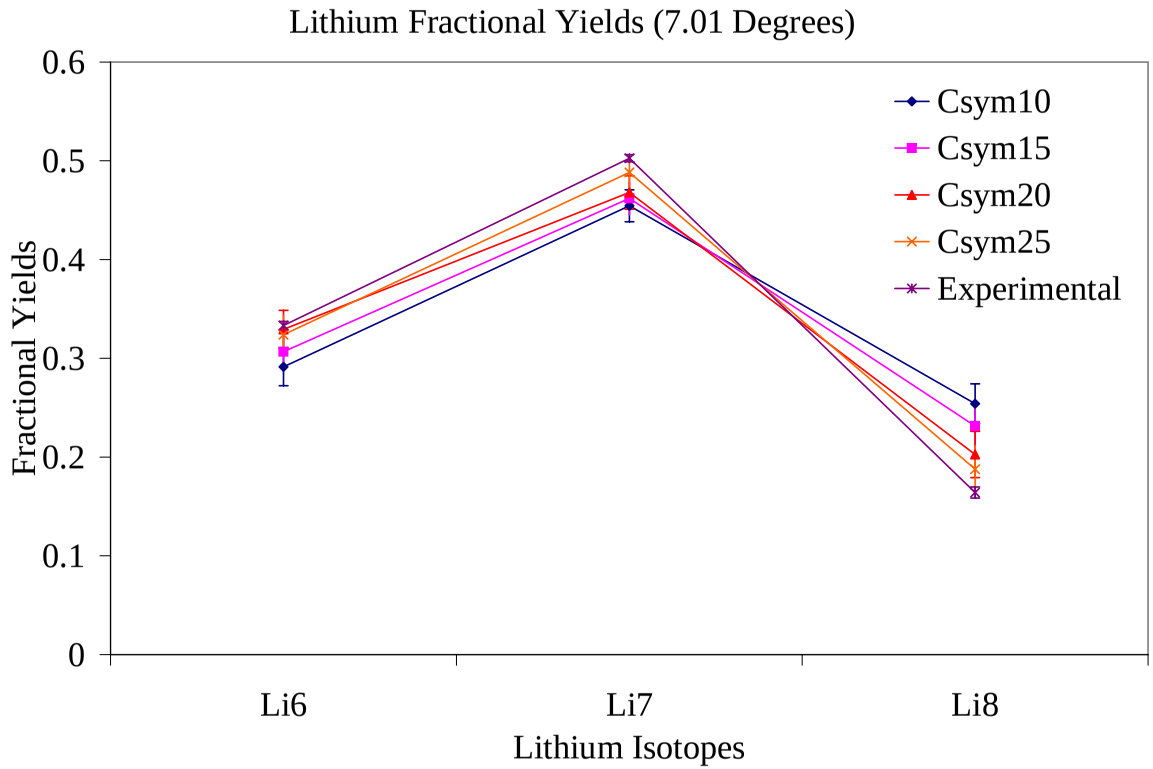


FIG. 83. (Color online) Lithium fractional yield comparisons between experiment and DIT/SMM using 10, 15, 20 and 25 MeV for the symmetry energy. This is from 32 MeV/nucleon $^{40}$Ar on $^{112}$Sn system at 7.01 degrees.

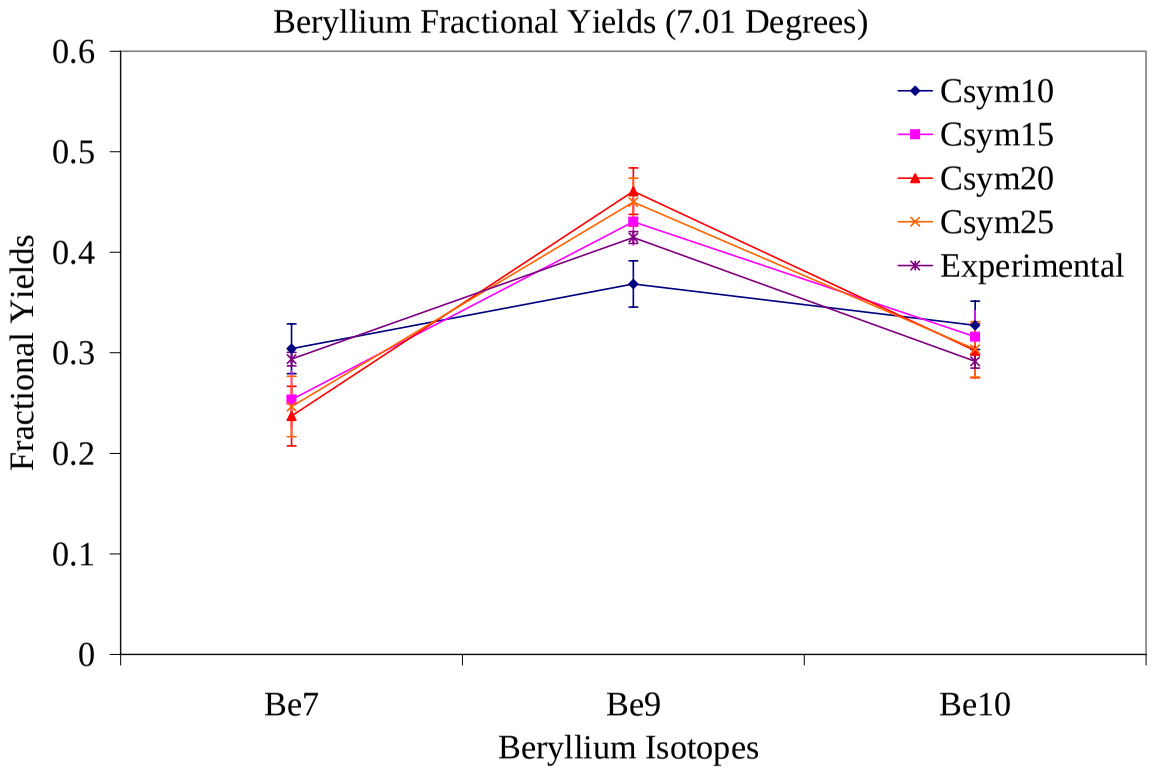


FIG. 84. (Color online) Beryllium fractional yield comparisons between experiment and DIT/SMM using 10, 15, 20 and 25 MeV for the symmetry energy. This is from 32 MeV/nucleon $^{40}$Ar on $^{112}$Sn system at 7.01 degrees.

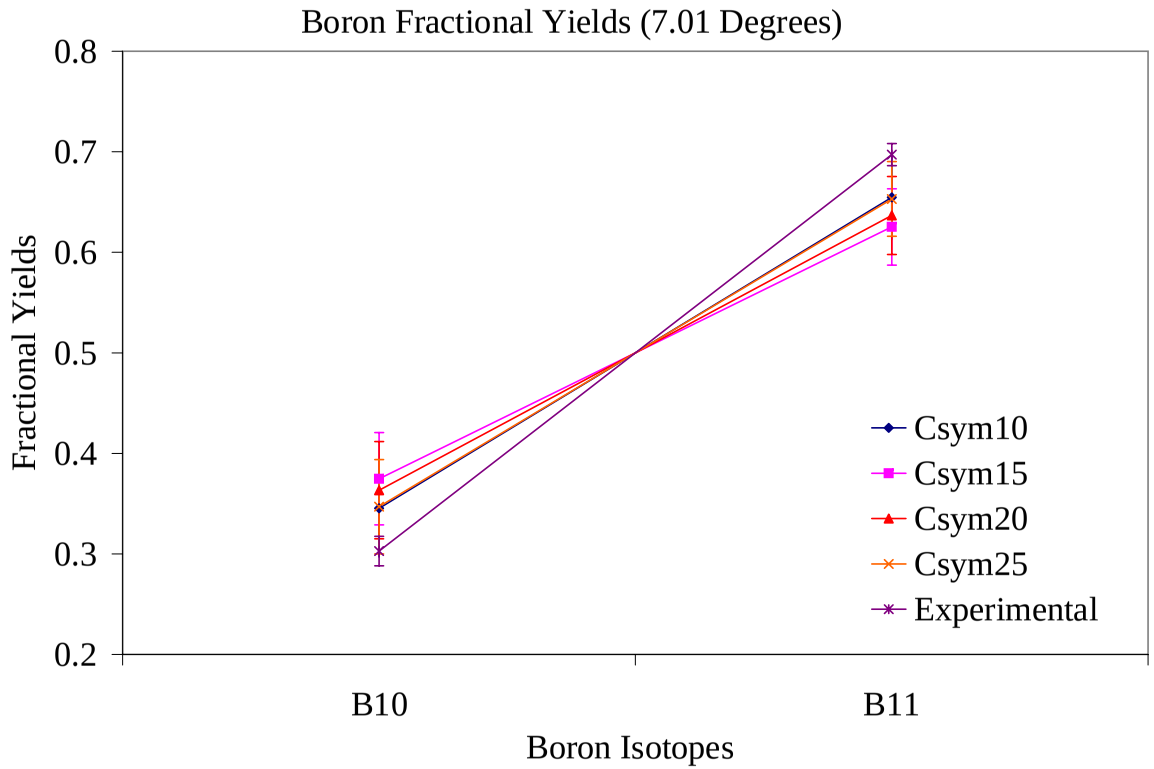


FIG. 85. (Color online) Boron fractional yield comparisons between experiment and DIT/SMM using 10, 15, 20 and 25 MeV for the symmetry energy. This is from 32 MeV/nucleon $^{40}$Ar on $^{112}$Sn system at 7.01 degrees.

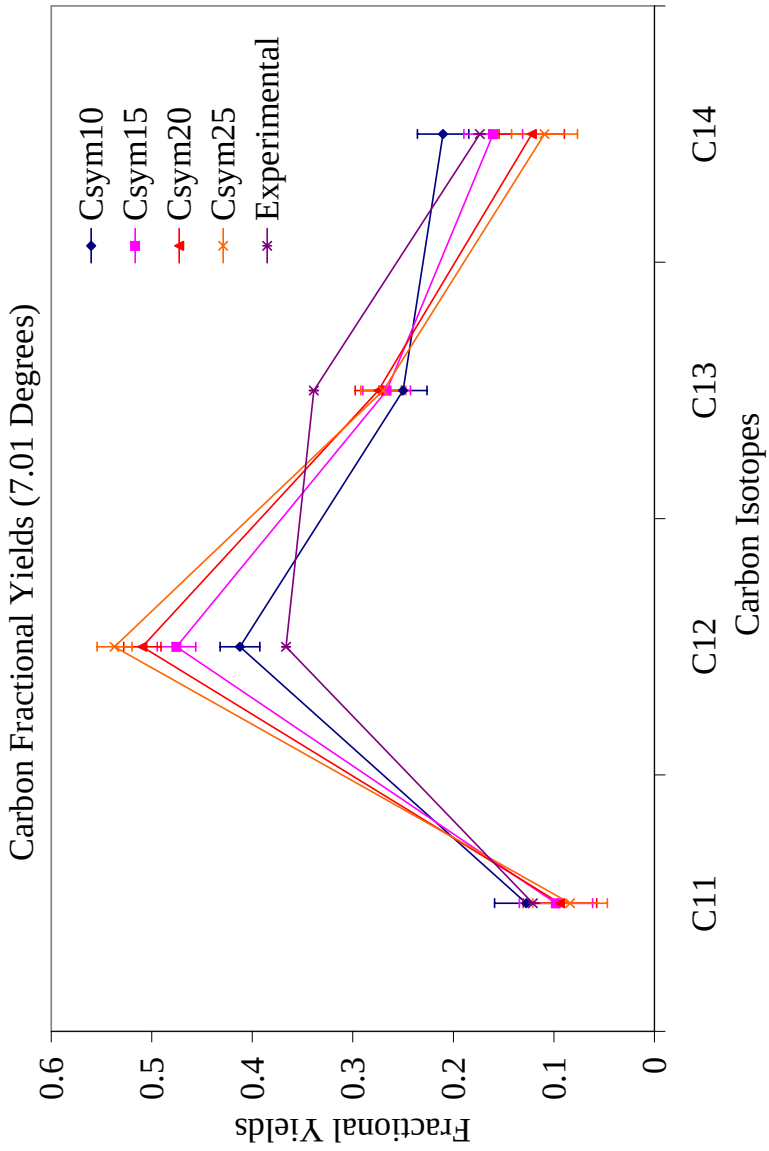


FIG. 86. (Color online) Carbon fractional yield comparisons between experiment and DIT/SMM using 10, 15, 20 and 25 MeV for the symmetry energy. This is from 32 MeV/nucleon $^{40}$Ar on $^{112}$Sn system at 7.01 degrees.

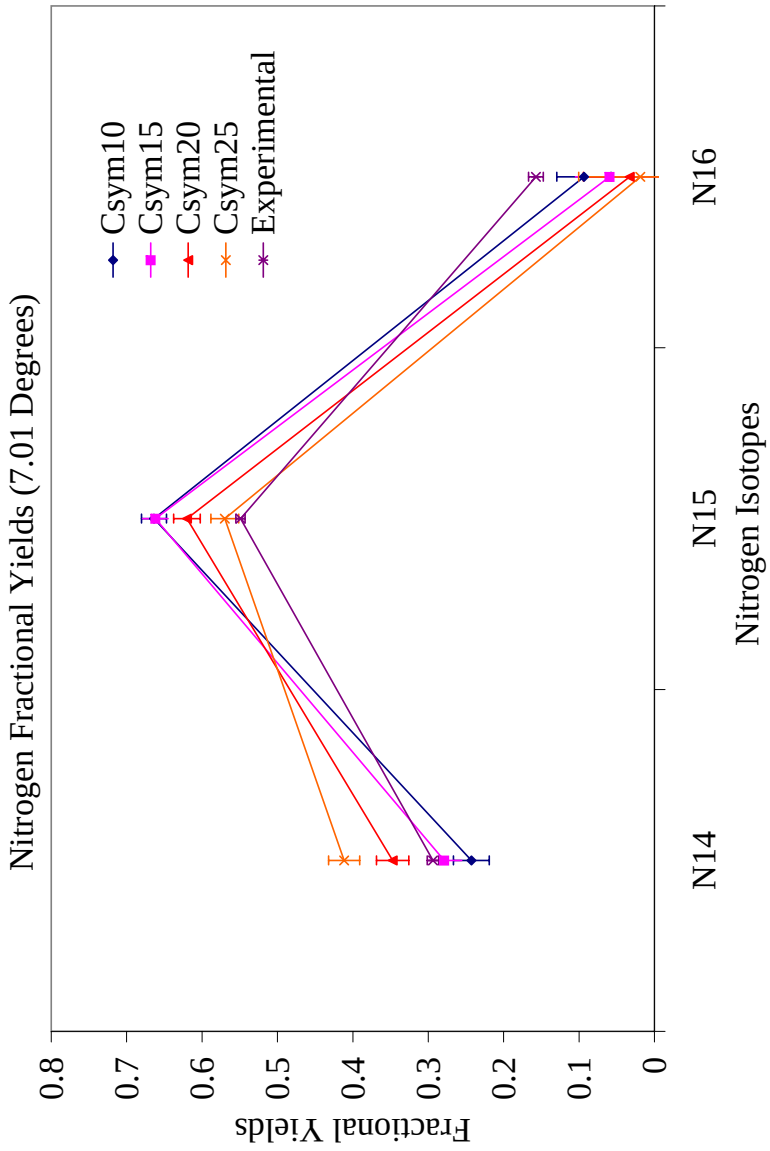


FIG. 87. (Color online) Nitrogen fractional yield comparisons between experiment and DIT/SMM using 10, 15, 20 and 25 MeV for the symmetry energy. This is from 32 MeV/nucleon $^{40}$Ar on $^{112}$Sn system at 7.01 degrees.

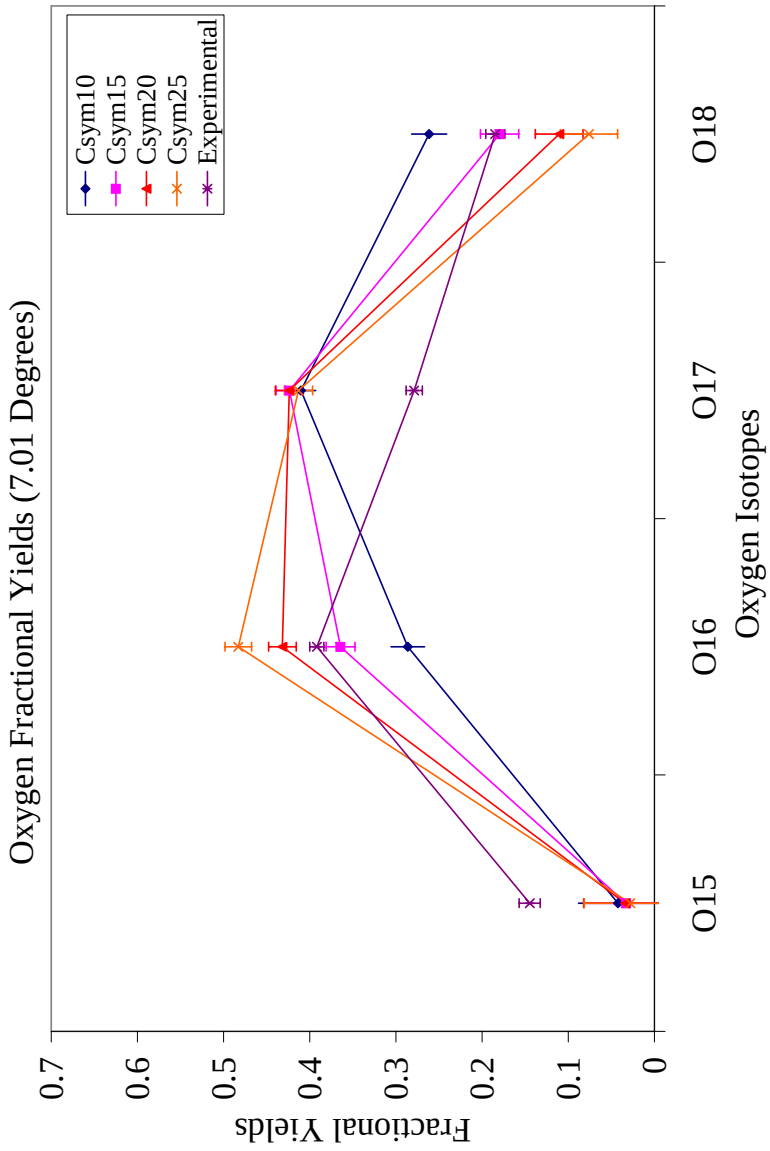


FIG. 88. (Color online) Oxygen fractional yield comparisons between experiment and DIT/SMM using 10, 15, 20 and 25 MeV for the symmetry energy. This is from 32 MeV/nucleon $^{40}$Ar on $^{112}$Sn system at 7.01 degrees.

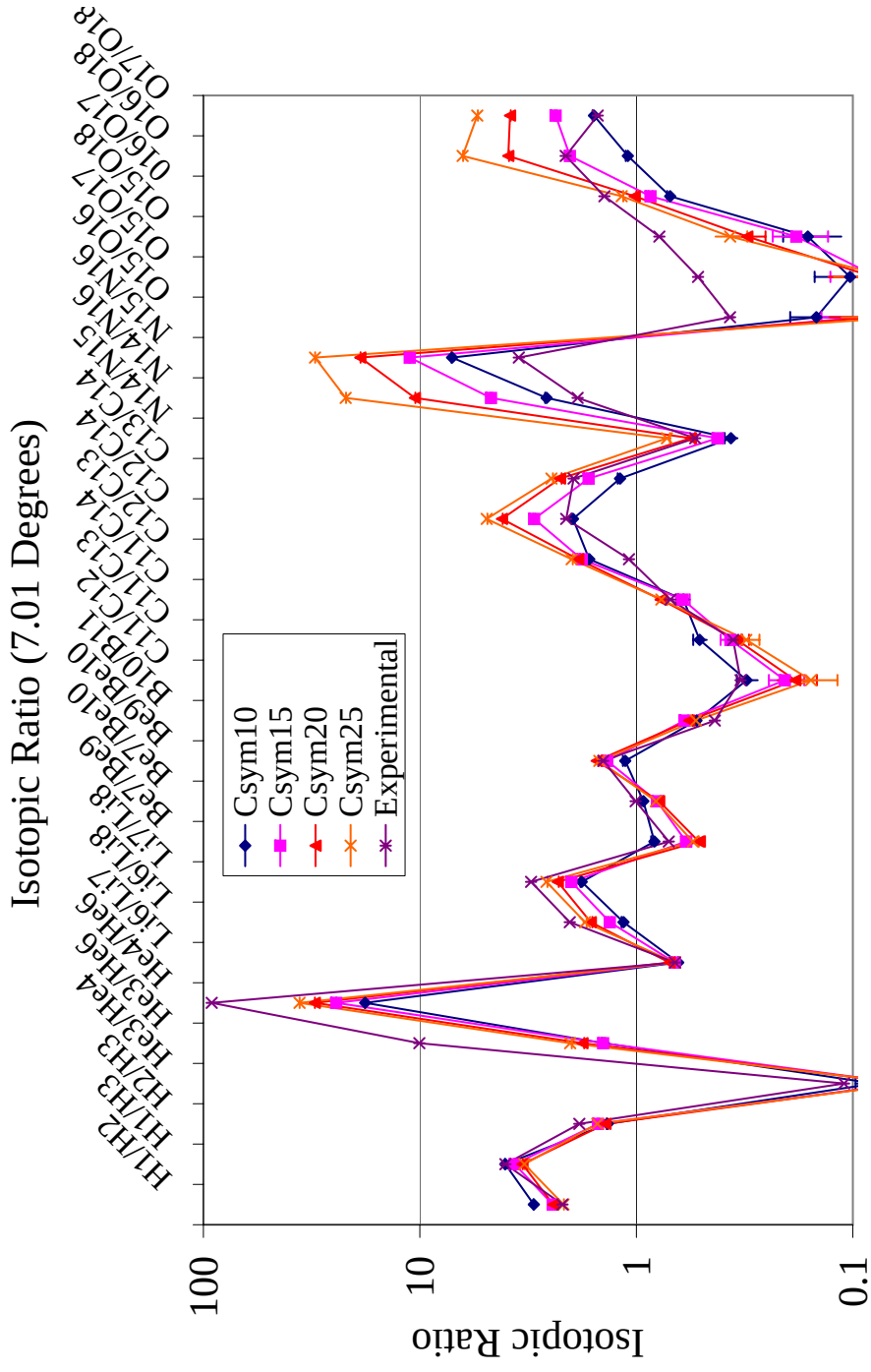


FIG. 89. (Color online) Isotopic yield ratio comparisons between experiment and DIT/SMM using 10, 15, 20 and 25 MeV for the symmetry energy. This is from 32 MeV/nucleon $^{40}$Ar on $^{112}$Sn system at 7.01 degrees.

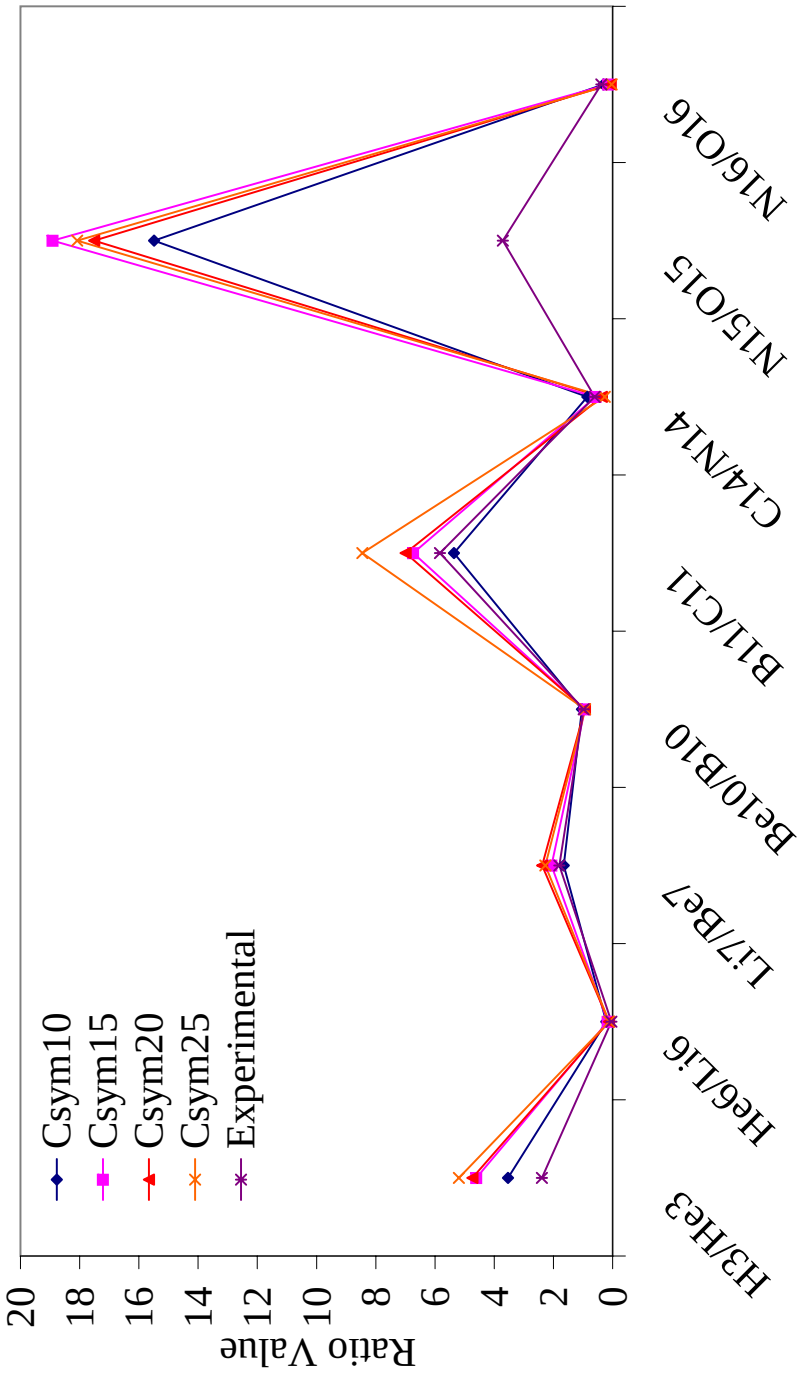


FIG. 90. (Color online) Isobaric yield ratio comparisons between experiment and DIT/SMM using 10, 15, 20 and 25 MeV for the symmetry energy. This is from 32 MeV/nucleon $^{40}$Ar on $^{112}$Sn system at 7.01 degrees.

### 4. Mean N/Z Comparisons

All the systems and angles exhibit similar trends, so only the 32 MeV/nucleon $^{40}$Ar on $^{112}$Sn at 7.01 degrees will be presented here. Figure 91 shows the mean N/Z with respect to charge with the experimental data represented by a star, the symmetry energy of 25 with a cross, 20 with a triangle, 15 with a square and 10 with a diamond. The bottom plot has the ratios scaled by dividing out the experimental data, which allows for an easier comparison between the different symmetry energy results. This means that the symmetry energy that is closest to unity is the best. For LCPs the symmetry energy of 25 is best, while for the IMFs the symmetry energy of 10 appears to be the best.

## C. Mass Distribution Studies

The experimental mass distributions for reconstructed sources were compared with the quasiprojectile source mass distributions from the simulations HIPSE, DIT, and BNV, which has two parameterizations of the nEOS. Tables XX and XXI show the mean values of the mass distributions along with the RMS values. Comparing the lower energy systems with the higher energy systems there is a slight decrease in the mean mass. The experimental mean values are next to the DIT/SMM/Filter mean values. The symmetry energy used in this version of SMM was the standard 25 MeV. The DIT/SMM/Filter mean values are all smaller than the DIT backtracked mean values. The DIT backtrack is just the distribution on the quasiprojectile N/Z from DIT from which the fragments came. Then the overall mean for all DIT events is given along with the overall means from HIPSE, BNV Soft and BNV Stiff.

BNV had very few statistics and should be run for about 10 times the number of events. There is not much difference seen between the two parameterizations of

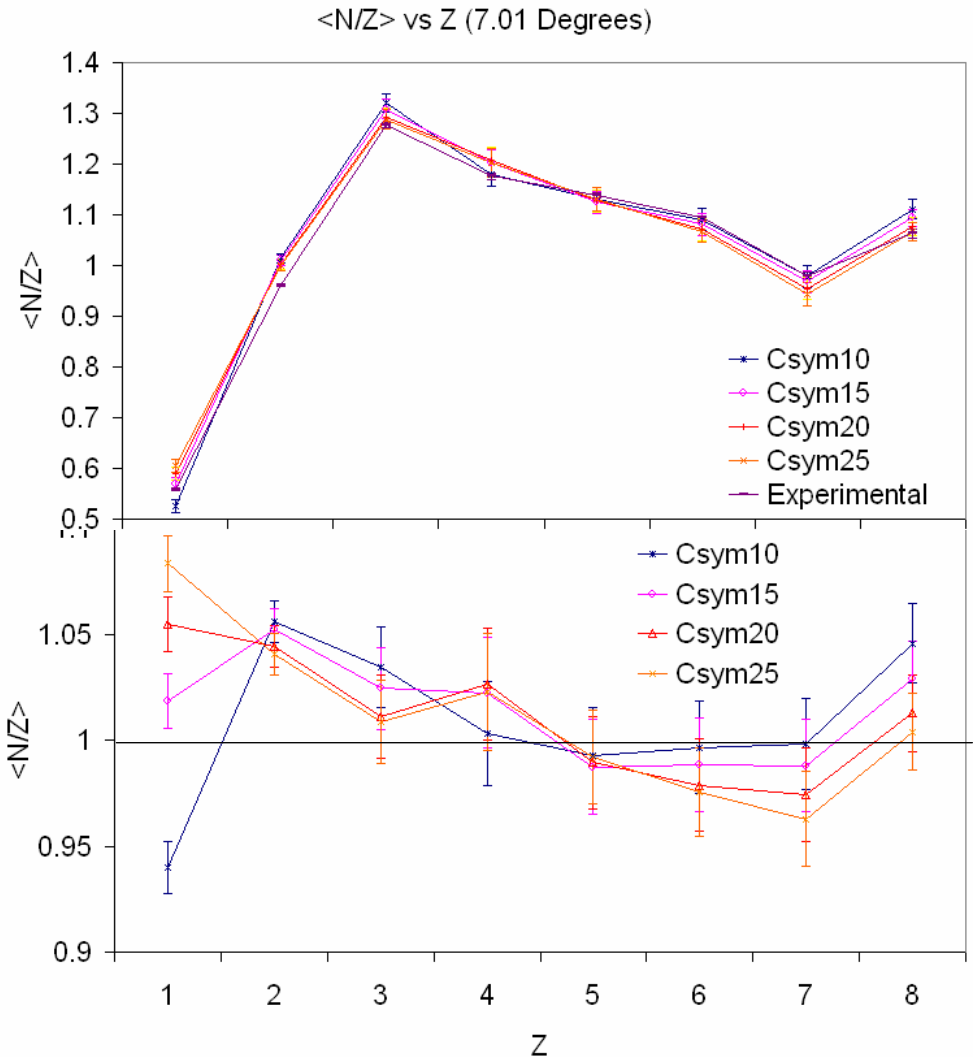


FIG. 91. (Color online) Mean N/Z with respect to charge comparisons between experiment and DIT/SMM using 10, 15, 20 and 25 MeV for the symmetry energy. This is from 32 MeV/nucleon $^{40}$Ar on $^{112}$Sn system at 7.01 degrees. Top are the ratio values, bottom are the scaled ratios, so experiment is equal to unity.

BNV, which is always 3 to 4 neutrons lower than the DIT and HIPSE mean masses. The DIT and HIPSE both show that the average N/Z of the quasiprojectile source is the mass and therefore N/Z of the projectile, with $^{40}$Ar = 1.2, $^{40}$Ca = 1.0 and $^{48}$Ca = 1.4.

## D. Summary

Two techniques were used to determine the N/Z of the quasiprojectiles. One technique used the isotopically resolved fragments to reconstruct the quasiprojectile sources, which is affected by undetected neutrons. The other technique used is the yield ratio fitting method, which is insensitive to neutron loss. The two techniques gave different values for the source N/Z. The question arose whether this was caused purely by the undetected neutrons. From the DIT/SMM study the results show that neutron loss is the cause for the discrepancy between the two methods. The other question was how good is the yield ratio fitting method. Again using DIT/SMM the results show that this method does predict the source N/Z well.

The symmetry energy was studied using DIT/SMM with SMM run with different values for the symmetry energy: 10, 15, 20 and 25. The theoretical results were compared with the experimental results using the fractional yields, isotopic ratios, isobaric ratios and mean N/Z. There is not a conclusive result, because there is variance of the experimental data throughout all symmetry energies, however the overall trend seems to be best approximated by a lower value of the symmetry energy.

Finally the mass distributions were compared to several theoretical codes: DIT, HIPSE and BNV, which was run with a soft and stiff parameterization of the nuclear equation-of-state. The results show that DIT and HIPSE are very similar, while BNV is several neutrons off, although possibly increasing statistics by running a few

TABLE XX. Mean values of experimental and theoretical mass distributions for the 32 MeV/nucleon systems. Note the BNV are Zqp = Zbeam +-2. Top are mean values, bottom are RMS values.

| System | Experimental | DIT/SMM/ Filter | DIT Backtrack | DIT | HIPSE | BNV Soft | BNV Stiff |
|---|---|---|---|---|---|---|---|
| $^{40}$Ar + $^{112}$Sn | 36.12 | 39.71 | 42.75 | 39.64 | 39.92 | 35.89 | 35.91 |
| $^{40}$Ar + $^{124}$Sn | 36.55 | 40.46 | 44.01 | 40.25 | 40.25 | 36.18 | 36.18 |
| $^{40}$Ca + $^{112}$Sn | 38.98 | 39.04 | 41.69 | 40.50 | 40.27 | 36.75 | 36.72 |
| $^{40}$Ca + $^{124}$Sn | 39.54 | 39.52 | 42.27 | 40.96 | 40.82 | 36.69 | 36.72 |
| $^{48}$Ca + $^{112}$Sn | 40.70 | 41.49 | 47.28 | 47.17 | 47.15 | 42.59 | 42.57 |
| $^{48}$Ca + $^{124}$Sn | 40.93 | 42.32 | 48.57 | 47.92 | 47.21 | 43.05 | 43.07 |
| $^{40}$Ar + $^{112}$Sn | 1.61 | 1.71 | 2.26 | 1.20 | 1.22 | 0.99 | 1.00 |
| $^{40}$Ar + $^{124}$Sn | 1.64 | 1.78 | 2.41 | 1.24 | 1.24 | 1.01 | 1.01 |
| $^{40}$Ca + $^{112}$Sn | 1.85 | 1.50 | 2.21 | 1.25 | 1.24 | 1.04 | 1.04 |
| $^{40}$Ca + $^{124}$Sn | 1.57 | 1.64 | 2.32 | 1.28 | 1.27 | 1.04 | 1.04 |
| $^{48}$Ca + $^{112}$Sn | 1.75 | 1.88 | 2.86 | 1.62 | 1.62 | 1.37 | 1.37 |
| $^{48}$Ca + $^{124}$Sn | 1.72 | 1.96 | 2.75 | 1.66 | 1.62 | 1.39 | 1.39 |

TABLE XXI. Mean values of experimental and theoretical mass distributions for the 45 MeV/nucleon systems. Note the BNV are Zqp = Zbeam +-2. Top are mean values, bottom are RMS values.

| System | Experimental | DIT/SMM/ Filter | DIT Backtrack | DIT | HIPSE | BNV Soft | BNV Stiff |
|---|---|---|---|---|---|---|---|
| $^{40}$Ar + $^{112}$Sn | 35.95 | 39.30 | 42.63 | 39.62 | 39.55 | 36.22 | 36.26 |
| $^{40}$Ar + $^{124}$Sn | 36.28 | 39.76 | 43.17 | 40.17 | 39.85 | 36.45 | 36.47 |
| $^{40}$Ca + $^{112}$Sn | 39.33 | 38.54 | 41.52 | 40.40 | 39.98 | 36.93 | 37.06 |
| $^{40}$Ca + $^{124}$Sn | 39.63 | 39.18 | 42.14 | 40.87 | 40.49 | 36.91 | 36.86 |
| $^{48}$Ca + $^{112}$Sn | 40.37 | 41.29 | 47.66 | 47.22 | 47.06 | 43.14 | 43.13 |
| $^{48}$Ca + $^{124}$Sn | 40.83 | 42.06 | 48.54 | 47.87 | 47.22 | 43.51 | 43.56 |
| $^{40}$Ar + $^{112}$Sn | 1.79 | 1.72 | 2.31 | 1.20 | 1.20 | 1.01 | 1.01 |
| $^{40}$Ar + $^{124}$Sn | 1.80 | 1.71 | 2.19 | 1.23 | 1.21 | 1.03 | 1.03 |
| $^{40}$Ca + $^{112}$Sn | 1.94 | 1.62 | 2.34 | 1.24 | 1.22 | 1.05 | 1.06 |
| $^{40}$Ca + $^{124}$Sn | 1.95 | 1.69 | 2.18 | 1.27 | 1.25 | 1.05 | 1.05 |
| $^{48}$Ca + $^{112}$Sn | 1.85 | 2.05 | 2.91 | 1.62 | 1.61 | 1.40 | 1.40 |
| $^{48}$Ca + $^{124}$Sn | 1.82 | 2.15 | 2.87 | 1.66 | 1.62 | 1.42 | 1.42 |

months might create a better distribution.

# CHAPTER VII

## CONCLUSIONS

When target and projectile nuclei have a difference in N/Z, the quasiprojectiles formed in the DIC have a mean N/Z between that of the N/Z of the target and the N/Z of the projectile. This depends on the amount of N/Z equilibration that occurred. Full N/Z equilibration would result with the quasiprojectile N/Z being the same as the composite system N/Z, which is a system that has proton number equal to the target proton number plus the projectile proton number; neutron number equal to the target neutron number plus the projectile neutron number. Six reaction systems at two beam energies (32 and 45 MeV/nucleon) were studied. The systems, in order of increasing difference between target and projectile N/Z (shown in parentheses), were $^{40}$Ar + $^{112}$Sn ($\Delta$N/Z = 0.018), $^{48}$Ca + $^{124}$Sn ($\Delta$N/Z = 0.080), $^{48}$Ca + $^{112}$Sn ($\Delta$N/Z = 0.160), $^{40}$Ca + $^{112}$Sn ($\Delta$N/Z = 0.240), $^{40}$Ar + $^{124}$Sn ($\Delta$N/Z = 0.258) and $^{40}$Ca + $^{124}$Sn ($\Delta$N/Z = 0.480). The projectiles were produced in the advanced ECRIS and accelerated by the Texas A&M University Cyclotron Institutes K500 superconducting cyclotron.

The fragments from the reactions were measured with FAUST, which was composed of 68 Si-CsI telescopes that had 90% angular coverage between 2 and 33 degrees. Isobaric, isotopic, fractional and mean N/Z yield comparisons were made between systems. These comparisons showed that the neutron richness of the system affected the fragment yields, with the neutron-rich nuclides populated preferentially by the neutron-rich systems; the neutron-poor nuclides populated preferentially by the neutron-poor systems.

Two techniques were used to determine the quasiprojectile N/Z. The first technique used the isotopically resolved fragments to reconstruct the quasiprojectile N/Z.

Reconstruction also provided a route for source determination by requiring that the quasiprojectile charge equaled the projectile charge plus or minus 2. This reconstruction was sensitive to neutron loss, which made the quasiprojectile N/Z determined lower than the true value. The second technique, developed in this thesis project, used fragment yield ratios and a simple equation to simultaneously fit all six systems to determine the quasiprojectile N/Z. This technique required good source determination, which was obtained from reconstruction.

The quasiprojectile N/Z values determined by the yield ratio technique were much larger than those determined by the reconstruction technique. The question arose whether this is caused purely from neutron loss. This question was resolved by using simulations to form and de-excite quasiprojectiles. The fragments formed were filtered to the acceptance of FAUST and then analyzed like experimental fragments, yielding similar results. In the simulations the quasiprojectile N/Z was known and compared to the results that used the yield ratio technique. The comparison showed that the yield ratio technique approximated the quasiprojectile N/Z. Further modification of the equation used in the yield ratio technique, such as taking into account masses of target and projectile, might improve the approximation. Since the quasiprojectile N/Z was known, the neutron loss was calculated and was shown that the more neutron rich systems lose more neutrons. This accounts for the differences between the reconstruction and yield ratio techniques.

The N/Z distribution of the fragment yields was studied to observe an inhomogeneous N/Z distribution between the LCPs and IMFs. The multiplicity of LCPs and IMFs were calculated and the results showed a new trend. Previous studies had shown that increased proton richness increases the LCP multiplicity dramatically, while the IMF multiplicity remained nearly constant. For increasing neutron richness the previous studies suggested that the neutron-rich LCP multiplicity would increase;

however, this work showed that the IMF multiplicity increases, while the LCP multiplicity stays nearly constant with increasing neutron richness. The inhomogeneous distribution of N/Z was also studied using the mean N/Z of the IMF divided by the mean N/Z of the LCP. The results were in accord with previous studies, however this work went further and showed that there was a dependence of the mean N/Z of the IMF on the quasiprojectile N/Z. Finally the inhomogeneous distribution of N/Z was studied using the mirror nuclei ratios t/$^{3}$He, $^{7}$Li/$^{7}$Be, $^{11}$B/$^{11}$C and $^{15}$N/$^{15}$O. Previous studies had only used the t/$^{3}$He ratio and observed an increase of the ratio with increasing quasiprojectile N/Z. This work demonstrated that all of the mirror ratios increased with increasing quasiprojectile N/Z.

The theoretical results, which used different values of the symmetry energy, were compared to experimental data to determine which symmetry energy best represents the experimental data. The comparison showed the experimental data was overall best fit with a lower value of the symmetry energy. These results were not conclusive and further investigation is required.

On the experimental front, the development of a Rare Ion Beam (RIB) Facility, and upgrades to other facilities, will allow for production of radioactive targets and beams. These facilities will allow for further research into N/Z equilibration and breakup of sources with a wider range of N/Z. On the theoretical front, the development of improved simulations can enhance the understanding of the mechanisms involved in these reactions.

# REFERENCES

[1] H. Johnston, T. White, J. Winger, D. Rowland, B. Hurst, F. Gimeno-Nogues, D. O'Kelly and S.J. Yennello, Phys. Lett. B **371**, 186 (1996).

[2] A.C. Merchant and W. Norenberg, Phys. Lett. B **104**, 15 (1981).

[3] V. Baran, M. Colonna, V. Greco and M. Di Toro, Phys. Rep. **410**, 335 (2005).

[4] H. Freiesleben and J.V. Kratz, Phys. Rep. **106**, 1 (1984).

[5] D.J. Rowland, thesis, Texas A&M University (2000).

[6] Q. Li and Z. Li, Phys. Rev. C **64**, 064612 (2001).

[7] S.S.M. Wong, *Introductory Nuclear Physics Second Edition*, (John Wiley and Sons, Inc, NY, 1998).

[8] A. Hombach, W. Cassing and U. Mosel, Eur. Phys. J. A **5**, 77 (1999).

[9] F. Rami,Y. Leifels, B. de Schauenburg, A. Gobbi, B. Hong, J. P. Alard, A. Andronic, R. Averbeck, V. Barret, Z. Basrak, N. Bastid, I. Belyaev, A. Bendarag, G. Berek, R. ? Caplar, N. Cindro, P. Crochet, A. Devismes, P. Dupieux, M. Delalija, M. Eskef, C. Finck, Z. Fodor, H. Folger, L. Fraysse, A. Genoux-Lubain, Y. Grigorian, Y. Grishkin, N. Herrmann, K. D. Hildenbrand, J. Kecskemeti, Y. J. Kim, P. Koczon, M. Kirejczyk, M. Korolija, R. Kotte, M. Kowalczyk, T. Kress, R. Kutsche, A. Lebedev, K. S. Lee, V. Manko, H. Merlitz, S. Mohren, D. Moisa, J. Msner, W. Neubert, A. Nianine, D. Pelte, M. Petrovici, C. Pinkenburg, C. Plettner, W. Reisdorf, J. Ritman, D. Schll, Z. Seres, B. Sikora, K. S. Sim, V. Simion, K. Siwek-Wilczynska, A. Somov, M. R. Stockmeier, G. Stoicea, M.

Vasiliev, P. Wagner, K. Wisniewski, D. Wohlfarth, J. T. Yang, I. Yushmanov and A. Zhilin *et al.*, Phys. Rev. Lett. **84**, 1120 (2000).

[10] E. Martin, R. Laforest, E. Ramakrishnan, D.J. Rowland, A. Ruangma, E.M. Winchester and S.J. Yennello, Phys. Rev. C **62**, 027601 (2000).

[11] E. Bell, thesis, Texas A&M University (2005).

[12] S.J. Yennello, B. Young, J. Lee, J.A. Winger, J.S. Winfield, G.D. Westfall, A. Vander Molen, B.M. Sherrill, J. Shea, E. Norbeck, D.J. Morrissey, T. Li, E. Gualtieri, D. Craig, W. Benenson and D. Bazin, Phys. Lett. B **321**, 15 (1994).

[13] B.A. Li and W.U. Schroder Editors, *Isospin Physics in Heavy-Ion Collisions at Intermediate Energies*, (Nova Science Publishers, Inc., New York, 2001).

[14] R.A. Arndt, Rev. Mod. Phys. **39**, 710 (1967).

[15] L.G. Sobotka, Acta Physica Polonica B **31**, 1535 (2000).

[16] M. Veselsky, R.W. Ibbotson, R. Laforest, E. Ramakrishnan, D.J. Rowland, A. Ruangma, E.M. Winchester, E. Martin and S.J. Yennello, Phys. Rev. C **62**, 041605R (2000).

[17] L. Tassan-Got and C. Stephan, Nucl. Phys. A **524**, 121 (1991).

[18] D.J. Rowland, R. Laforest, E. Ramakrishnan, M. Veselsky, E.M. Winchester, A. Ruangma, E. Martin and S.J. Yennello, Phys. Rev C **67**, 064602 (2003).

[19] B.A. Li, C.M. Ko and W. Bauer, International. Jour. Mod. Phys. E **7**, 147 (1998).

[20] G. Audi, A.H. Wapstra and C. Thibault, Nucl. Phys. A **729**, 337 (2003).

[21] A.H. Wapstra, G. Audi and C. Thibault, Nucl. Phys. A **729**, 129 (2003).

[22] G. Audi, O. Bersillon, J. Blachot and A.H. Wapstra, Nucl. Phys. A **729**, 3 (2003).

[23] C.F.v. Weizsacker, Z. Phys. **96**, 431 (1935).

[24] W.N. Cottingham and D.A. Greenwood, *An Introduction to Nuclear Physics Second Edition*, (Cambridge University Press, 2001).

[25] W.D. Myers and W.J. Swiatecki, Nucl. Phys. **81**, 1 (1966).

[26] E.R. Hilf, H. von Groote and K. Takahashi, 3rd International Conference on Nuclei Far Off Stability, Cargese, Corsica, (May 19th-26th 1976).

[27] P. Moller, J.R. Nix, W.D. Myers and W.J. Swiatecki, Atomic Data and Nuclear Data Tables **59**, 185 (1995).

[28] W.D. Myers and W.J. Swiatecki, Ann. Phys. **55**, 395 (1969).

[29] G. Friedlander, J.W. Kennedy, E.S. Macias, and J.M. Miller, *Nuclear and Radiochemistry 3rd Edition*, (John Wiley & Sons, New York, 1981).

[30] K.S. Krane, *Introductory Nuclear Physics*, (John Wiley & Sons, 1988).

[31] S. Wanajo, S. Goriely, M. Samyn and N. Itoh, Astrophys. J. **606**, 1057 (2004).

[32] G. Levai, J. Cseh, P. Van Isacker and O. Juillet, RIKEN Review **26**, 45 (2000).

[33] B.A. Li., Phys. Rev. C **69**, 034614 (2004).

[34] G. Ferini, T. Gaitanos, M. Colonna, M. Di Toro and H.H. Wolter, Phys. Rev. Lett. **97**, 202301 (2006).

[35] D.V. Shetty, A.S. Botvina, S.J. Yennello, G.A. Souliotis, E. Bell and A. Keksis, Phys. Rev. C **71**, 024602 (2005).

[36] A. Le Fevre, G. Auger, M.L. Begemann-Blaich, N. Bellaize, R. Bittiger, F. Bocage, B. Borderie, R. Bougault, B. Bouriquet, J.L. Charvet, A. Chbihi, R. Dayras, D. Durand, J.D. Frankland, E. Galichet, D. Gourio, D. Guinet, S. Hudan, G. Imme, P. Lautesse, F. Lavaud, R. Legrain, O. Lopez, J. Lukasik, U. Lynen, W.F.J. Muller, L. Nalpas, H. Orth, E. Plagnol, G. Raciti, E. Rosato, A. Saija, C. Schwarz, W. Siedel, C. Sfienti, B. Tamain, W. Trautmann, A. Trzcinski, K. Turzo, E. Vient, M. Vigilante, C. Volant, B. Zwieglinski and A.S. Botvina, Phys. Rev. Lett. **94**, 162701 (2005).

[37] D. Henzlova, A.S. Botvina, K.-H. Schmidt, V. Henzl, P. Napolitani and M.V. Ricciardi, nucl-ex: 10507003 (2005).

[38] J. Iglio, D.V. Shetty, S.J. Yennello, G.A. Souliotis, M. Jandel, A.L. Keksis, S.N. Soisson, B.C. Stein and S. Wuenschel, Phys. Rev. C **74**, 024605 (2006).

[39] H.-J. Schulze, A. Polls, A. Ramos and I. Vidana, Phys. Rev. C **73**, 058801 (2006).

[40] D.J. Nice, E.M. Splaver, I.H. Stairs, O. Lohmer, A. Jessner, M. Kramer and J.M. Cordes, Astrophys. J. **634**, 1242 (2005).

[41] M. Ashworth, A.G. Lyne and F.G. Smith, Nature **301**, 313 (1983).

[42] J.M. Lattimer and M. Prakash, Science **304**, 536 (2004).

[43] J.M. Lattimer and M. Prakash, Phys. Rep. **333**, 121 (2000).

[44] W.H. Lee, Rev. Mex. AA (Serie de Conferencias) **10**, 176 (2001)

[45] P.O. Slane, D.J. Helfand and S.S. Murray, Astrophys. J. Lett. **571**, L45 (2002).

[46] $^{208}$Pb Radius Experiment website, http://hallaweb.jlab.org/parity/prex/ (2006).

[47] J. Carriere, C.J. Horowitz and J. Piekarewicz, Astrophys. J. **593**, 463 (2003).

[48] A.W. Steiner and B.-A. Li, Phys. Rev. C **72**, 041601R (2005).

[49] M.B. Tsang, C.K. Gelbke, X.D. Liu, W.G. Lynch, W.P. Tan, G. Verde, H.S. Xu, W.A. Friedman, R. Donangelo, S.R. Souza, C.B. Das, S.D. Gupta and D. Zhabinsky, Phys. Rev. C **64**, 054615 (2001).

[50] G.A. Souliotis, M. Veselsky, D.V. Shetty and S.J. Yennello, Phys. Lett. B **588**, 35 (2004).

[51] F. Gimeno-Nogues, D.J. Rowland, R.A. Gutierrez, R. Olsen, Y.-W. Lui and S.J. Yennello, Progress in Research, (Cyclotron Institute, Texas A&M University, 1994-1995), 201.

[52] F. Gimeno-Nogues, D.J. Rowland, R.A. Gutierrez, R. Olsen, S. Ferro, H. Johnston, Y.-W. Lui, E. Ramakrishnan, S. Vasal and S.J. Yennello, Progress in Research, (Cyclotron Institute, Texas A&M University, 1995-1996), 137.

[53] F. Gimeno-Nogues, D.J. Rowland, E. Ramakrishnan, S. Ferro, S. Vasal, R.A. Gutierrez, R. Olsen, Y.-W. Lui, R. Laforest, H. Johnston and S.J. Yennello, Nucl. Instr. Meth. A **399**, 94 (1997).

[54] D.J. Rowland, F. Gimeno-Nogues, E. Ramakrishnan, R. Laforest, S. Ferro, Y.-W. Lui, B. Delafield, S. Guzman, S. Vasal, H. Johnston and S.J. Yennello, Progress in Research, (Cyclotron Institute, Texas A&M University, 1996-1997), II-6.

[55] ROOT webpage, http://root.cern.ch/, Rene Brun and Fons Rademakers, 2005.

[56] A.L. Keksis, M. Veselsky, G.A. Souliotis, E. Martin, A. Ruangma, D. Shetty, E.M. Winchester and S.J. Yennello, Progress in Research, (Cyclotron Institute, Texas A&M University, 2001-2002), II-38.

[57] A.L. Keksis, M. Veselsky, G.A. Souliotis, E. Martin, D. Shetty and S.J. Yennello, Progress in Research, (Cyclotron Institute, Texas A&M University, 2002-2003), II-11.

[58] A.L. Keksis, M. Veselsky, G.A. Souliotis, E. Bell, M. Jandel, A. Ruangma, D.V. Shetty, E.M. Winchester and S.J. Yennello, Progress in Research, (Cyclotron Institute, Texas A&M University, 2003-2004), II-23.

[59] C. Richers. Cyclotron Institute, Texas A&M University. Private Communications (2003).

[60] L. Tassan-Got, Nucl. Instrum. Meth. B **194**, 503 (2002).

[61] DONNA Program. W.G. Meyer, University of Maryland, 1978 (unpublished program).

[62] A.L. Keksis, M. Veselsky, G.A. Souliotis, E. Bell, M. Jandel, A. Ruangma, D. Shetty, E.M. Winchester and S.J. Yennello, Progress in Research, (Cyclotron Institute, Texas A&M University, 2004-2005), II-25.

[63] A.L. Keksis, M. Veselsky, G.A. Souliotis, D.V. Shetty, M. Jandel, E. Bell, A. Ruangma, E.M. Winchester, J. Garey, S. Parketon, C. Richers and S.J. Yennello, Progress in Research, (Cyclotron Institute, Texas A&M University, 2005-2006), II-36.

[64] D.V. Shetty, A. Keksis, E. Martin, A. Ruangma, G.A. Souliotis, M. Veselsky, E.M. Winchester, S.J. Yennello, K. Hagel, Y.G. Ma, A. Makeev, N. Marie, M. Murray, J.B. Natowitz, L. Qin, P. Smith, R. Wada, J. Wang, M. Cinausero, E. Fioretto, G. Prete, D. Fabris, M. Lunardon, G. Nebbia, V. Rizzi, G. Viesti, J.

Cibor, Z. Majka, P. Staszel, R. Alfaro, A. Martinez-Davalos, A. Menchaca-Rocha, Y. El Masri and T. Keutgen, Phys. Rev. C **68**, 054605 (2003).

[65] E.M. Winchester, J.A. Winger, R. Laforest, E. Martin, E. Ramakrishnan, D.J. Rowland, A. Ruangma, S.J. Yennello, G.D. Westfall, A. Vander Molen and E. Norbeck, Phys. Rev. C **63**, 014601 (2001).

[66] L. Tassan-Got, thesis, Universite Paris Sud (1988).

[67] D. Lacroix, A. Van Lauwe and D. Durand, Phys. Rev. C **69**, 054604 (2004).

[68] Z. Kohley. Cyclotron Institute, Texas A&M University. Private Communications. (2006)

[69] TWINGO Program. A. Guarnera, University Caen, (1996).

[70] B.A. Li, C.B. Das, S.D. Gupta and C. Gale, Nucl. Phys. A **735**, 563 (2004).

[71] L.W. Chen. Institute of Theoretical Physics, Shanghai Jiao Tong University. Private Communications. (2007)

[72] A.S. Botvina, A.S. Iljinov, I.N. Mishustin, J.P. Bondorf, R. Donangelo and K. Sneppen, Nucl. Phys. A **475**, 663 (1987).

[73] A.S. Botvina, A.S. Iljinov and I.N. Mishustin, Nucl. Phys. A **507**, 649 (1990).

[74] A.S. Botvina, A.D. Jackson and I.N. Mishustin, Phys. Rev. E **62**, R64 (2000).

[75] A.S. Botvina and I.N. Mishustin, Phys. Rev. C **63**, 061601 (2001).

[76] G.A. Souliotis. Cyclotron Institute, Texas A&M University. Private Communications (2006).

# APPENDIX A

## RECONSTRUCTION EXAMPLE

One event from the experimental data was selected from the reaction 32 MeV/nucleon $^{48}$Ca on $^{124}$Sn. The event has a multiplicity of seven and will be worked through completely. The information known about the event is shown in Table XXII.

The first step is to find the laboratory angles from the detector number, which are provided by a lookup table called angle.txt. These angles are in degrees and are then converted into radians. Theta is the angle off the beam axis and phi is the angle from 0-360 around the array. Table XXIII summarizes this information.

Next the mass excess of each fragment needs to be calculated, there is a lookup table called massexcess.txt that contains all the known mass excesses from the work of Audi *et al.* [22, 21, 20]. Table XXIV shows the mass excess of each fragment.

Knowing the mass excess of the fragment, the mass of the fragment can then be calculated for each fragment using the equation:

$$m_{fragment} = 931.5A_{fragment} + MassExcess_{fragment} \tag{A.1}$$

where 931.5 converts mass to energy. Table XXIV list the fragment masses. Now the total energy is calculated for each fragment from the addition of the Silicon energy and CsI energy (Table XXV).

TABLE XXII. List of fragment properties from the example event.

| Fragment | Fragment Z | Fragment A | Si E (MeV) | CsI E (MeV) | Detector Number |
|---|---|---|---|---|---|
| 1 | 6 | 12 | 50.0563 | 207.0580 | 12 |
| 2 | 4 | 7 | 27.246 | 89.6386 | 18 |
| 3 | 3 | 7 | 21.909 | 60.0734 | 24 |
| 4 | 2 | 4 | 4.0014 | 120.009 | 28 |
| 5 | 2 | 3 | 2.7358 | 165.764 | 29 |
| 6 | 2 | 4 | 3.1650 | 153.059 | 31 |
| 7 | 1 | 1 | 0.4606 | 58.9270 | 32 |

The total Z of the quasiprojectile source is just the sum over the fragment Zs. In this case 6 + 4 + 3 + 2 + 2 + 2 + 1 = 20. So the reconstructed Z is 20. The total apparent A (since neutrons were not detected) of the quasiprojectile source is the sum of the fragment As. In this case 12 + 7 + 7 + 4 + 3 + 4 + 1 = 38. So the reconstructed apparent A is 38.

The velocity of the fragments can now be calculated by rearranging equation A.2 to equation A.3. The velocities of the fragments are summarized in table XXVI.

$$E = \frac{1}{2}mv^2 \tag{A.2}$$

$$v = \sqrt{2E/m} \tag{A.3}$$

Now this velocity vector must be transformed into its Cartesian parts using the following relations:

TABLE XXIII. Conversion of detector number into angle.

| Fragment | Detector | Θ Degrees | Φ Degrees | Θ Radians | Φ Radians |
|---|---|---|---|---|---|
| 1 | 12 | 9.32 | 314.99 | 0.1627 | 5.4976 |
| 2 | 18 | 9.32 | 134.99 | 0.1627 | 2.3560 |
| 3 | 24 | 12.81 | 333.18 | 0.2236 | 5.8151 |
| 4 | 28 | 12.81 | 243.18 | 0.2236 | 4.2443 |
| 5 | 29 | 16.17 | 225.00 | 0.2822 | 3.9270 |
| 6 | 31 | 11.47 | 180.00 | 0.2002 | 3.1416 |
| 7 | 32 | 12.81 | 153.18 | 0.2236 | 2.6735 |

TABLE XXIV. Mass excesses and the masses of the fragments.

| Fragment | Z | A | Nuclide | Mass Excess ($MeV/c^2$) | Constant * A + Mass Excess = Mass |
|---|---|---|---|---|---|
| 1 | 6 | 12 | 12C | 0.000 | 931.5 * 12 + 0.000 = 11178.000 |
| 2 | 4 | 7 | 7Be | 15.768 | 931.5 * 7 + 15.768 = 6536.266 |
| 3 | 3 | 7 | 7Li | 14.907 | 931.5 * 7 + 14.907 = 6535.407 |
| 4 | 2 | 4 | 4He | 2.424 | 931.5 * 4 + 2.424 = 3728.424 |
| 5 | 2 | 3 | 3He | 14.931 | 931.5 * 3 + 14.931 = 2809.431 |
| 6 | 2 | 4 | 4He | 2.424 | 931.5 * 4 + 2.424 = 3728.424 |
| 7 | 1 | 1 | 1H | 7.289 | 931.5 * 1 + 7.289 = 938.789 |

TABLE XXV. Fragment energies.

| Fragment | Silicon Energy (MeV) | CsI Energy (MeV) | Total Energy (MeV) |
|---|---|---|---|
| 1 | 50.0563 | 207.058 | 257.1143 |
| 2 | 27.246 | 89.6386 | 116.8846 |
| 3 | 21.909 | 60.0734 | 81.9824 |
| 4 | 4.0014 | 120.009 | 124.0104 |
| 5 | 2.7358 | 165.764 | 168.4998 |
| 6 | 3.165 | 153.059 | 156.2240 |
| 7 | 0.4606 | 58.927 | 59.3876 |

$$v_x = vsin(\Theta)cos(\Phi) \tag{A.4}$$

$$v_y = vsin(\Theta)sin(\Phi) \tag{A.5}$$

$$v_z = vcos(\Theta) \tag{A.6}$$

The results are summarized in table XXVI.

Next the momentum of each fragment is calculated using:

$$p = mv \tag{A.7}$$

where p is the momentum, m is the fragment mass and v is the velocity. This is done for each coordinate, x, y and z. The results are summarized in table XXVII.

Now the total momentum for all fragments can be calculated by adding up the individual fragment momentum in each coordinate space. $p_x$ = 274.9788 - 141.8370 + 204.5584 - 96.1933 - 191.6032 - 214.7572 - 66.0907 = - 230.944, $p_y$ = - 274.9788 +

TABLE XXVI. Fragment velocity and components in Cartesian coordinates.

| Fragment | Velocity | $v_x$ | $v_y$ | $v_z$ |
|---|---|---|---|---|
| 1 | 0.2145c | 0.0246 | -0.0246 | 0.2117 |
| 2 | 0.1891c | -0.0217 | 0.0217 | 0.1866 |
| 3 | 0.1584c | 0.0313 | -0.0158 | 0.1545 |
| 4 | 0.2579c | -0.0258 | -0.0510 | 0.2515 |
| 5 | 0.3463c | -0.0682 | -0.0682 | 0.3326 |
| 6 | 0.2895c | -0.0576 | 0.0000 | 0.2837 |
| 7 | 0.3557c | -0.0704 | 0.0356 | 0.3468 |

TABLE XXVII. Fragment momenta in Cartesian coordinates.

| Fragment | $p_x$ | $p_y$ | $p_z$ |
|---|---|---|---|
| 1 | 274.9788 | -274.9788 | 2366.3826 |
| 2 | -141.8370 | 141.8370 | 1219.6672 |
| 3 | 204.5584 | -103.2594 | 1009.7204 |
| 4 | -96.1933 | -190.1496 | 937.6986 |
| 5 | -191.6032 | -191.6032 | 934.4168 |
| 6 | -214.7572 | 0.0000 | 1057.7539 |
| 7 | -66.0907 | 33.4209 | 325.5720 |

141.8370 - 103.2594 - 190.1496 - 191.6032 + 0.0000 + 33.4209 = - 584.7331, and $p_z$ = 2366.3826 + 1219.6672 + 1009.7204 + 937.6986 + 934.4168 + 1057.7539 + 325.5720 = 7851.2115. The total mass for all the fragments is just the sum of the individual fragment masses. $m_{total} = 11178.000 + 6536.266 + 6535.407 + 3728.424 + 2809.431 + 3728.424 + 938.789 = 35454.741$. Now the quasiprojectile velocity can be calculated in the center of mass using equation A.8. The velocity of the quasiprojectile in x, y, and z is -0.0065, -0.0165 and 0.2214, respectfully.

$$v = p/m \tag{A.8}$$

Now the quasiprojectile velocity in the center of mass is converted to spherical coordinates using the relations:

$$v = \sqrt{v_x^2 + v_y^2 + v_z^2} \tag{A.9}$$

$$\Theta = acos(v_z/v) \tag{A.10}$$

$$\Phi = atan(v_y/v_x) + \pi(if\, v_x < 0) \tag{A.11}$$

The quasiprojectile velocity is then 0.2221, $\Theta$ is 0.0794 and $\Phi$ is 4.3371. The fragment velocities can now be calculated in the center of mass using Equation A.12 in each coordinate. The results are summarized in table XXVIII.

$$v_{f_{com}} = v_f - v_{qp} \tag{A.12}$$

Now the velocity of each fragment in the center of mass can be calculated in the spherical coordinate frame using equations A.9 to A.11 as was done for the quasiprojectile. Results are summarized in table XXVIII. Then using equation A.2 the energy of each fragment in the center of mass can be calculated (table XXIX).

TABLE XXVIII. Fragment velocities in center of mass in Cartesian and spherical coordinates.

| Fragment | $v_{xf_{com}}$ | $v_{yf_{com}}$ | $v_{zf_{com}}$ | $v_{com}$ | $\Theta_{com}$ | $Phi_{com}$ |
|---|---|---|---|---|---|---|
| 1 | 0.0311 | -0.0081 | -0.0097 | 0.0336 | 1.8637 | -0.2548 |
| 2 | -0.0152 | 0.0382 | -0.0348 | 0.0539 | 2.2727 | 1.9495 |
| 3 | 0.0378 | 0.0007 | -0.0669 | 0.0768 | 2.6282 | 0.0185 |
| 4 | -0.0193 | -0.0345 | 0.0301 | 0.0497 | 0.9200 | 4.2023 |
| 5 | -0.0617 | -0.0517 | 0.1112 | 0.1373 | 0.6268 | 3.8390 |
| 6 | -0.0511 | 0.0165 | 0.0623 | 0.0822 | 0.7107 | 2.8293 |
| 7 | -0.0639 | 0.0521 | 0.1254 | 0.1501 | 0.5819 | 2.4576 |

TABLE XXIX. Energy of the fragments.

| Fragment | Energy (MeV) |
|---|---|
| 1 | 6.3098 |
| 2 | 9.4946 |
| 3 | 19.2737 |
| 4 | 4.6048 |
| 5 | 26.4807 |
| 6 | 12.5962 |
| 7 | 10.5755 |

TABLE XXX. Final reconstructed event in reconstructed physics tape format.

| Multiplicity | $Z_{qp}$ | $A_{qp}$ | $E_{qp}$ | $V_{qp_{cms}}$ | $\Theta$ | $\Phi$ |
|---|---|---|---|---|---|---|
| 7 | 20 | 38 | 169.1353 | 0.2221 | 0.0794 | 4.3371 |
| | $Z_f$ | $A_f$ | $E_f$ | $V_{f_{cms}}$ | $\Theta$ | $\Phi$ |
| | 6 | 12 | 6.3098 | 0.0336 | 1.8637 | -0.2548 |
| | 4 | 7 | 9.4946 | 0.0539 | 2.2727 | 1.9495 |
| | 3 | 7 | 19.2737 | 0.0768 | 2.6282 | 0.0185 |
| | 2 | 4 | 4.6048 | 0.0497 | 0.9200 | 4.2023 |
| | 2 | 3 | 26.4807 | 0.1373 | 0.6268 | 3.8390 |
| | 2 | 4 | 12.5962 | 0.0822 | 0.7107 | 2.8293 |
| | 1 | 1 | 10.5755 | 0.1501 | 0.5819 | 2.4576 |

The quasiprojectile mass excess can also be found in the lookup table, massexcess.txt, as were the fragment mass excesses. For charge 20 and mass number 38 the mass excess is -22.059 MeV. Now the mass of the quasiprojectile can be calculated using equation A.1 giving 35374.941 MeV. Then the excitation energy of the quasiprojectile can be calculated from the balance of energy given by:

$$E^*_{qp} = \sum(m_f + E_{f_{com}}) - m_{qp} \tag{A.13}$$

So then $E^*_{qp}$ = (11178.000 + 6.3098) + (6536.266 + 9.4946) + (6535.407 + 19.2737) + (3728.424 + 4.6048) + (2809.431 + 26.4807) + (3728.424 + 12.5962) + (938.789 + 10.5755) - 35374.941 = 169.1353 MeV or 4.4509 MeV/nucleon.

The last part is to write out the final reconstructed event in physics tape format (table XXX).

# APPENDIX B

## ADDITIONAL FRACTIONAL YIELD PLOTS

This section contains the fractional yield plots for all available elements at the other 12 laboratory angles. All elements that have fractional yield ratios are shown in figures 92 to 159 at the other 12 angles and trends are consistent with results from 7.01 degrees as discussed in chapter IV.

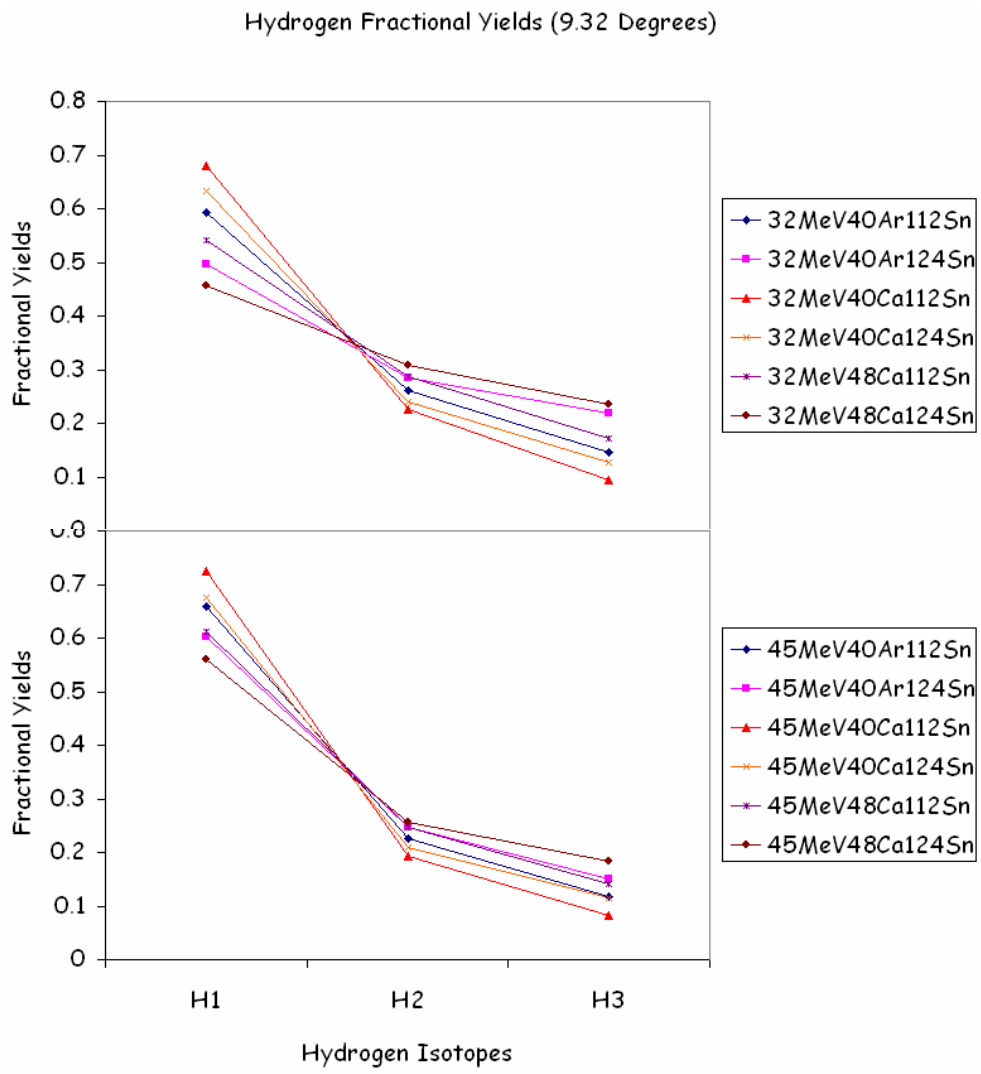


FIG. 92. (Color online) Hydrogen fractional yield ratio plot of the 32 MeV systems (top) and 45 MeV systems (bottom) at 9.32 degrees.

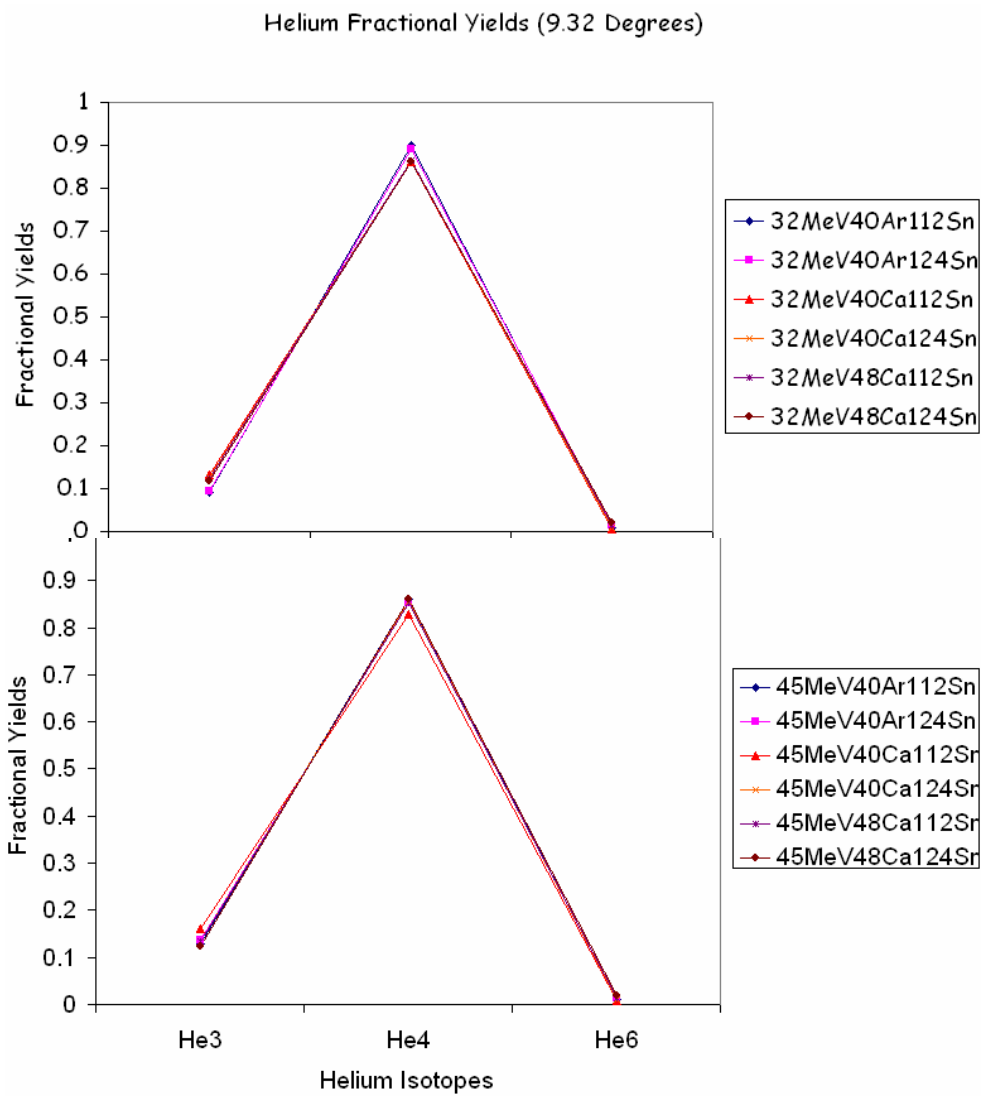


FIG. 93. (Color online) Helium fractional yield ratio plot of the 32 MeV systems (top) and 45 MeV systems (bottom) at 9.32 degrees.

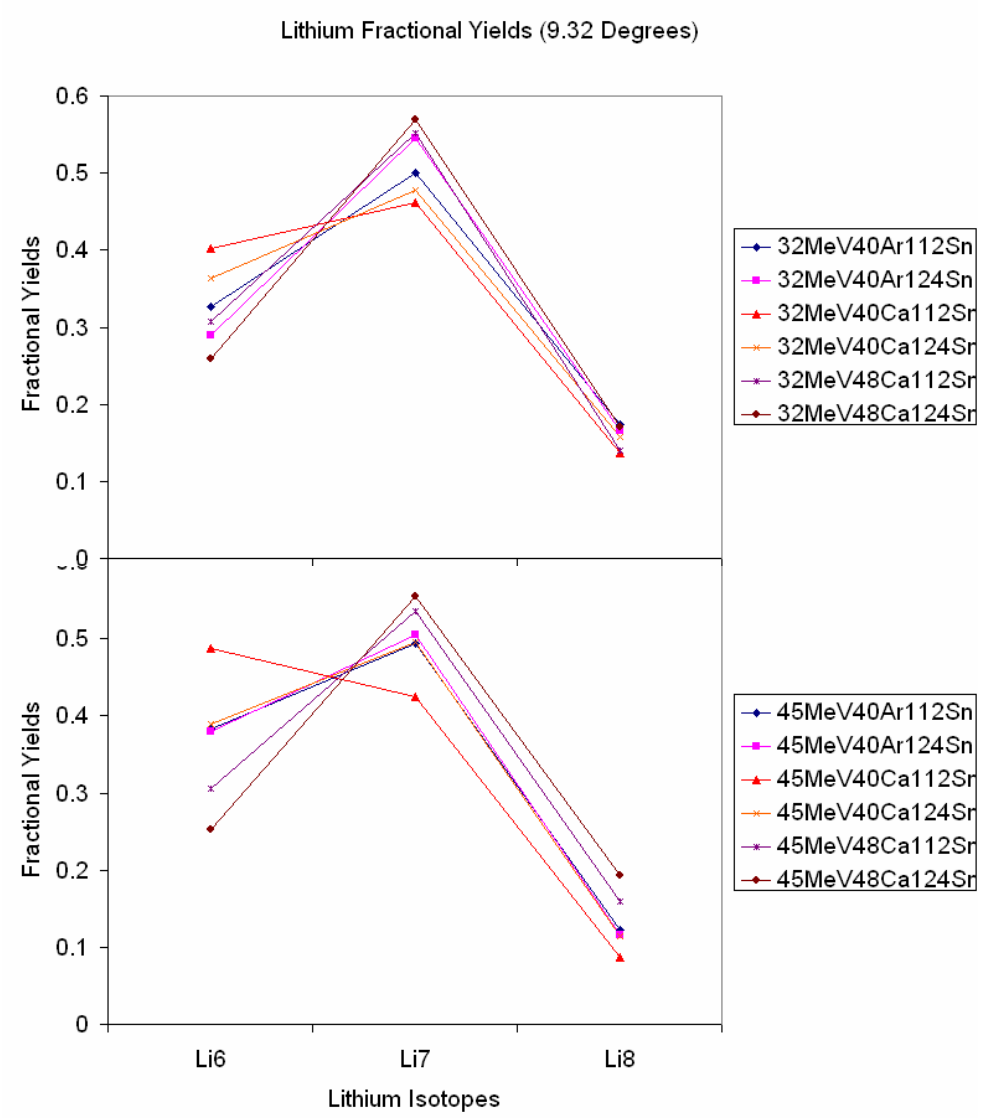


FIG. 94. (Color online) Lithium fractional yield ratio plot of the 32 MeV systems (top) and 45 MeV systems (bottom) at 9.32 degrees.

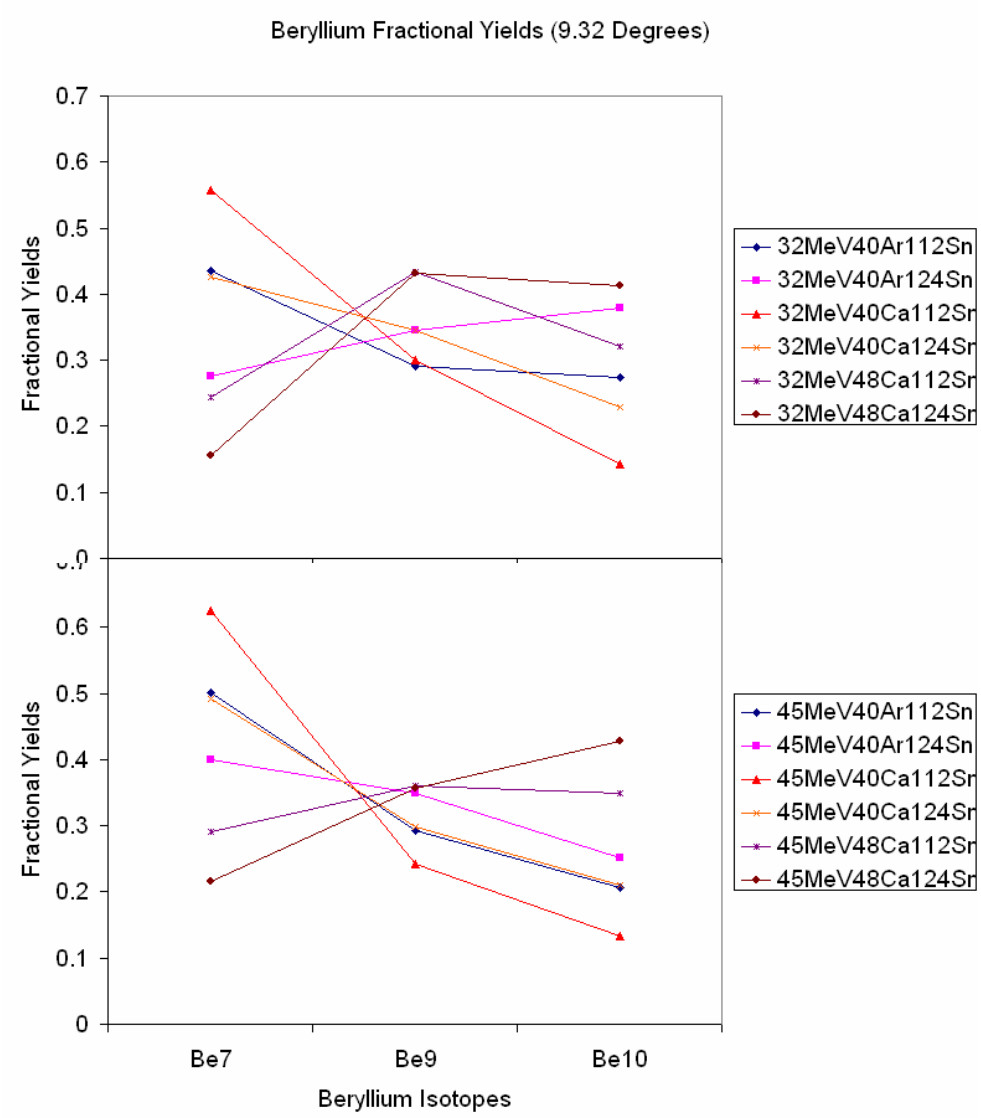


FIG. 95. (Color online) Beryllium fractional yield ratio plot of the 32 MeV systems (top) and 45 MeV systems (bottom) at 9.32 degrees.

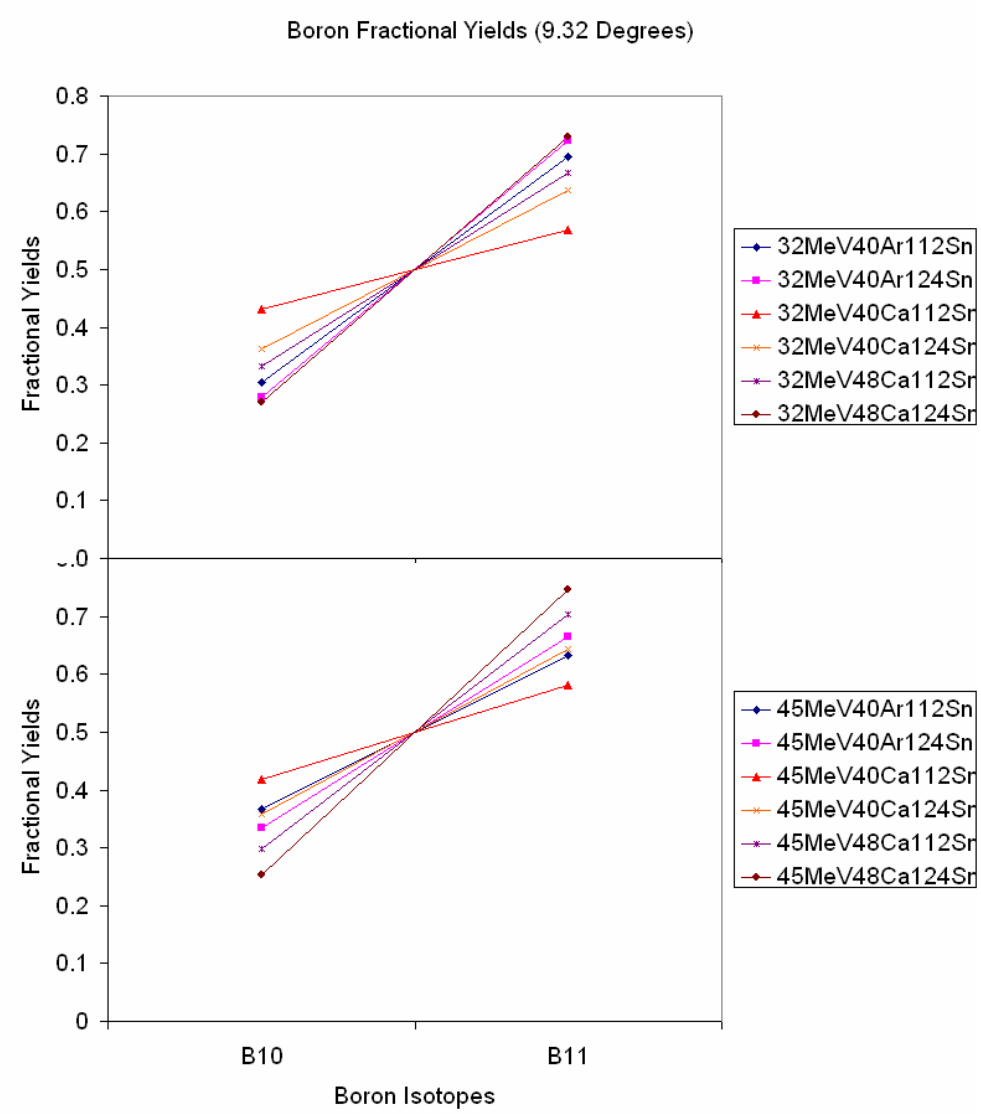


FIG. 96. (Color online) Boron fractional yield ratio plot of the 32 MeV systems (top) and 45 MeV systems (bottom) at 9.32 degrees.

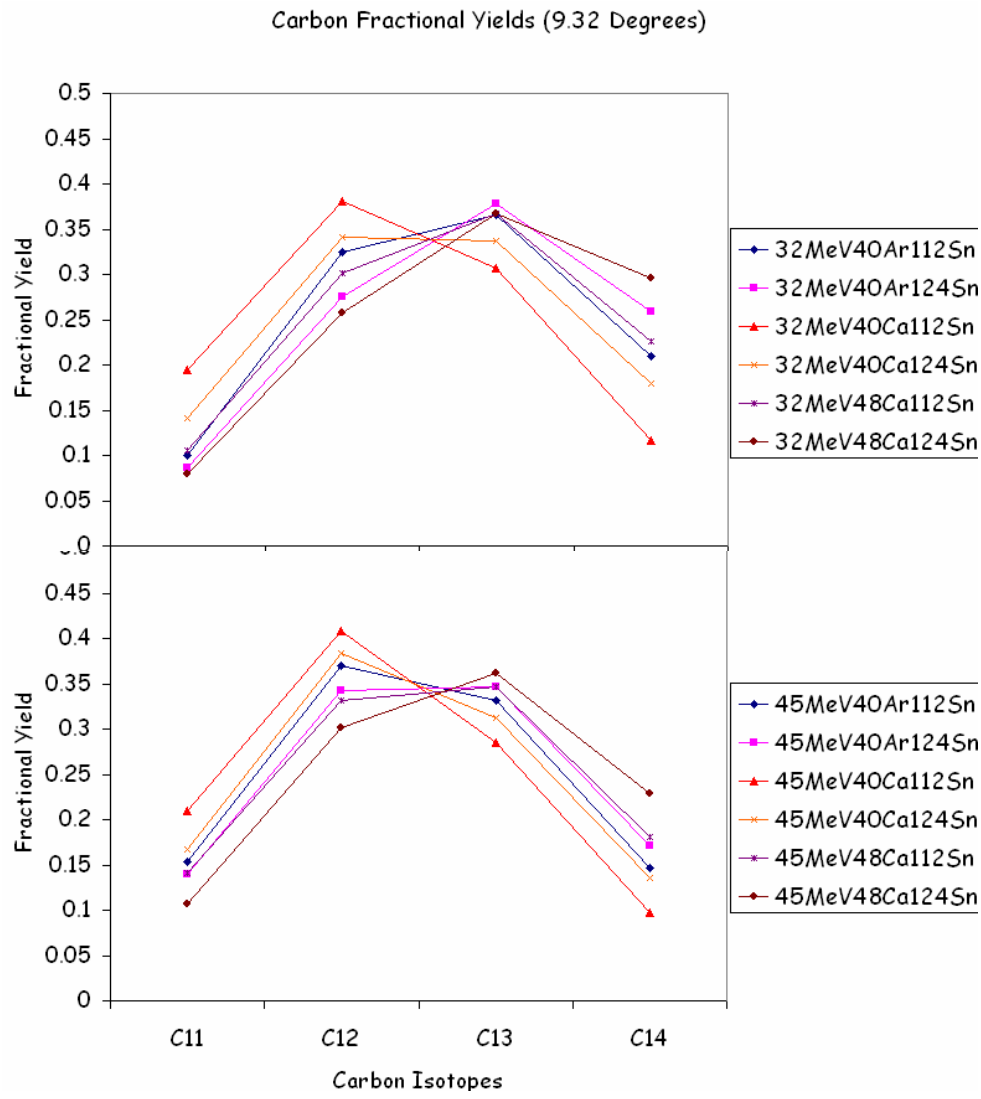


FIG. 97. (Color online) Carbon fractional yield ratio plot of the 32 MeV systems (top) and 45 MeV systems (bottom) at 9.32 degrees.

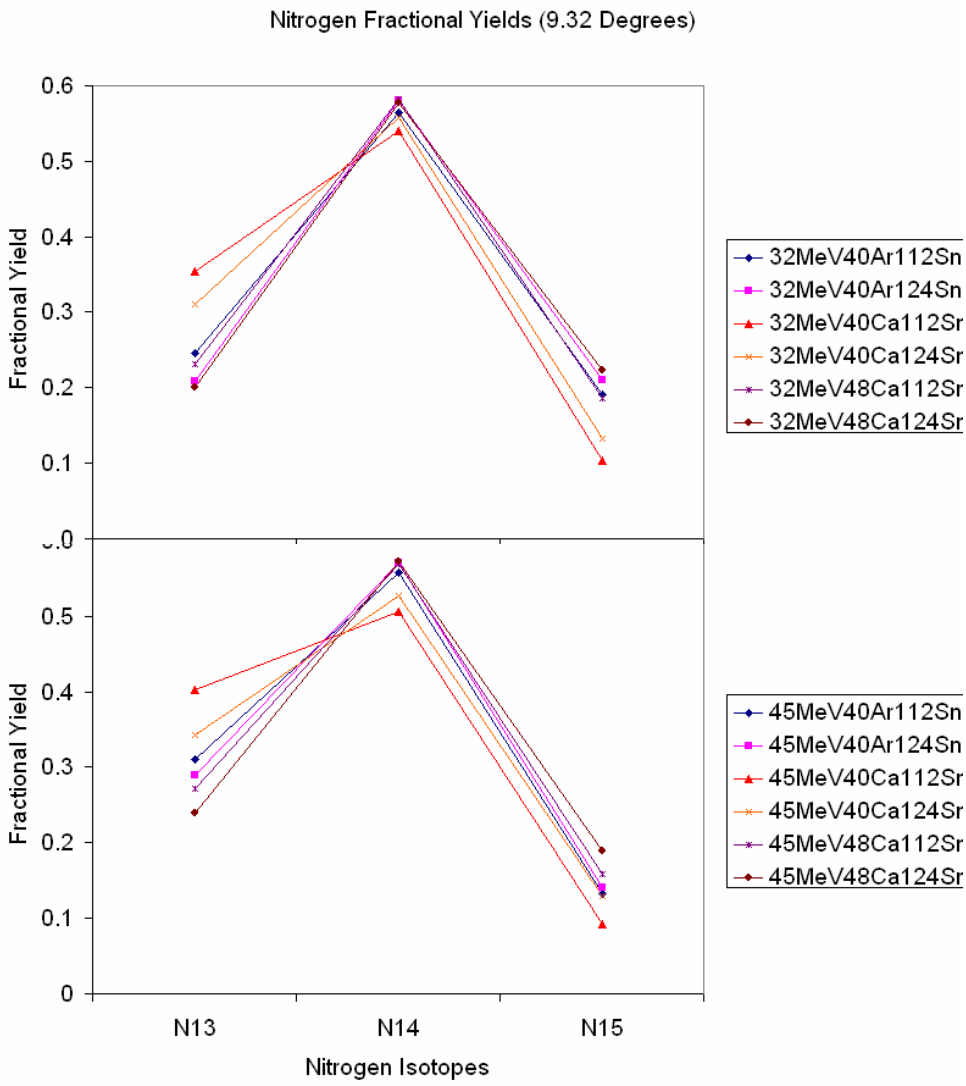


FIG. 98. (Color online) Nitrogen fractional yield ratio plot of the 32 MeV systems (top) and 45 MeV systems (bottom) at 9.32 degrees.

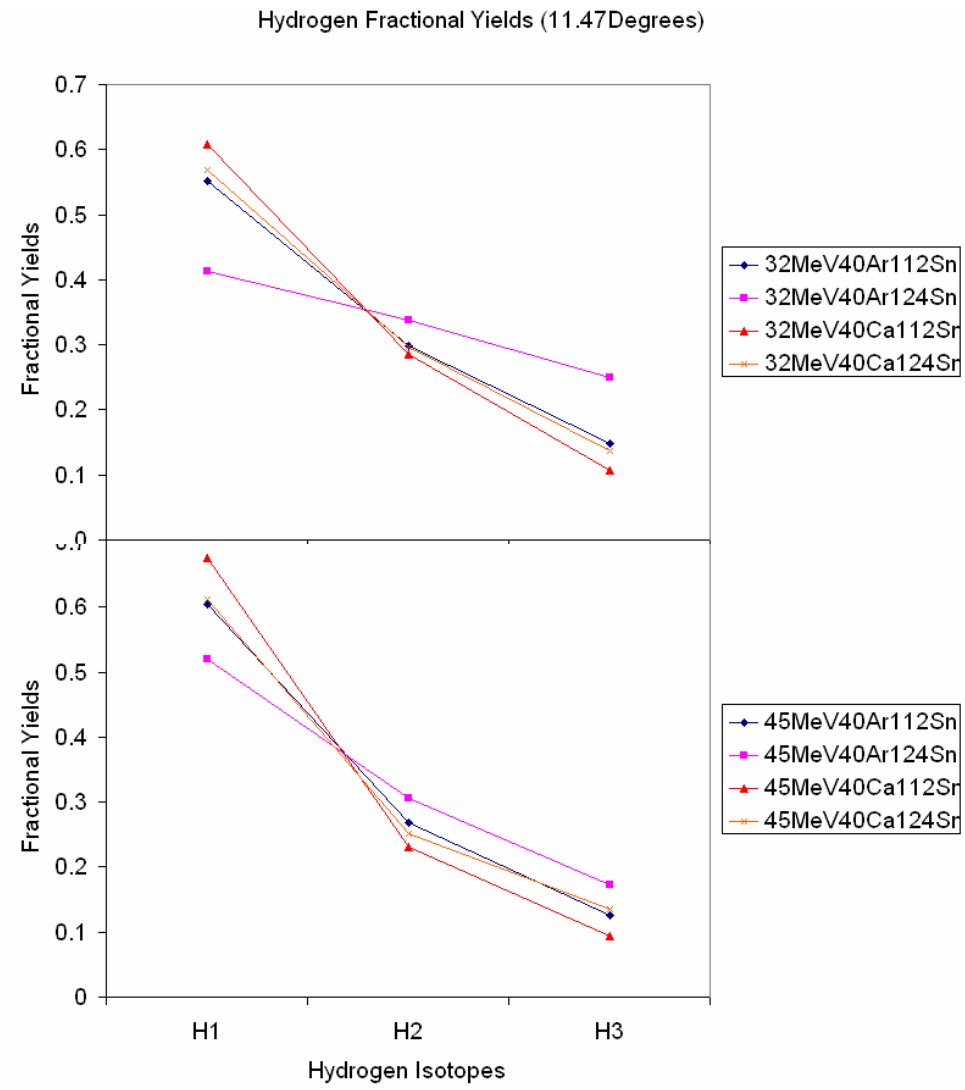


FIG. 99. (Color online) Hydrogen fractional yield ratio plot of the 32 MeV systems (top) and 45 MeV systems (bottom) at 11.47 degrees.

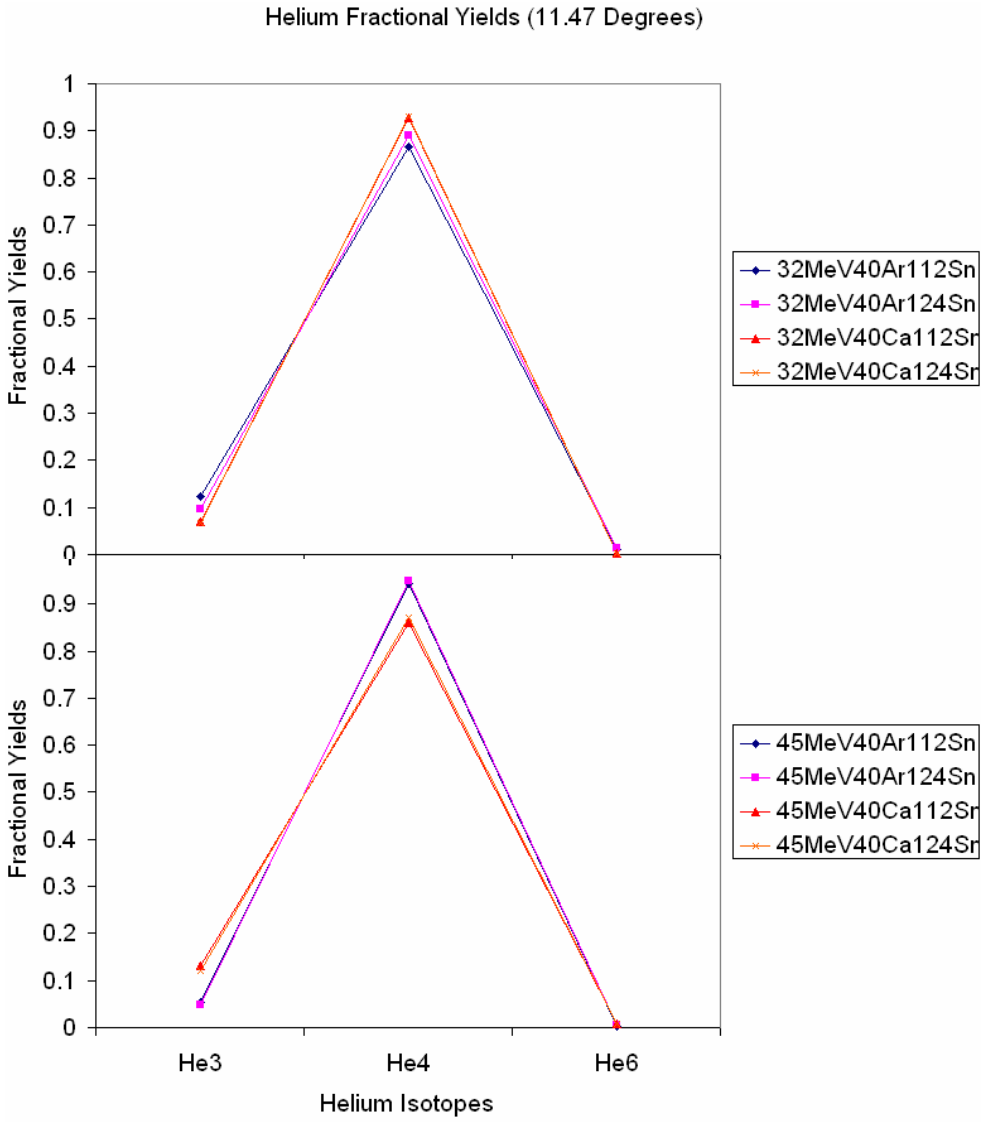


FIG. 100. (Color online) Helium fractional yield ratio plot of the 32 MeV systems (top) and 45 MeV systems (bottom) at 11.47 degrees.

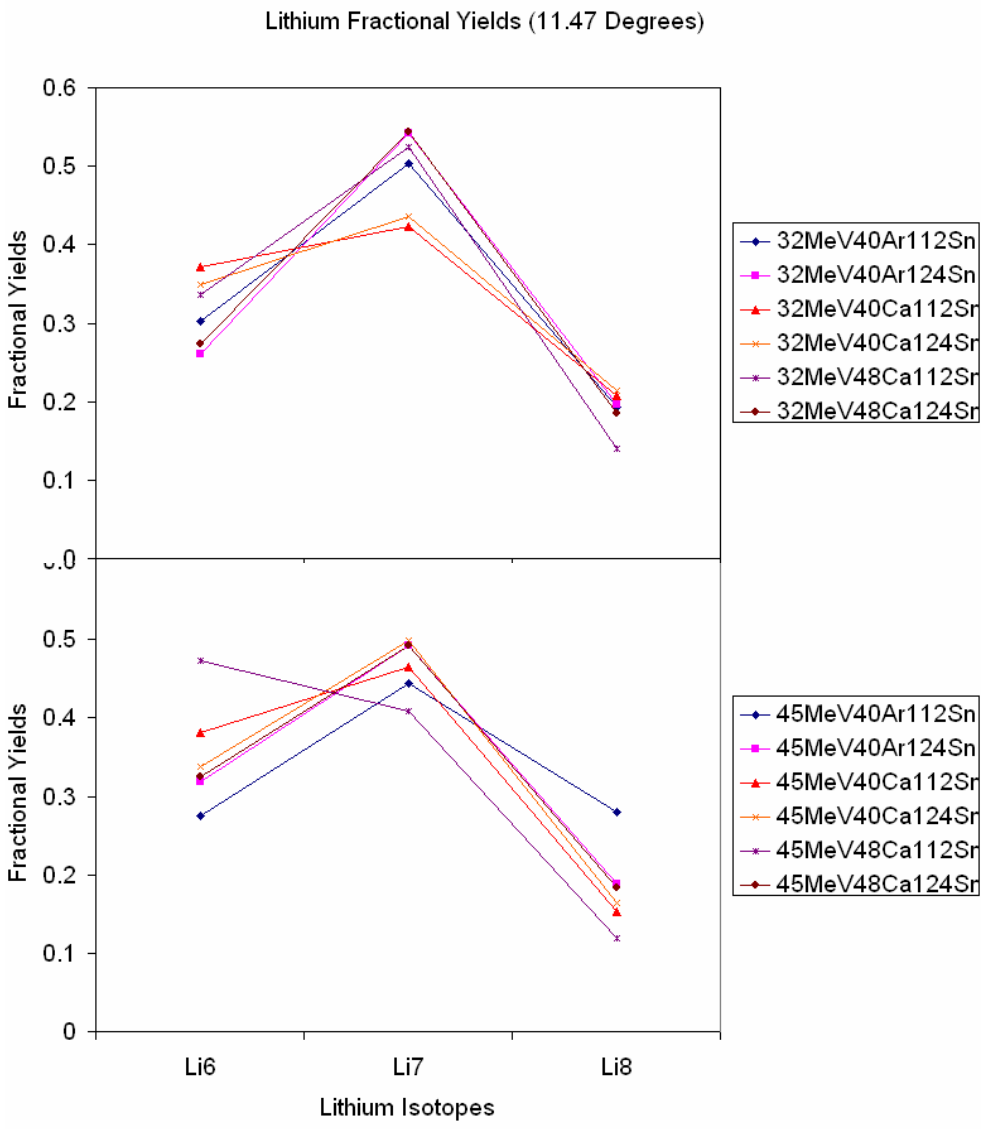


FIG. 101. (Color online) Lithium fractional yield ratio plot of the 32 MeV systems (top) and 45 MeV systems (bottom) at 11.47 degrees.

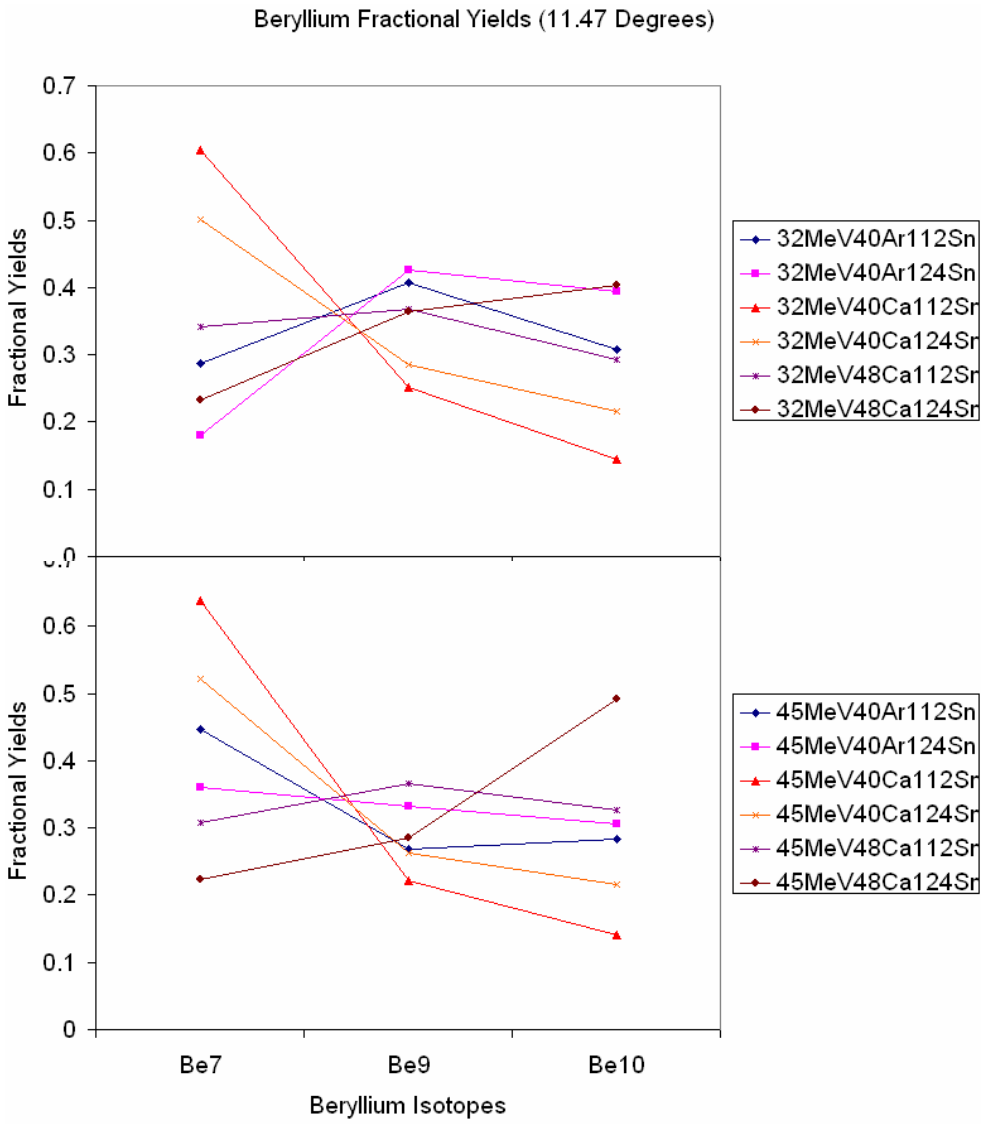


FIG. 102. (Color online) Beryllium fractional yield ratio plot of the 32 MeV systems (top) and 45 MeV systems (bottom) at 11.47 degrees.

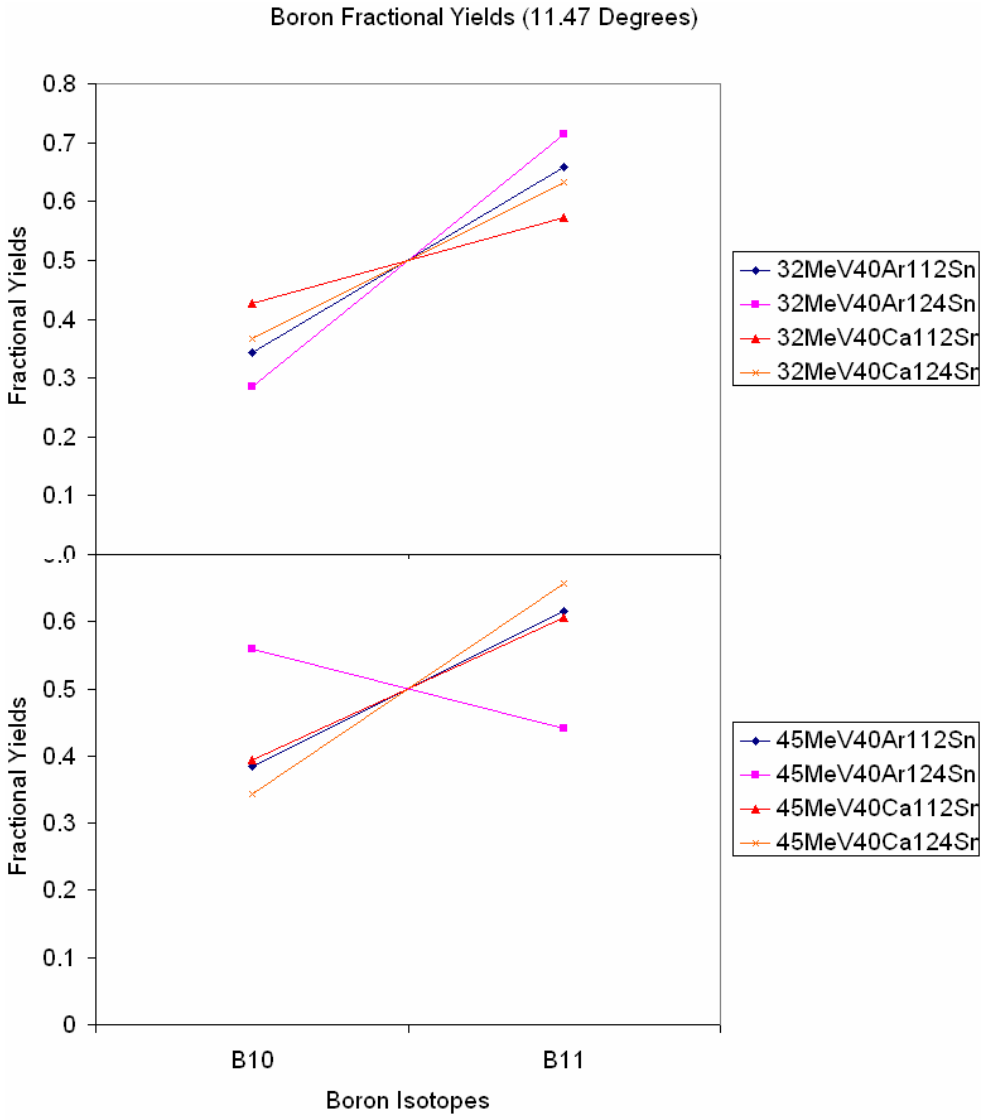


FIG. 103. (Color online) Boron fractional yield ratio plot of the 32 MeV systems (top) and 45 MeV systems (bottom) at 11.47 degrees.

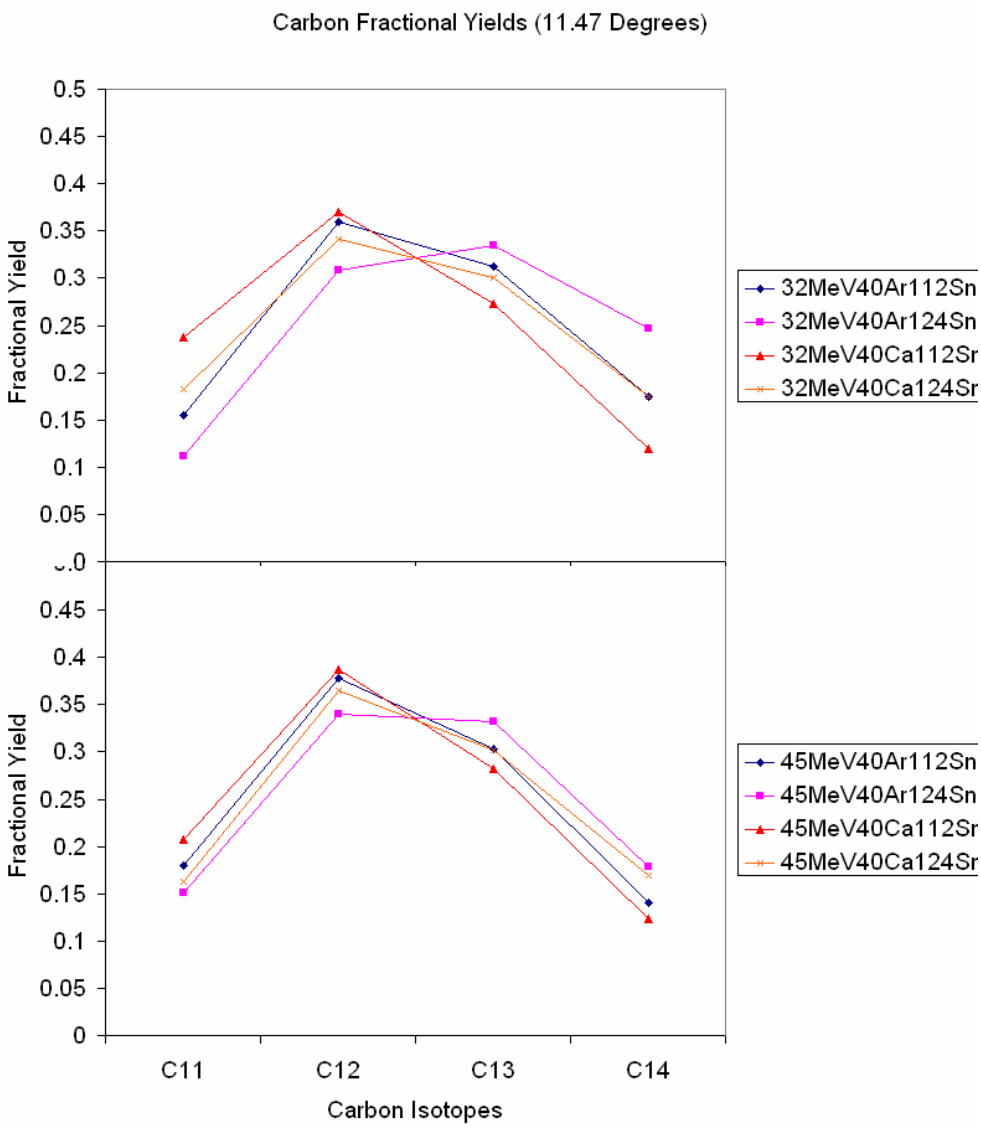


FIG. 104. (Color online) Carbon fractional yield ratio plot of the 32 MeV systems (top) and 45 MeV systems (bottom) at 11.47 degrees.

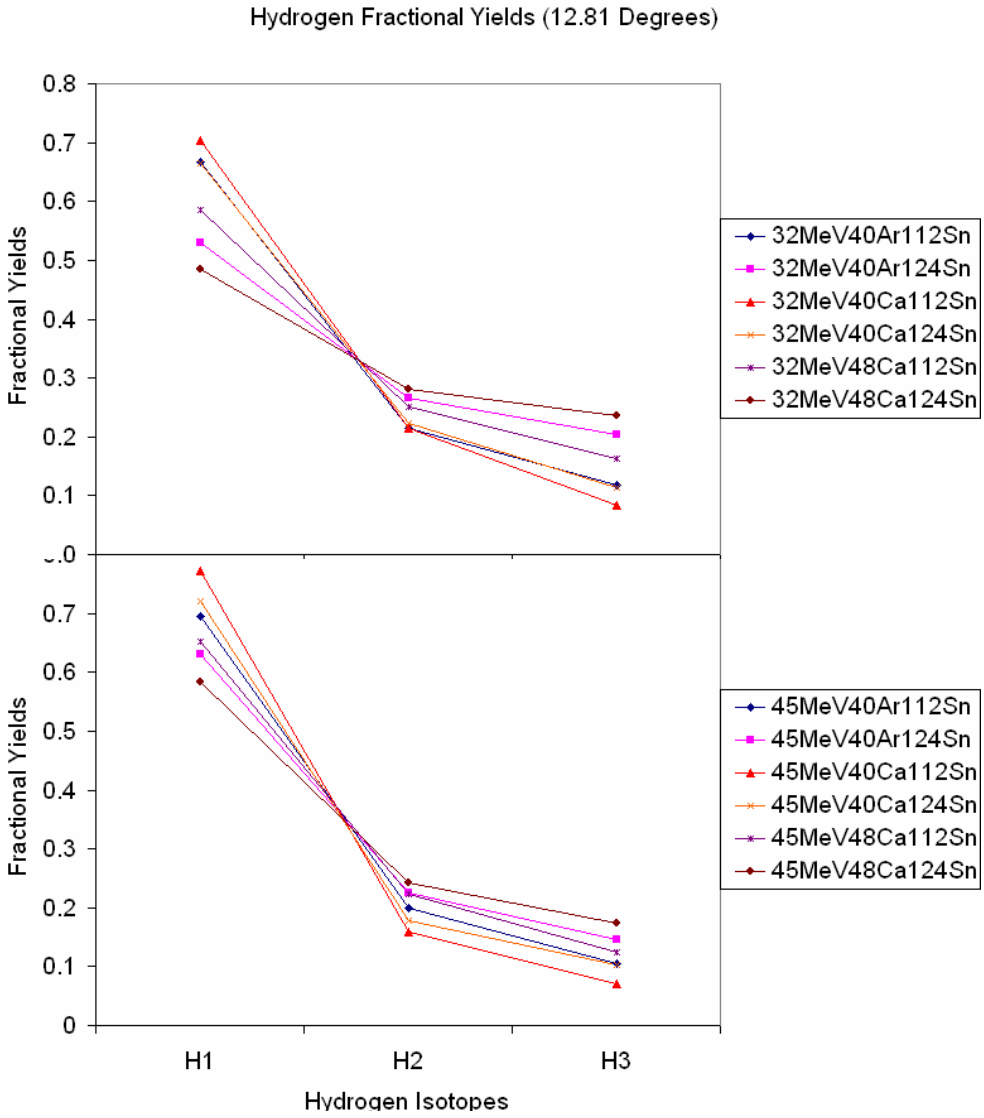


FIG. 105. (Color online) Hydrogen fractional yield ratio plot of the 32 MeV systems (top) and 45 MeV systems (bottom) at 12.81 degrees.

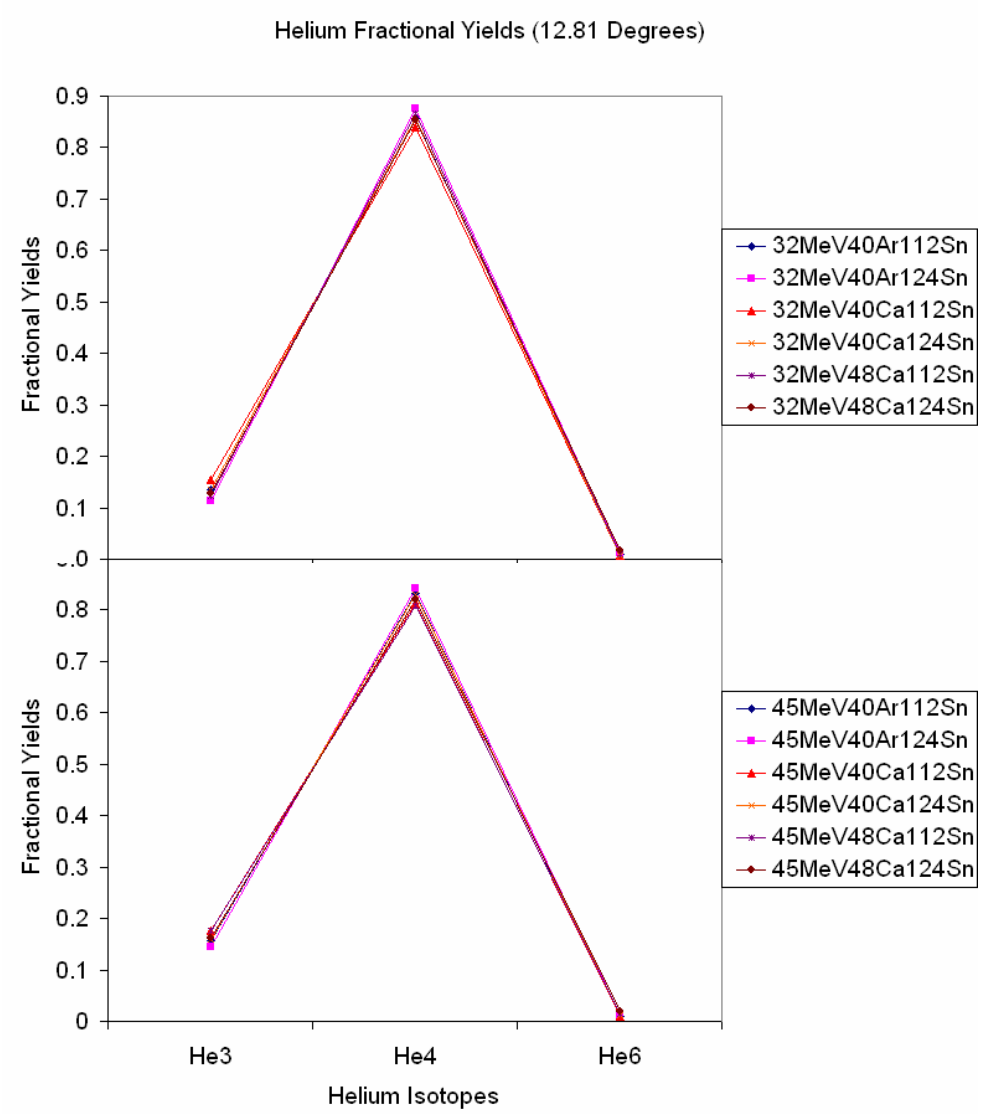


FIG. 106. (Color online) Helium fractional yield ratio plot of the 32 MeV systems (top) and 45 MeV systems (bottom) at 12.81 degrees.

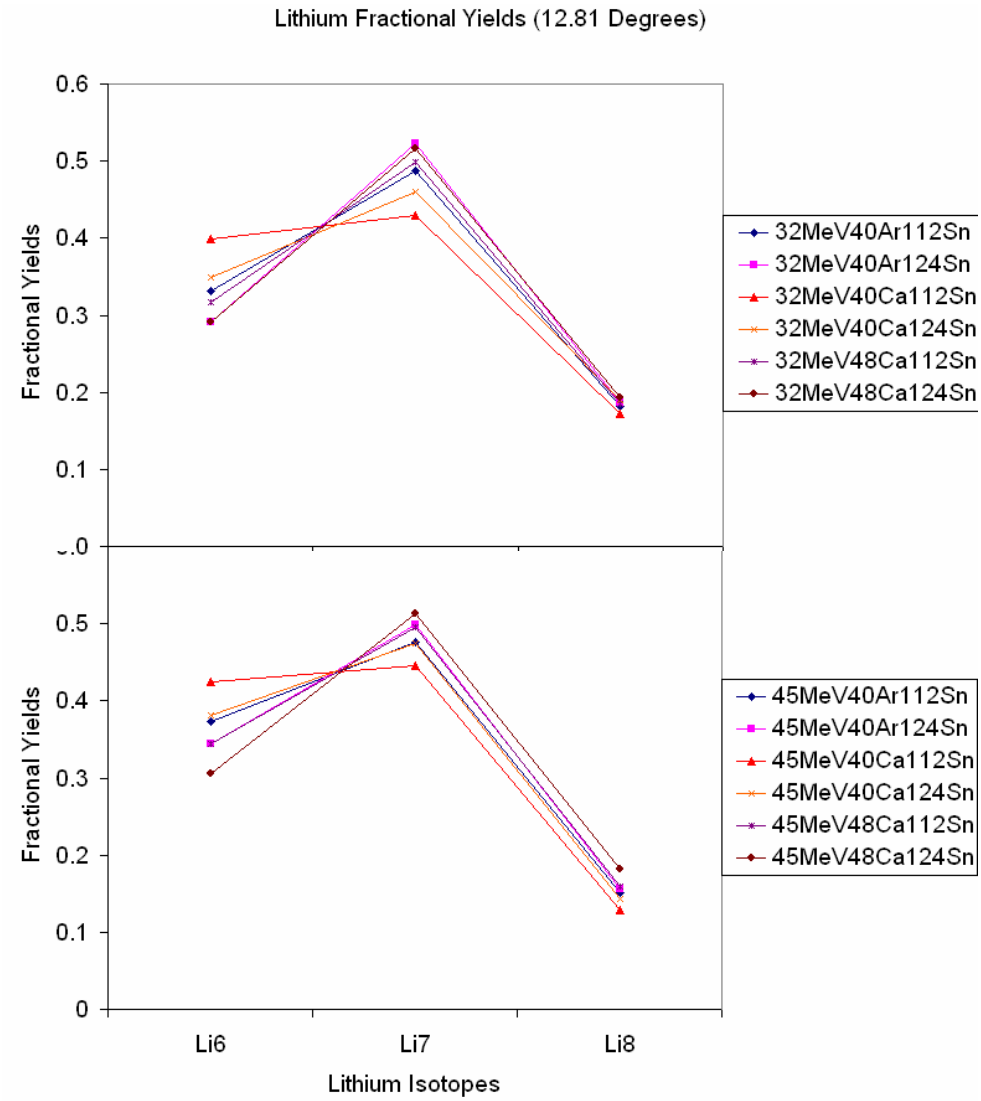


FIG. 107. (Color online) Lithium fractional yield ratio plot of the 32 MeV systems (top) and 45 MeV systems (bottom) at 12.81 degrees.

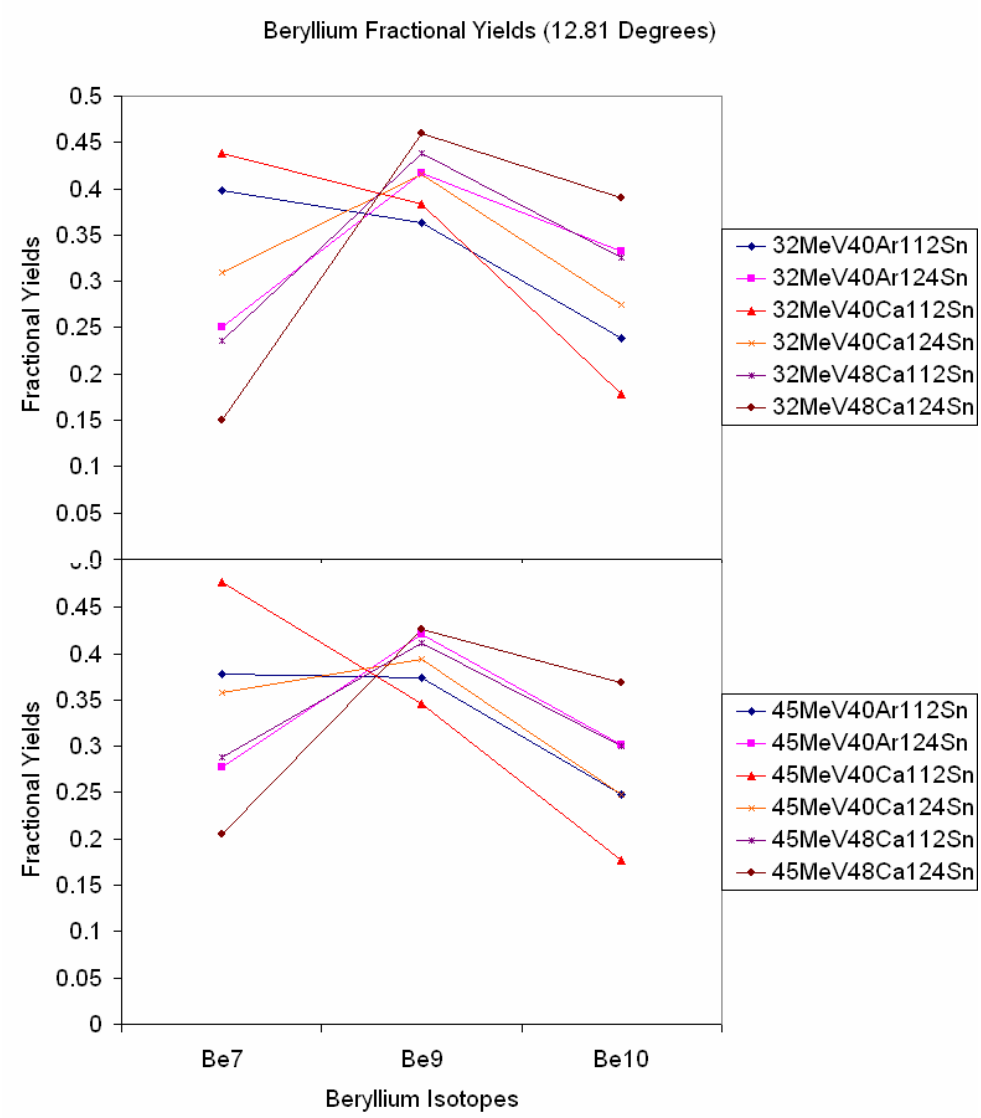


FIG. 108. (Color online) Beryllium fractional yield ratio plot of the 32 MeV systems (top) and 45 MeV systems (bottom) at 12.81 degrees.

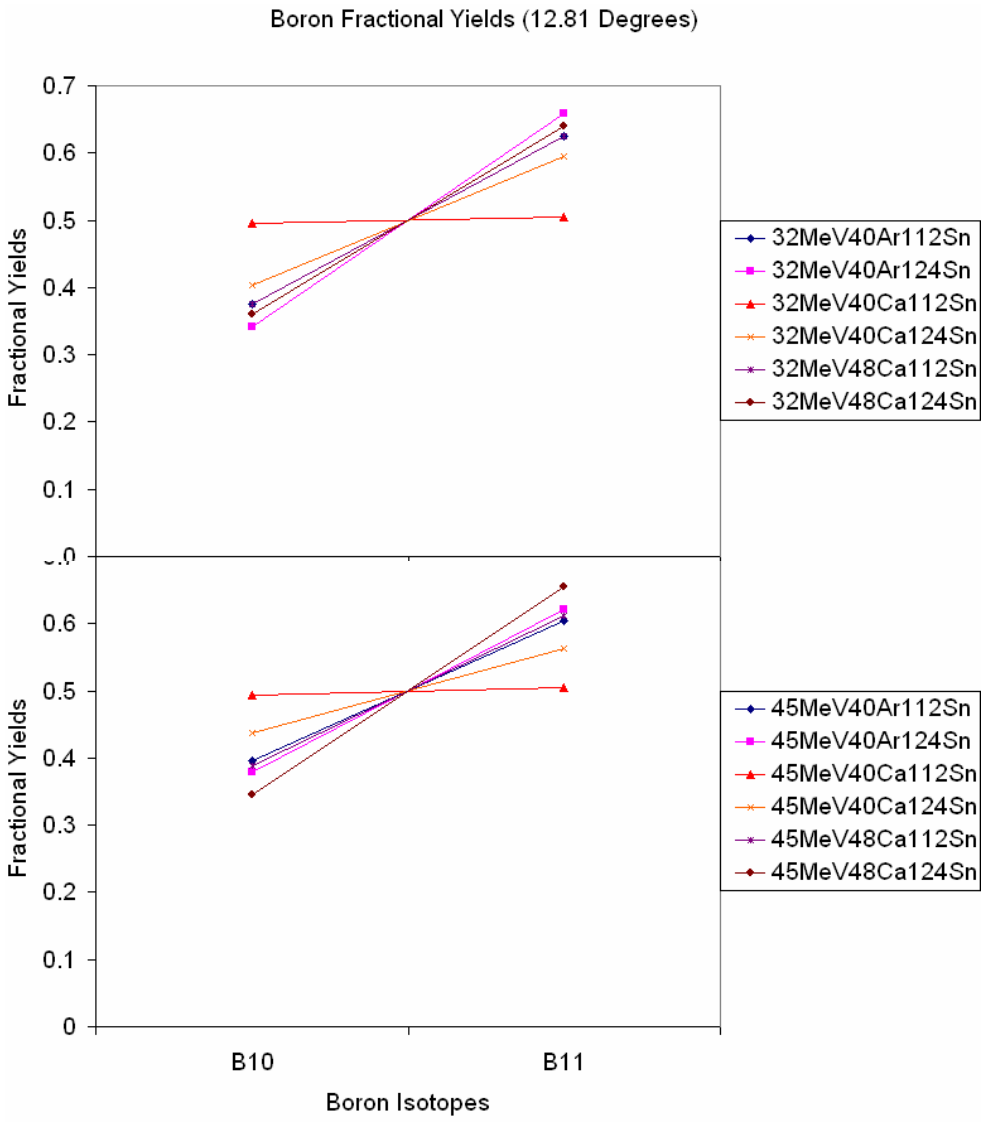


FIG. 109. (Color online) Boron fractional yield ratio plot of the 32 MeV systems (top) and 45 MeV systems (bottom) at 12.81 degrees.

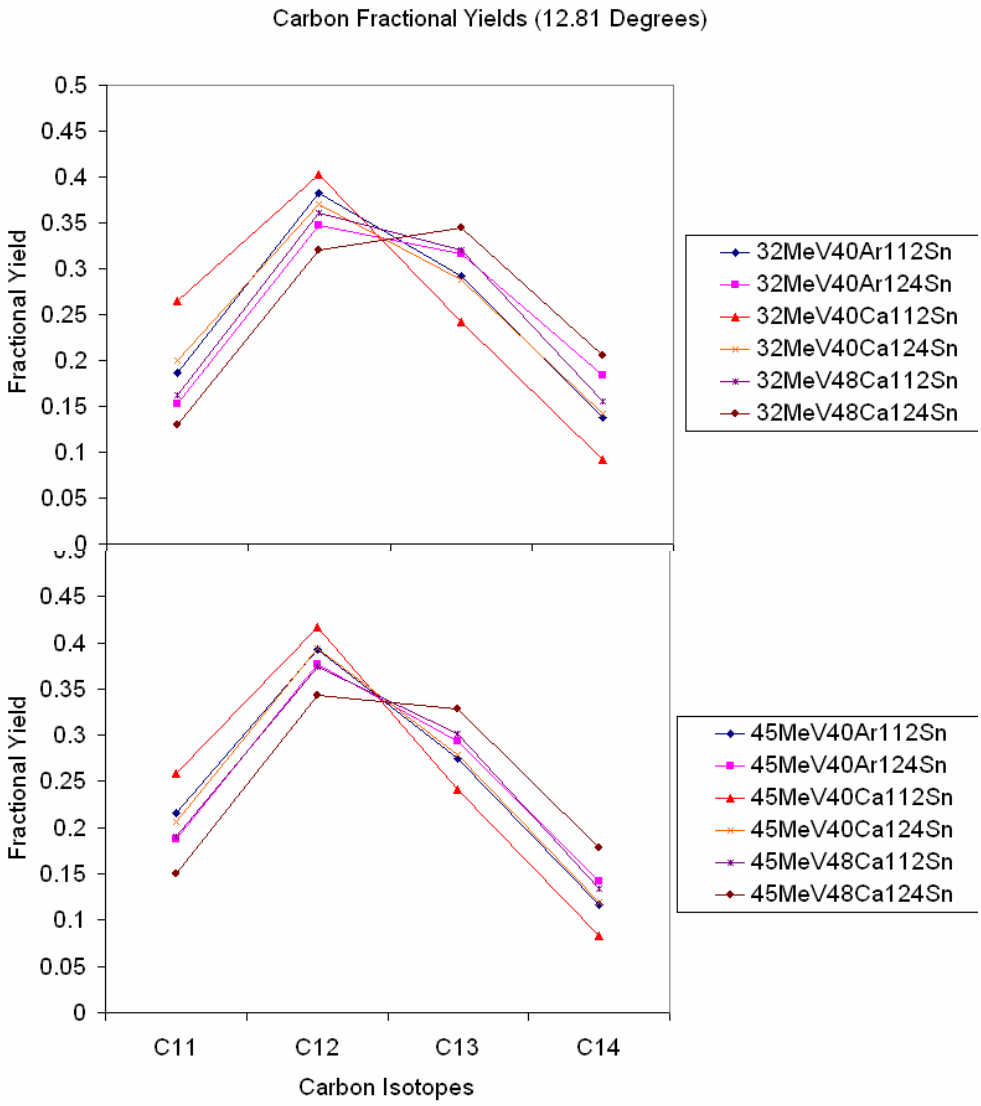


FIG. 110. (Color online) Carbon fractional yield ratio plot of the 32 MeV systems (top) and 45 MeV systems (bottom) at 12.81 degrees.

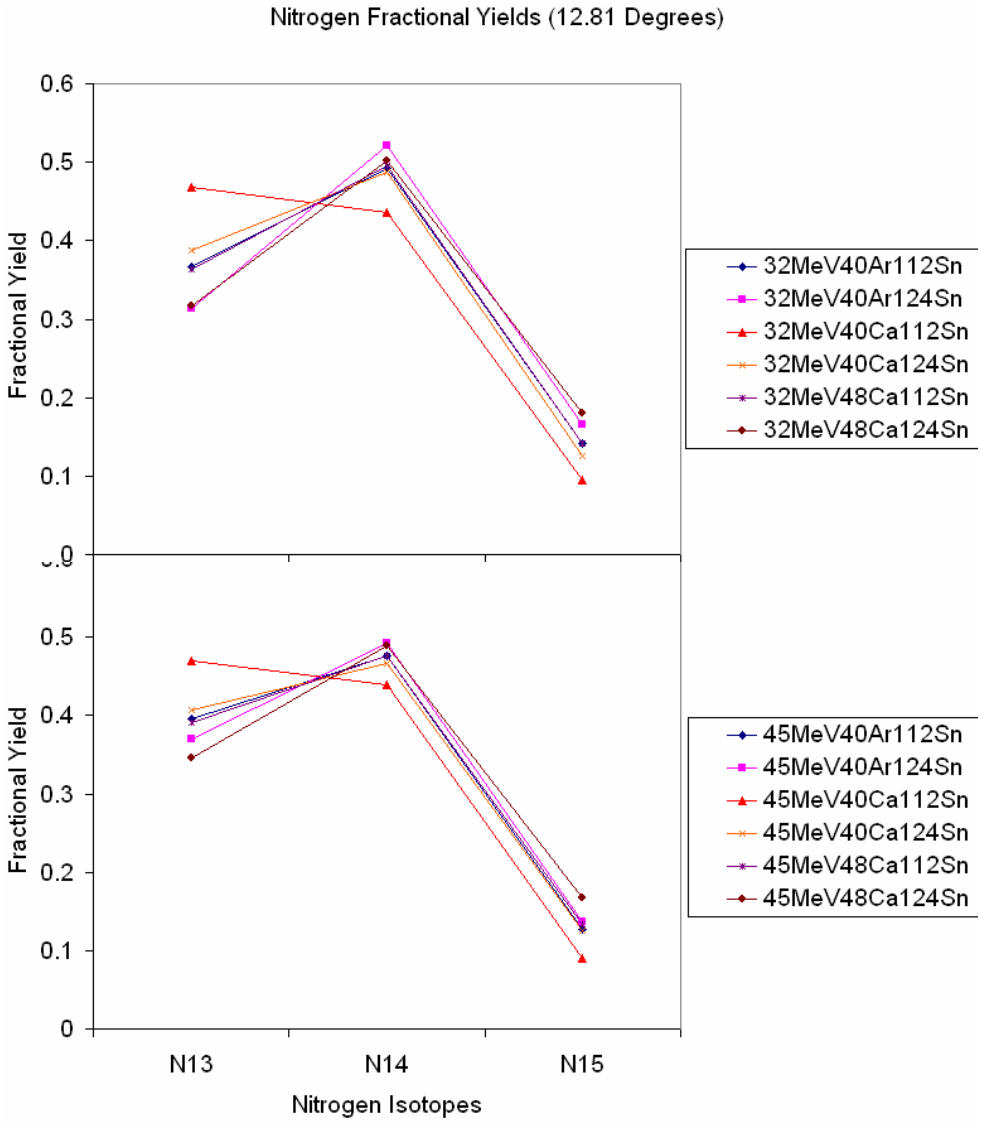


FIG. 111. (Color online) Nitrogen fractional yield ratio plot of the 32 MeV systems (top) and 45 MeV systems (bottom) at 12.81 degrees.

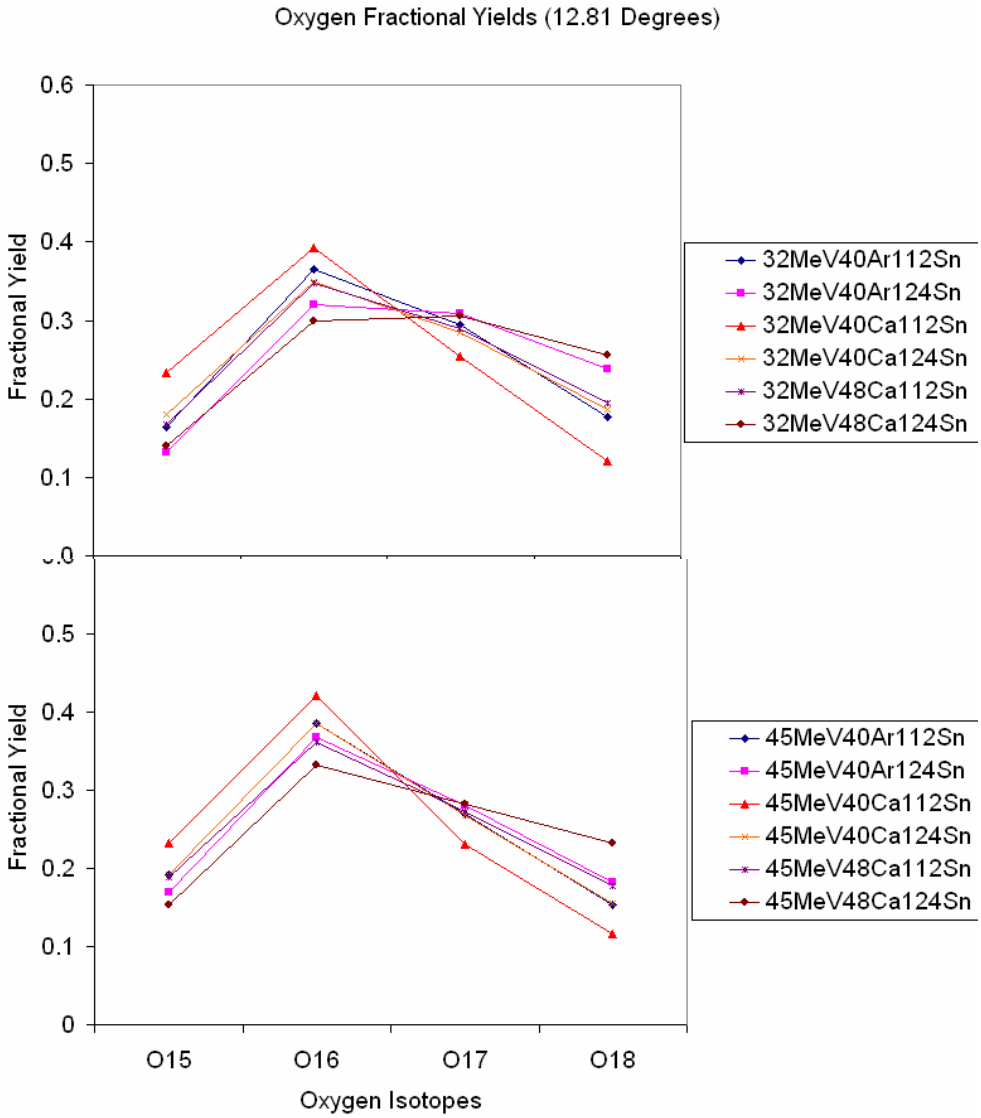


FIG. 112. (Color online) Oxygen fractional yield ratio plot of the 32 MeV systems (top) and 45 MeV systems (bottom) at 12.81 degrees.

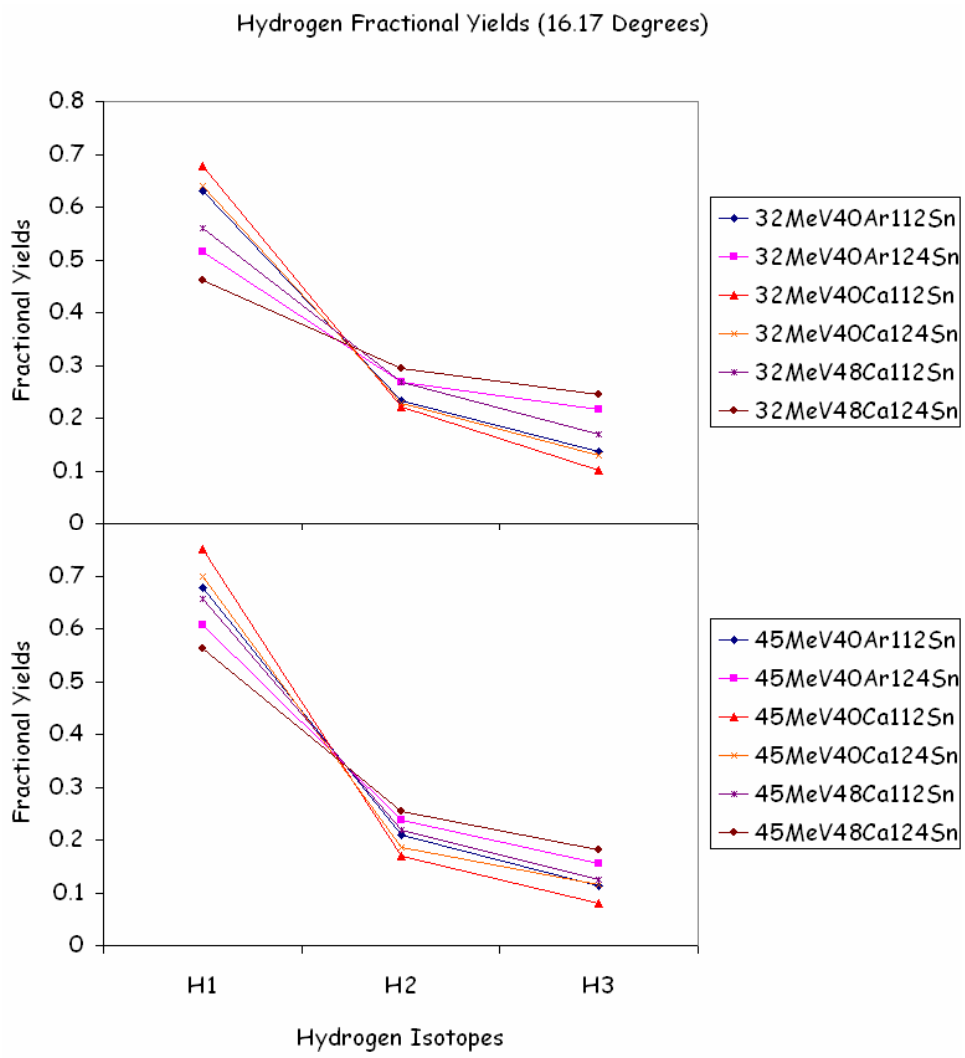


FIG. 113. (Color online) Hydrogen fractional yield ratio plot of the 32 MeV systems (top) and 45 MeV systems (bottom) at 16.17 degrees.

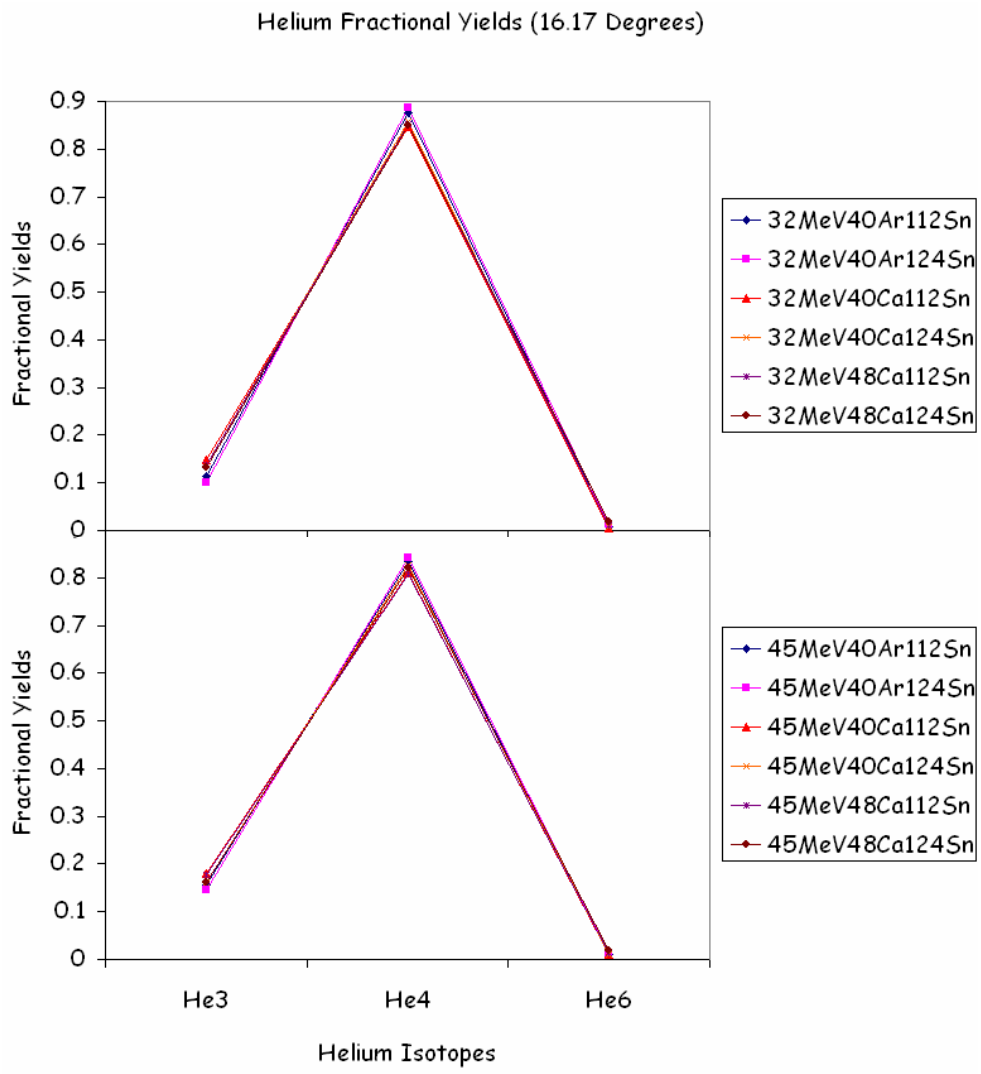


FIG. 114. (Color online) Helium fractional yield ratio plot of the 32 MeV systems (top) and 45 MeV systems (bottom) at 16.17 degrees.

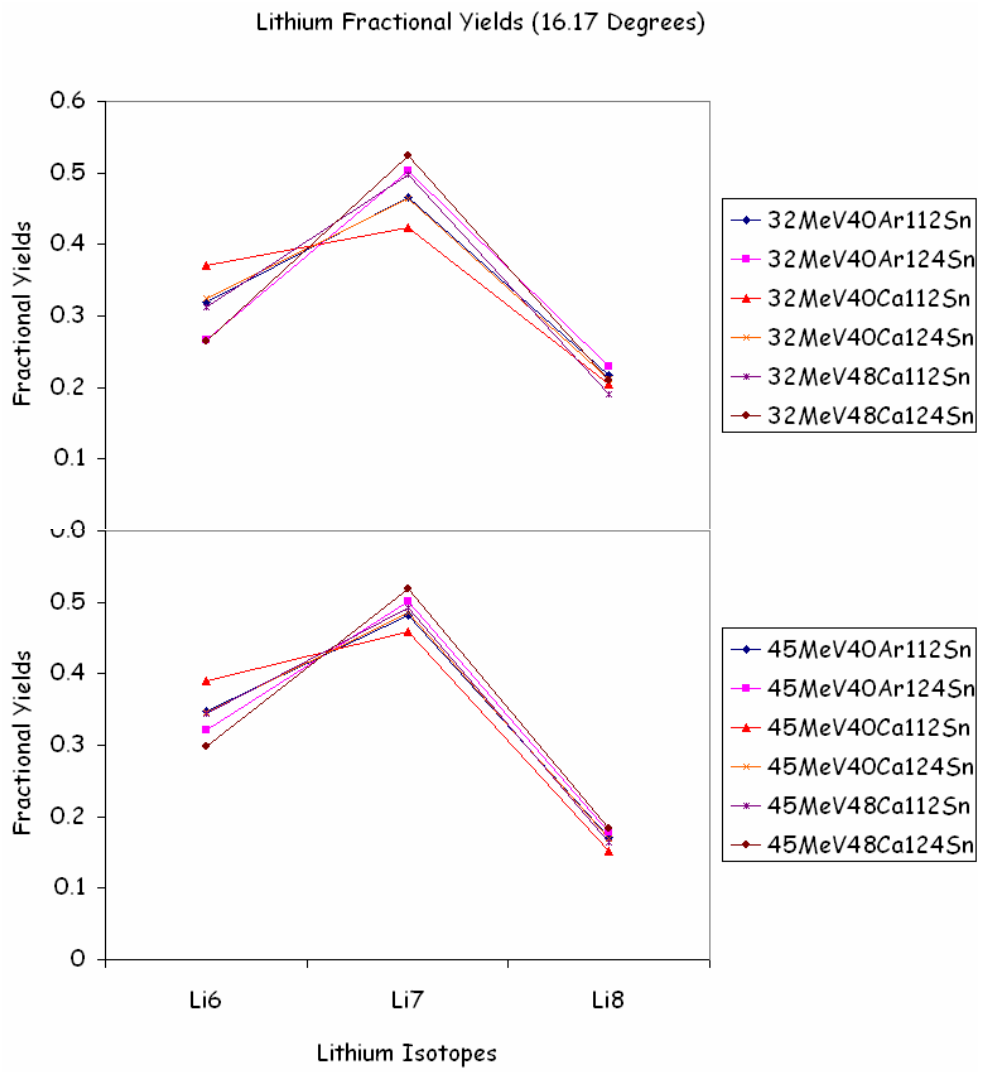


FIG. 115. (Color online) Lithium fractional yield ratio plot of the 32 MeV systems (top) and 45 MeV systems (bottom) at 16.17 degrees.

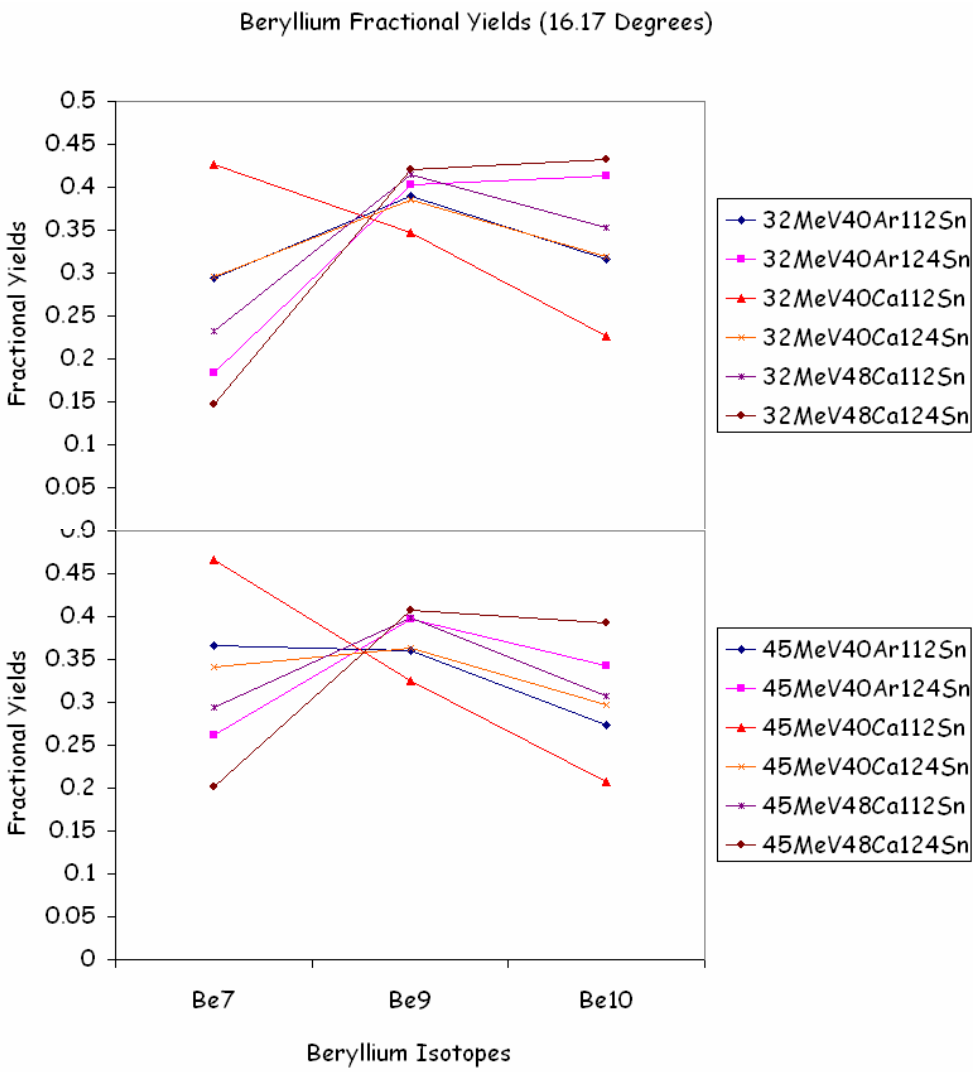


FIG. 116. (Color online) Beryllium fractional yield ratio plot of the 32 MeV systems (top) and 45 MeV systems (bottom) at 16.17 degrees.

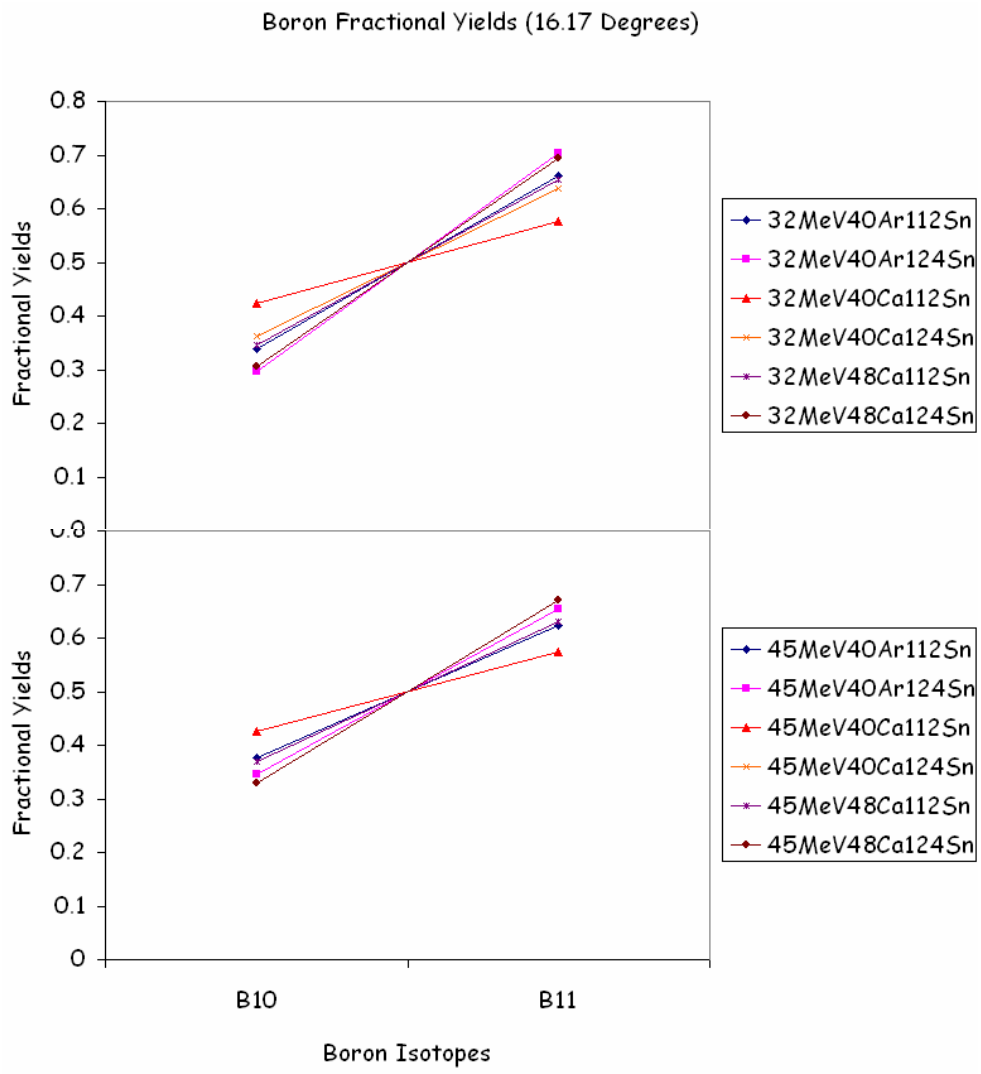


FIG. 117. (Color online) Boron fractional yield ratio plot of the 32 MeV systems (top) and 45 MeV systems (bottom) at 16.17 degrees.

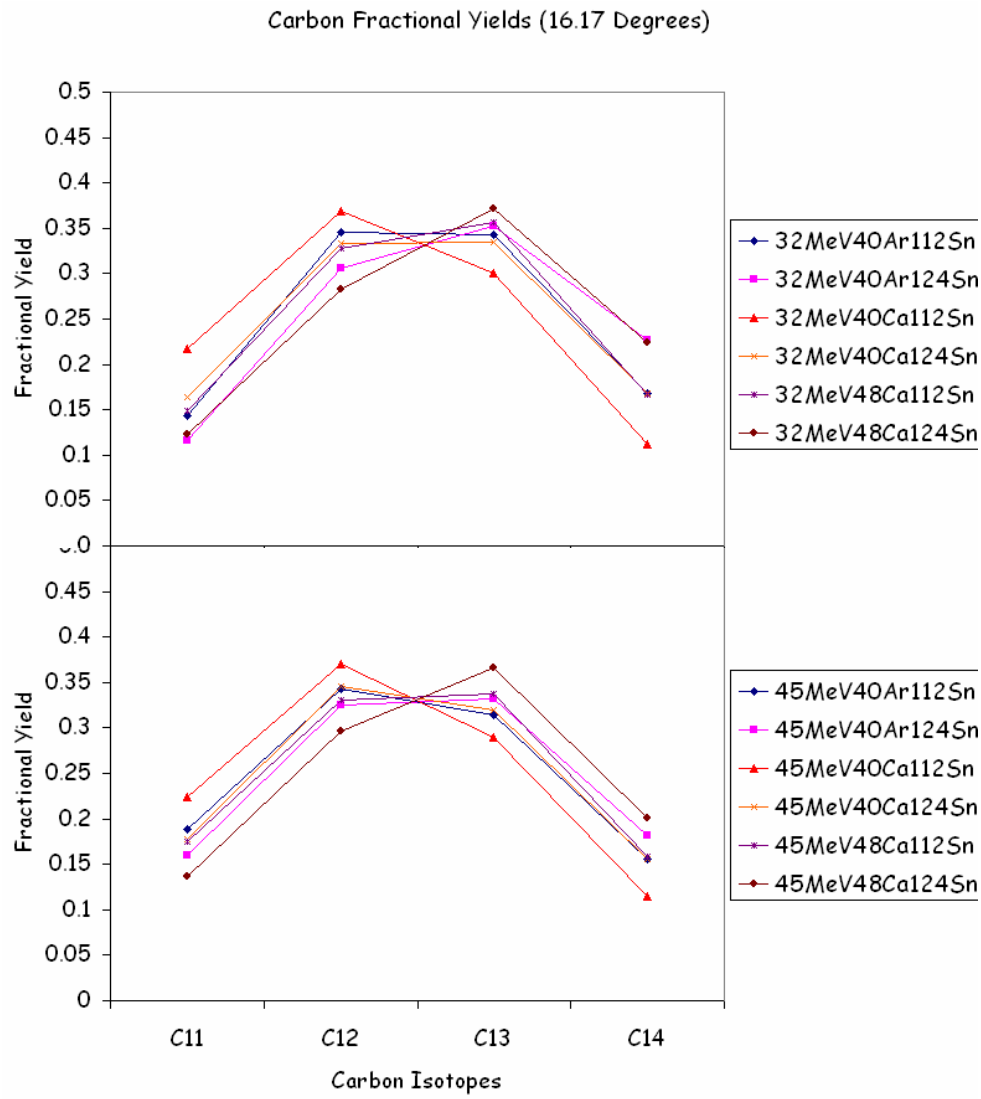


FIG. 118. (Color online) Carbon fractional yield ratio plot of the 32 MeV systems (top) and 45 MeV systems (bottom) at 16.17 degrees.

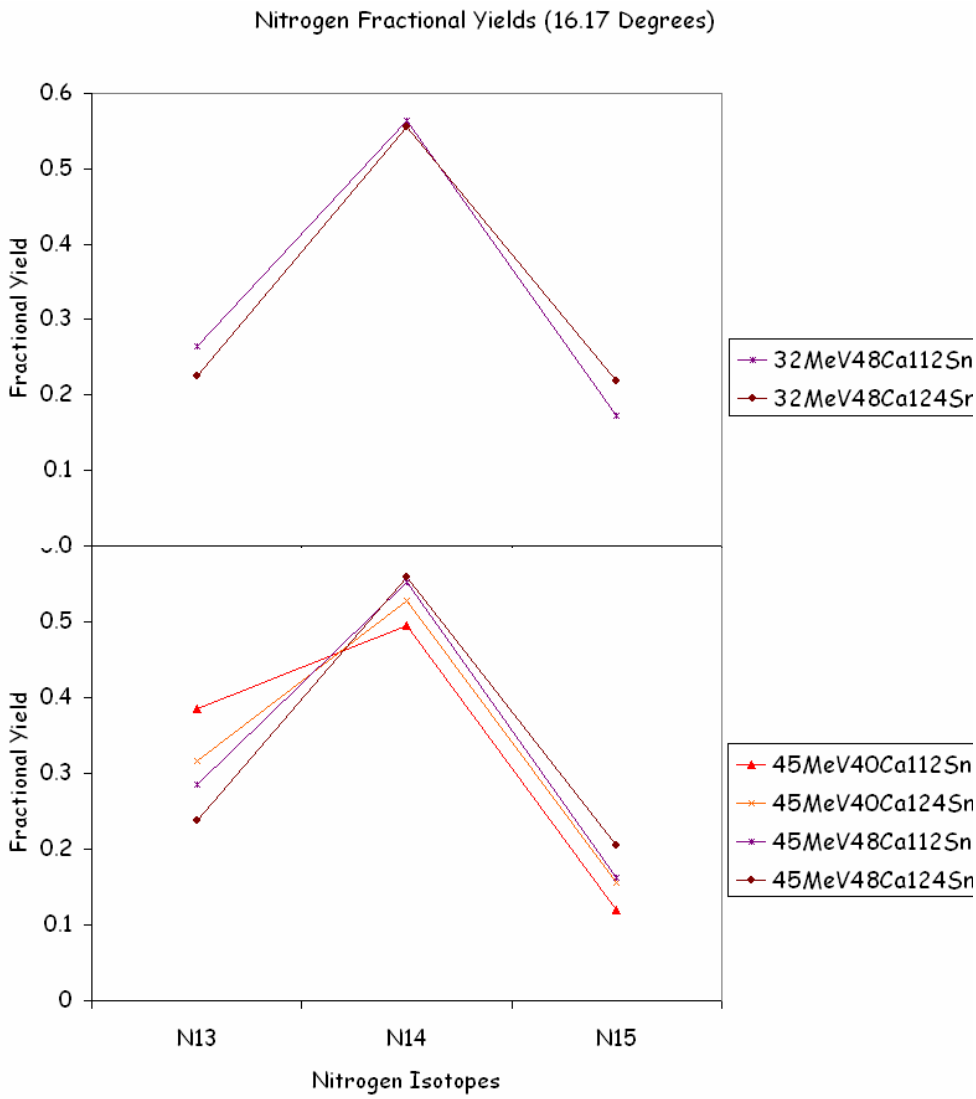


FIG. 119. (Color online) Nitrogen fractional yield ratio plot of the 32 MeV systems (top) and 45 MeV systems (bottom) at 16.17 degrees.

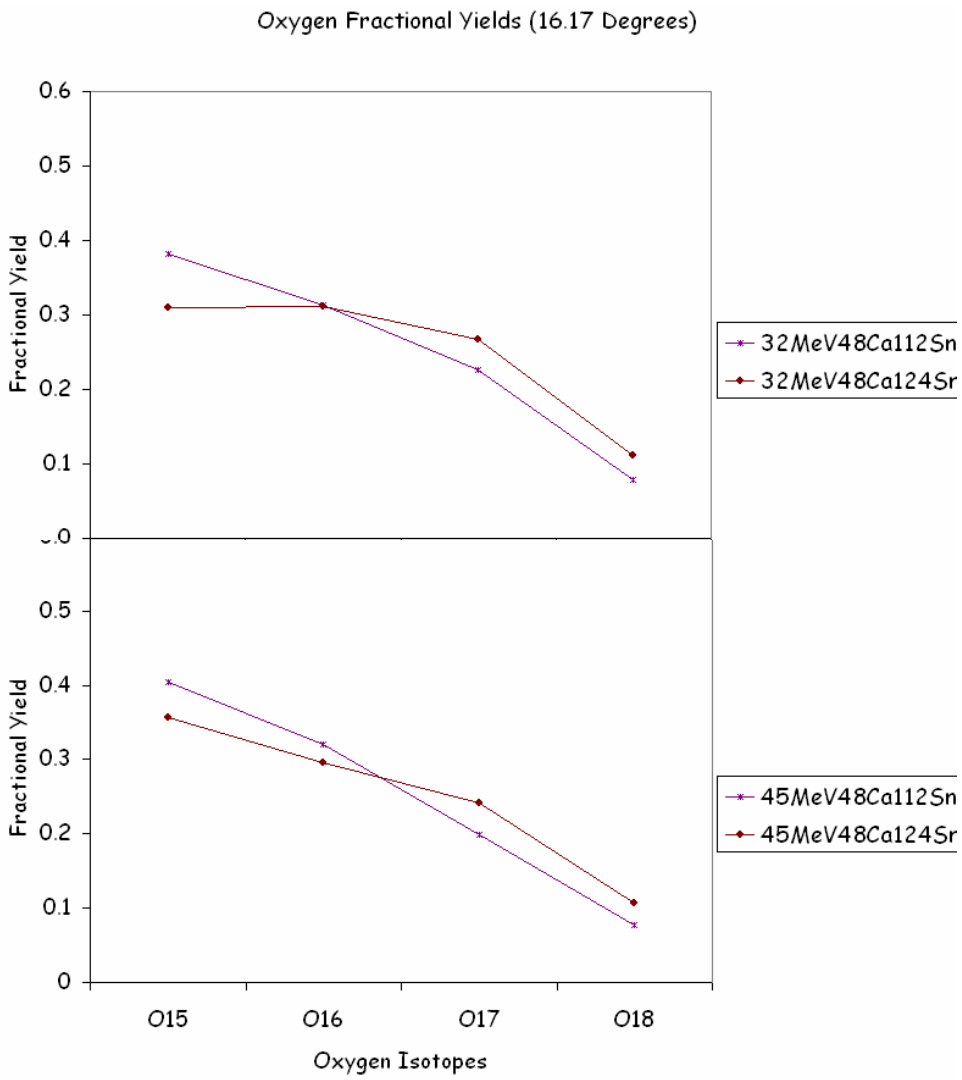


FIG. 120. (Color online) Oxygen fractional yield ratio plot of the 32 MeV systems (top) and 45 MeV systems (bottom) at 16.17 degrees.

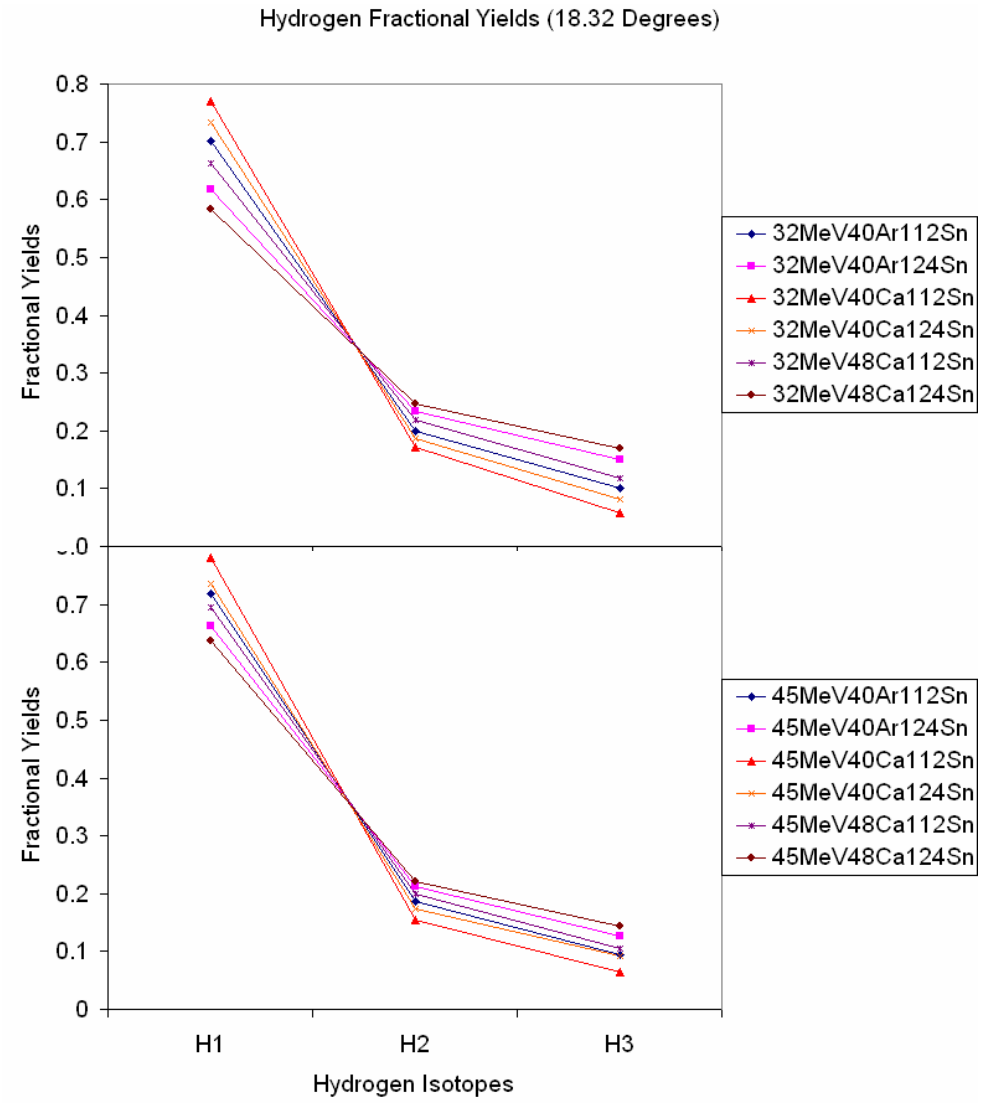


FIG. 121. (Color online) Hydrogen fractional yield ratio plot of the 32 MeV systems (top) and 45 MeV systems (bottom) at 18.32 degrees.

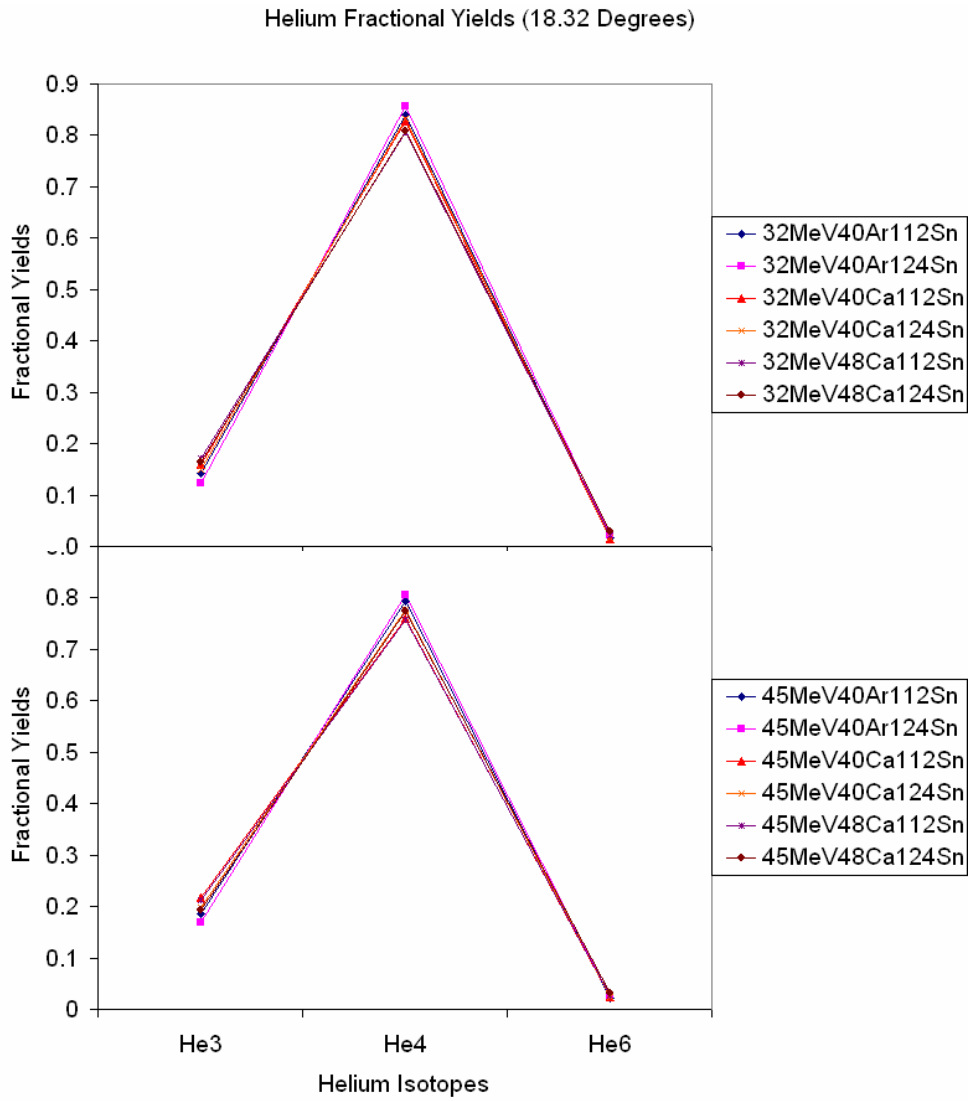


FIG. 122. (Color online) Helium fractional yield ratio plot of the 32 MeV systems (top) and 45 MeV systems (bottom) at 18.32 degrees.

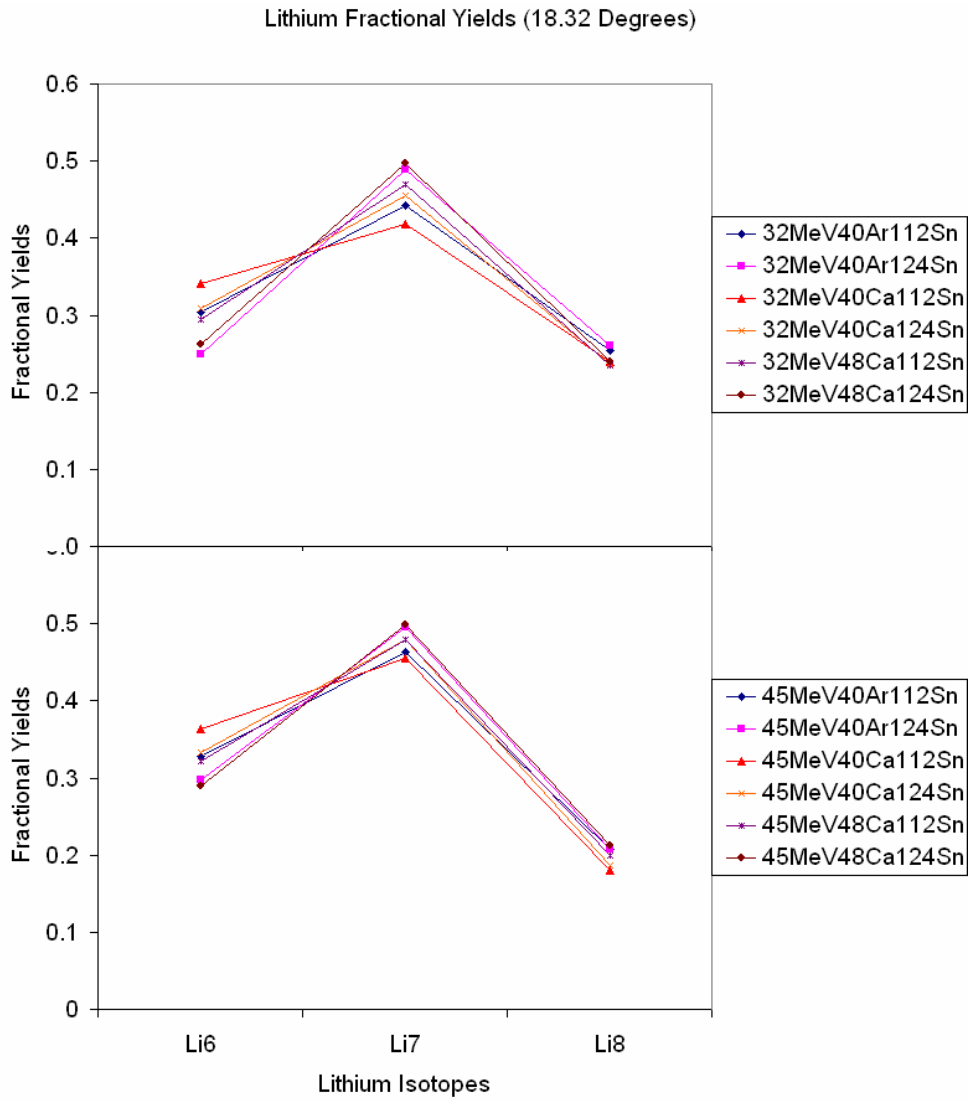


FIG. 123. (Color online) Lithium fractional yield ratio plot of the 32 MeV systems (top) and 45 MeV systems (bottom) at 18.32 degrees.

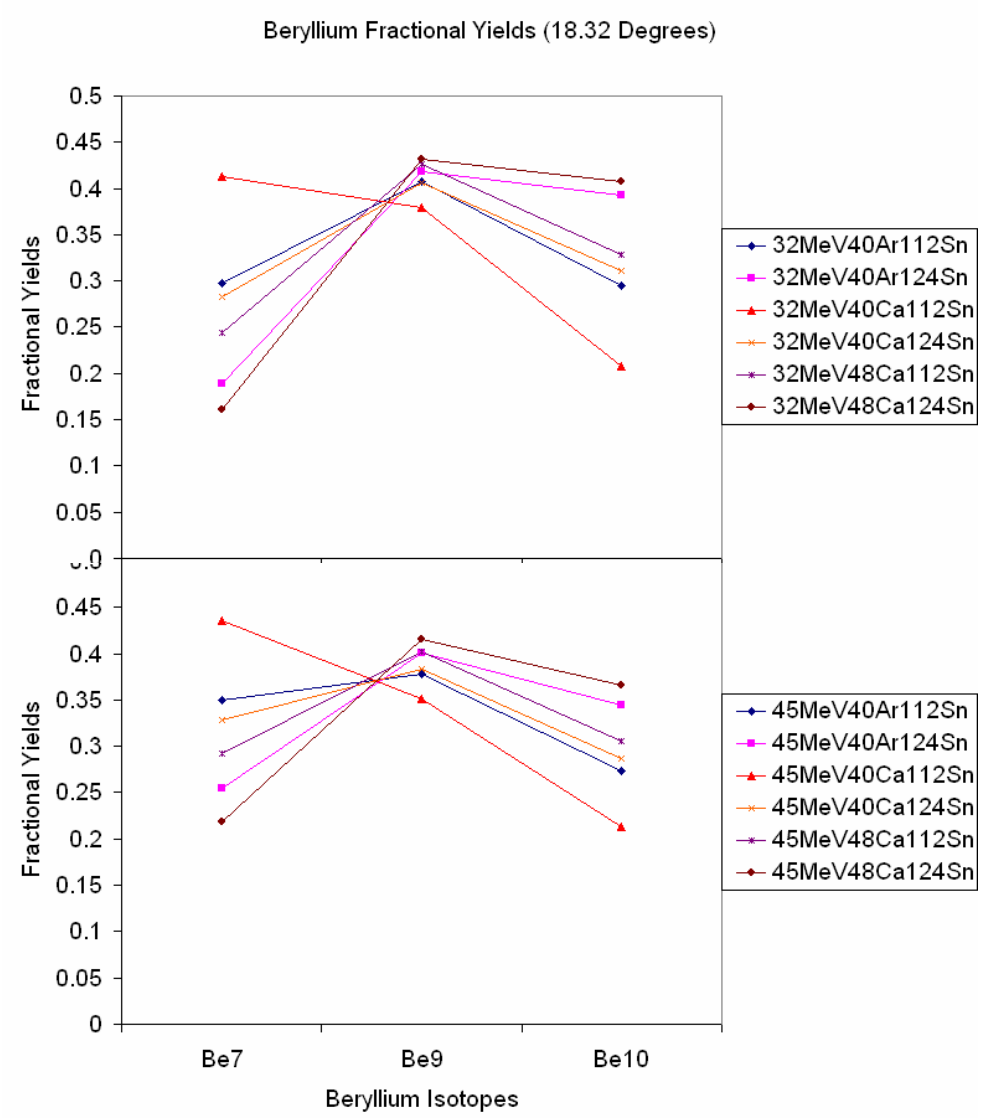


FIG. 124. (Color online) Beryllium fractional yield ratio plot of the 32 MeV systems (top) and 45 MeV systems (bottom) at 18.32 degrees.

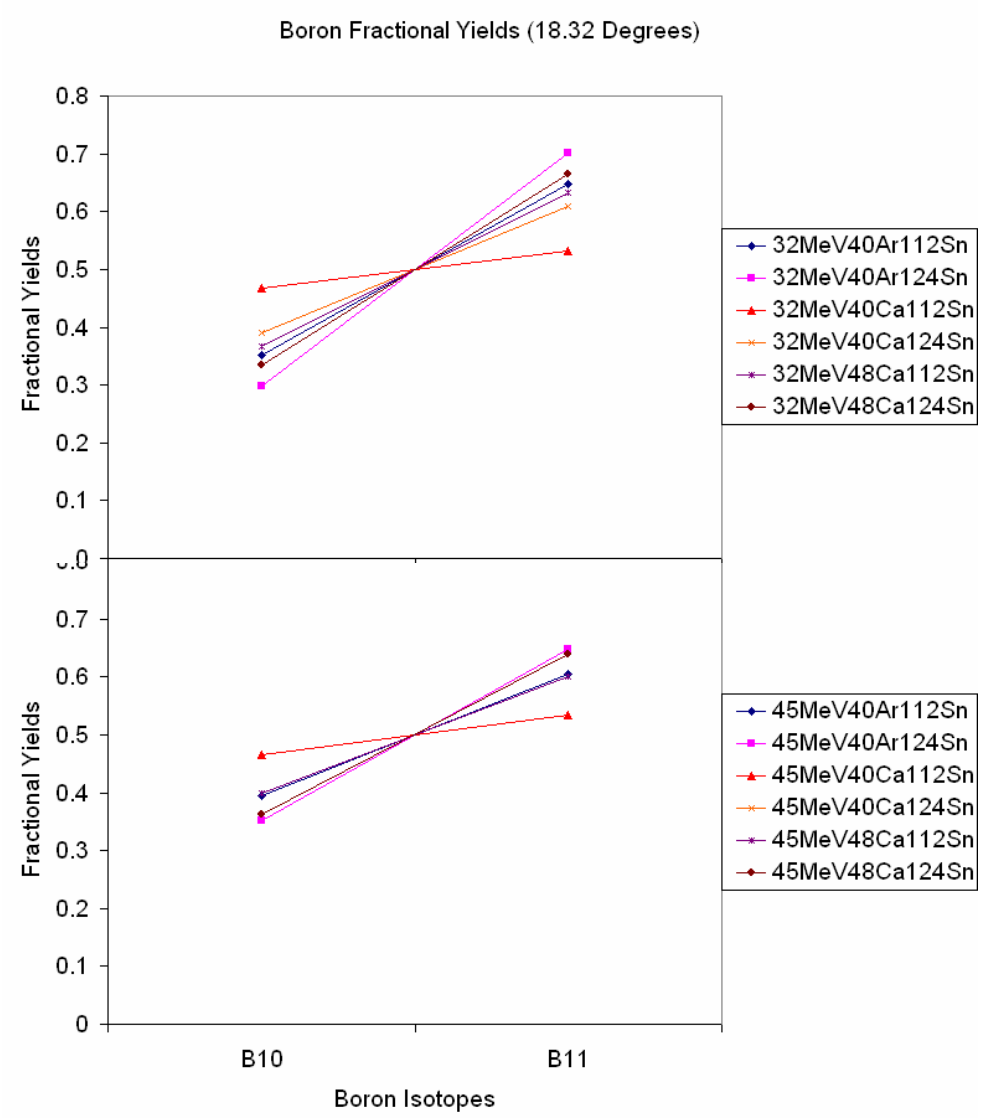


FIG. 125. (Color online) Boron fractional yield ratio plot of the 32 MeV systems (top) and 45 MeV systems (bottom) at 18.32 degrees.

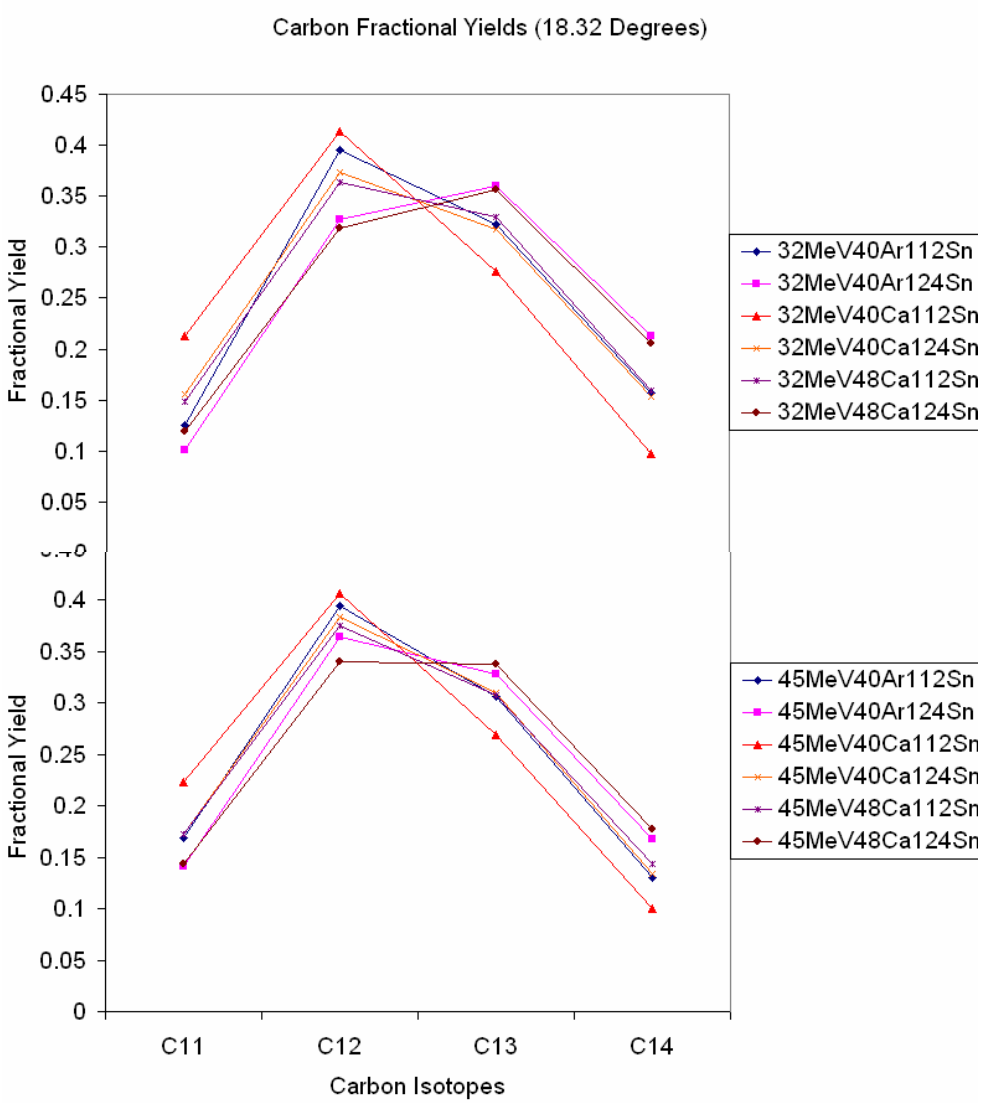


FIG. 126. (Color online) Carbon fractional yield ratio plot of the 32 MeV systems (top) and 45 MeV systems (bottom) at 18.32 degrees.

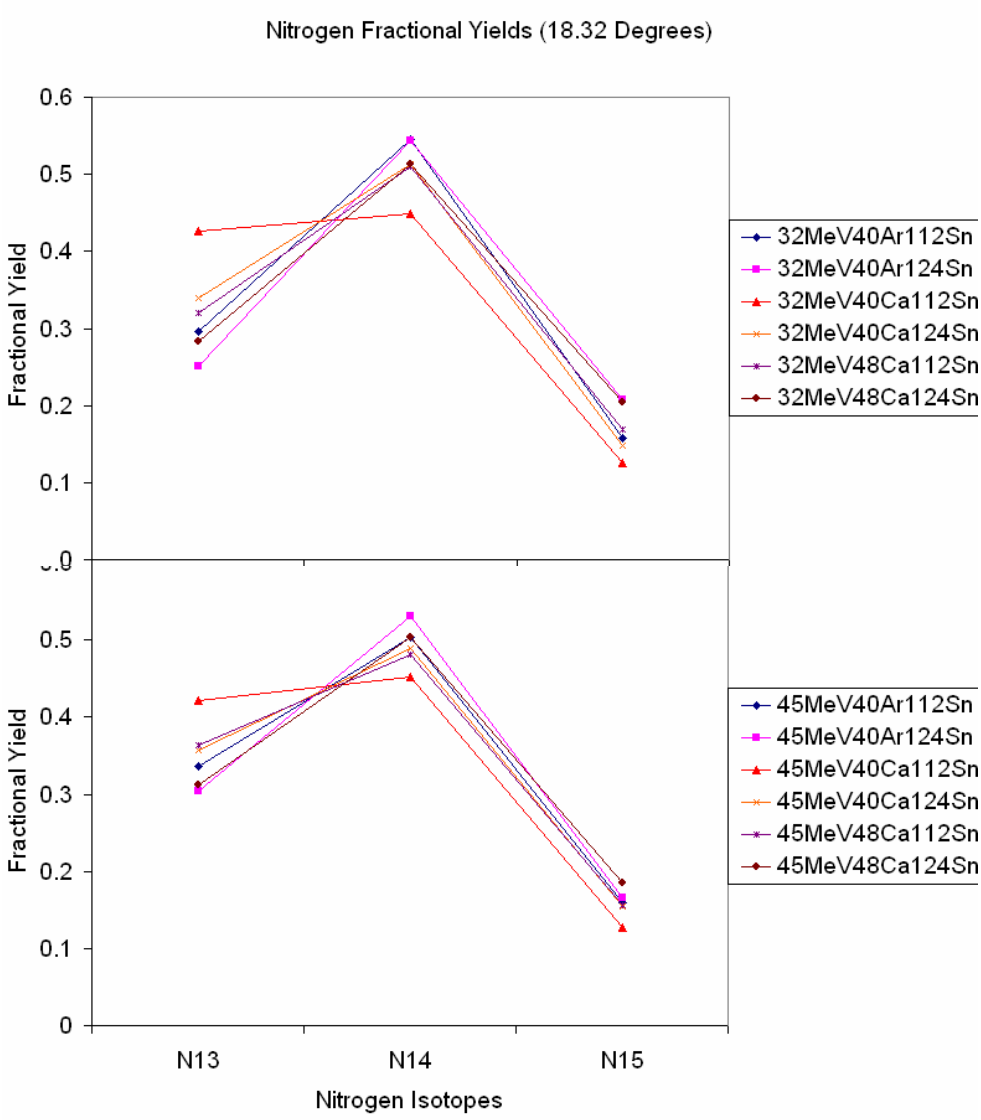


FIG. 127. (Color online) Nitrogen fractional yield ratio plot of the 32 MeV systems (top) and 45 MeV systems (bottom) at 18.32 degrees.

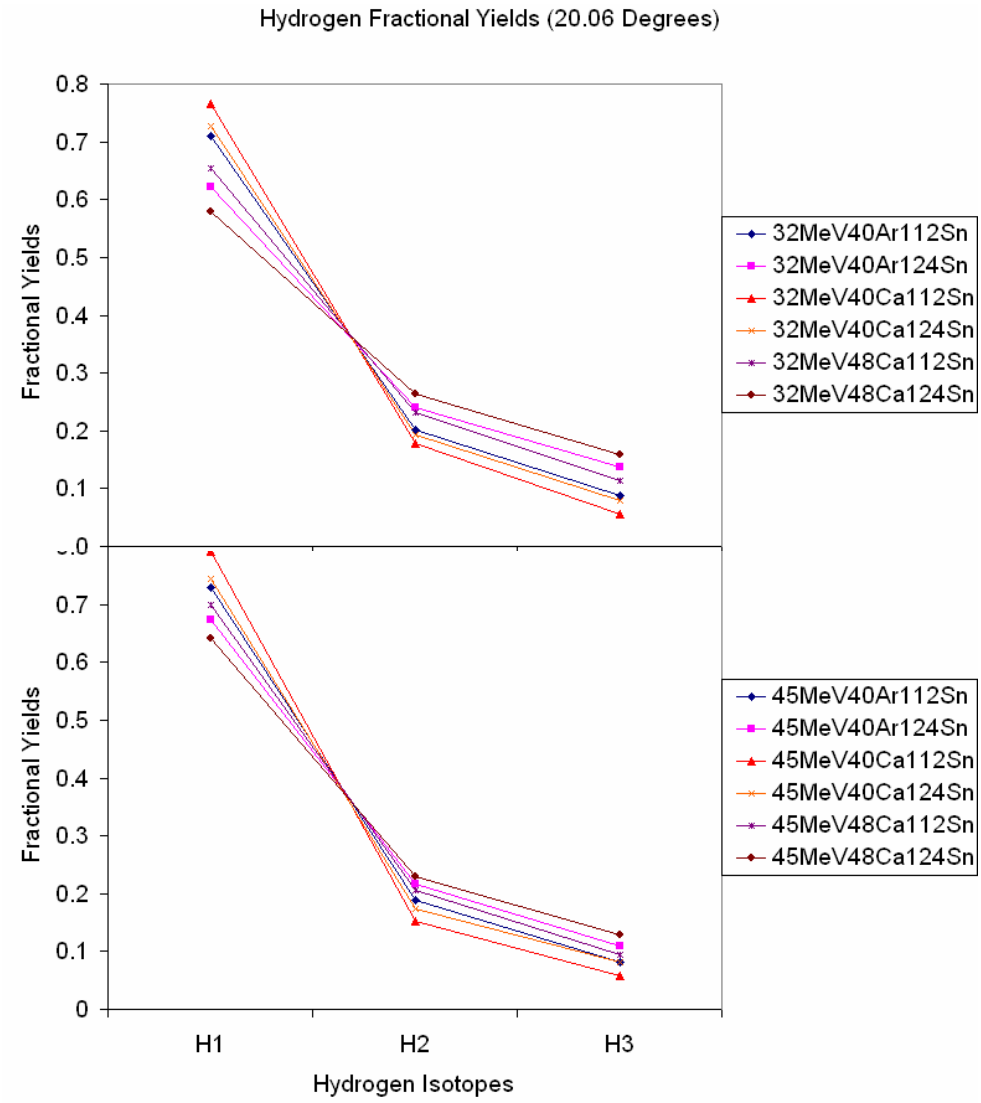


FIG. 128. (Color online) Hydrogen fractional yield ratio plot of the 32 MeV systems (top) and 45 MeV systems (bottom) at 20.06 degrees.

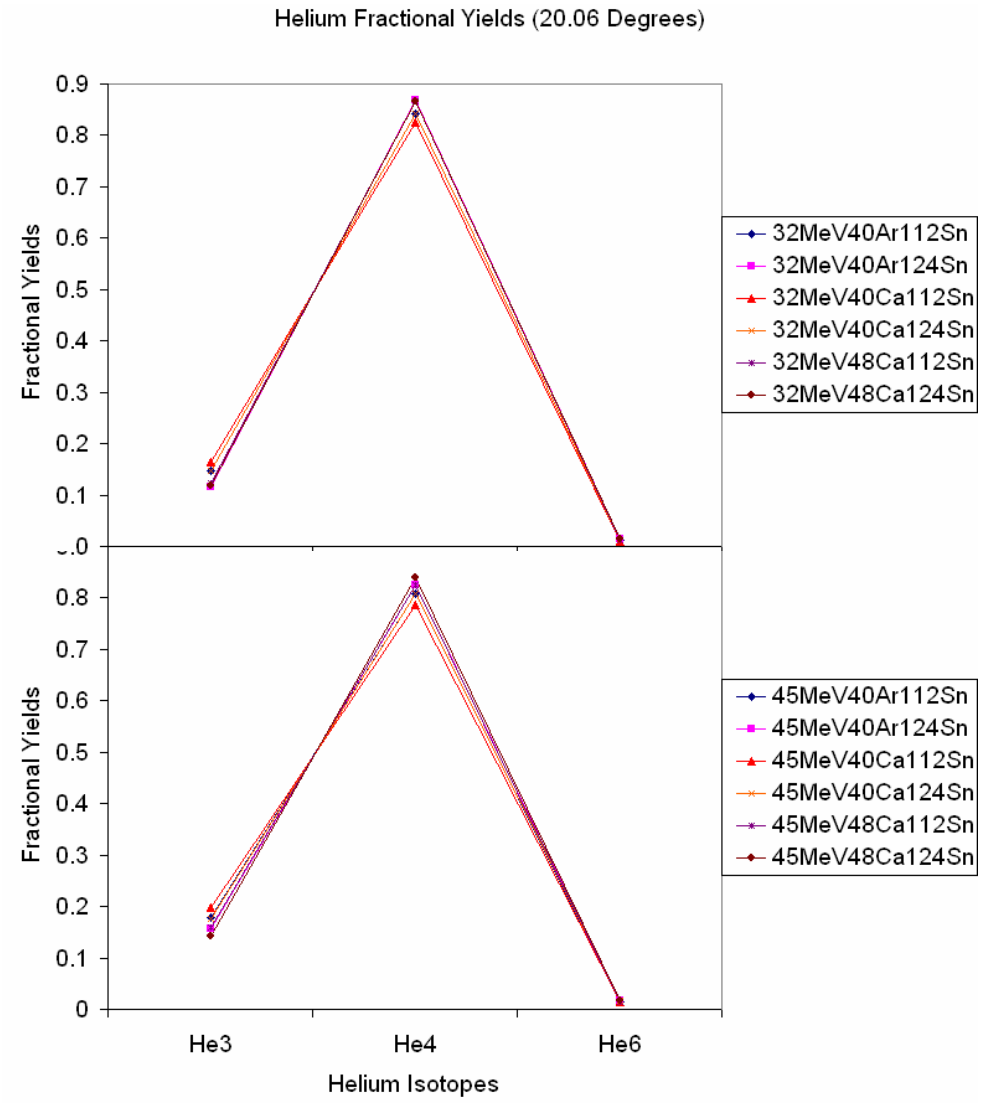


FIG. 129. (Color online) Helium fractional yield ratio plot of the 32 MeV systems (top) and 45 MeV systems (bottom) at 20.06 degrees.

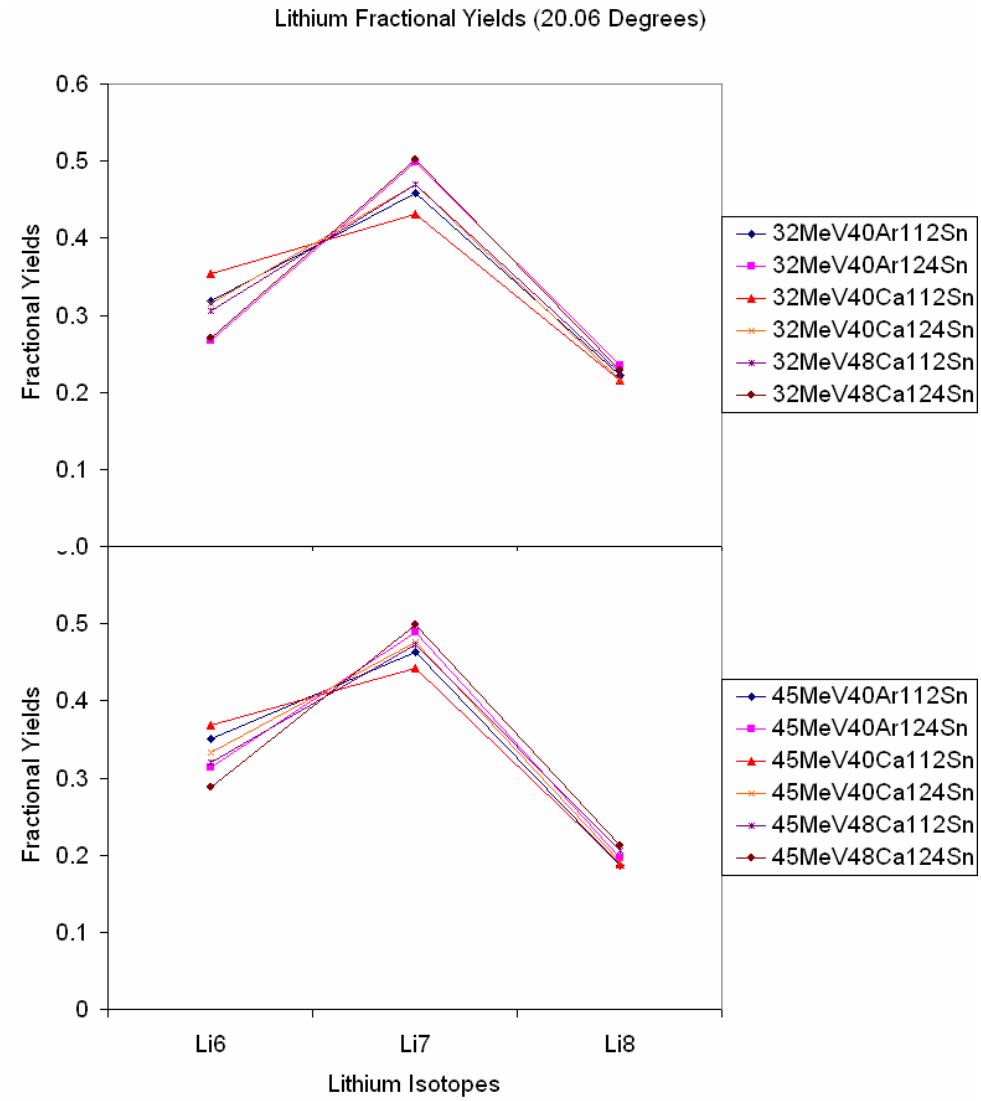


FIG. 130. (Color online) Lithium fractional yield ratio plot of the 32 MeV systems (top) and 45 MeV systems (bottom) at 20.06 degrees.

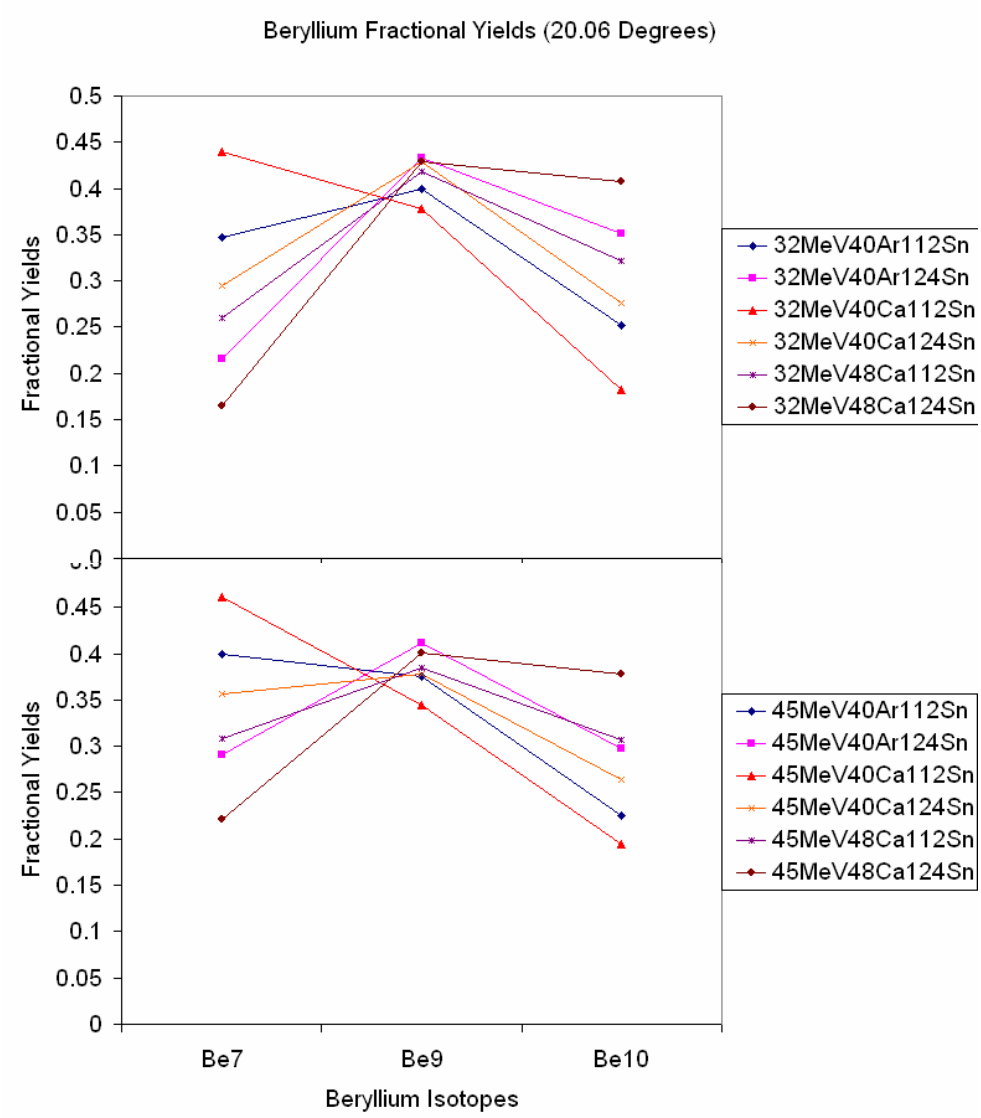


FIG. 131. (Color online) Beryllium fractional yield ratio plot of the 32 MeV systems (top) and 45 MeV systems (bottom) at 20.06 degrees.

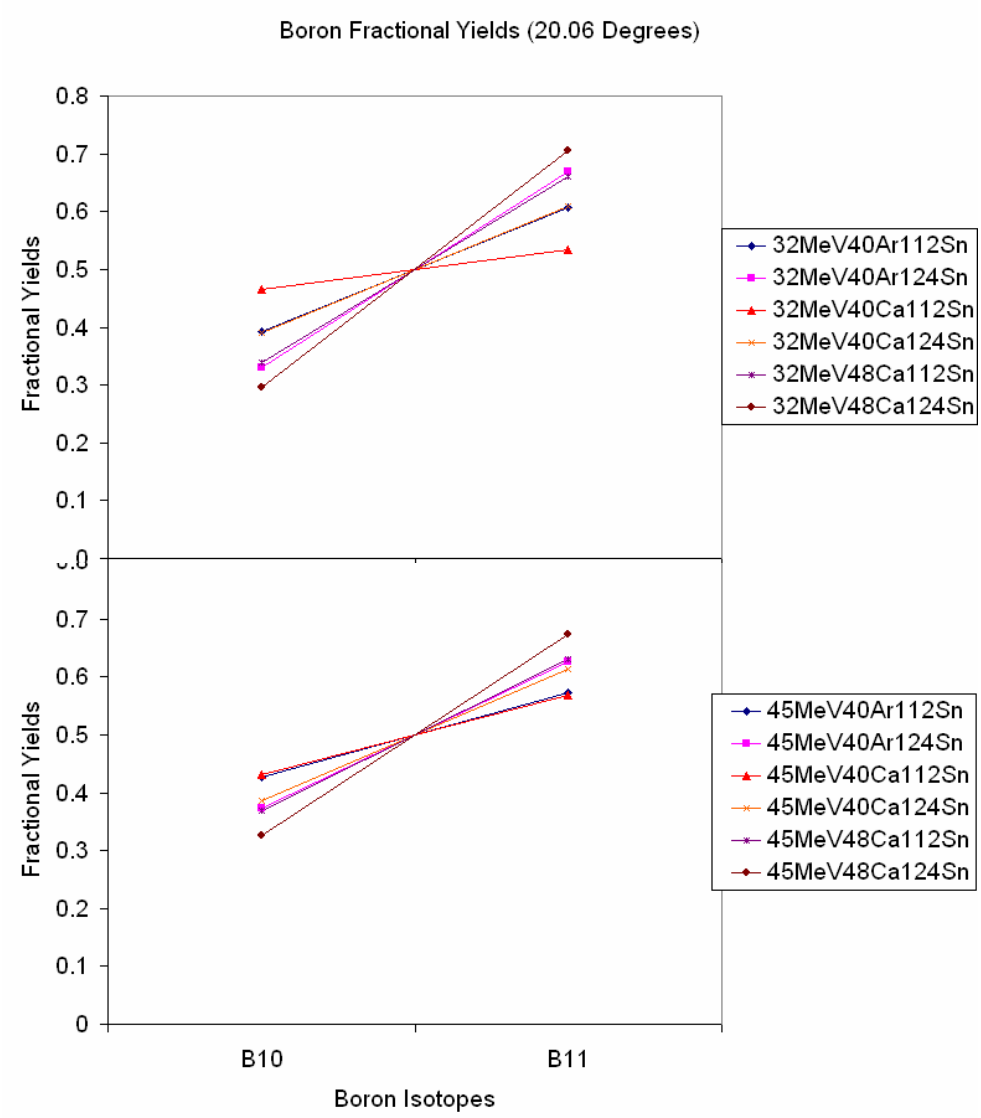


FIG. 132. (Color online) Boron fractional yield ratio plot of the 32 MeV systems (top) and 45 MeV systems (bottom) at 20.06 degrees.

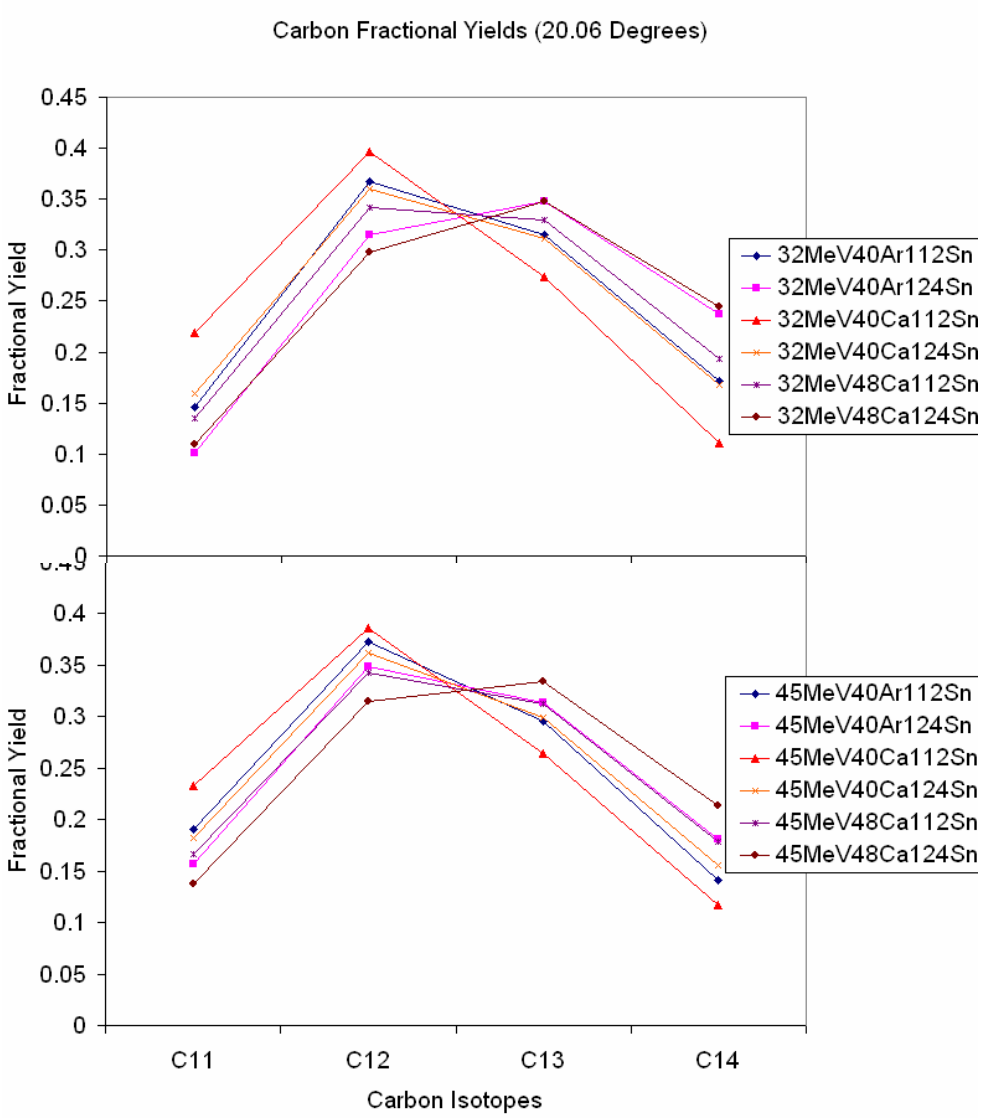


FIG. 133. (Color online) Carbon fractional yield ratio plot of the 32 MeV systems (top) and 45 MeV systems (bottom) at 20.06 degrees.

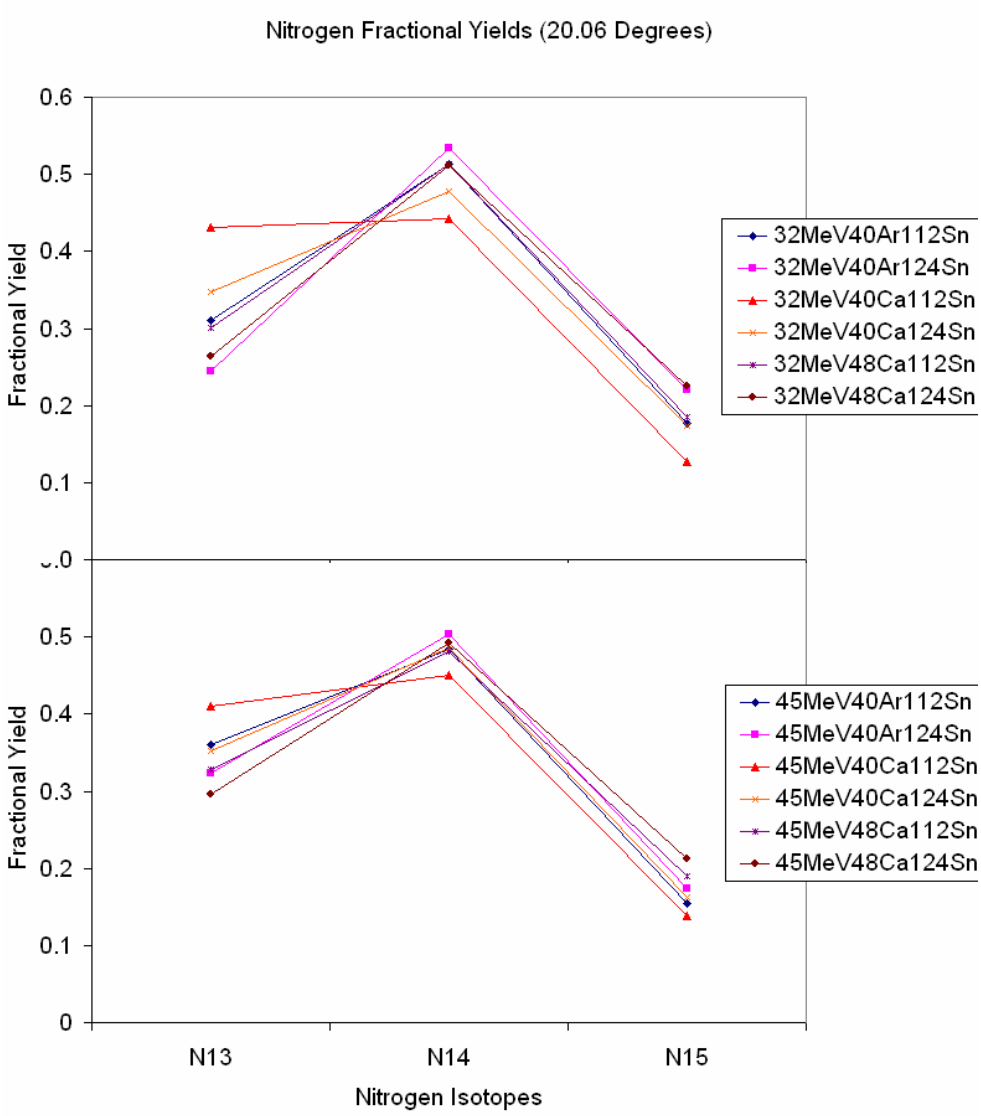


FIG. 134. (Color online) Nitrogen fractional yield ratio plot of the 32 MeV systems (top) and 45 MeV systems (bottom) at 20.06 degrees.

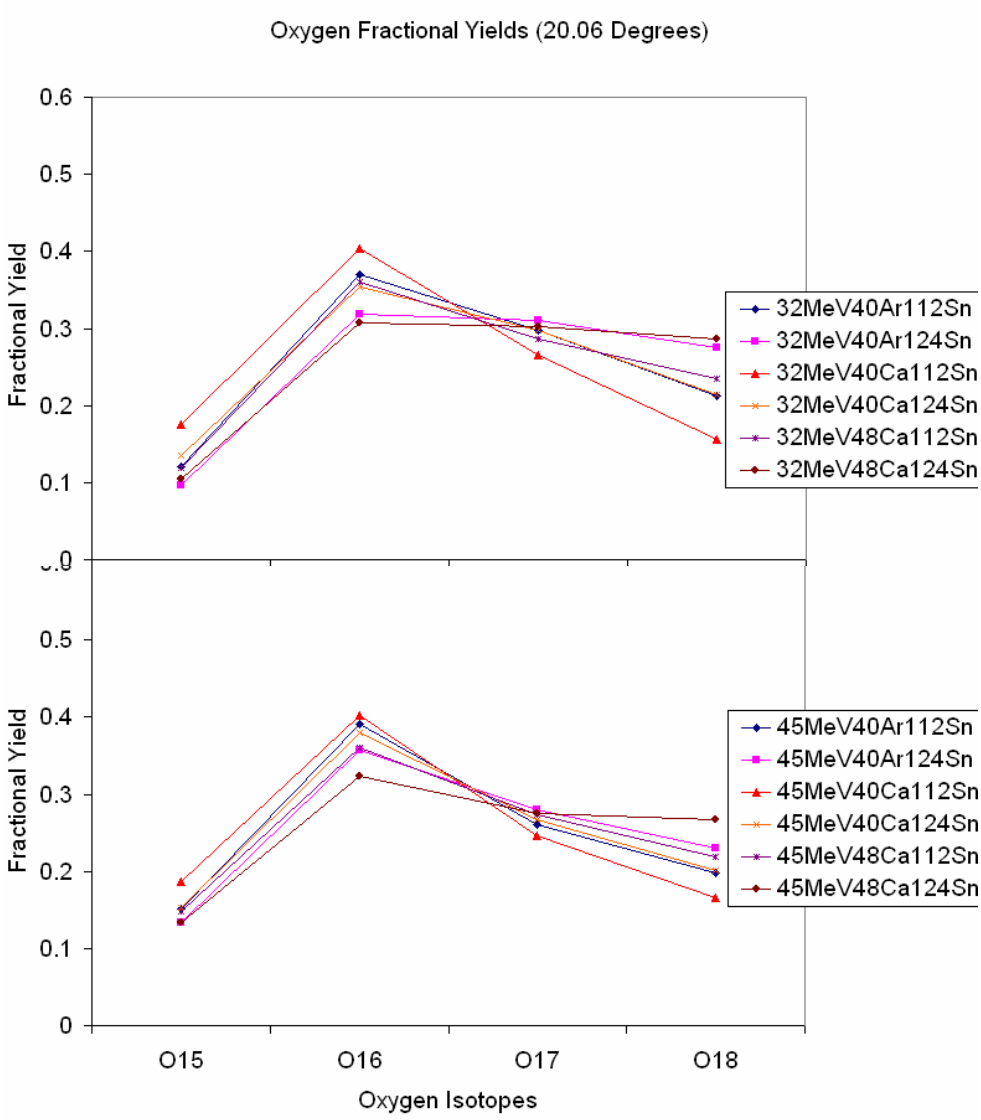


FIG. 135. (Color online) Oxygen fractional yield ratio plot of the 32 MeV systems (top) and 45 MeV systems (bottom) at 20.06 degrees.

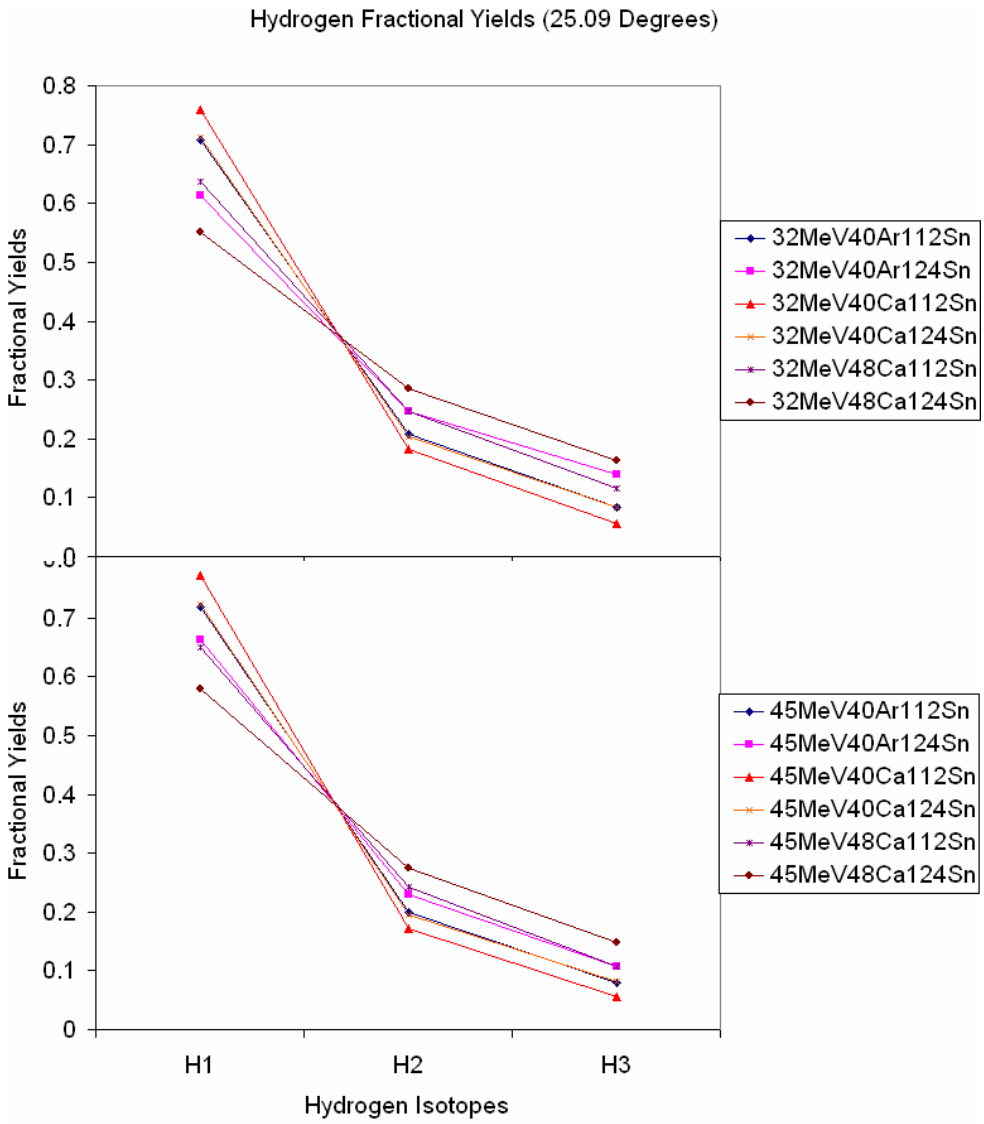


FIG. 136. (Color online) Hydrogen fractional yield ratio plot of the 32 MeV systems (top) and 45 MeV systems (bottom) at 25.09 degrees.

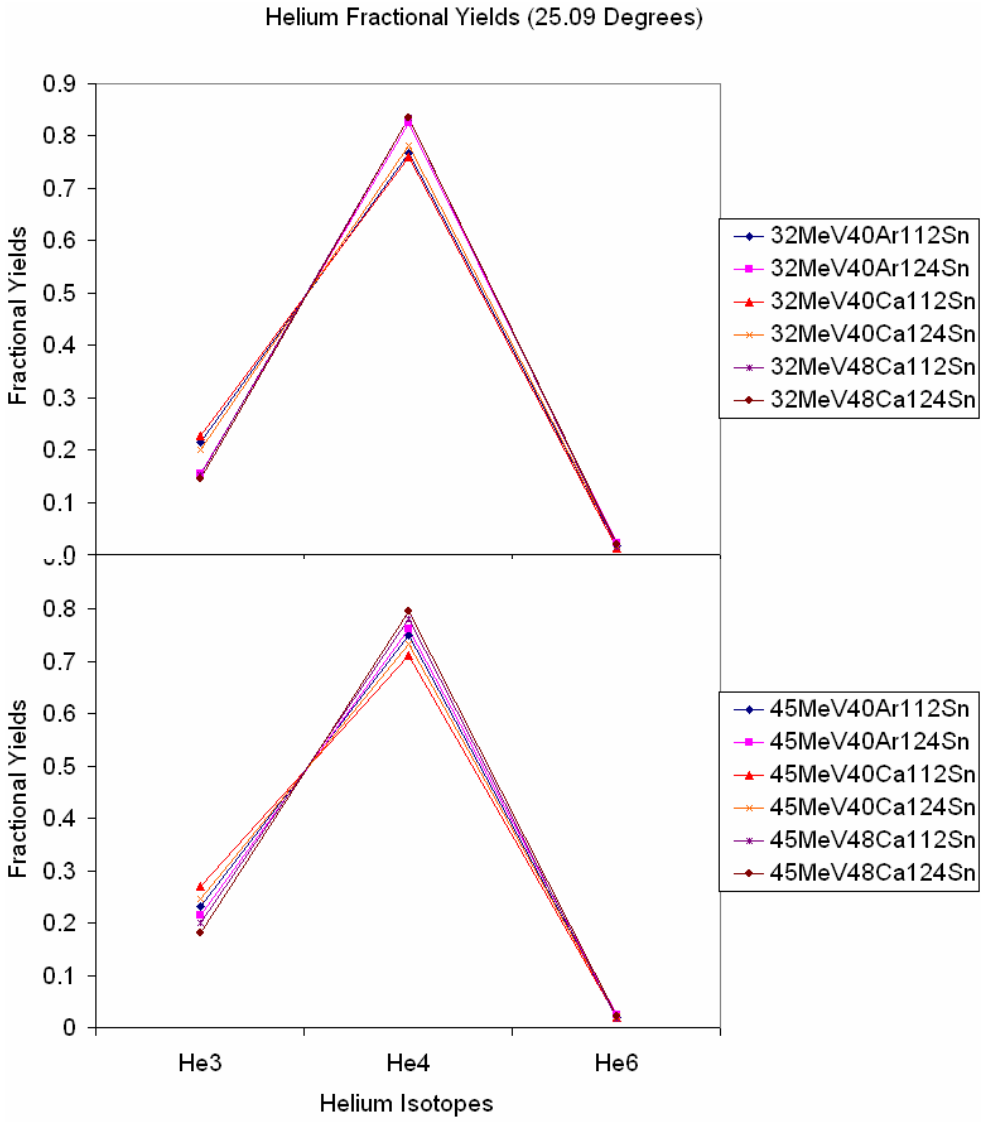


FIG. 137. (Color online) Helium fractional yield ratio plot of the 32 MeV systems (top) and 45 MeV systems (bottom) at 25.09 degrees.

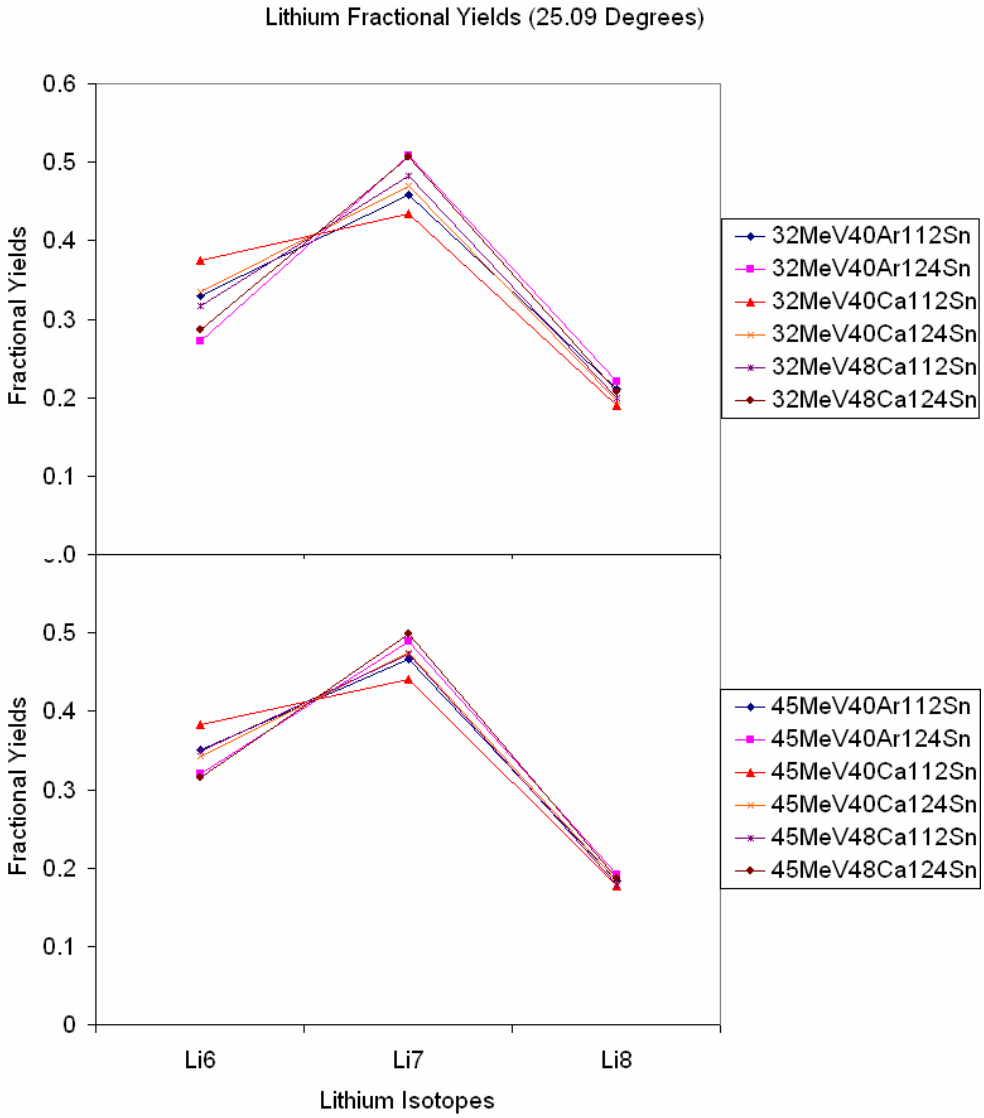


FIG. 138. (Color online) Lithium fractional yield ratio plot of the 32 MeV systems (top) and 45 MeV systems (bottom) at 25.09 degrees.

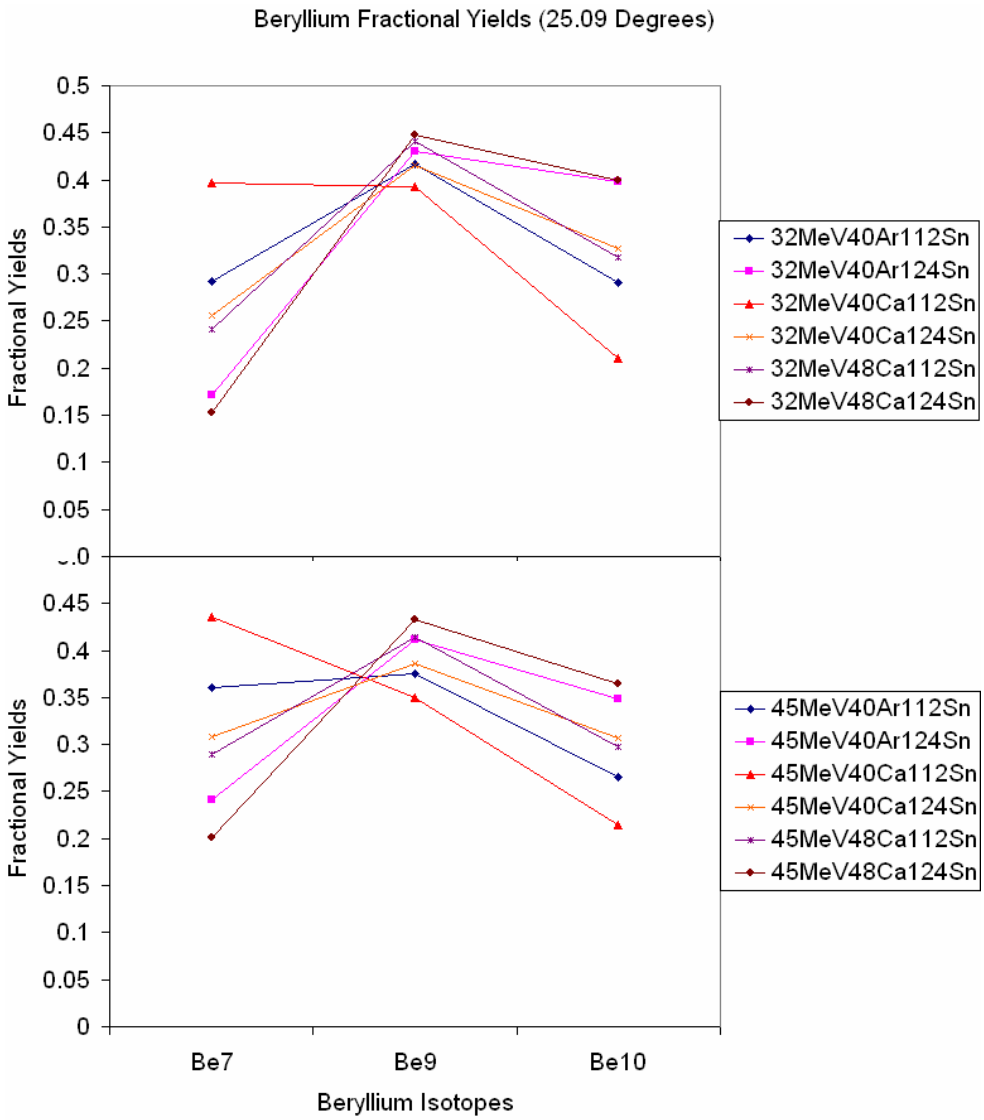


FIG. 139. (Color online) Beryllium fractional yield ratio plot of the 32 MeV systems (top) and 45 MeV systems (bottom) at 25.09 degrees.

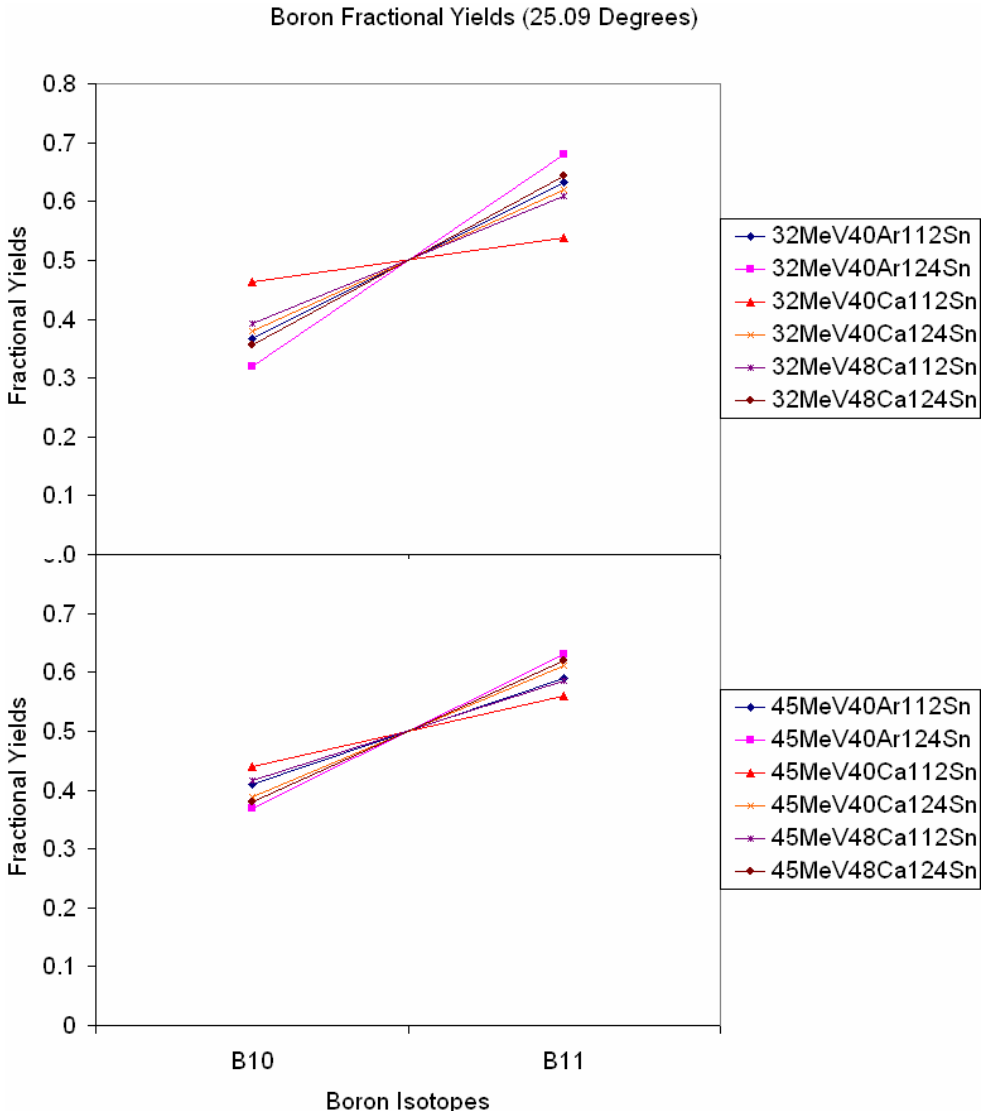


FIG. 140. (Color online) Boron fractional yield ratio plot of the 32 MeV systems (top) and 45 MeV systems (bottom) at 25.09 degrees.

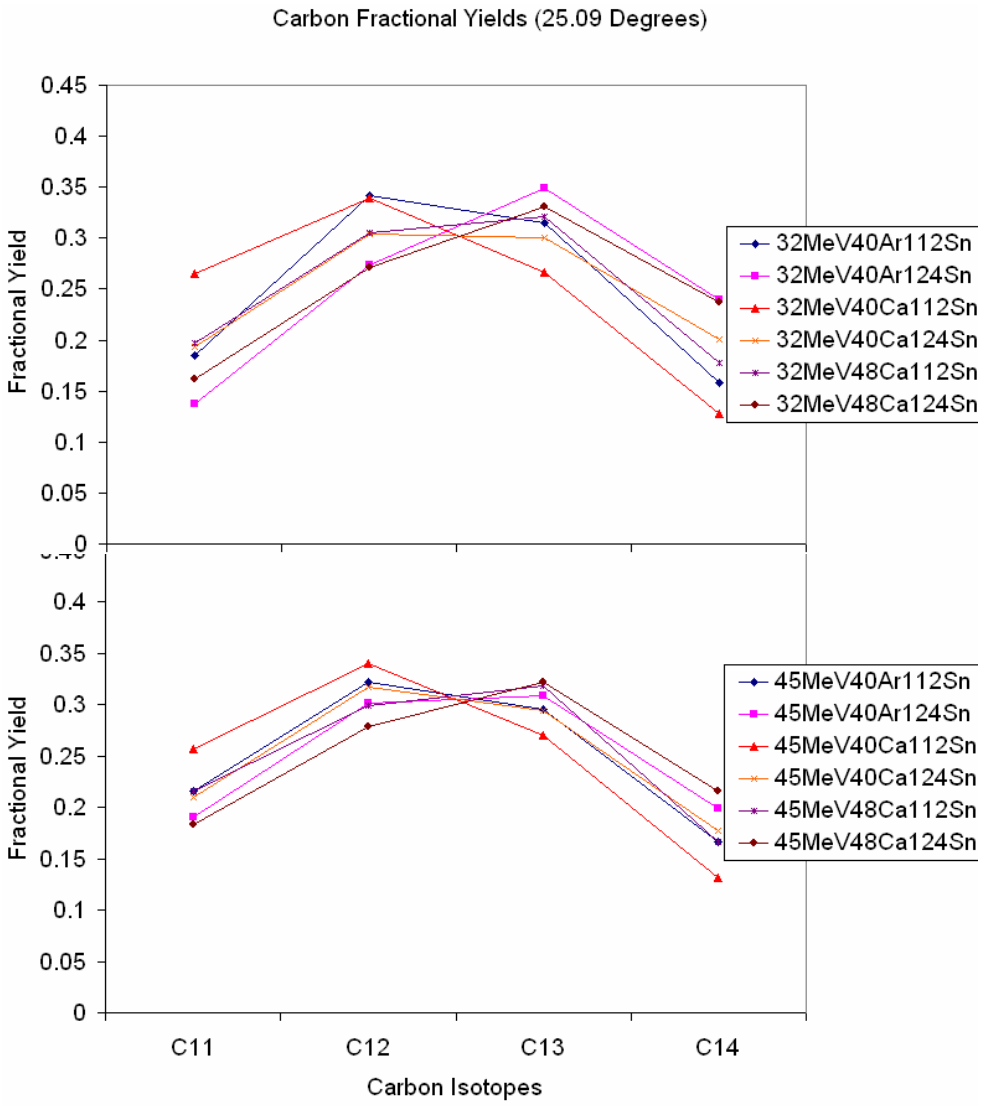


FIG. 141. (Color online) Carbon fractional yield ratio plot of the 32 MeV systems (top) and 45 MeV systems (bottom) at 25.09 degrees.

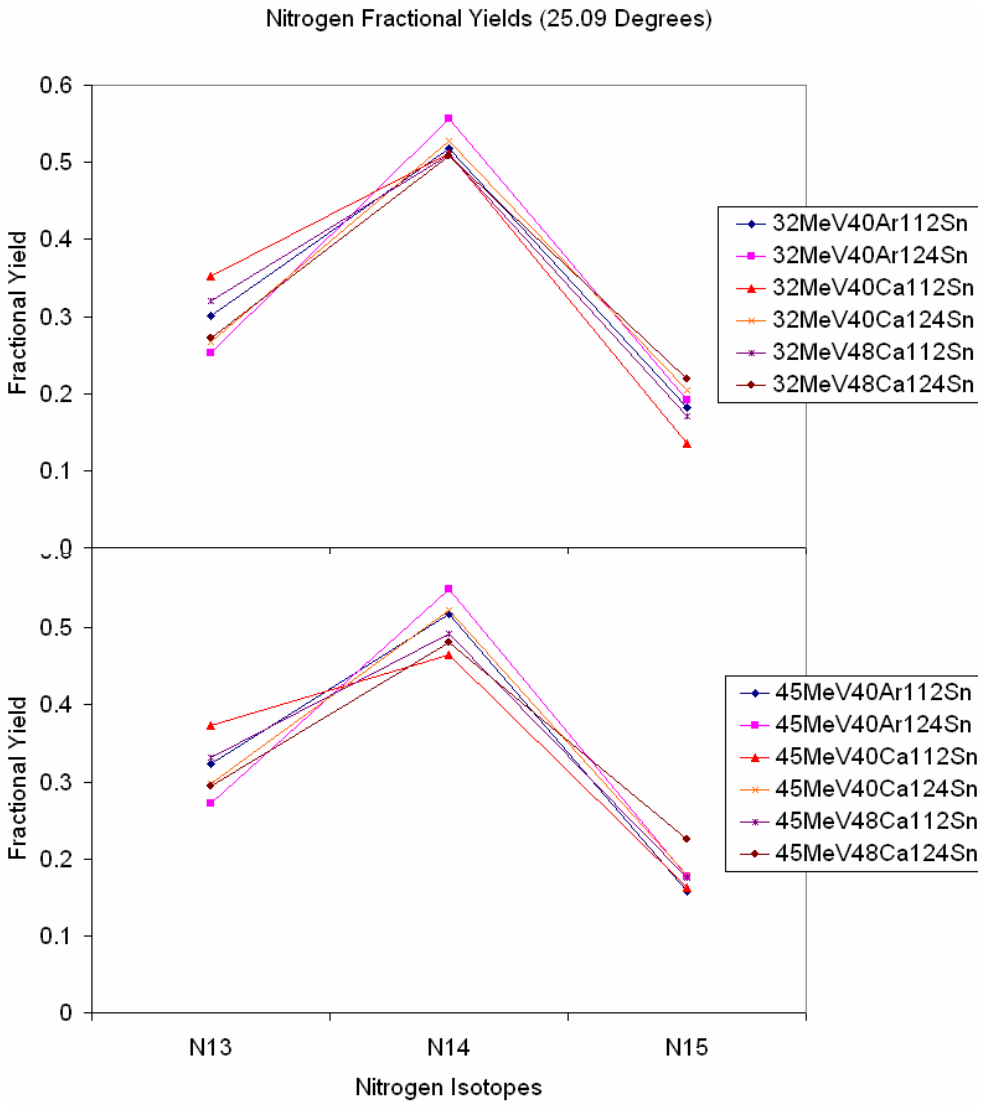


FIG. 142. (Color online) Nitrogen fractional yield ratio plot of the 32 MeV systems (top) and 45 MeV systems (bottom) at 25.09 degrees.

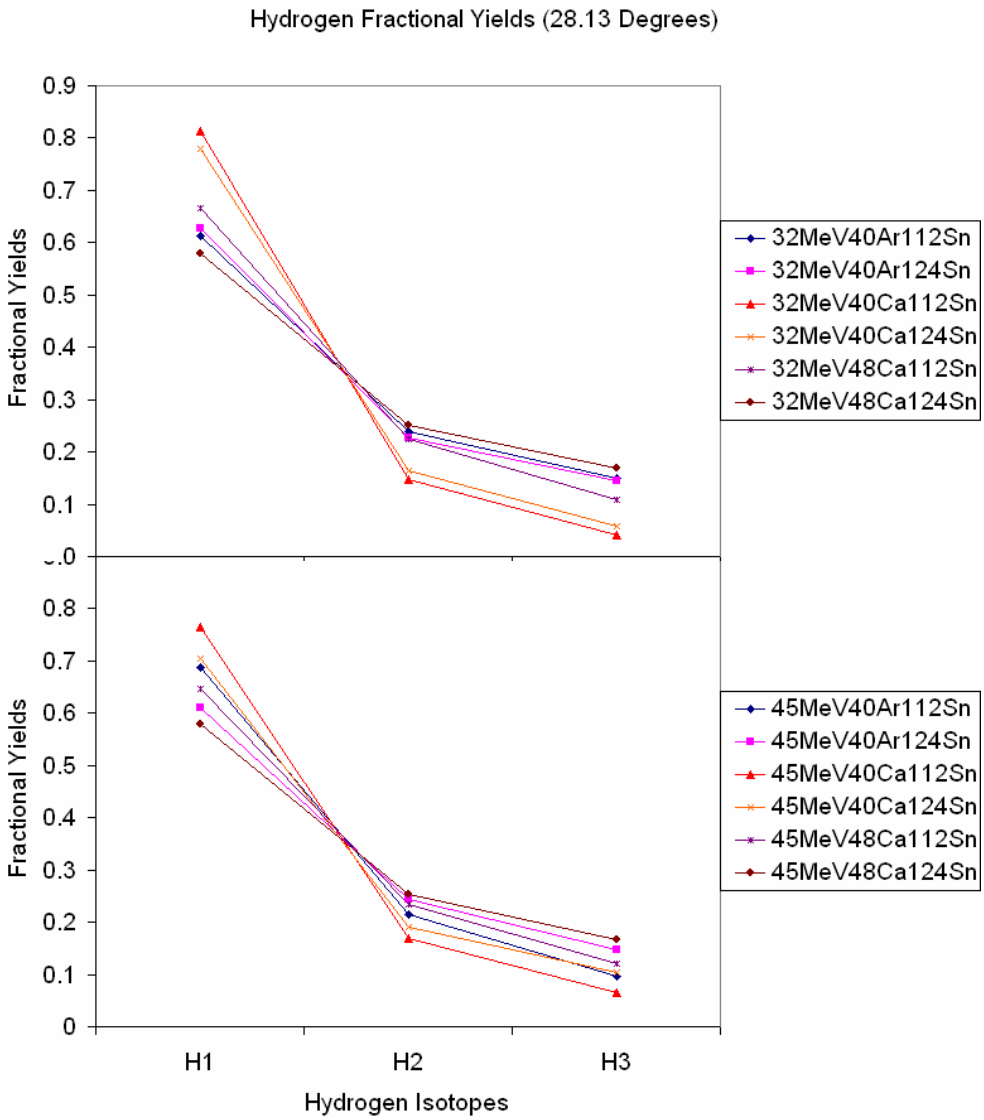


FIG. 143. (Color online) Hydrogen fractional yield ratio plot of the 32 MeV systems (top) and 45 MeV systems (bottom) at 28.13 degrees.

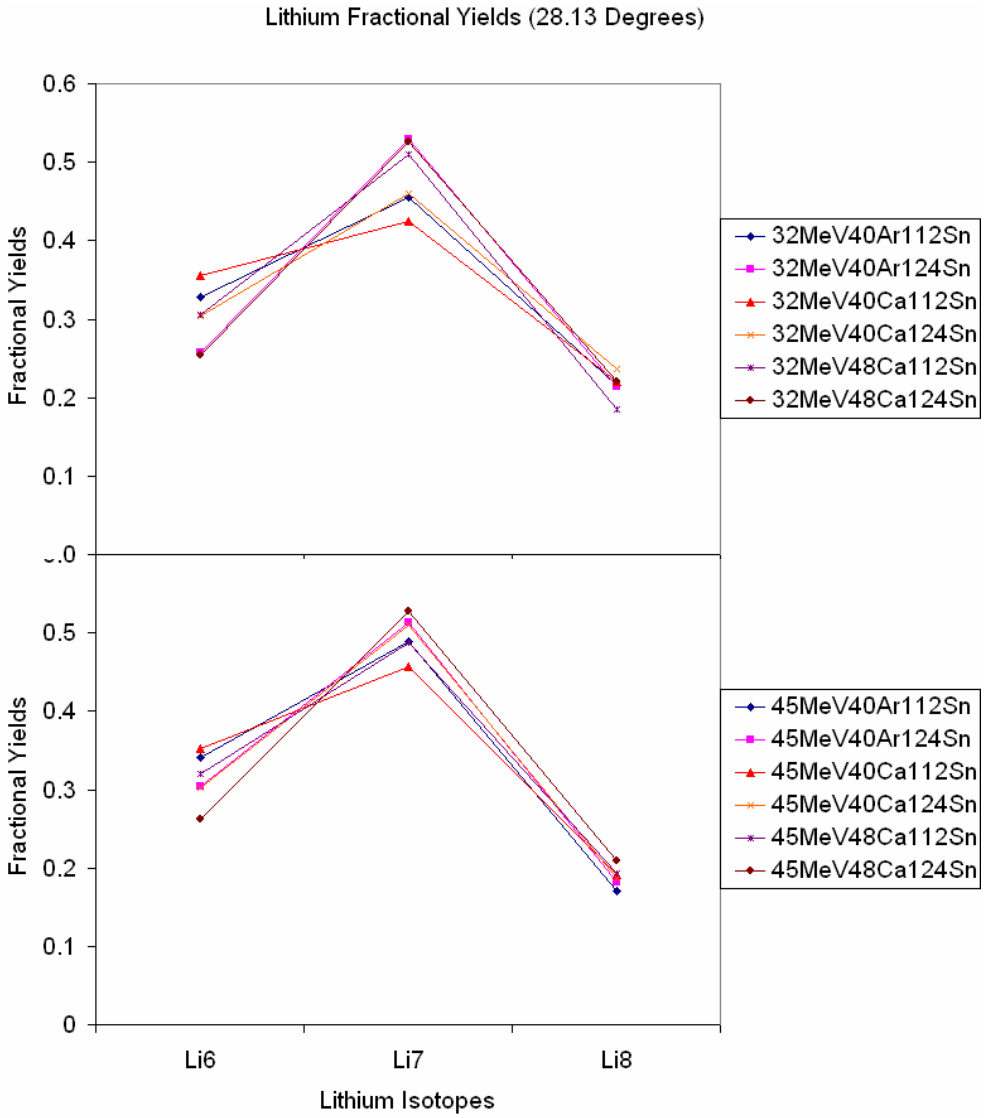


FIG. 144. (Color online) Lithium fractional yield ratio plot of the 32 MeV systems (top) and 45 MeV systems (bottom) at 28.13 degrees.

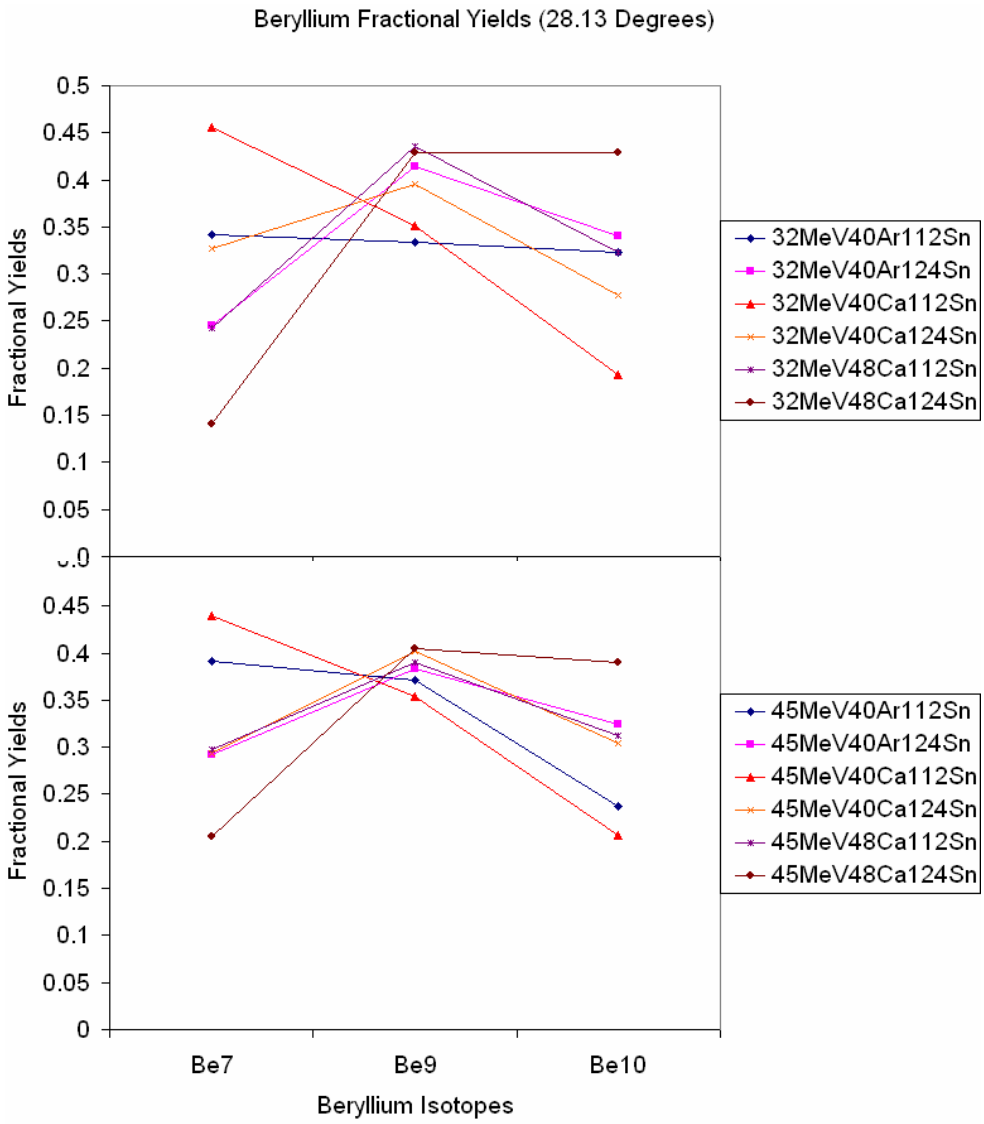


FIG. 145. (Color online) Beryllium fractional yield ratio plot of the 32 MeV systems (top) and 45 MeV systems (bottom) at 28.13 degrees.

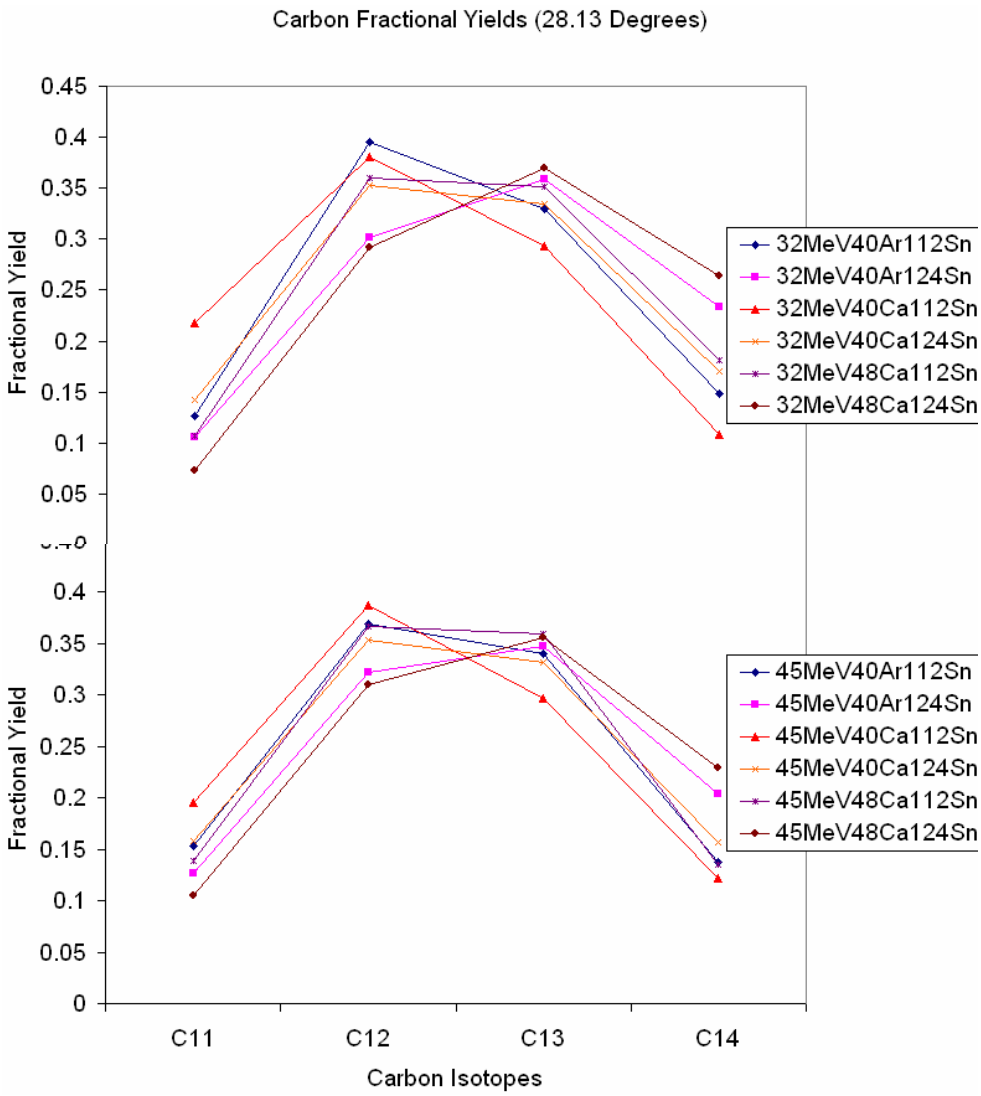


FIG. 146. (Color online) Carbon fractional yield ratio plot of the 32 MeV systems (top) and 45 MeV systems (bottom) at 28.13 degrees.

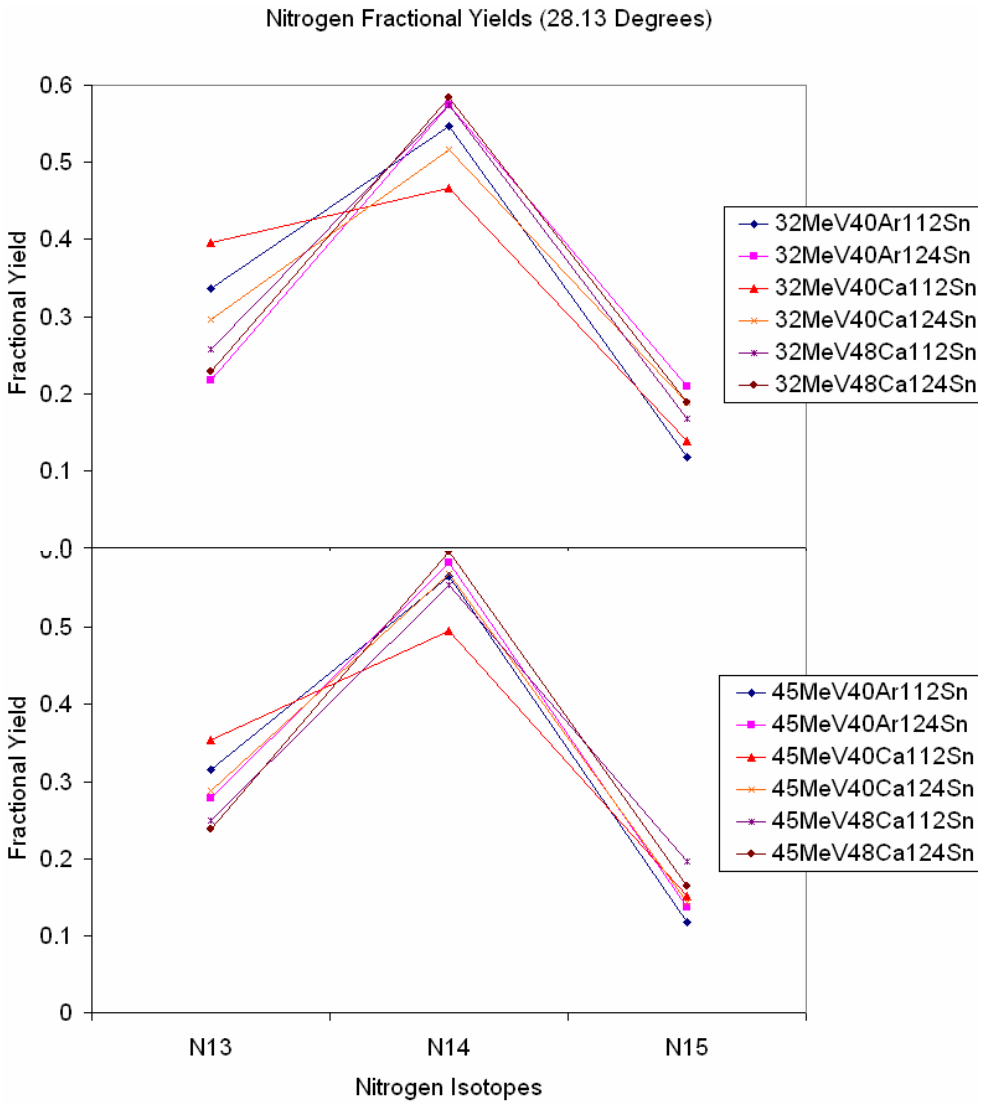


FIG. 147. (Color online) Nitrogen fractional yield ratio plot of the 32 MeV systems (top) and 45 MeV systems (bottom) at 28.13 degrees.

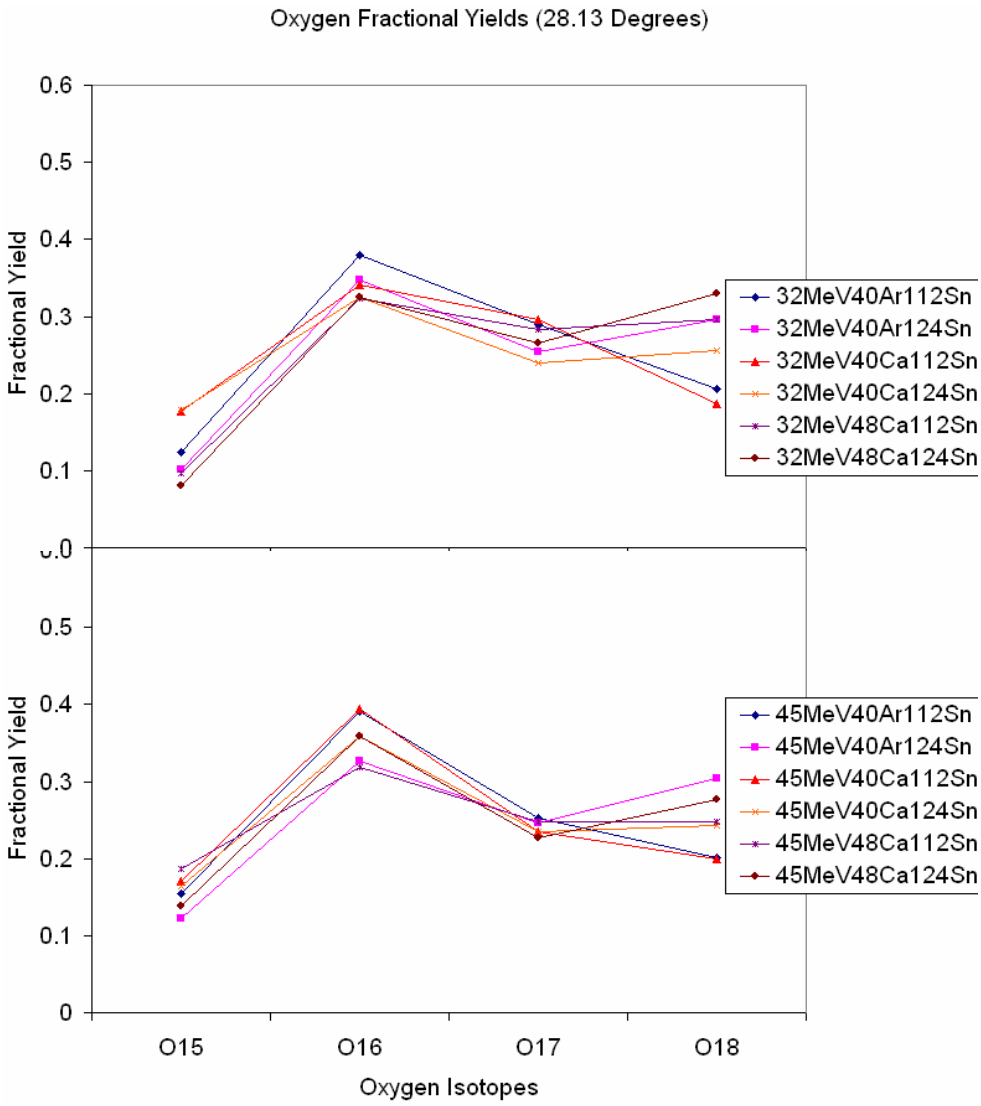


FIG. 148. (Color online) Oxygen fractional yield ratio plot of the 32 MeV systems (top) and 45 MeV systems (bottom) at 28.13 degrees.

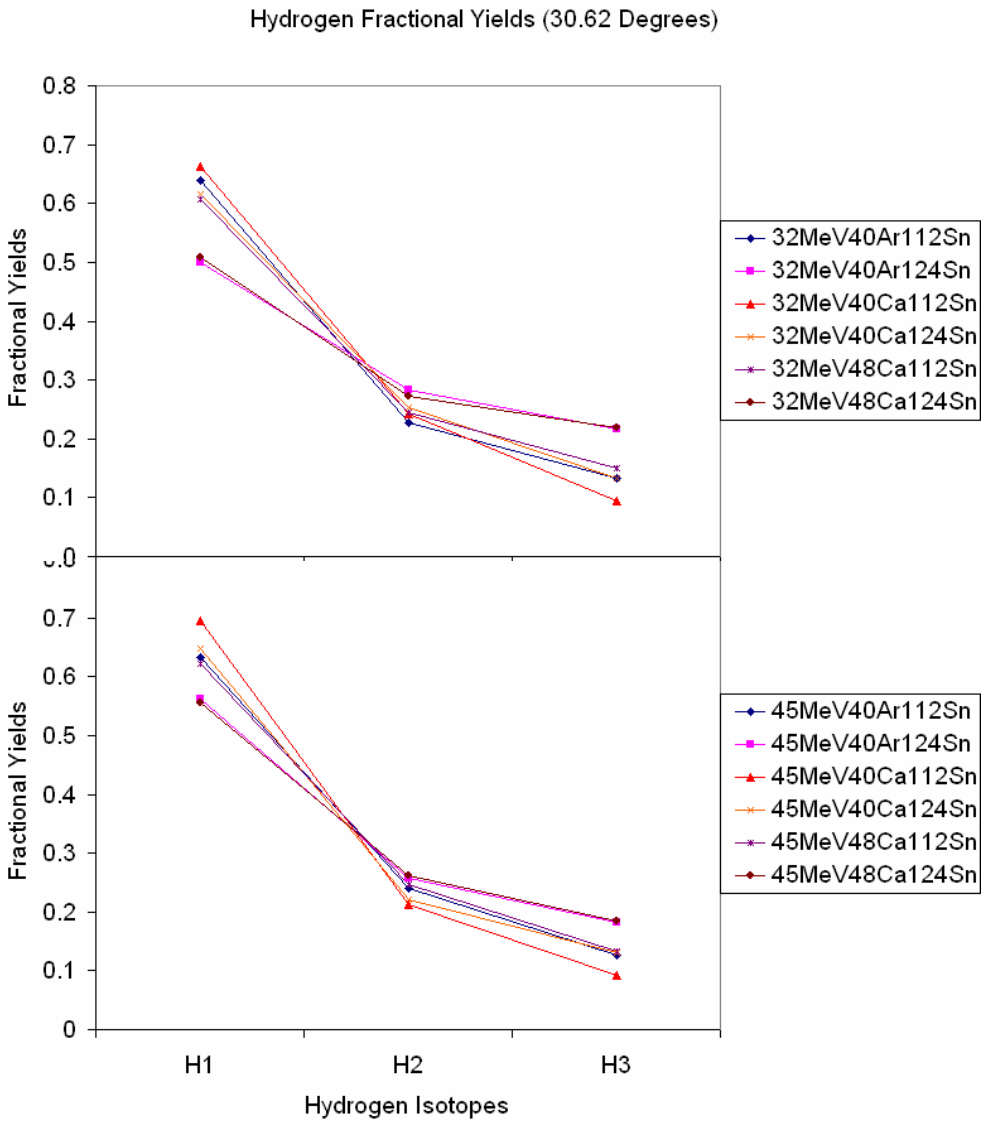


FIG. 149. (Color online) Hydrogen fractional yield ratio plot of the 32 MeV systems (top) and 45 MeV systems (bottom) at 30.62 degrees.

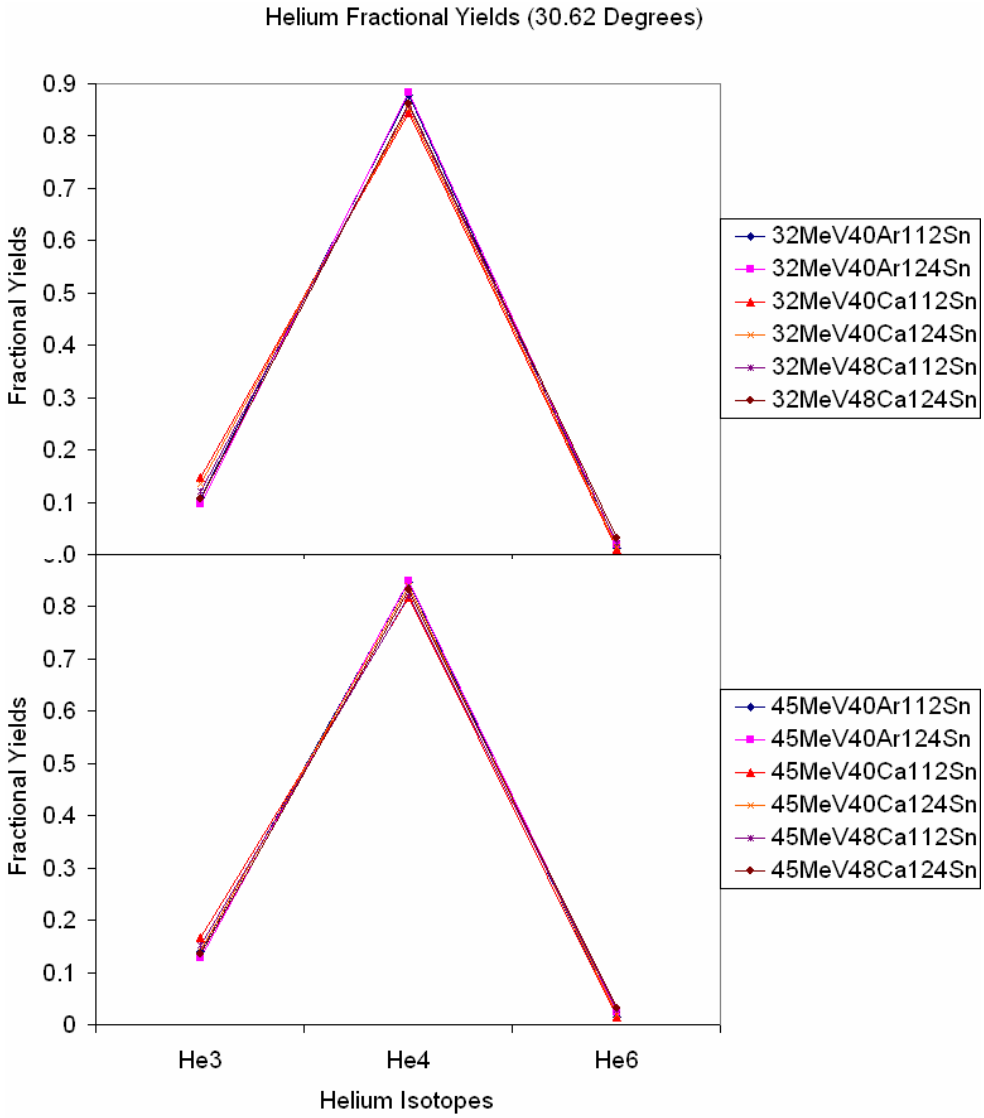


FIG. 150. (Color online) Helium fractional yield ratio plot of the 32 MeV systems (top) and 45 MeV systems (bottom) at 30.62 degrees.

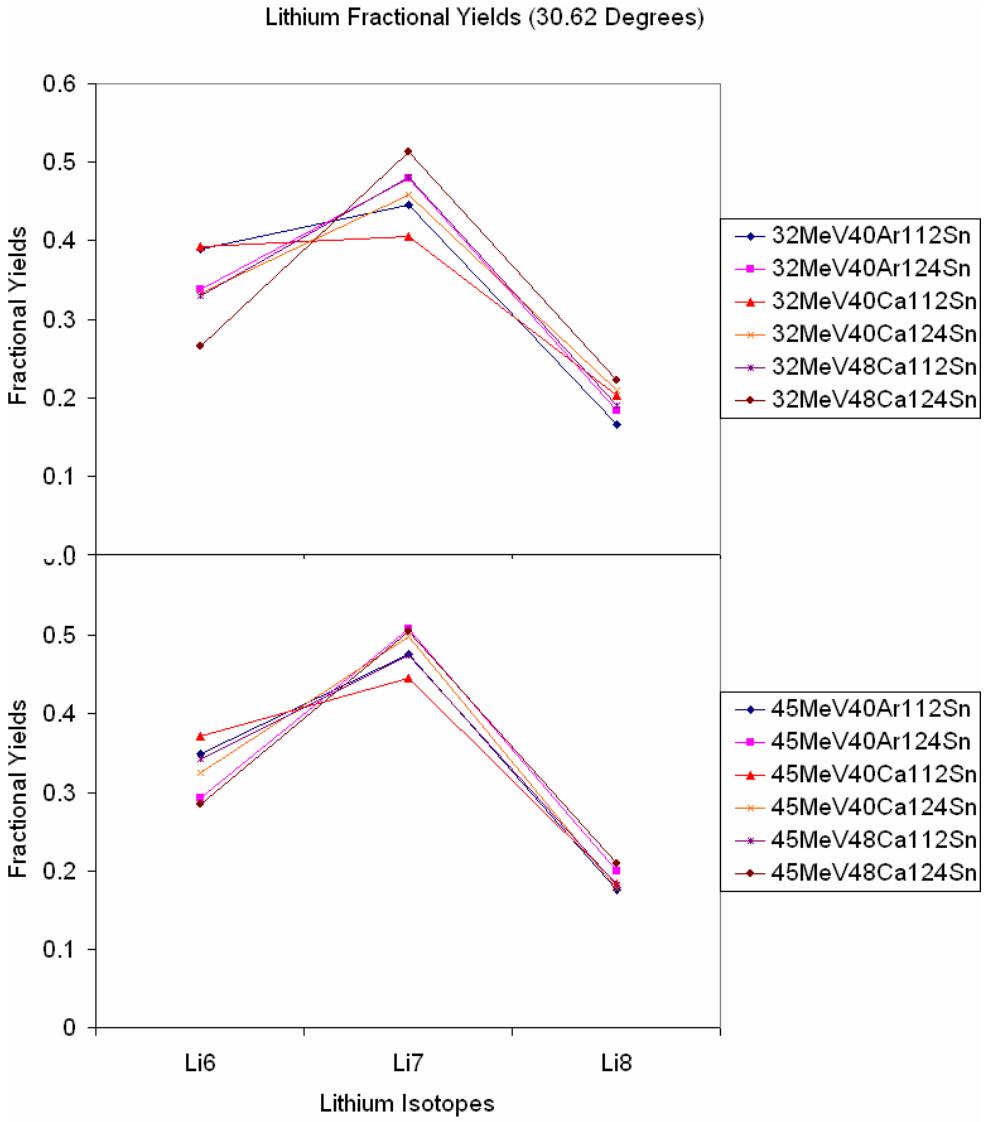


FIG. 151. (Color online) Lithium fractional yield ratio plot of the 32 MeV systems (top) and 45 MeV systems (bottom) at 30.62 degrees.

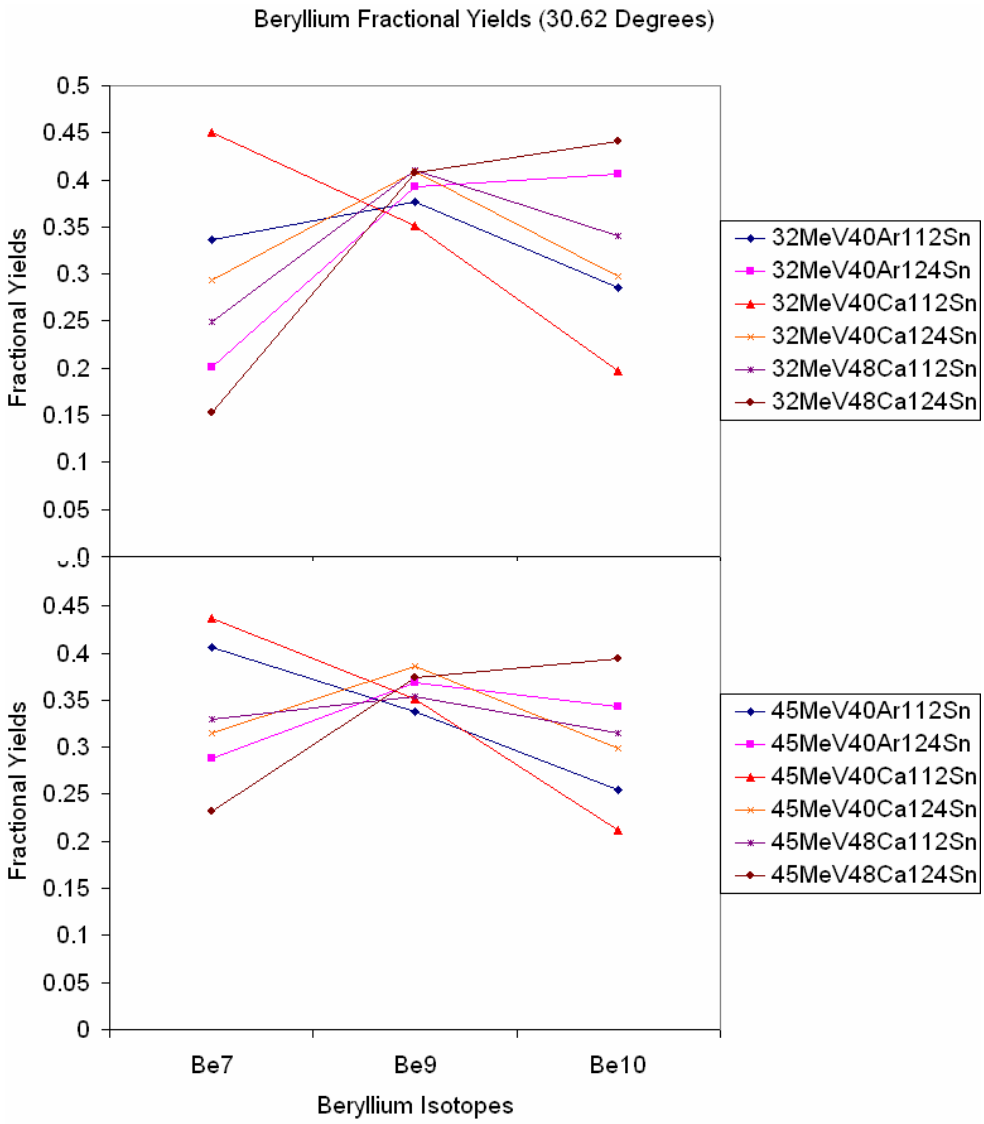


FIG. 152. (Color online) Beryllium fractional yield ratio plot of the 32 MeV systems (top) and 45 MeV systems (bottom) at 30.62 degrees.

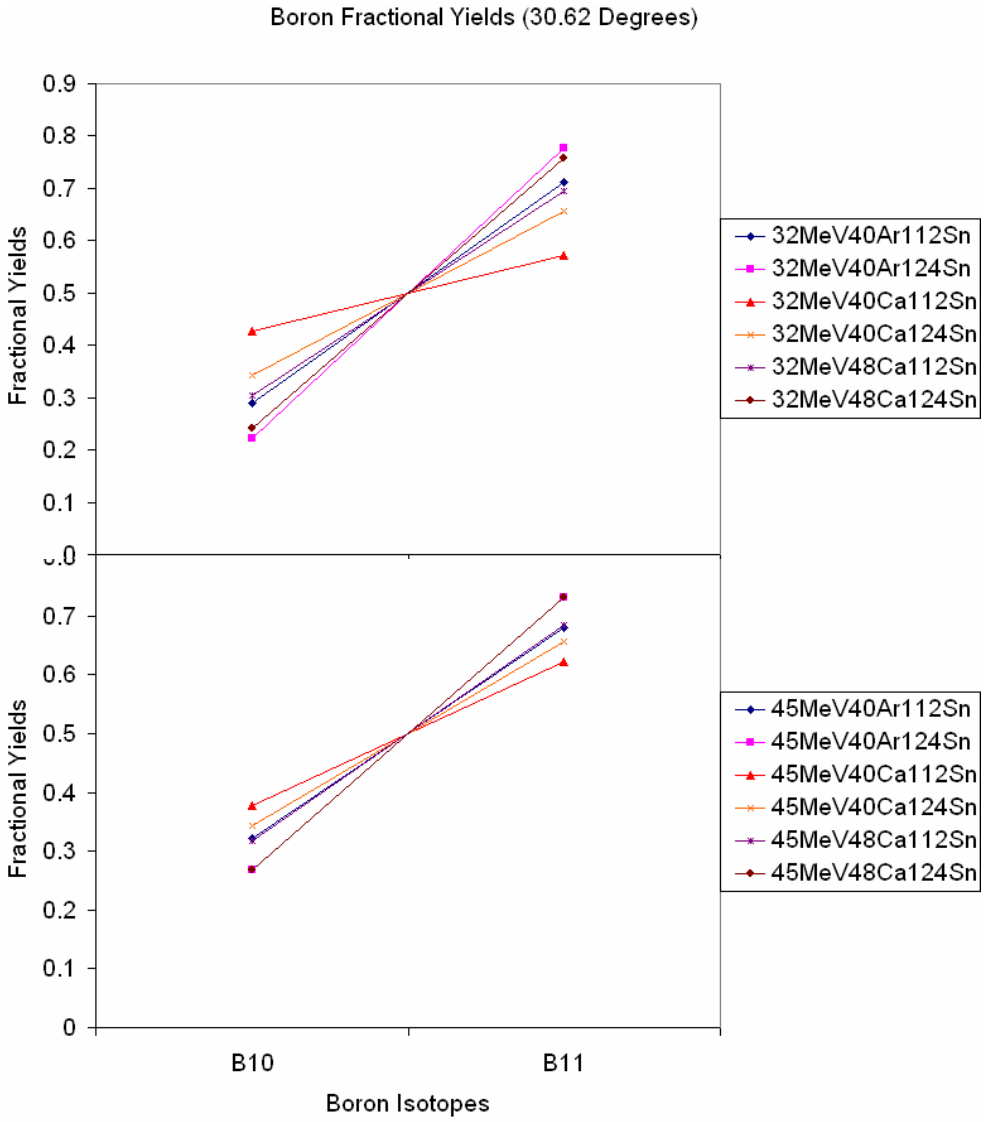


FIG. 153. (Color online) Boron fractional yield ratio plot of the 32 MeV systems (top) and 45 MeV systems (bottom) at 30.62 degrees.

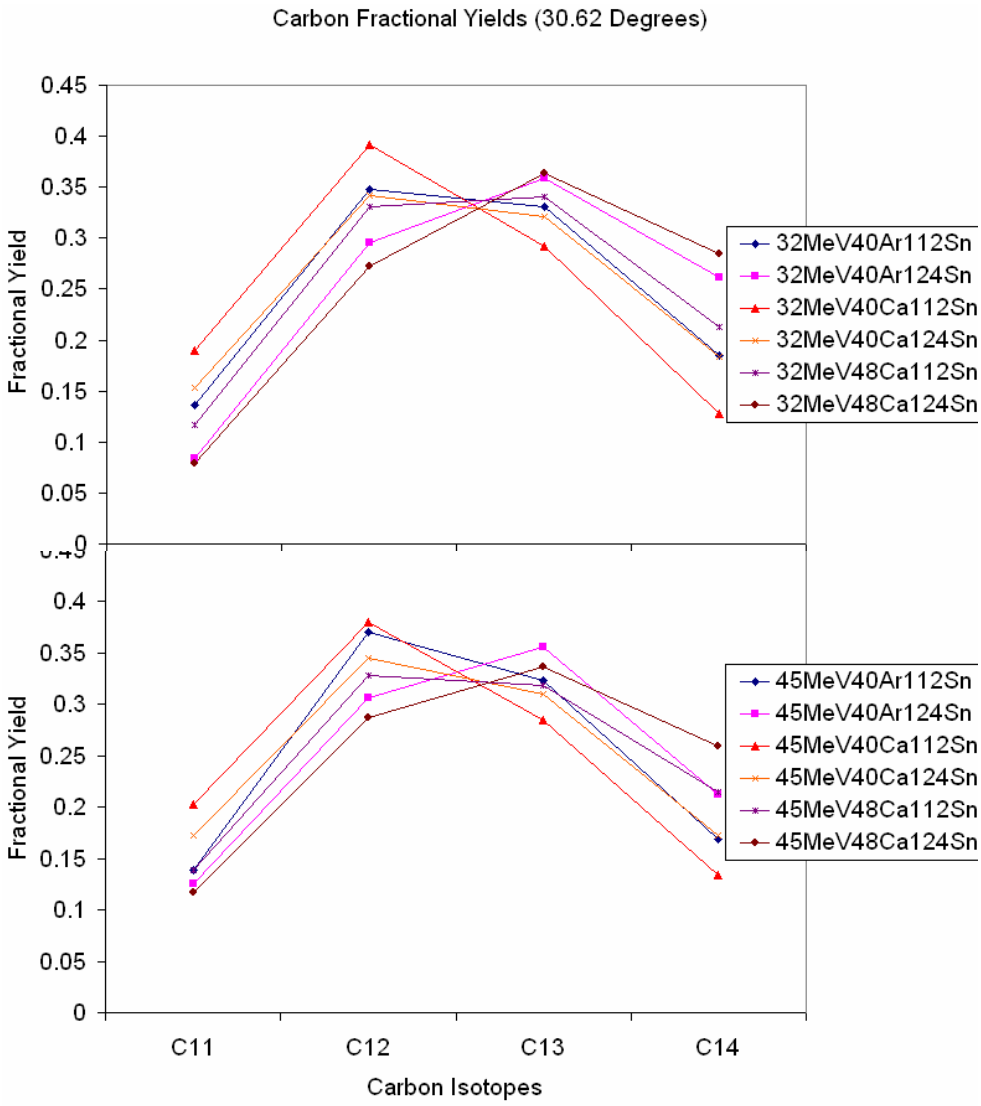


FIG. 154. (Color online) Carbon fractional yield ratio plot of the 32 MeV systems (top) and 45 MeV systems (bottom) at 30.62 degrees.

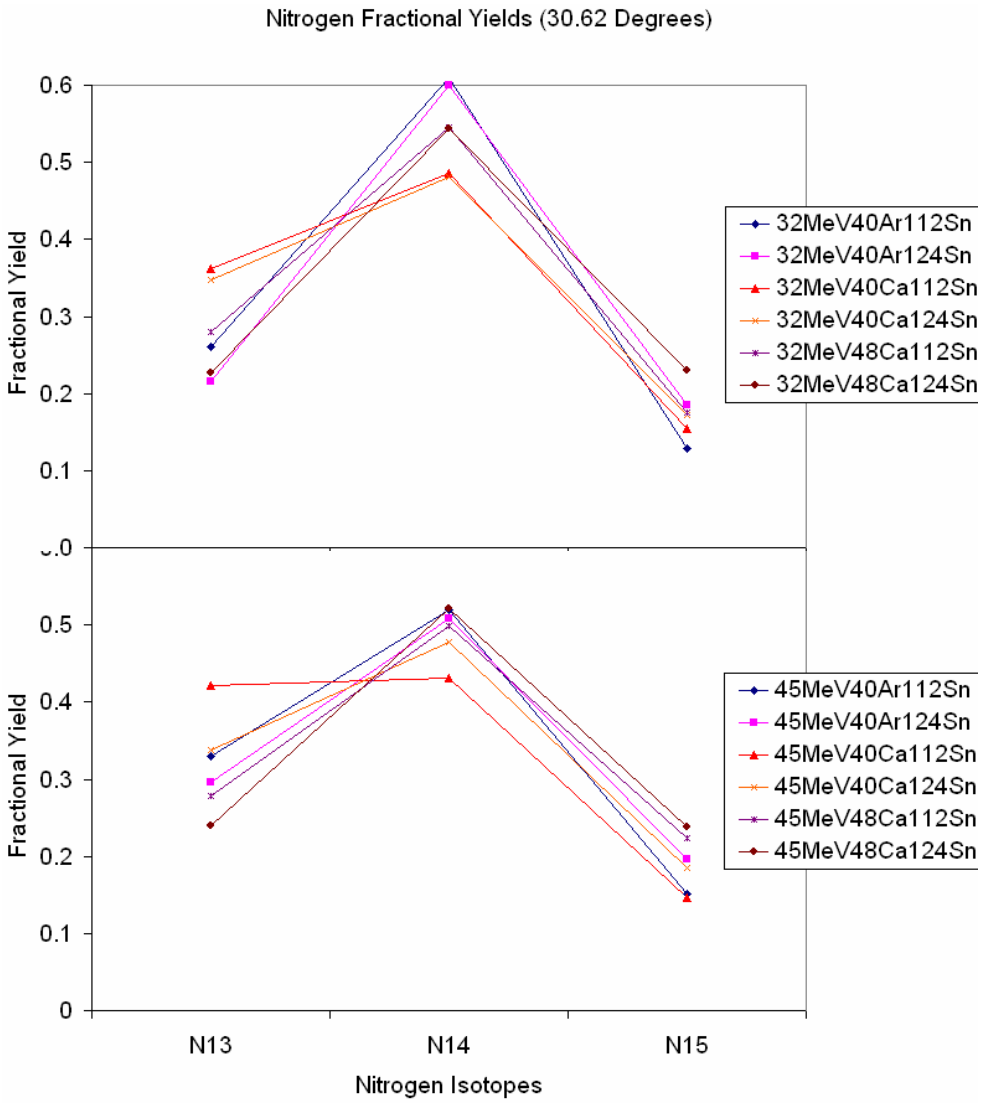


FIG. 155. (Color online) Nitrogen fractional yield ratio plot of the 32 MeV systems (top) and 45 MeV systems (bottom) at 30.62 degrees.

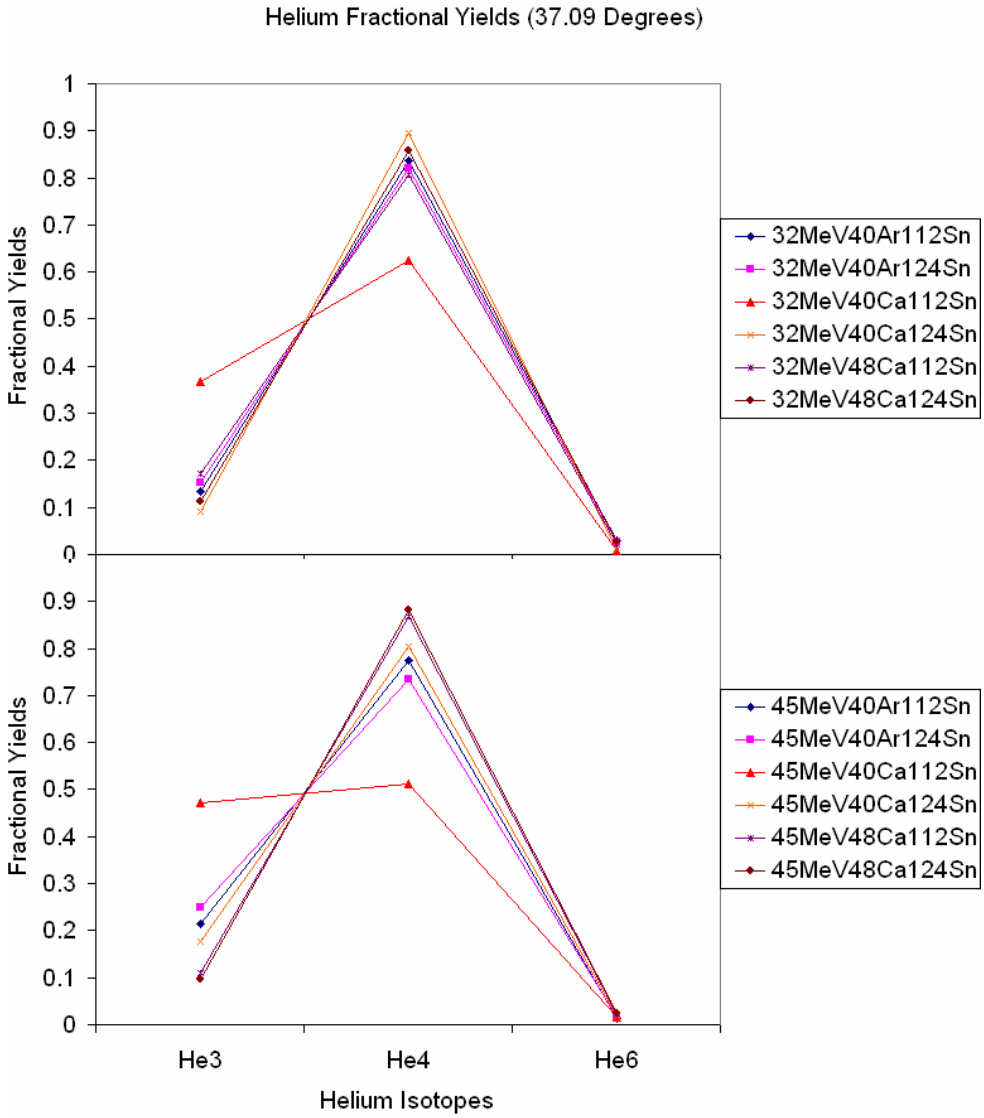


FIG. 156. (Color online) Helium fractional yield ratio plot of the 32 MeV systems (top) and 45 MeV systems (bottom) at 37.09 degrees.

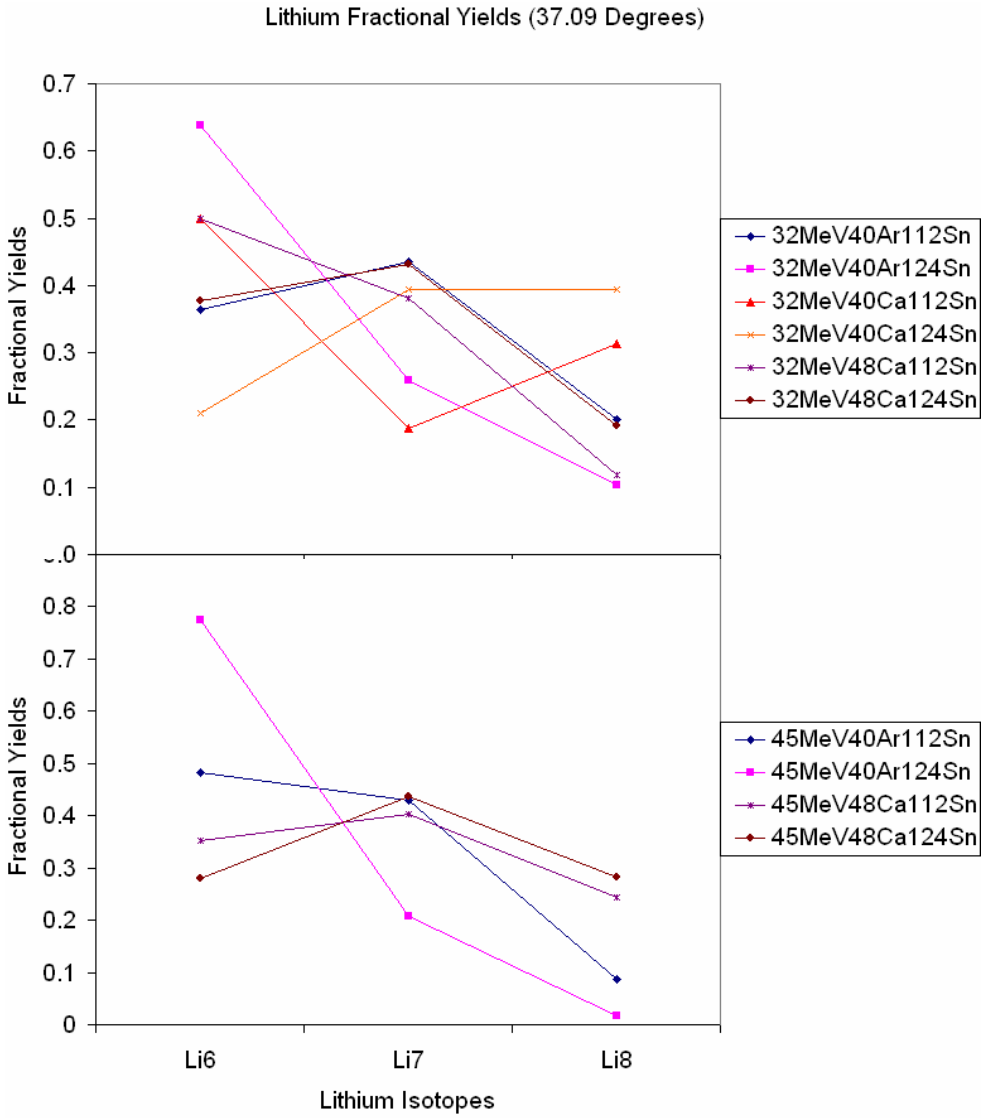


FIG. 157. (Color online) Lithium fractional yield ratio plot of the 32 MeV systems (top) and 45 MeV systems (bottom) at 37.09 degrees.

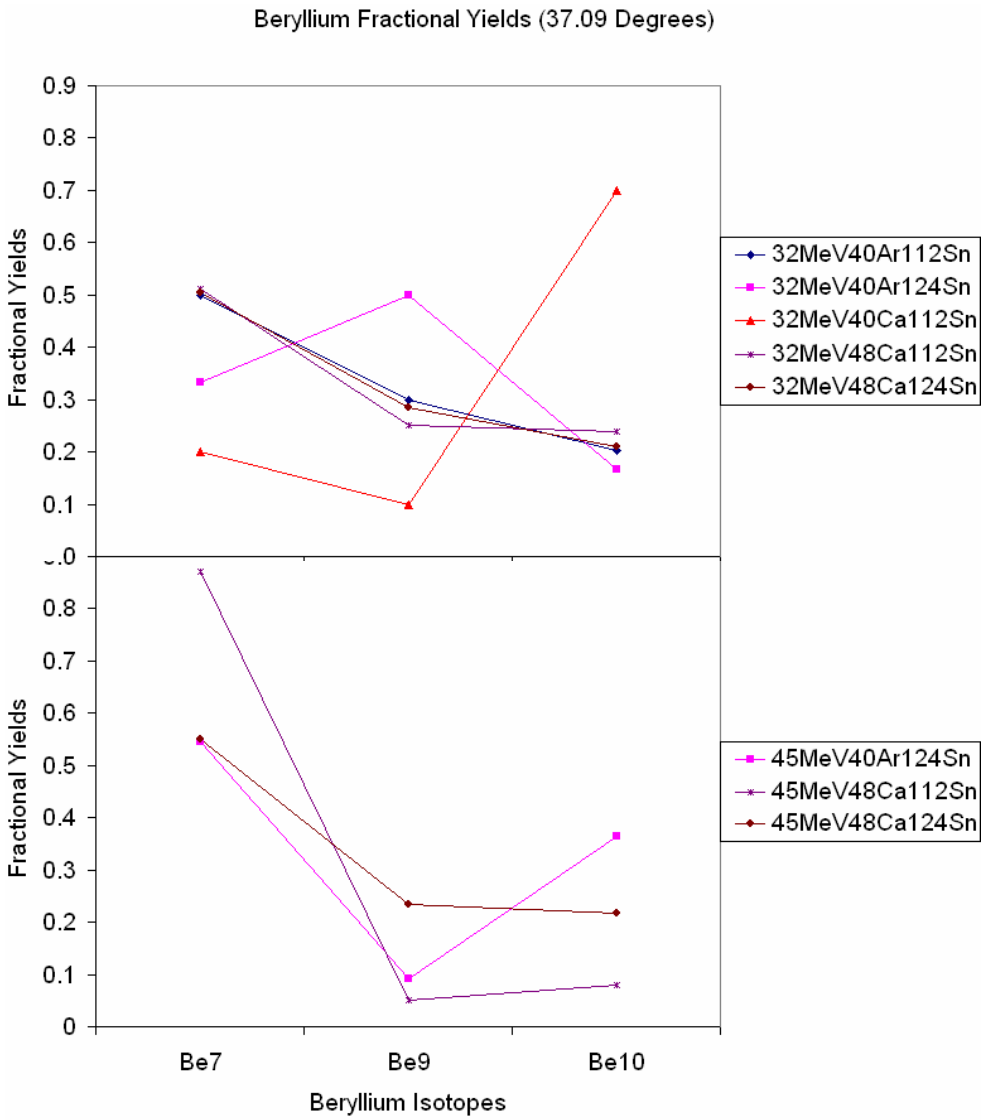


FIG. 158. (Color online) Beryllium fractional yield ratio plot of the 32 MeV systems (top) and 45 MeV systems (bottom) at 37.09 degrees.

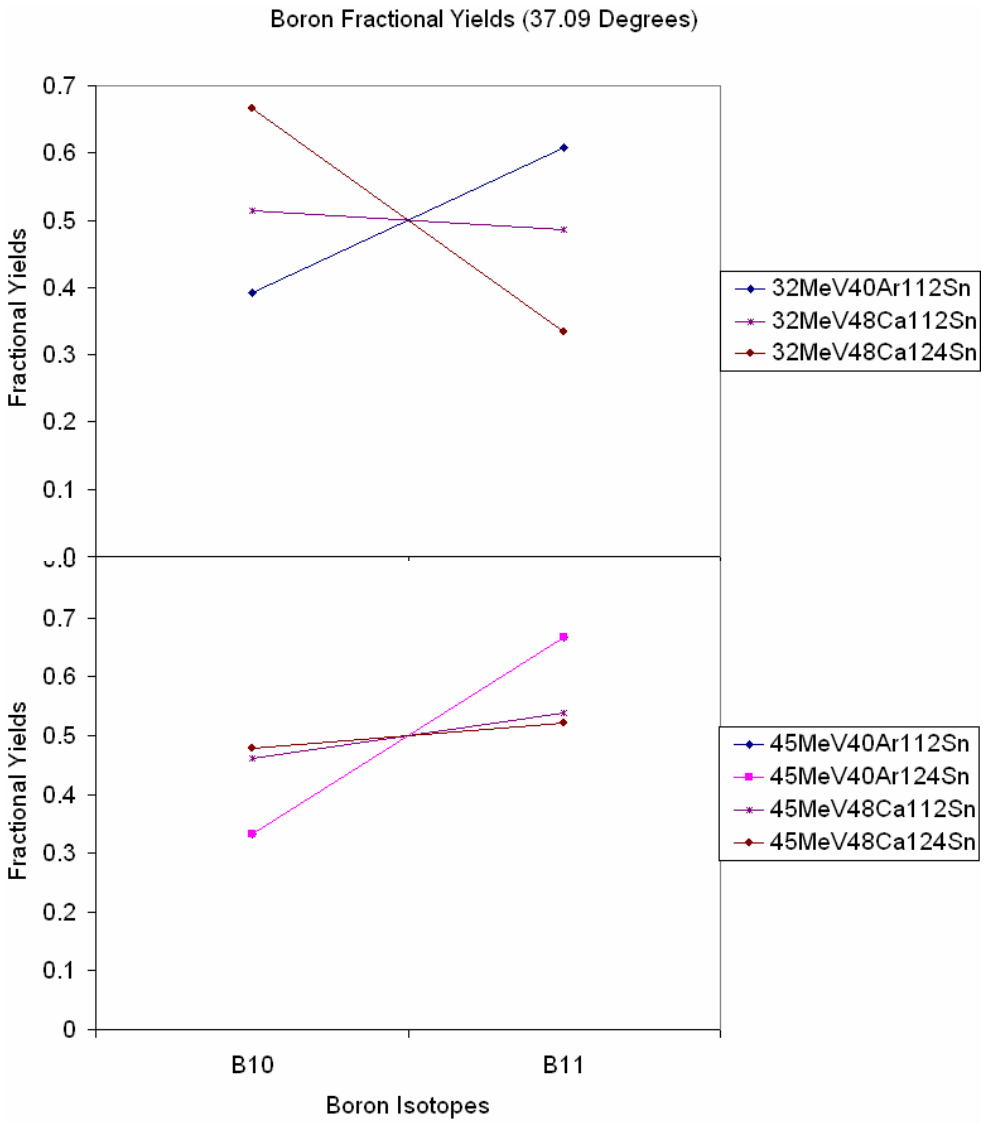


FIG. 159. (Color online) Boron fractional yield ratio plot of the 32 MeV systems (top) and 45 MeV systems (bottom) at 37.09 degrees.

# APPENDIX C

## ADDITIONAL ISOTOPIC YIELD RATIO PLOTS

This section contains the isotopic yield ratio plots for the other 12 laboratory angles. All nuclides that have isotopic yield ratios are shown at the other 12 angles in figures 160 to 170 and trends are consistent with results from 7.01 degrees as discussed in chapter IV.

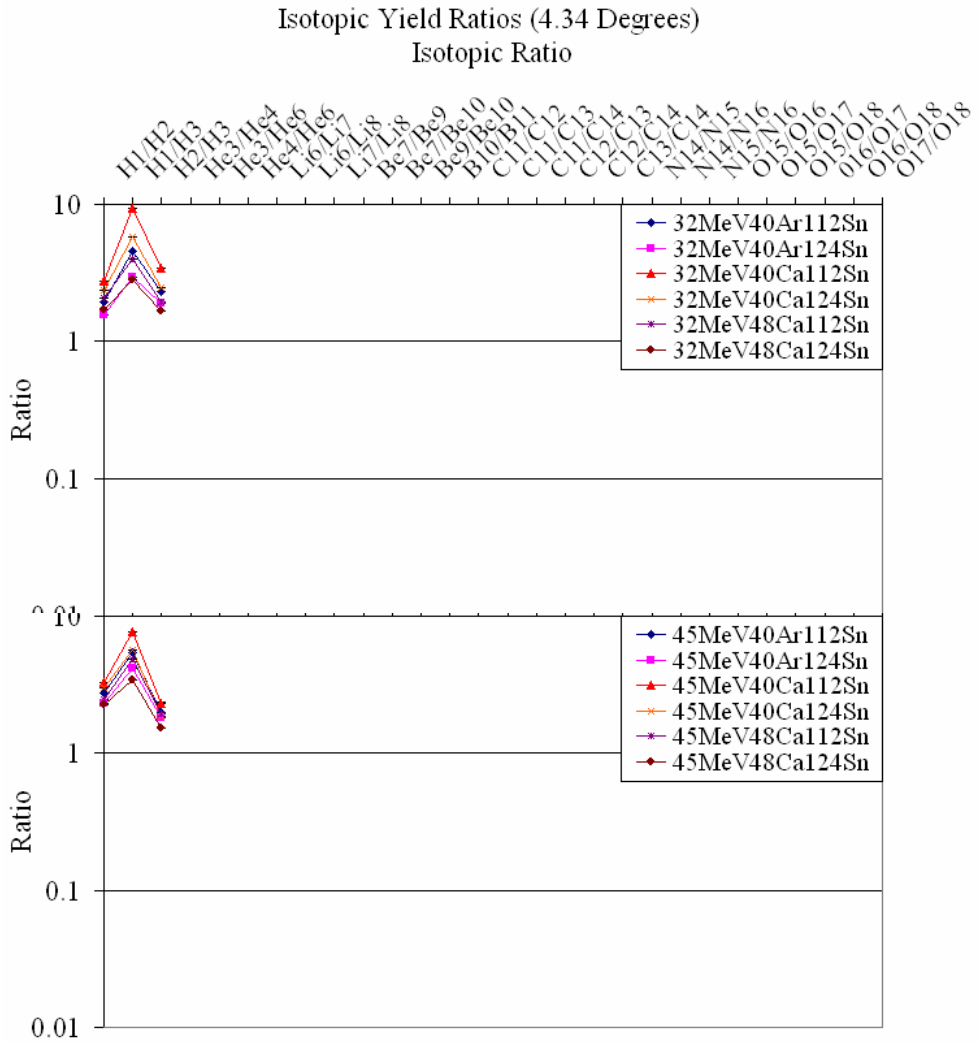


FIG. 160. (Color online) Isotopic yield ratio plot of the 32 MeV systems (top) and 45 MeV systems (bottom) at 4.34 degrees.

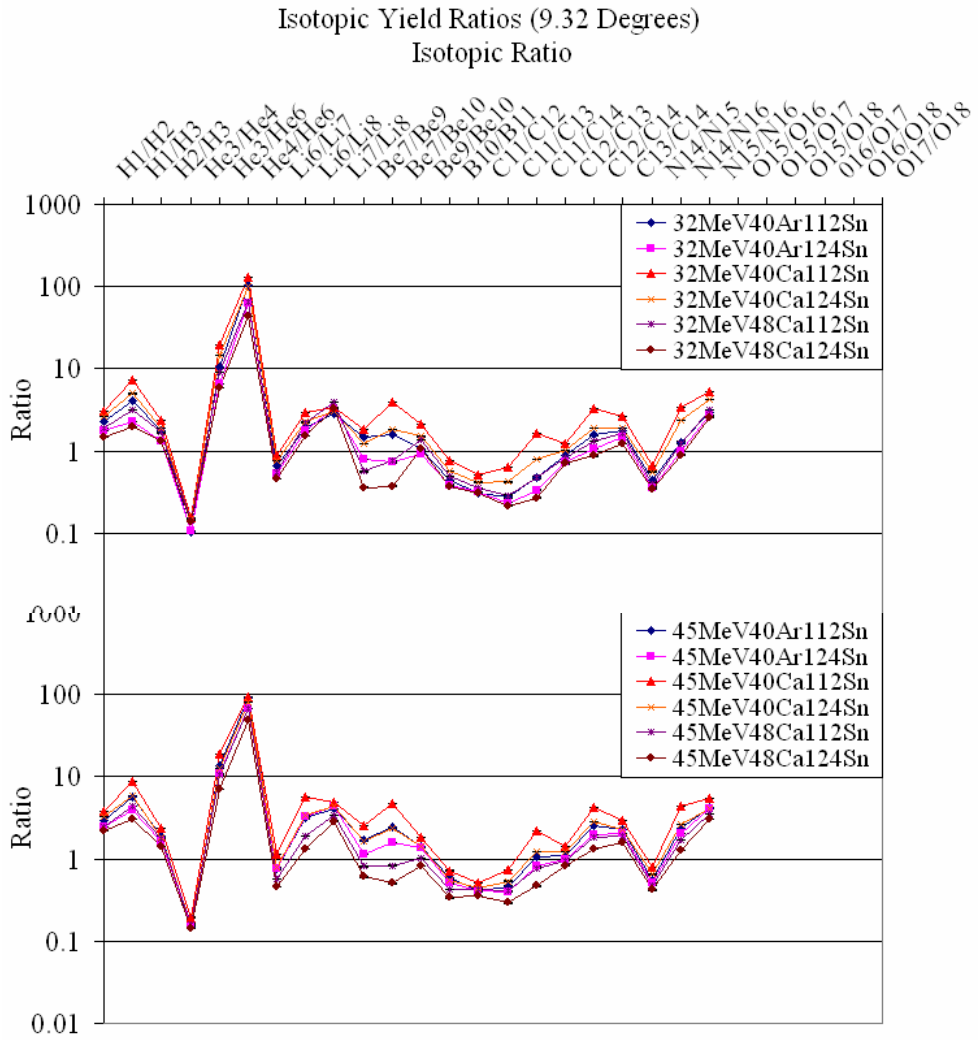


FIG. 161. (Color online) Isotopic yield ratio plot of the 32 MeV systems (top) and 45 MeV systems (bottom) at 9.32 degrees.

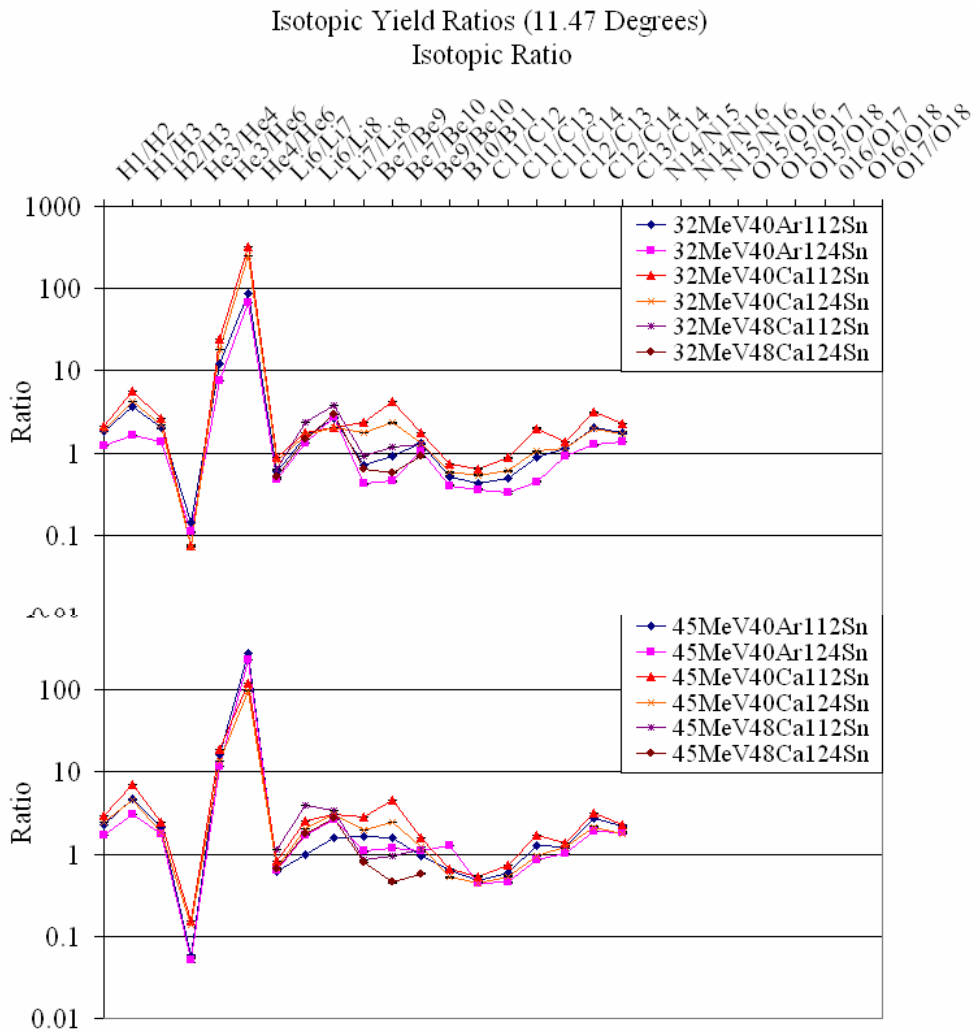


FIG. 162. (Color online) Isotopic yield ratio plot of the 32 MeV systems (top) and 45 MeV systems (bottom) at 11.47 degrees.

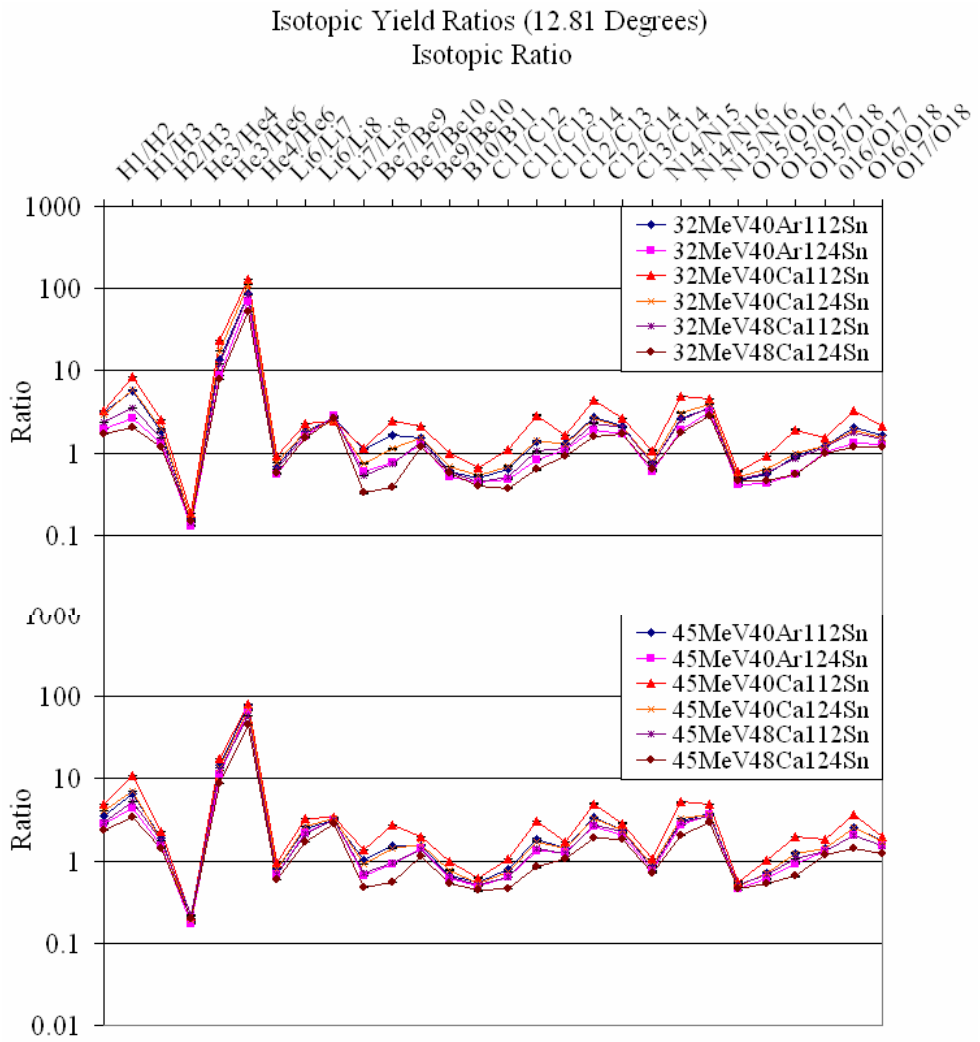


FIG. 163. (Color online) Isotopic yield ratio plot of the 32 MeV systems (top) and 45 MeV systems (bottom) at 12.81 degrees.

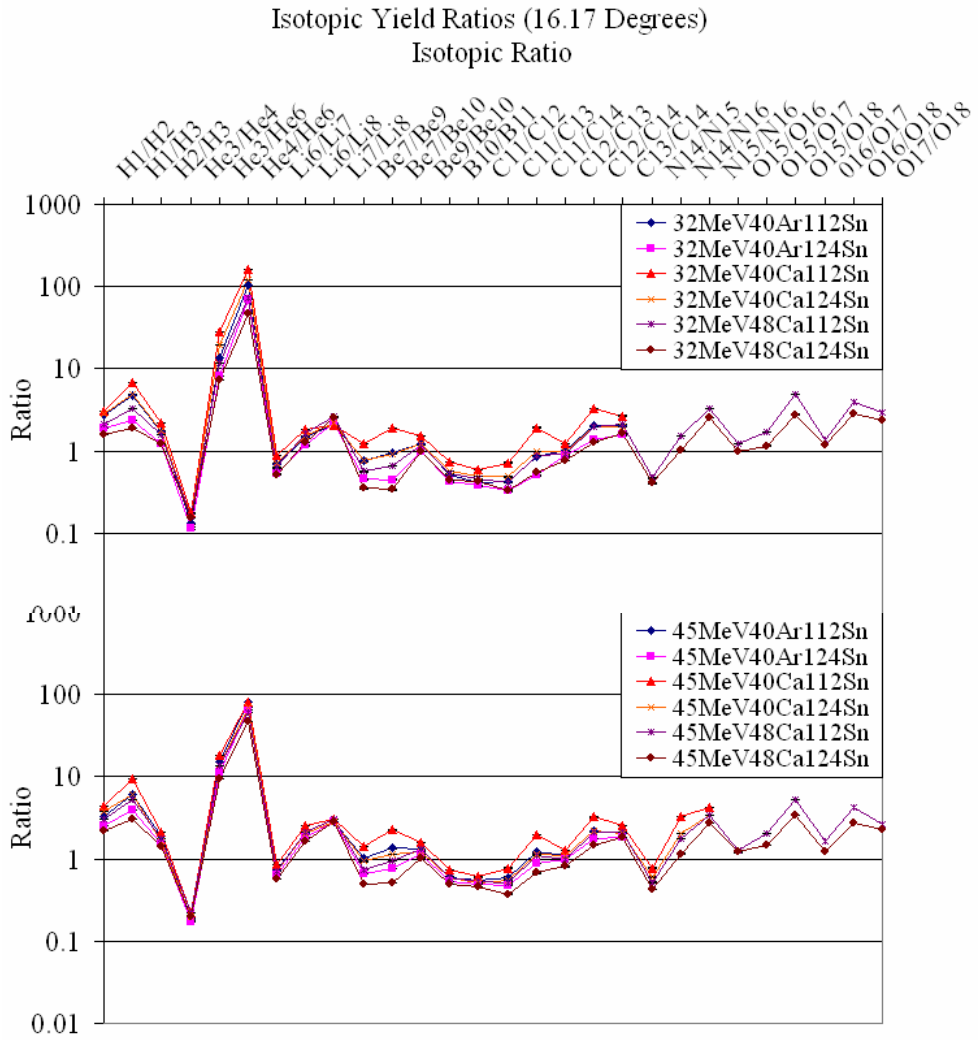


FIG. 164. (Color online) Isotopic yield ratio plot of the 32 MeV systems (top) and 45 MeV systems (bottom) at 16.17 degrees.

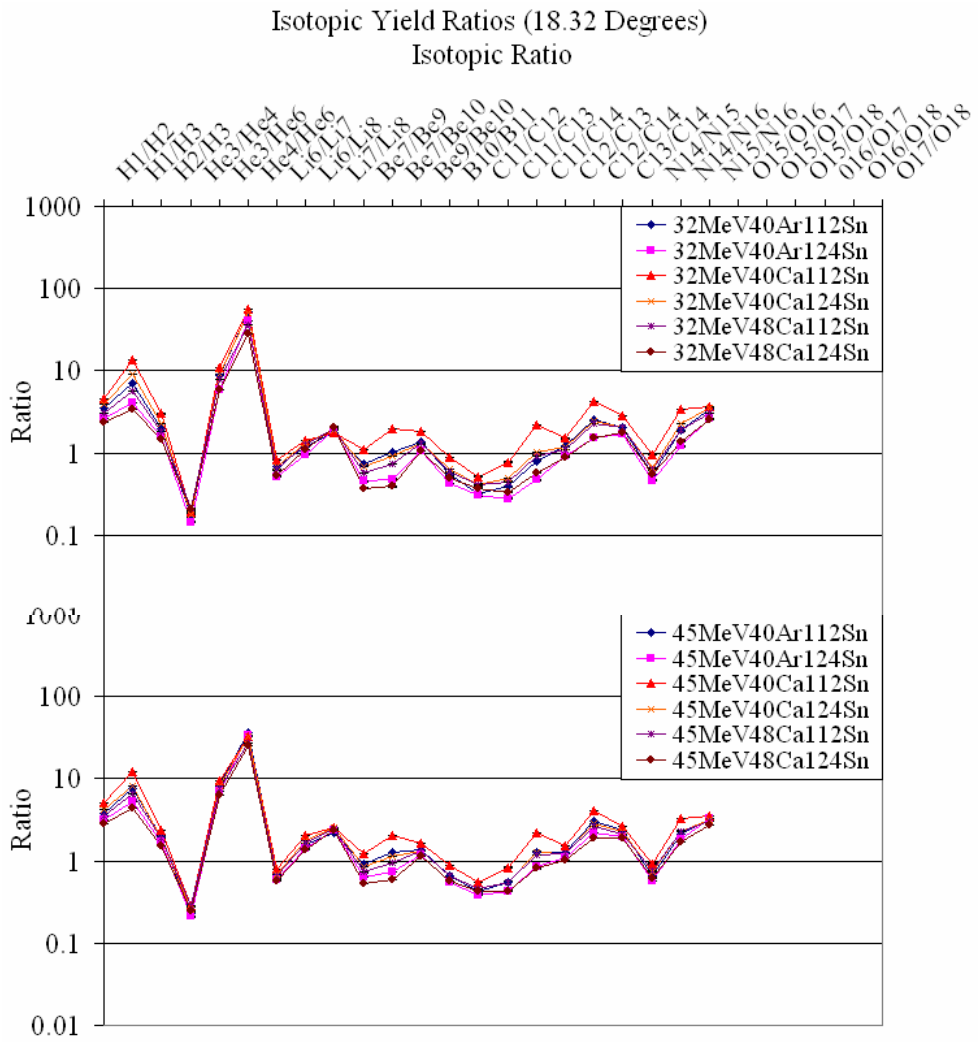


FIG. 165. (Color online) Isotopic yield ratio plot of the 32 MeV systems (top) and 45 MeV systems (bottom) at 18.32 degrees.

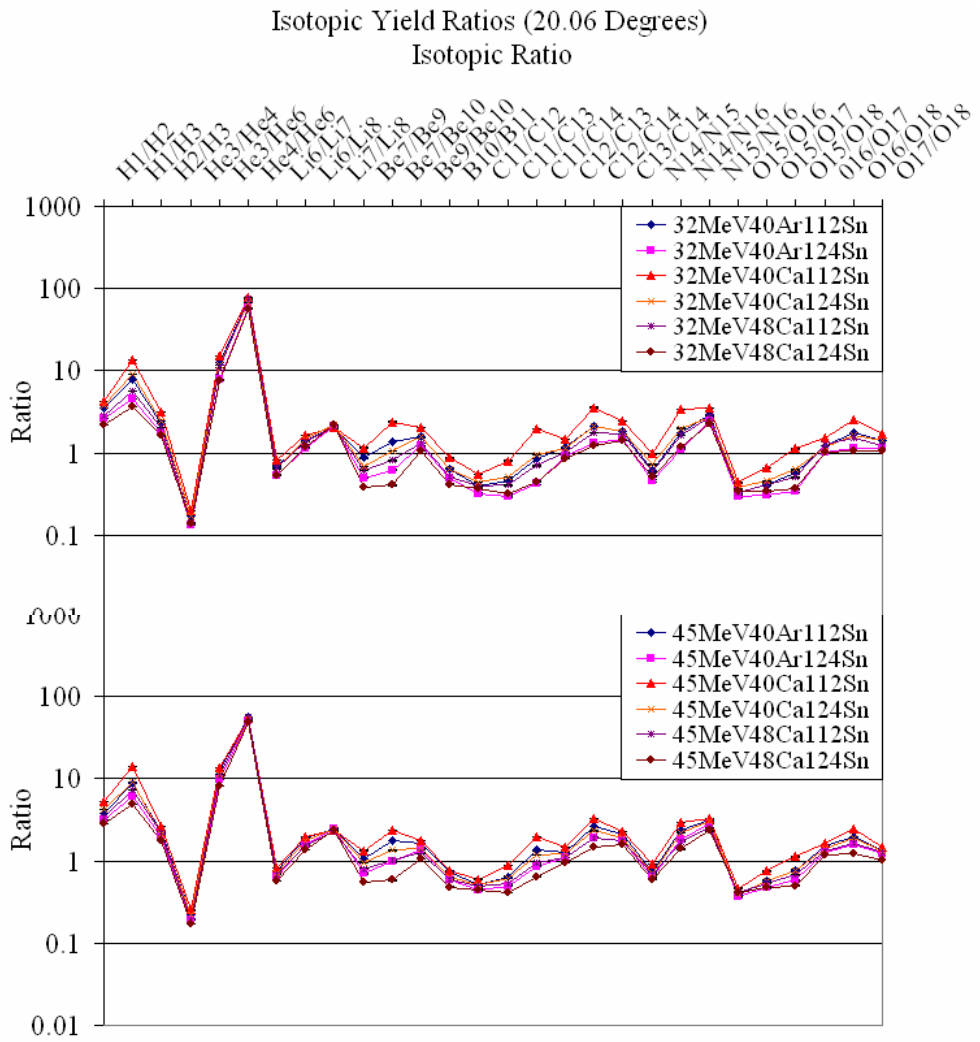


FIG. 166. (Color online) Isotopic yield ratio plot of the 32 MeV systems (top) and 45 MeV systems (bottom) at 20.06 degrees.

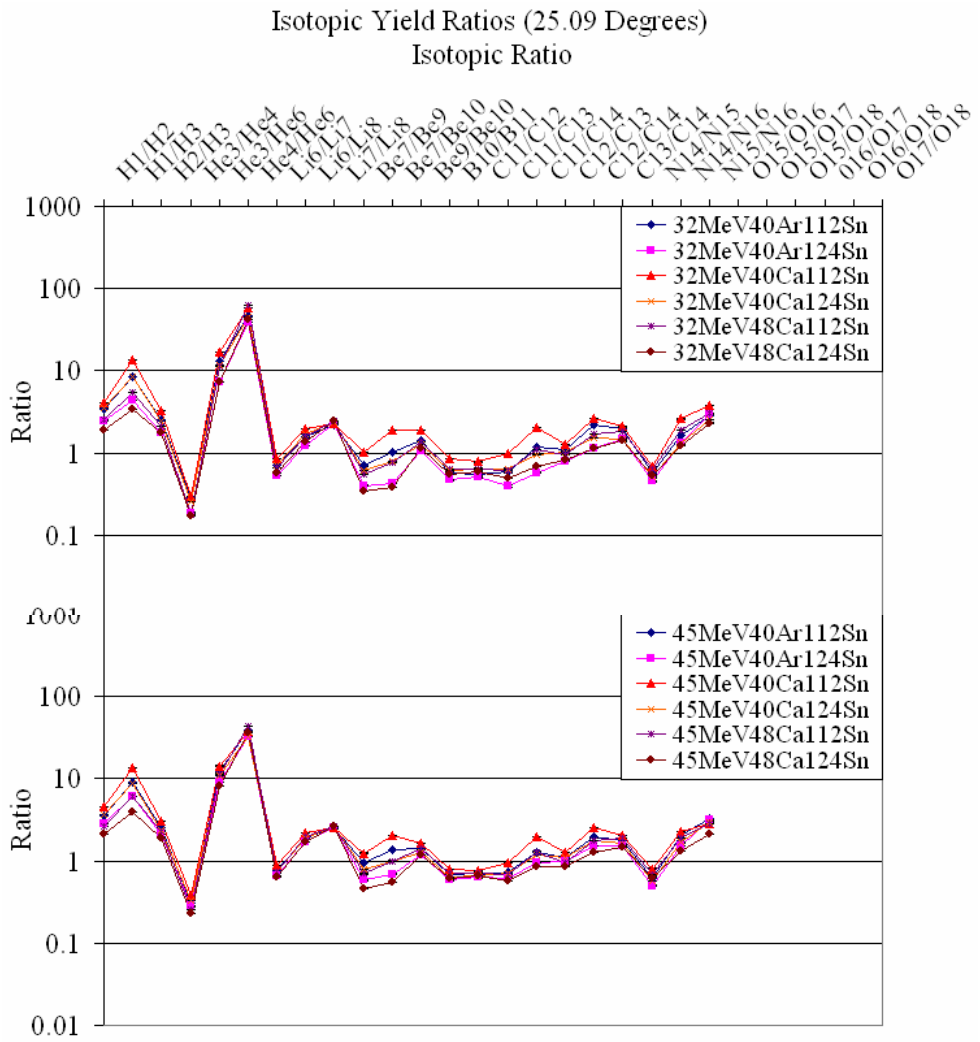


FIG. 167. (Color online) Isotopic yield ratio plot of the 32 MeV systems (top) and 45 MeV systems (bottom) at 25.09 degrees.

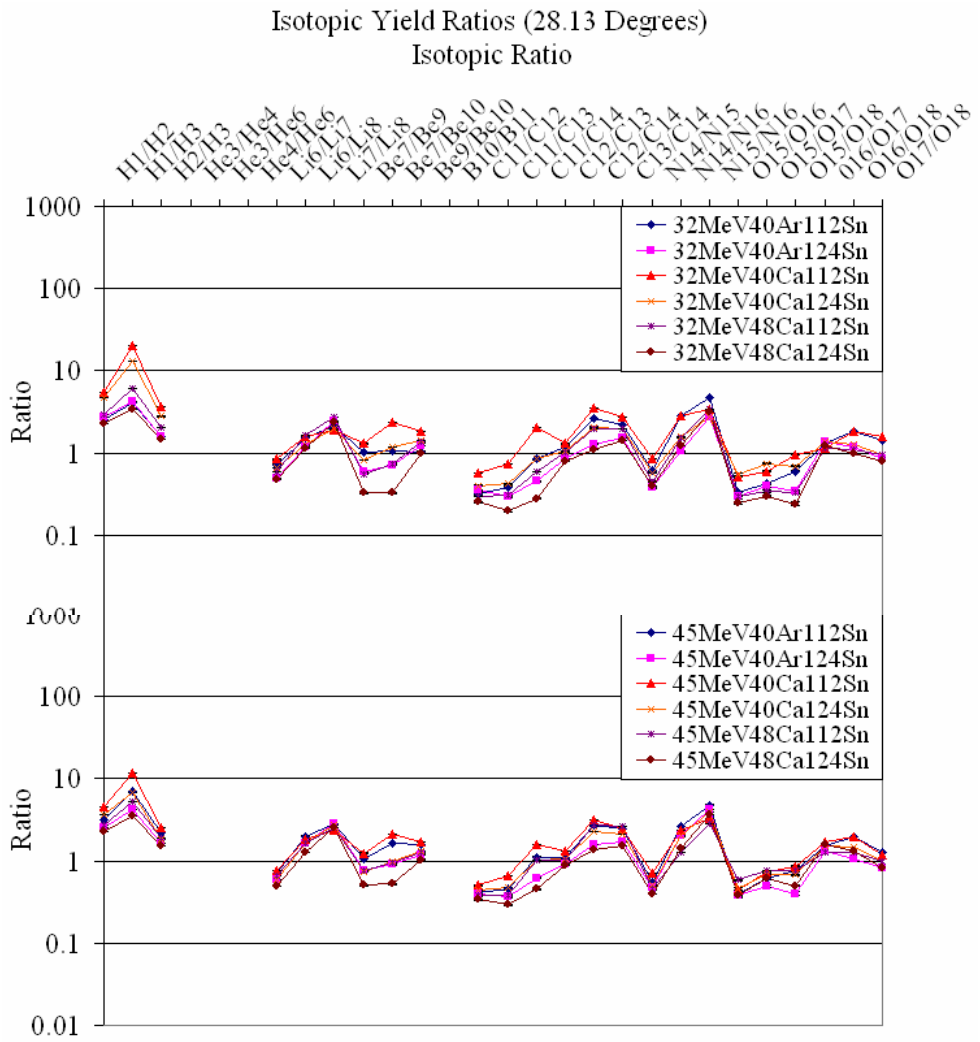


FIG. 168. (Color online) Isotopic yield ratio plot of the 32 MeV systems (top) and 45 MeV systems (bottom) at 28.13 degrees.

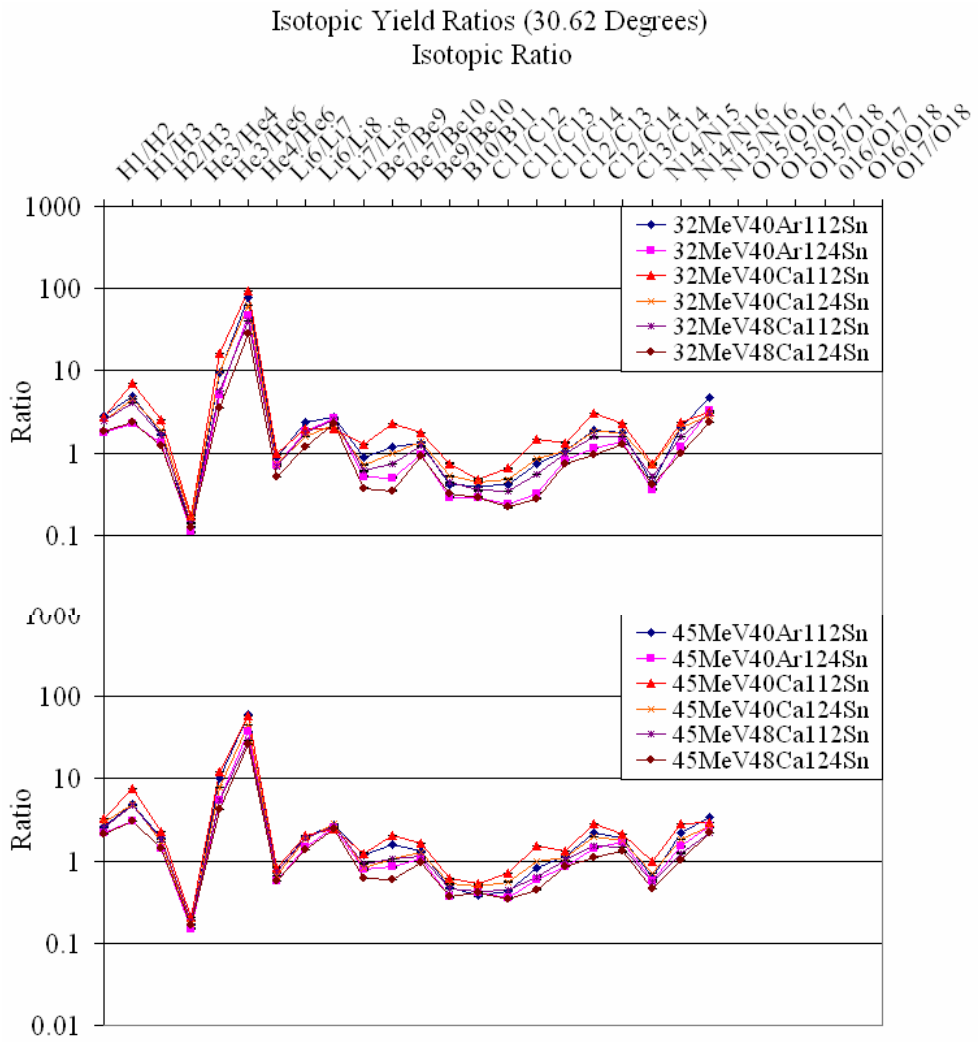


FIG. 169. (Color online) Isotopic yield ratio plot of the 32 MeV systems (top) and 45 MeV systems (bottom) at 30.62 degrees.

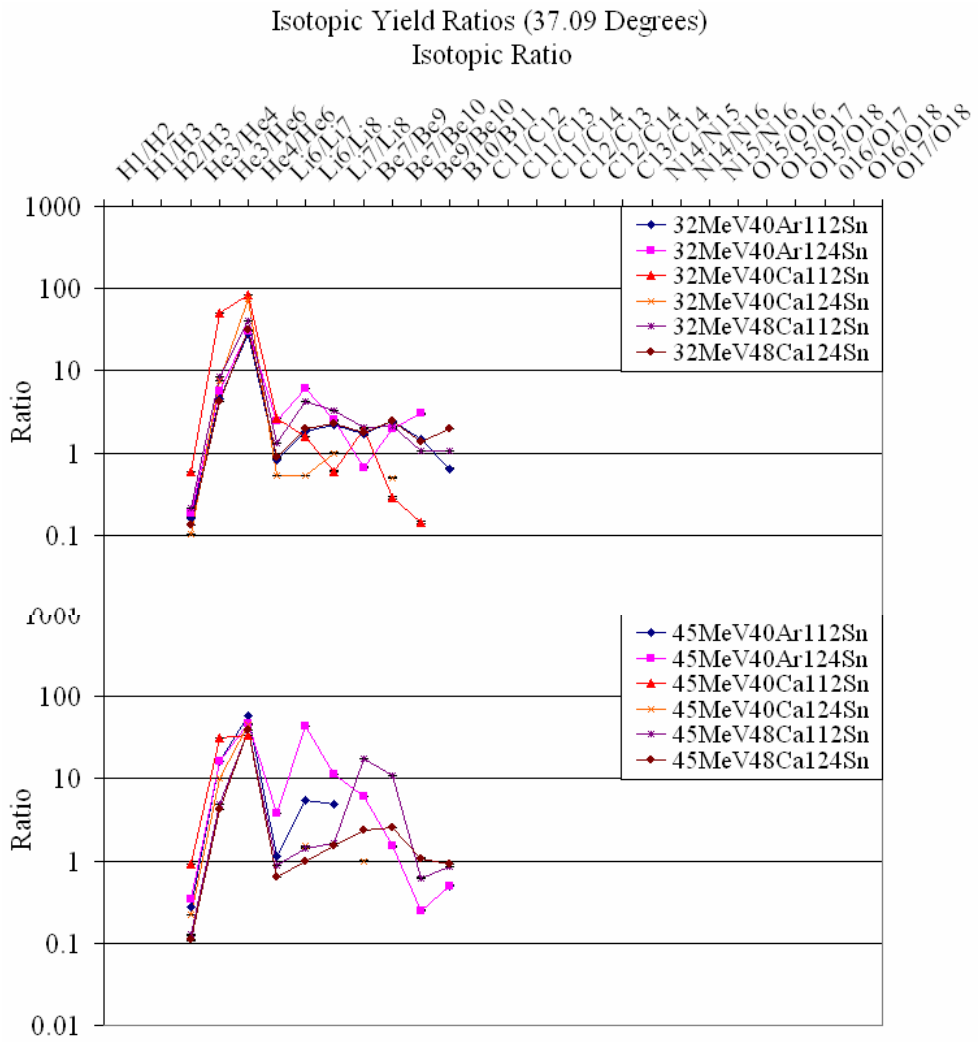


FIG. 170. (Color online) Isotopic yield ratio plot of the 32 MeV systems (top) and 45 MeV systems (bottom) at 37.09 degrees.

# APPENDIX D

## ADDITIONAL ISOBARIC YIELD RATIO PLOTS

This section contains the isobaric yield ratio plots for the other 12 laboratory angles. The angles 3.07 and 4.34 do not have any isobaric yield ratios. The figures 171 to 180 show all the isobaric yield ratios that exist at each angle and trends are consistent with results from 7.01 degrees as discussed in chapter IV.

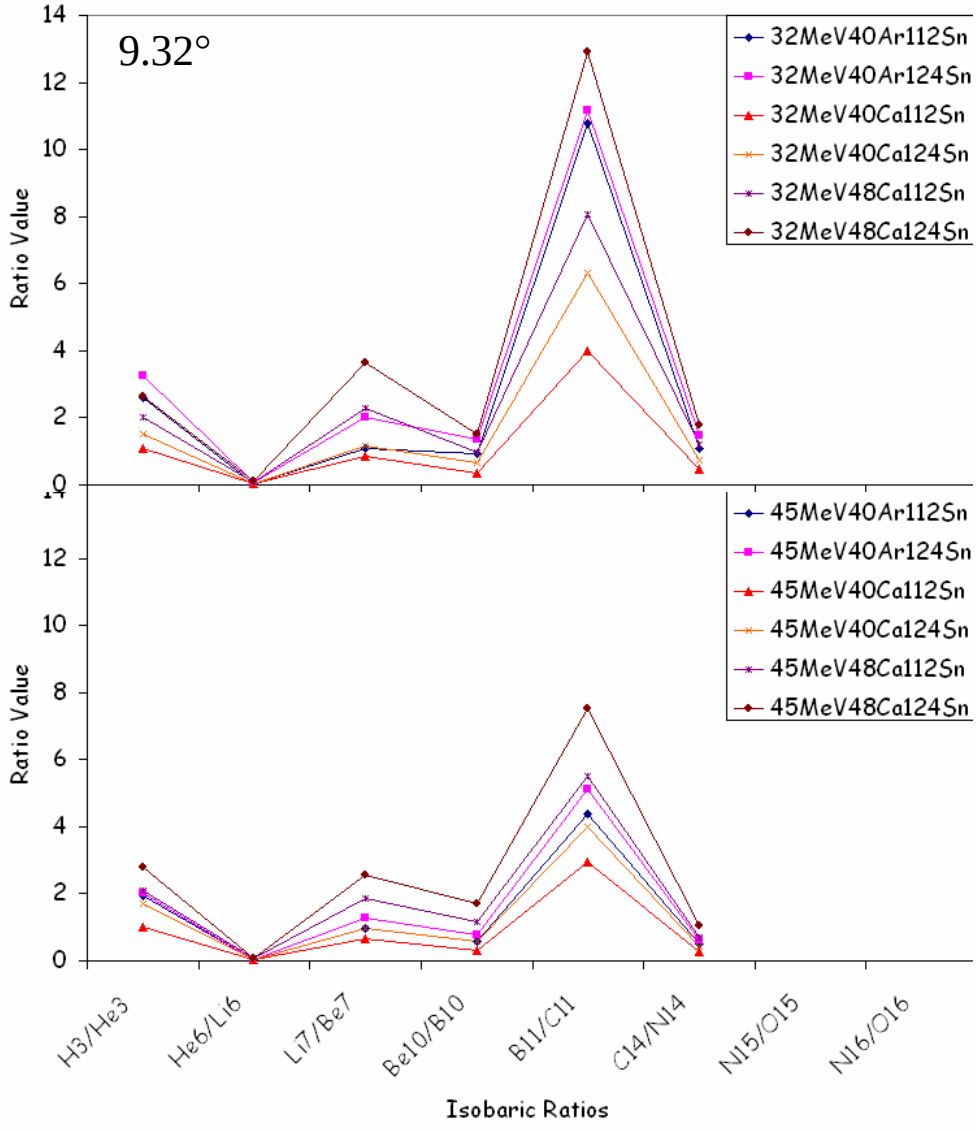


FIG. 171. (Color online) Isobaric yield ratio plot of the 32 MeV systems (top) and 45 MeV systems (bottom) at 9.32 degrees.

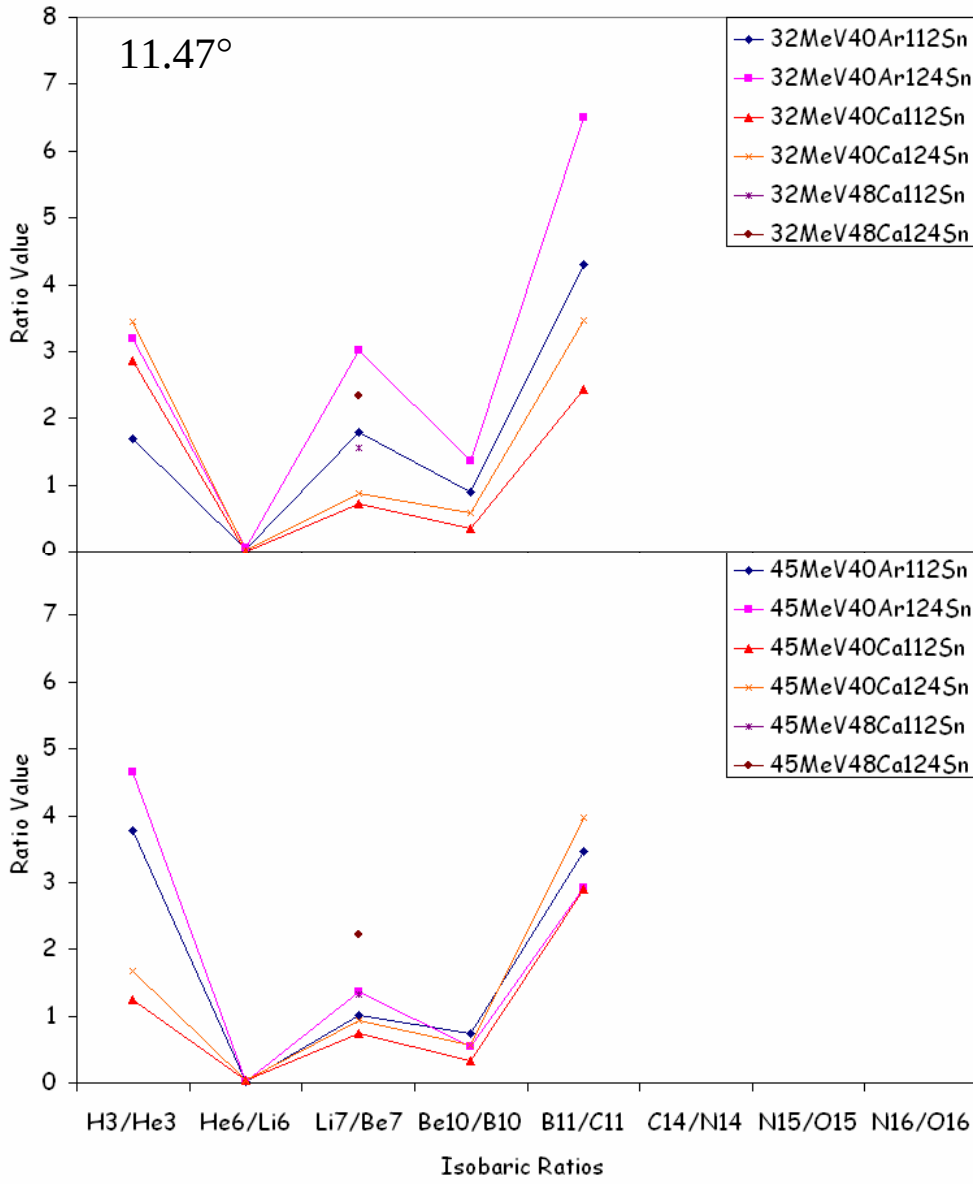


FIG. 172. (Color online) Isobaric yield ratio plot of the 32 MeV systems (top) and 45 MeV systems (bottom) at 11.47 degrees.

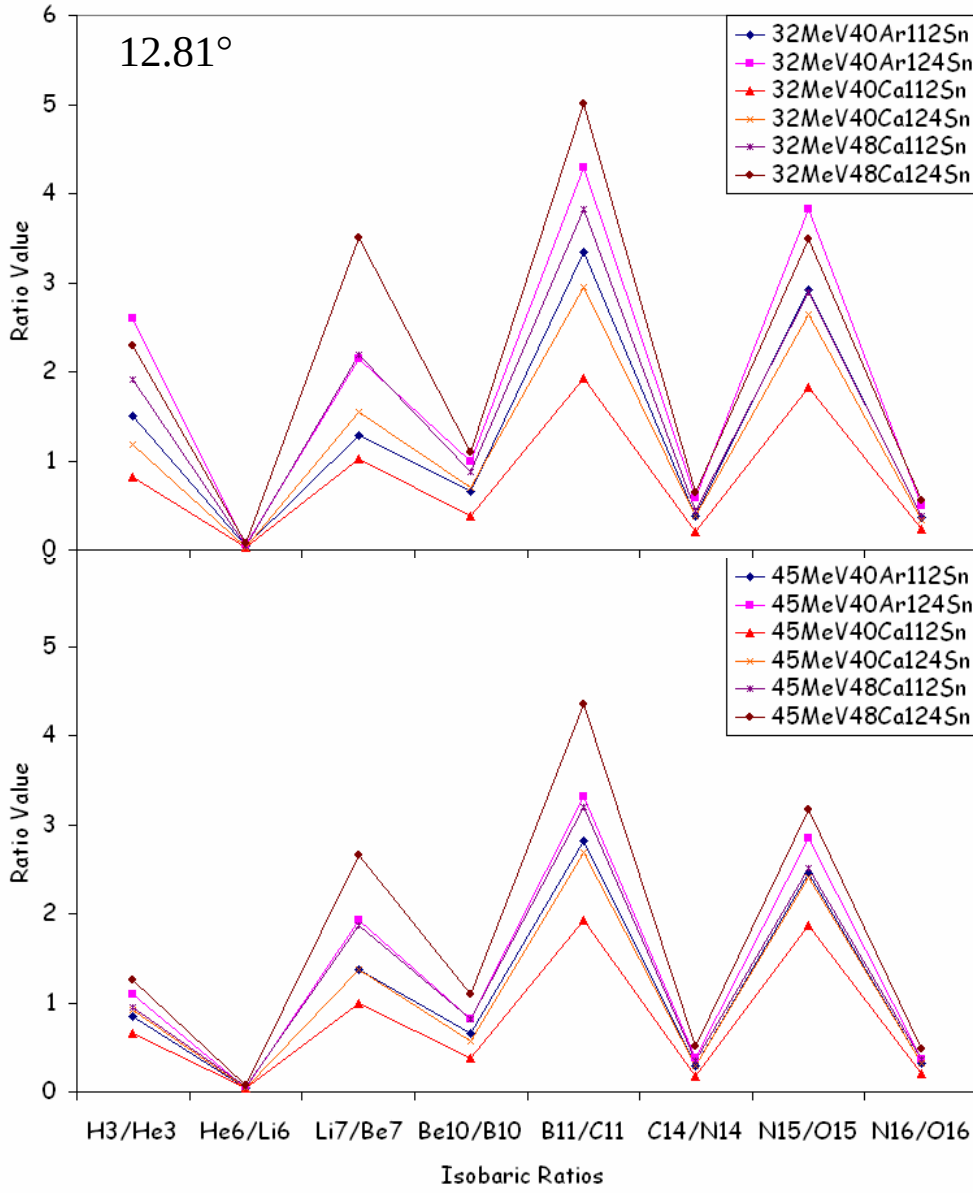


FIG. 173. (Color online) Isobaric yield ratio plot of the 32 MeV systems (top) and 45 MeV systems (bottom) at 12.81 degrees.

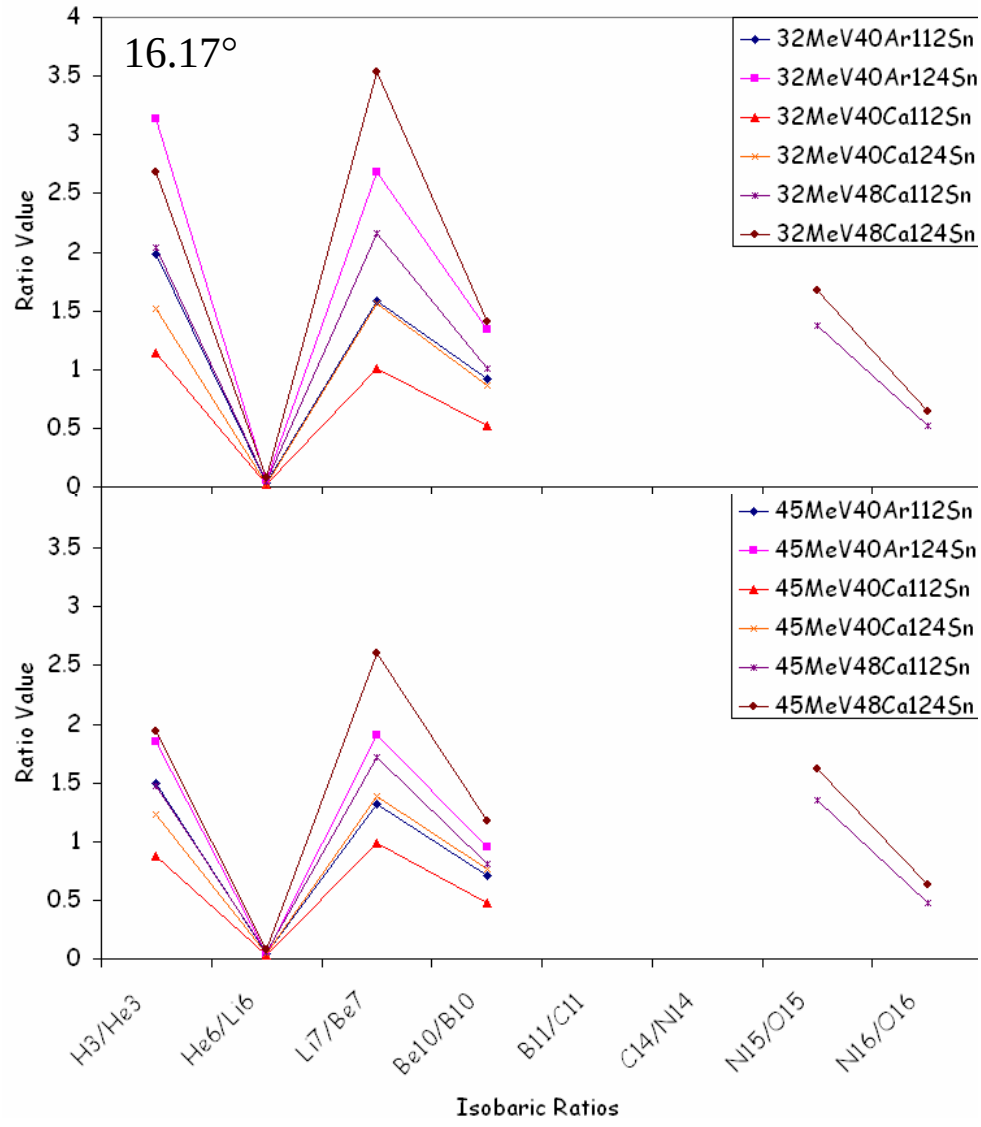


FIG. 174. (Color online) Isobaric yield ratio plot of the 32 MeV systems (top) and 45 MeV systems (bottom) at 16.17 degrees.

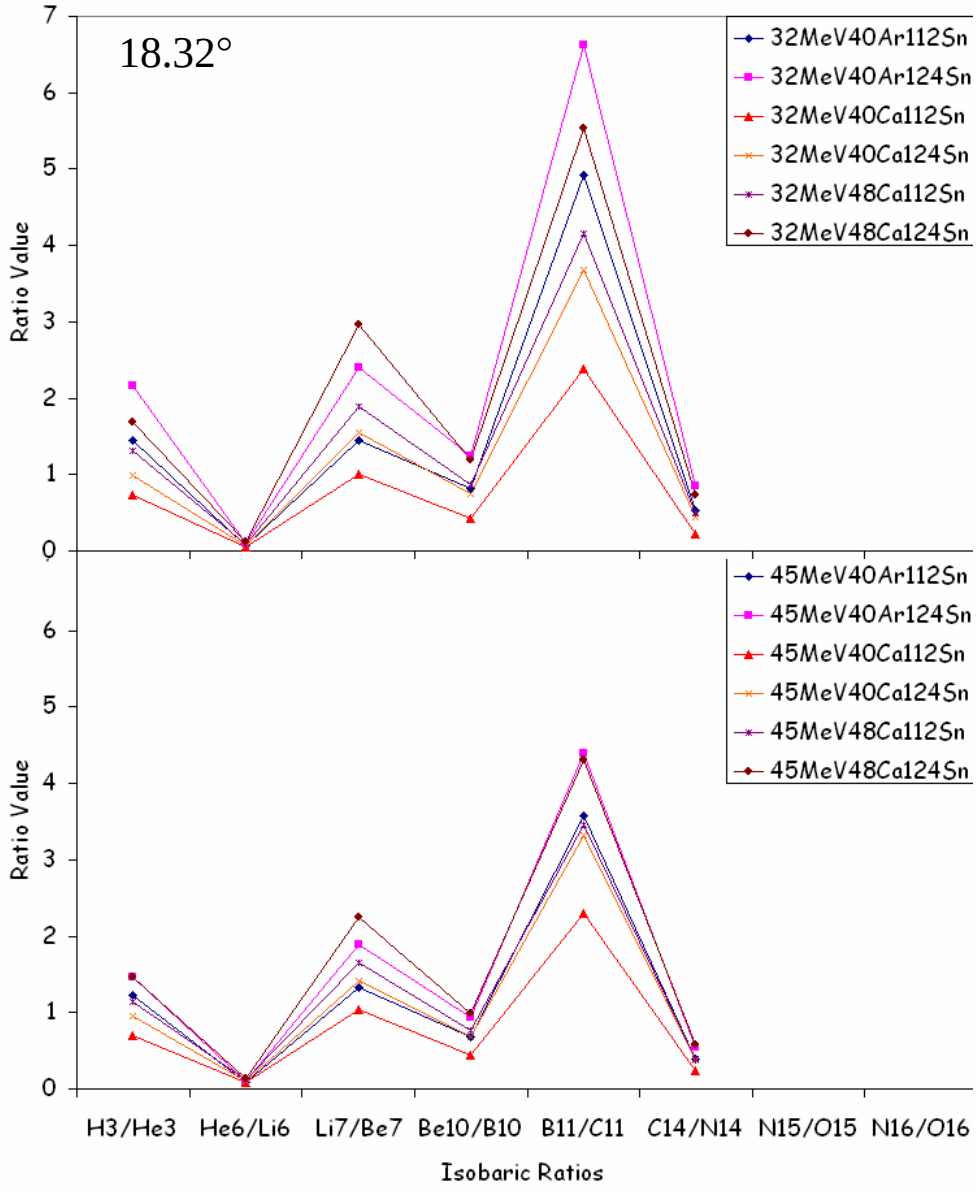


FIG. 175. (Color online) Isobaric yield ratio plot of the 32 MeV systems (top) and 45 MeV systems (bottom) at 18.13 degrees.

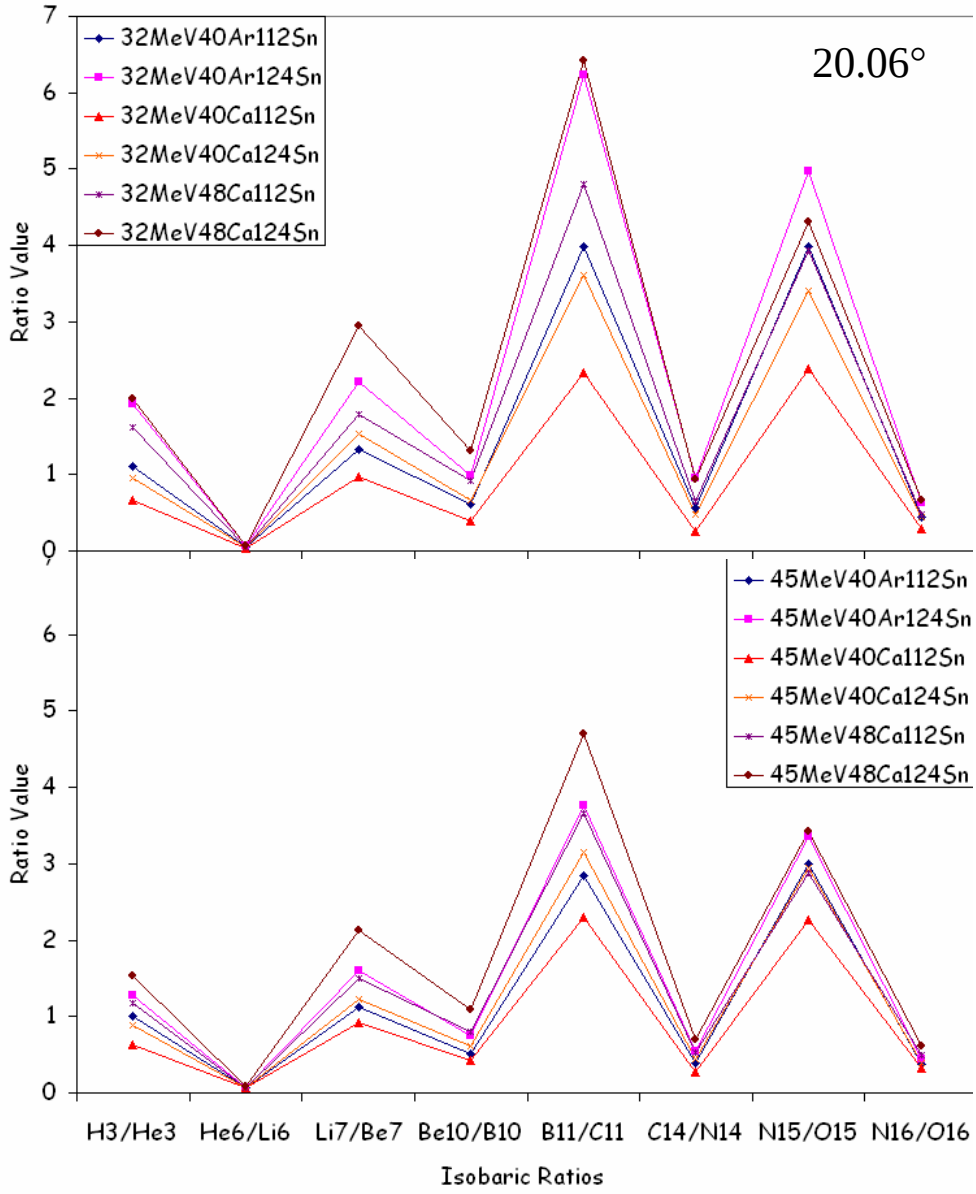


FIG. 176. (Color online) Isobaric yield ratio plot of the 32 MeV systems (top) and 45 MeV systems (bottom) at 20.06 degrees.

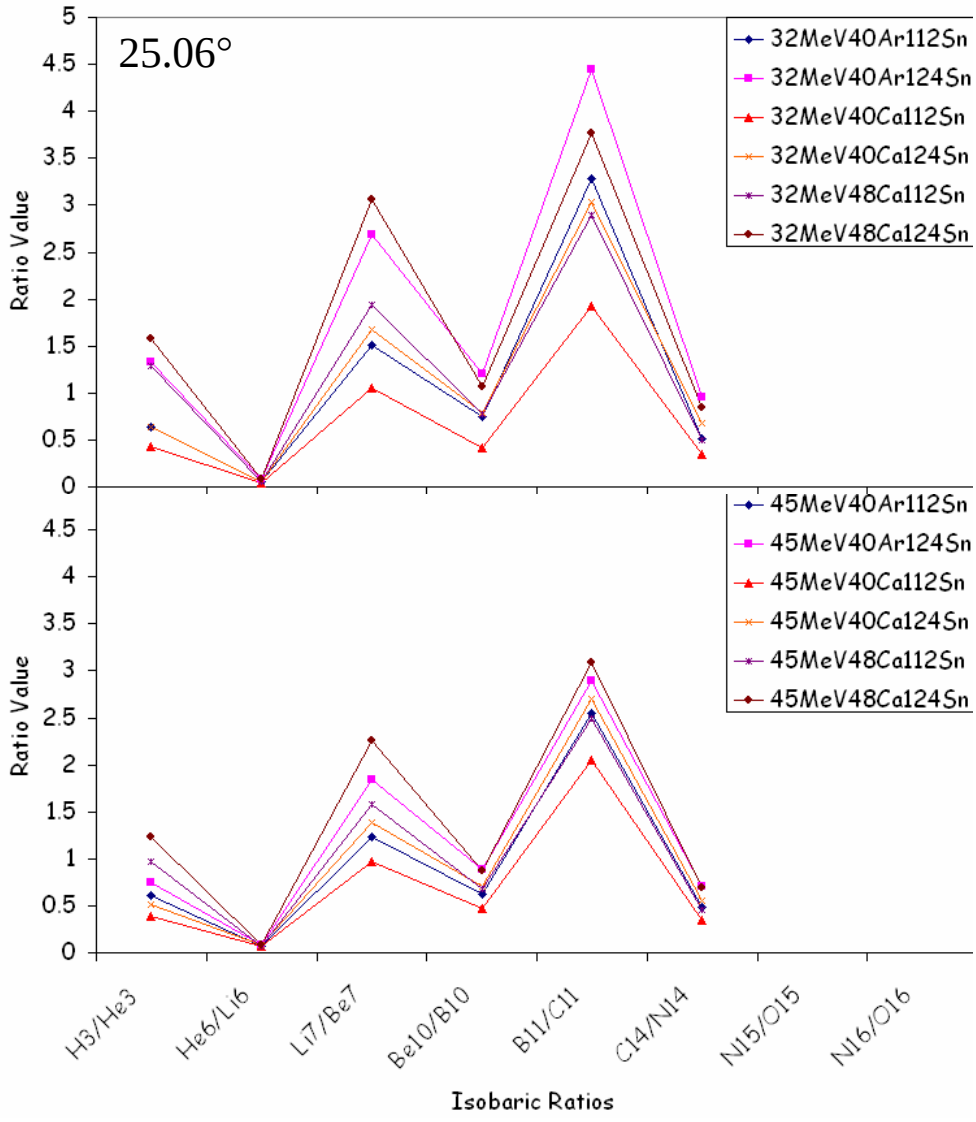


FIG. 177. (Color online) Isobaric yield ratio plot of the 32 MeV systems (top) and 45 MeV systems (bottom) at 25.06 degrees.

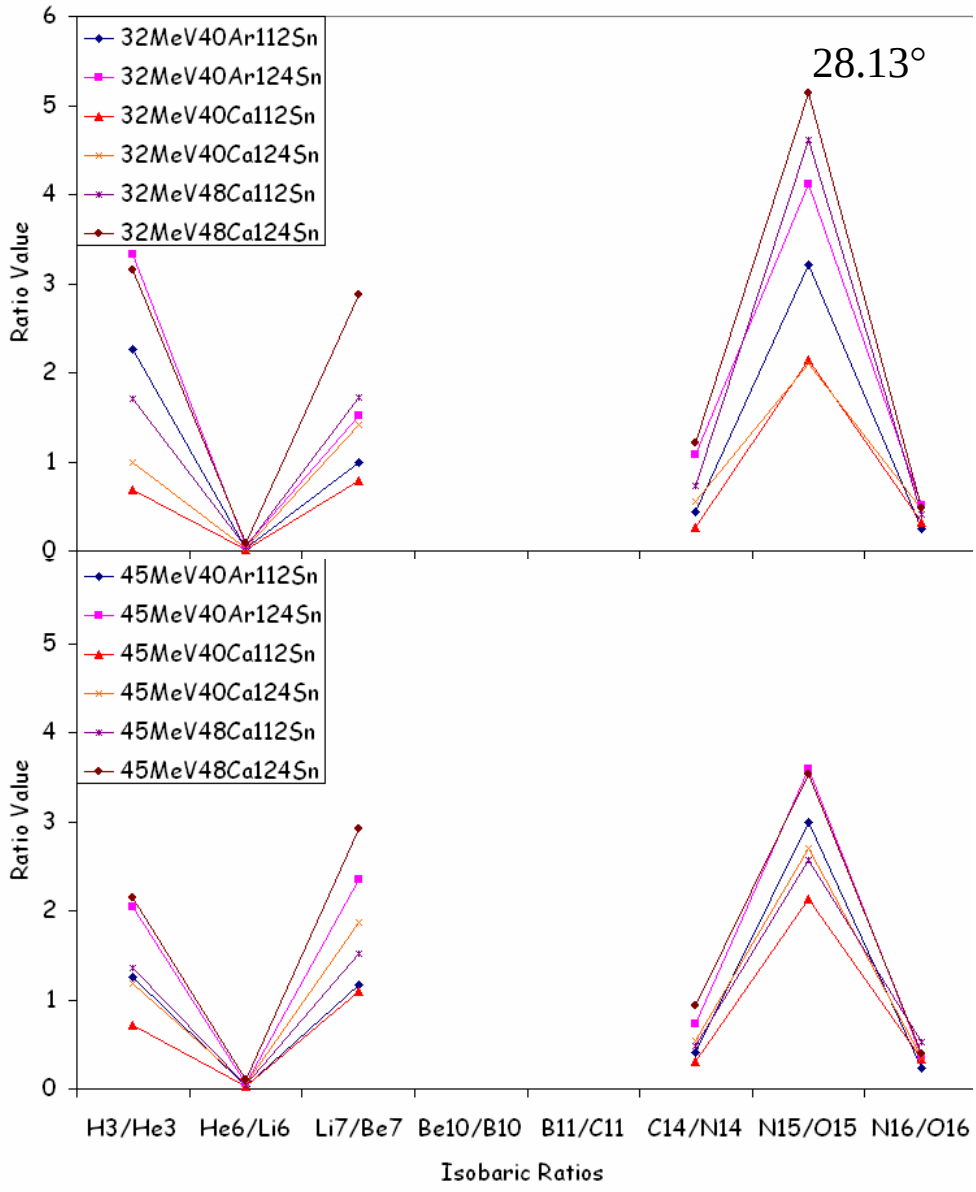


FIG. 178. (Color online) Isobaric yield ratio plot of the 32 MeV systems (top) and 45 MeV systems (bottom) at 28.13 degrees.

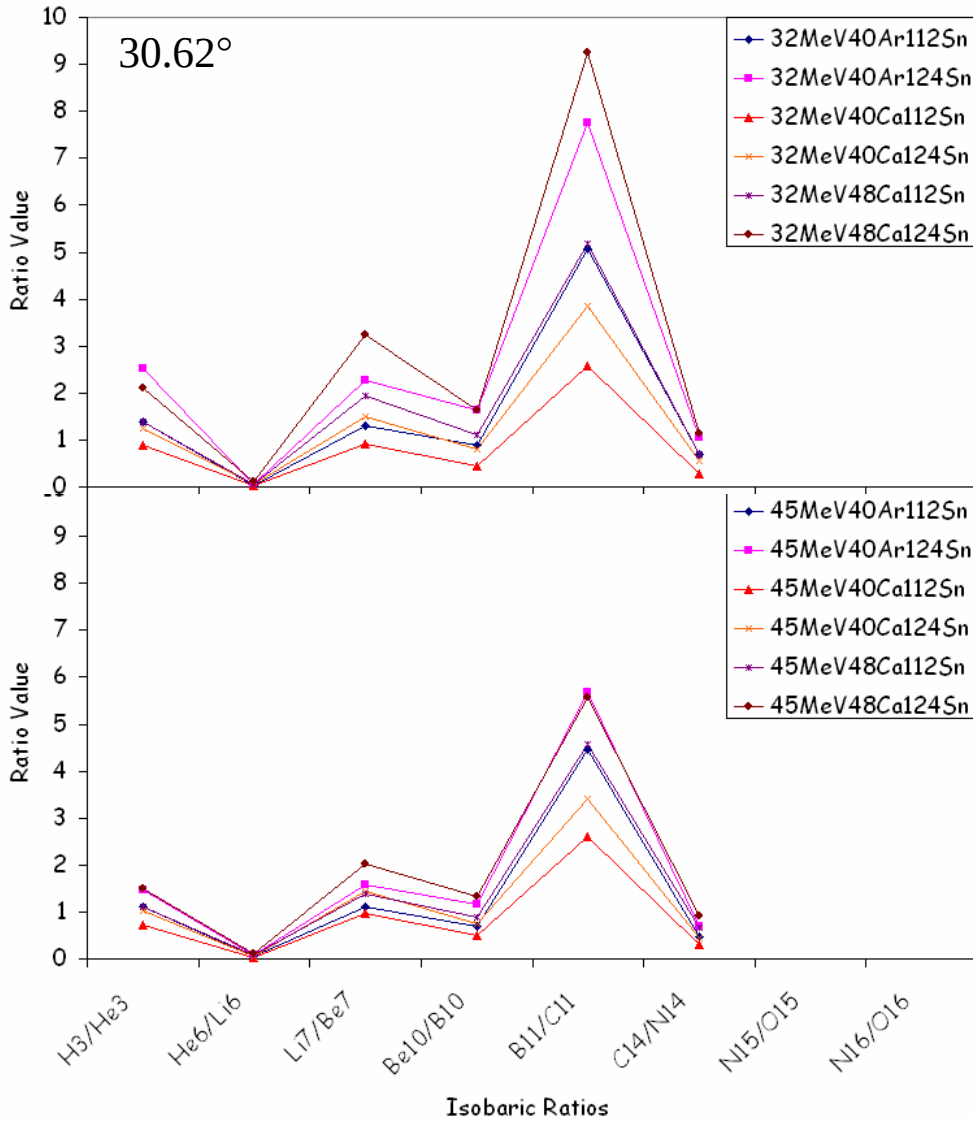


FIG. 179. (Color online) Isobaric yield ratio plot of the 32 MeV systems (top) and 45 MeV systems (bottom) at 30.62 degrees.

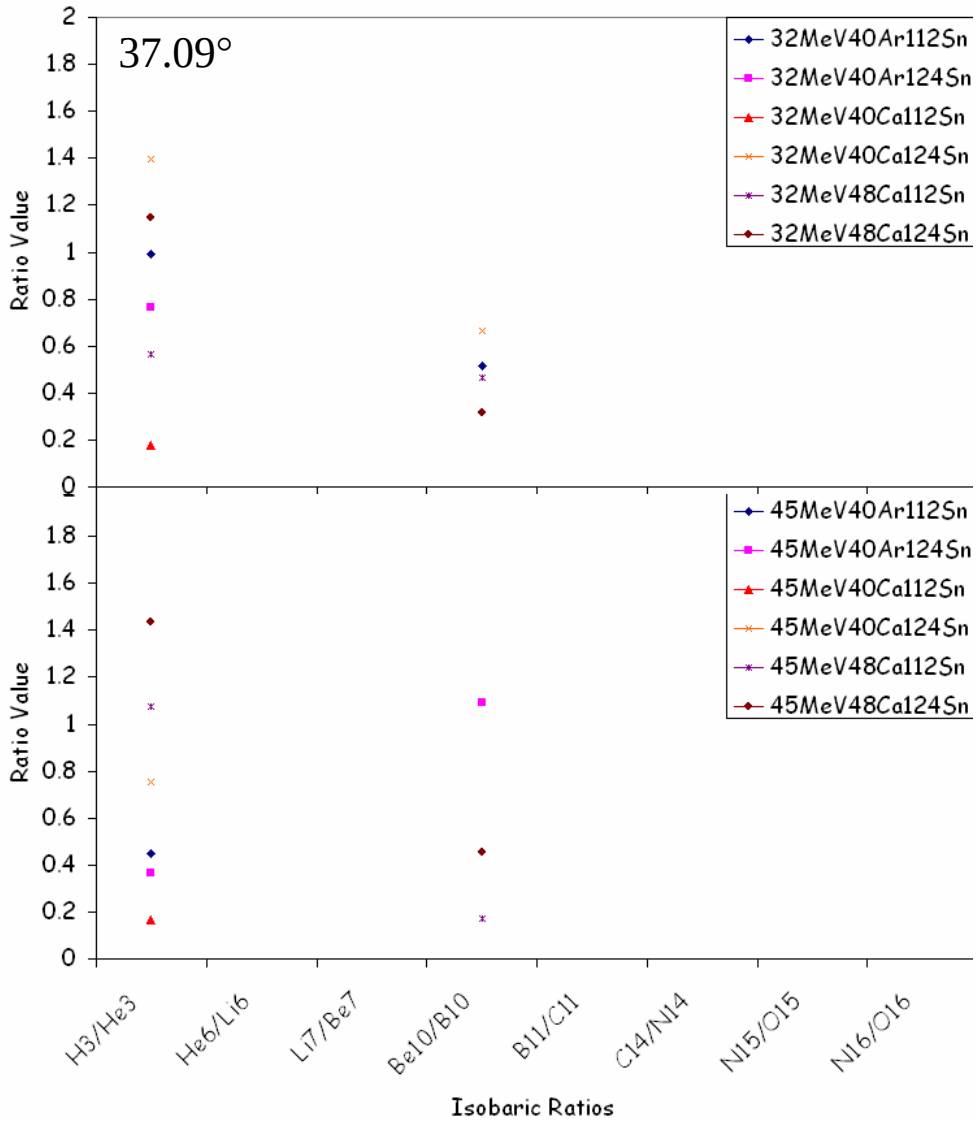


FIG. 180. (Color online) Isobaric yield ratio plot of the 32 MeV systems (top) and 45 MeV systems (bottom) at 37.09 degrees.

# APPENDIX E

## ADDITIONAL MEAN N/Z PLOTS

The figures 181 to 191 show the mean N/Z plots for the other 12 laboratory angles. 3.07 degrees does not have any nuclides that can give mean N/Z. 4.34 degrees only has the mean N/Z for hydrogen. All elements that have a mean N/Z are shown at the other 10 angles and trends are consistent with results from 7.01 degrees as discussed in chapter IV.

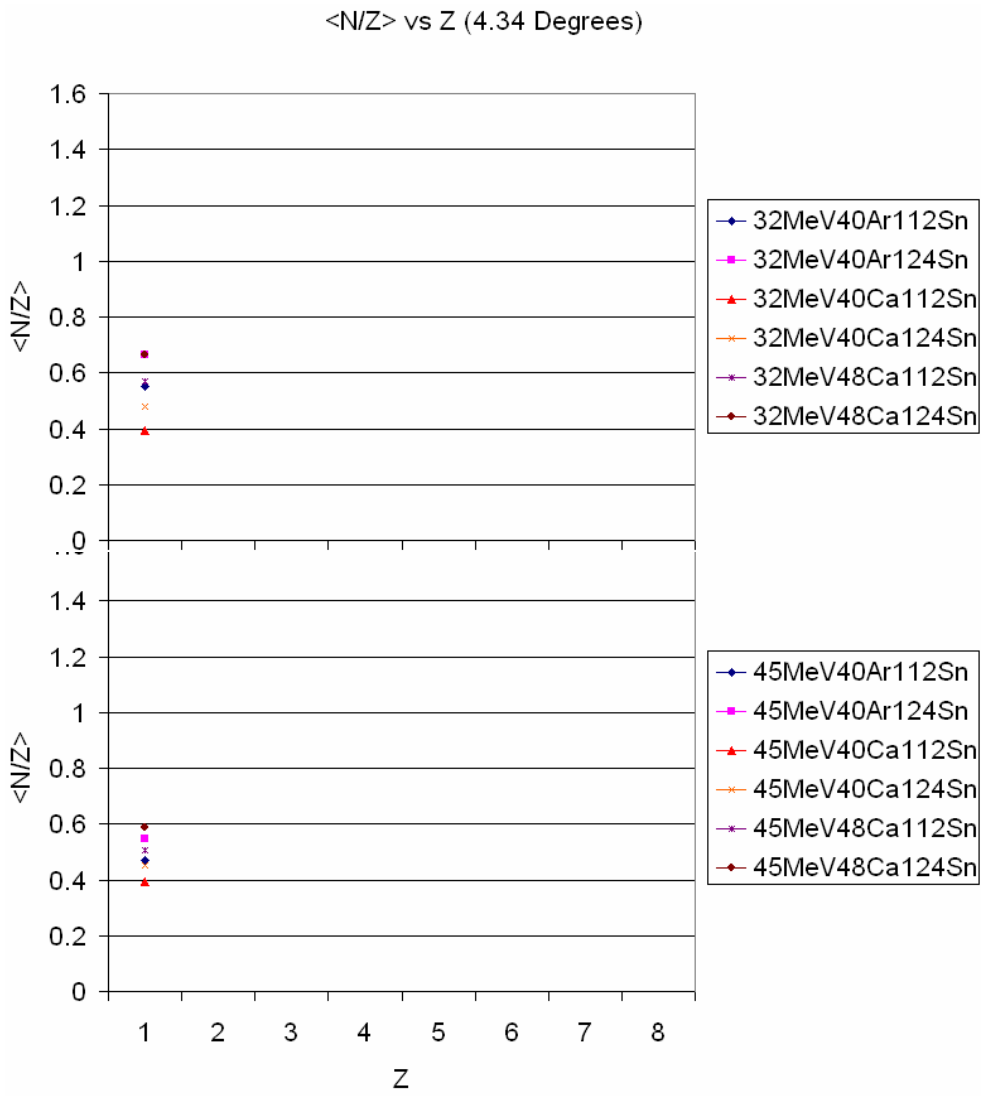


FIG. 181. (Color online) Mean N/Z versus Z plot of the 32 MeV systems (top) and 45 MeV systems (bottom) at 4.34 degrees.

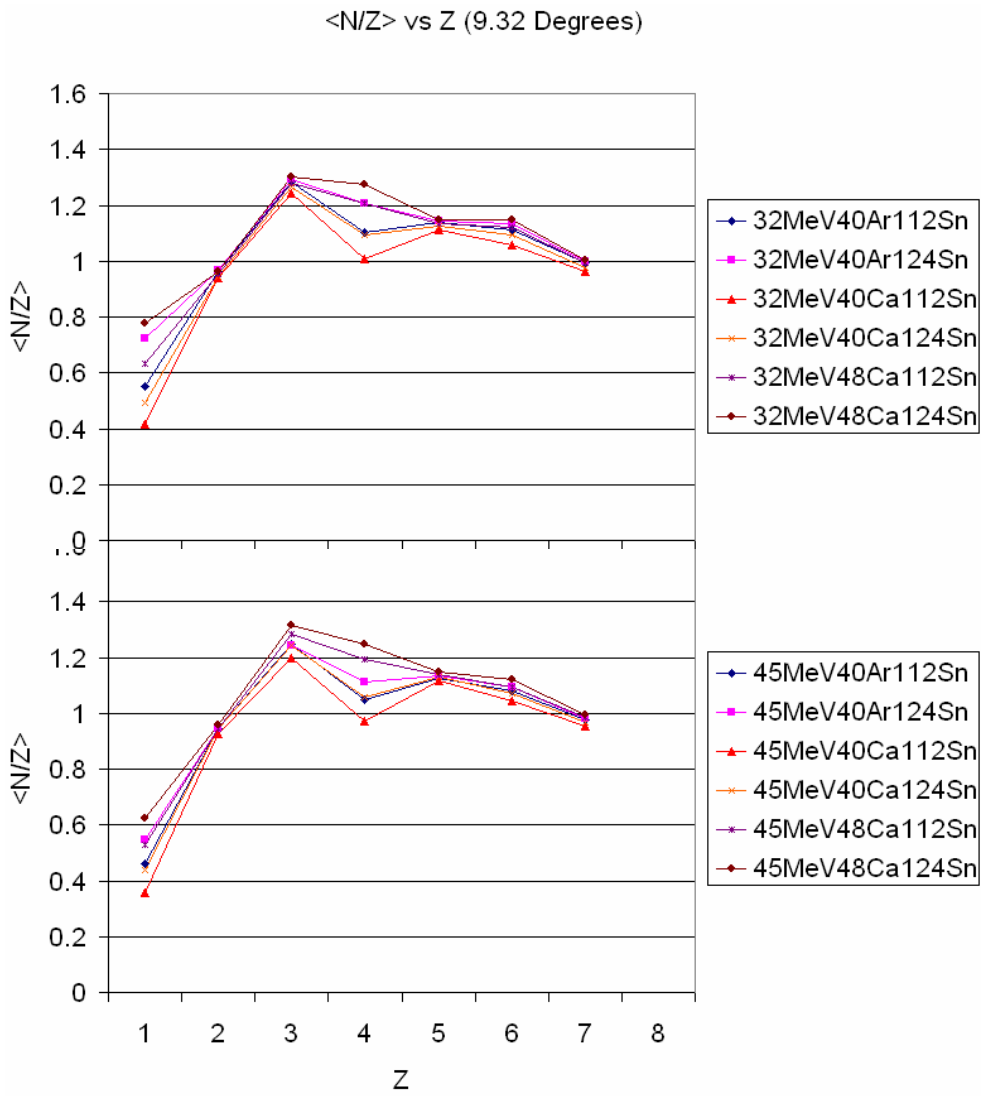


FIG. 182. (Color online) Mean N/Z versus Z plot of the 32 MeV systems (top) and 45 MeV systems (bottom) at 9.32 degrees.

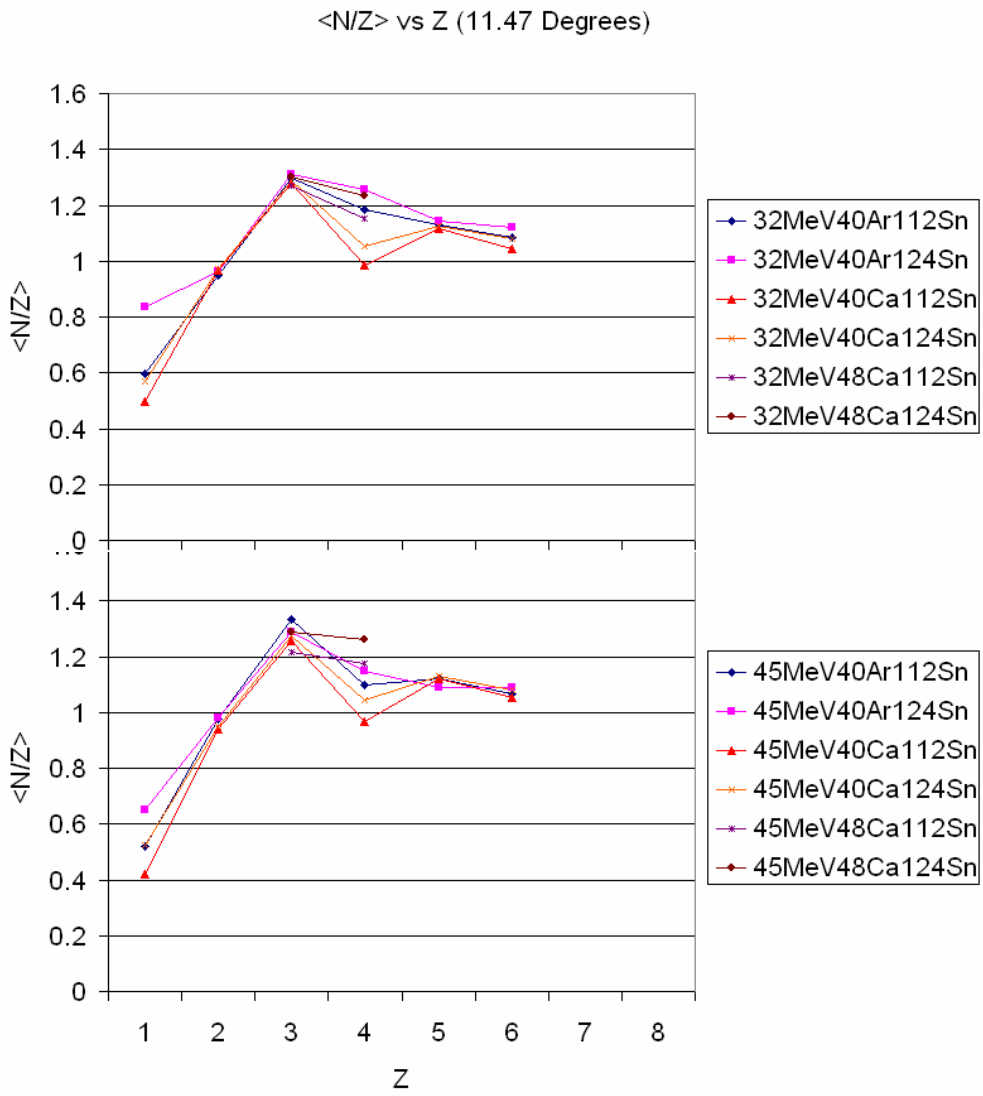


FIG. 183. (Color online) Mean N/Z versus Z plot of the 32 MeV systems (top) and 45 MeV systems (bottom) at 11.47 degrees.

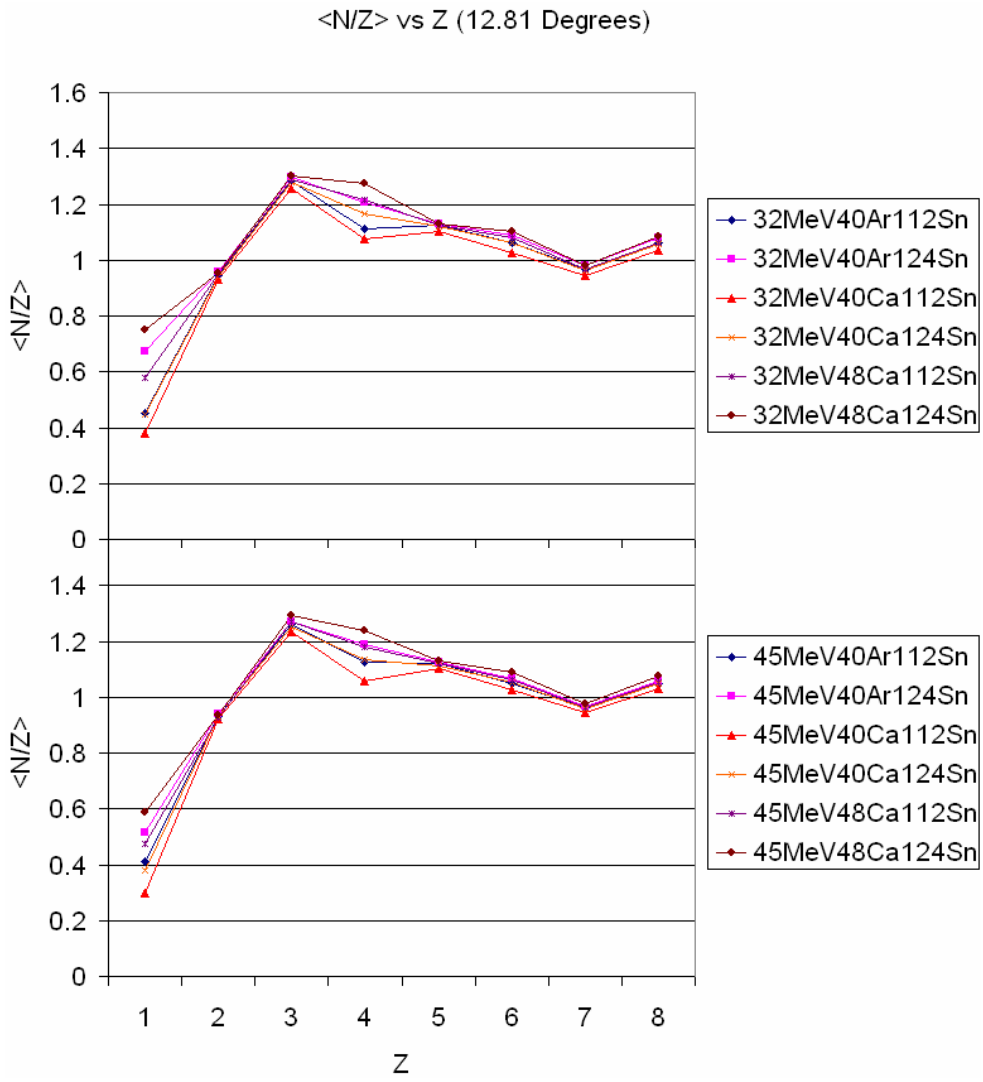


FIG. 184. (Color online) Mean N/Z versus Z plot of the 32 MeV systems (top) and 45 MeV systems (bottom) at 12.81 degrees.

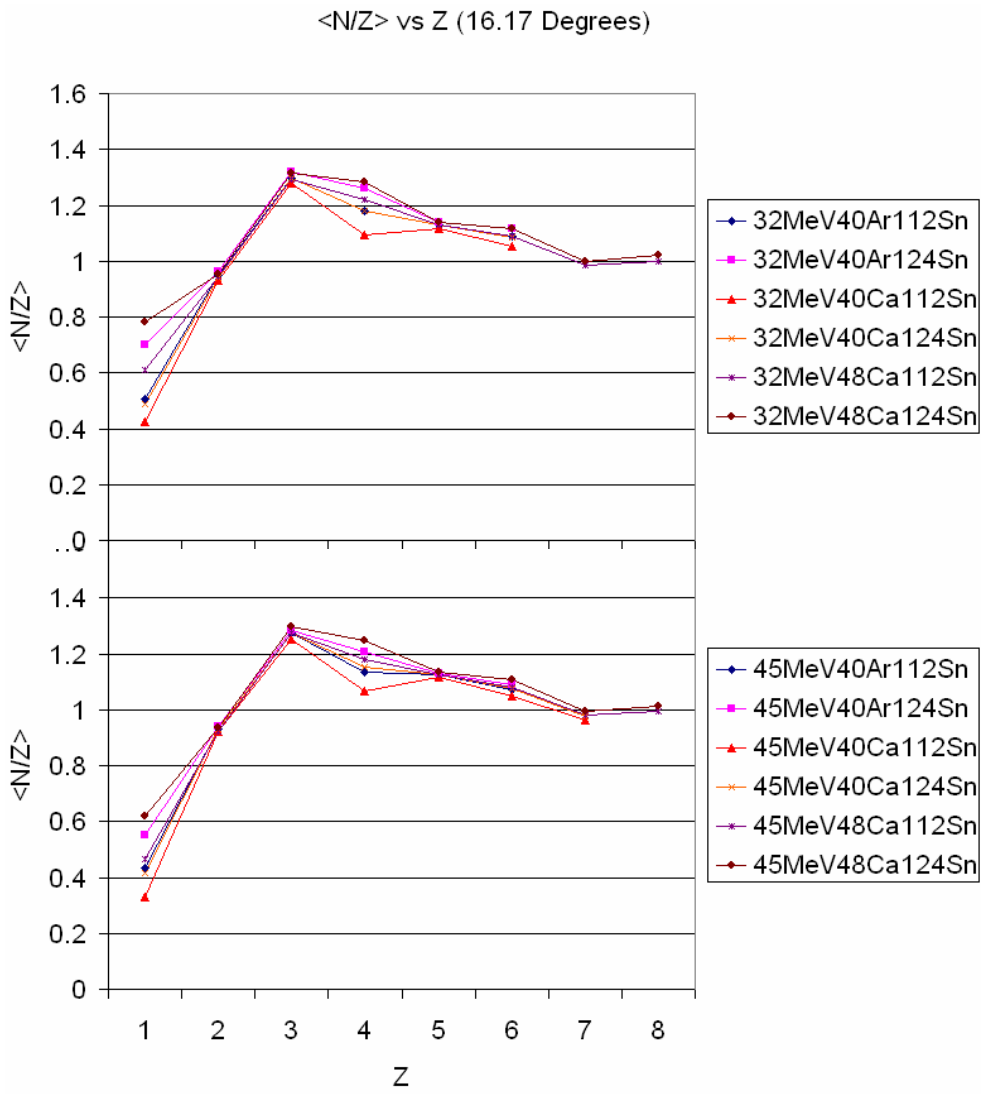


FIG. 185. (Color online) Mean N/Z versus Z plot of the 32 MeV systems (top) and 45 MeV systems (bottom) at 16.17 degrees.

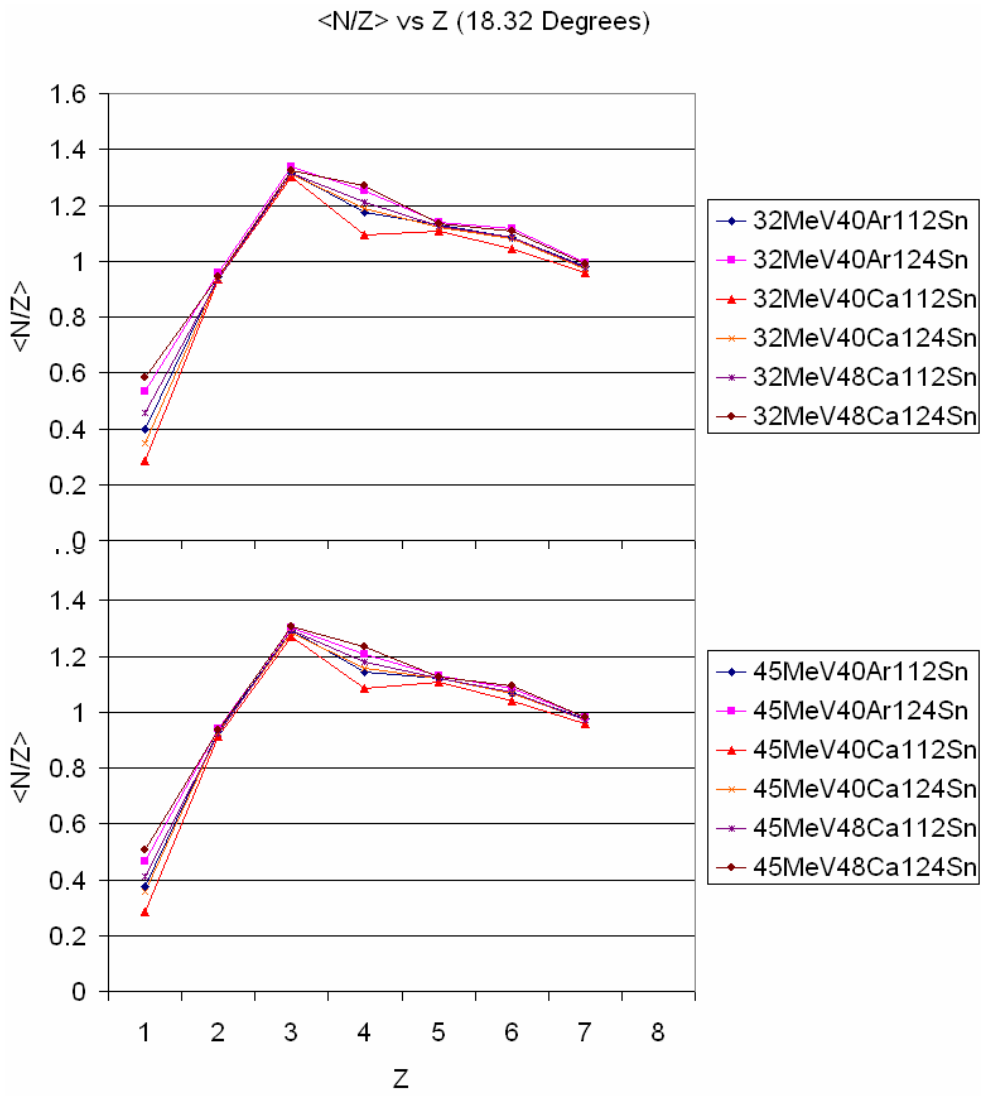


FIG. 186. (Color online) Mean N/Z versus Z plot of the 32 MeV systems (top) and 45 MeV systems (bottom) at 18.32 degrees.

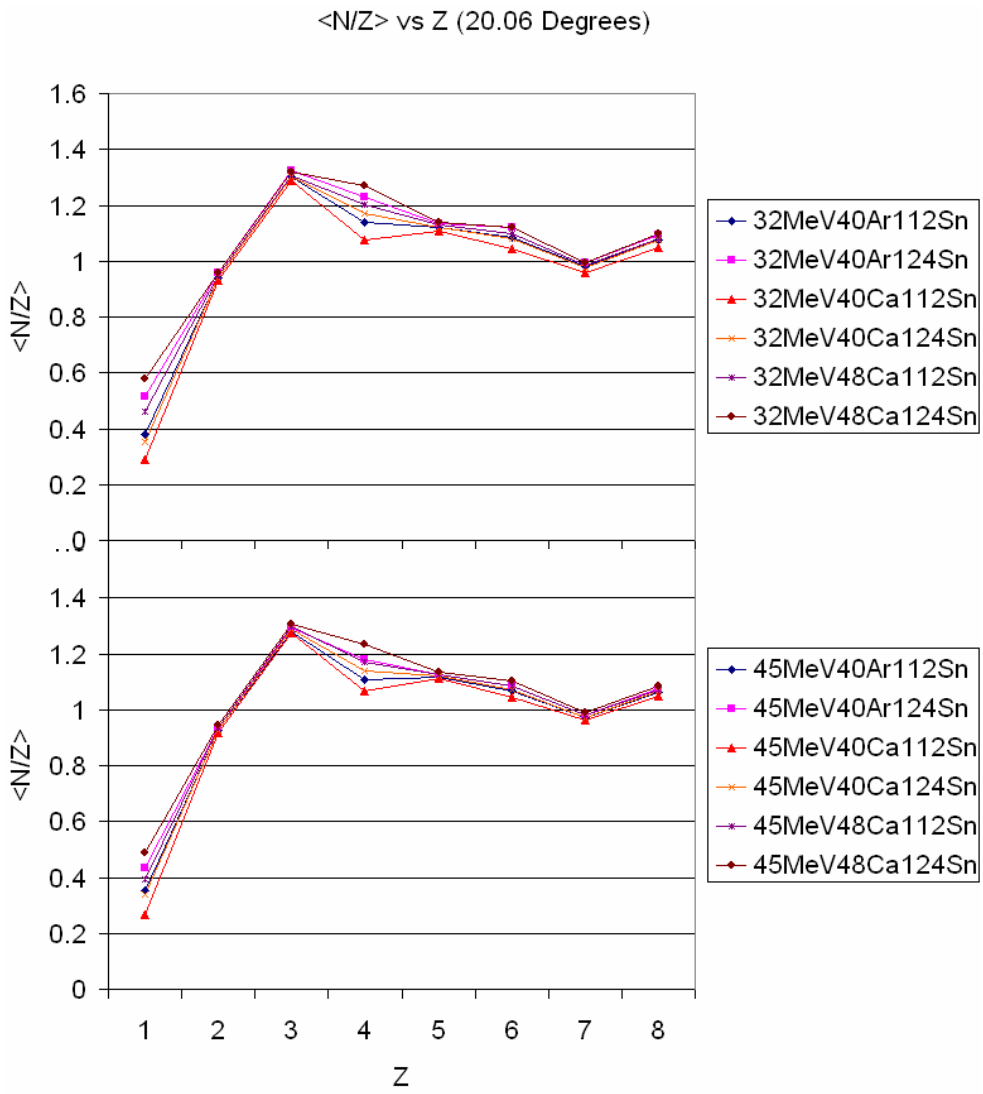


FIG. 187. (Color online) Mean N/Z versus Z plot of the 32 MeV systems (top) and 45 MeV systems (bottom) at 20.06 degrees.

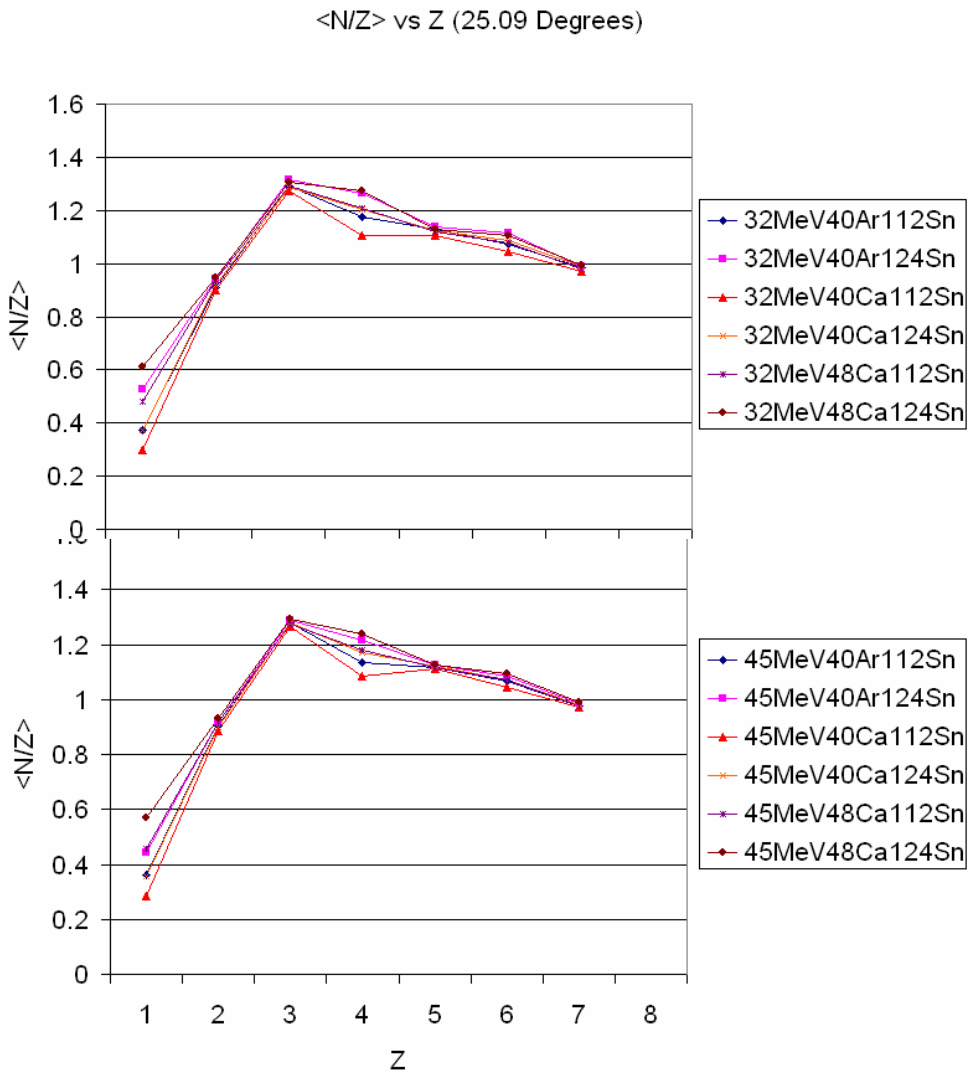


FIG. 188. (Color online) Mean N/Z versus Z plot of the 32 MeV systems (top) and 45 MeV systems (bottom) at 25.09 degrees.

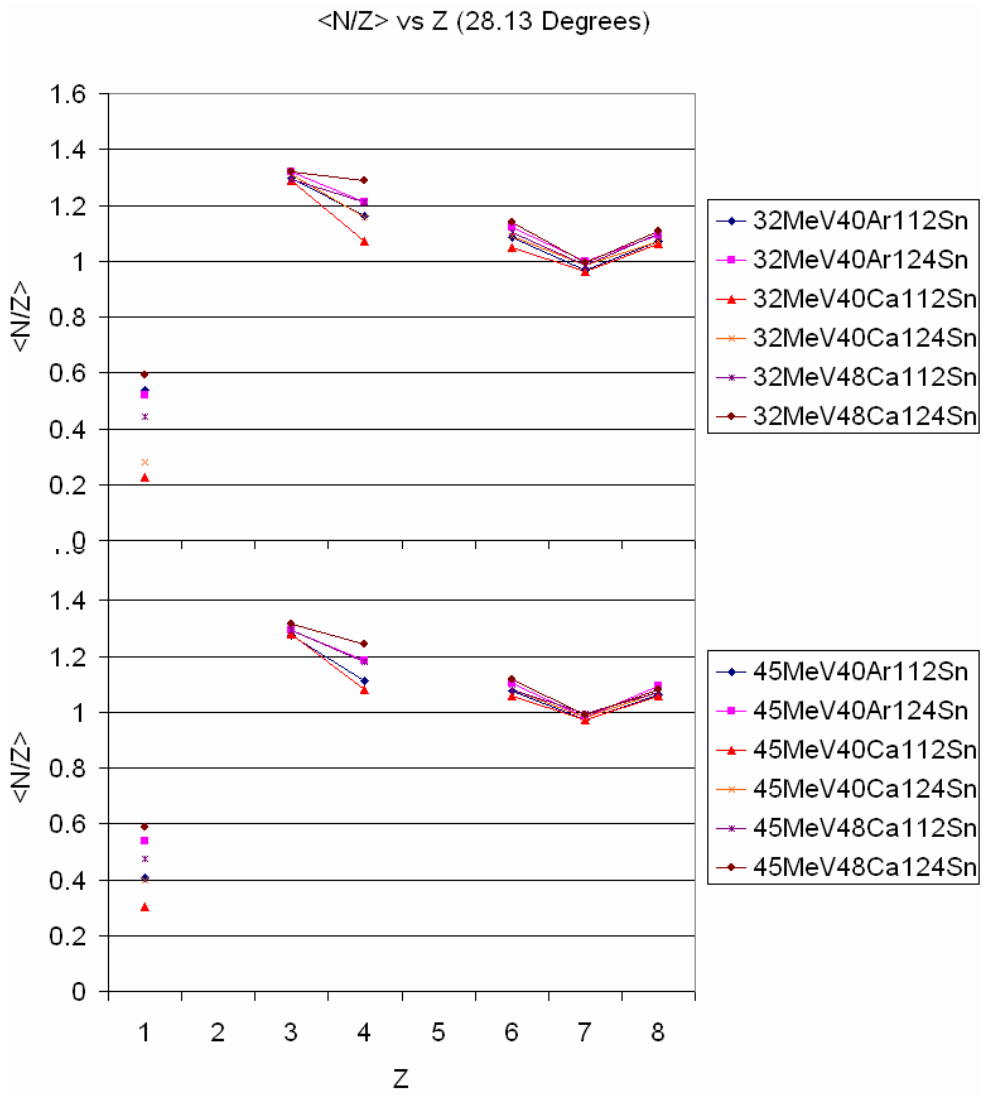


FIG. 189. (Color online) Mean N/Z versus Z plot of the 32 MeV systems (top) and 45 MeV systems (bottom) at 28.13 degrees.

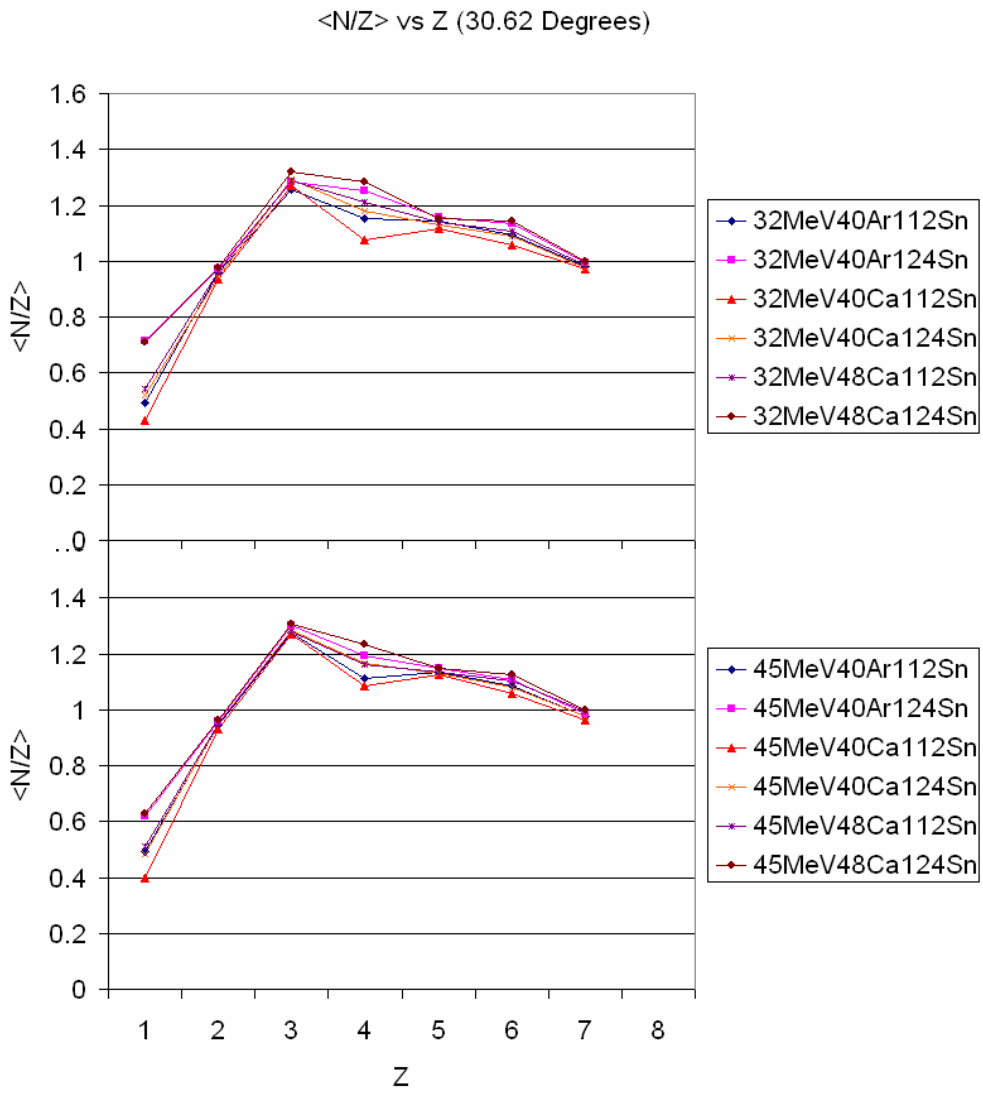


FIG. 190. (Color online) Mean N/Z versus Z plot of the 32 MeV systems (top) and 45 MeV systems (bottom) at 30.62 degrees.

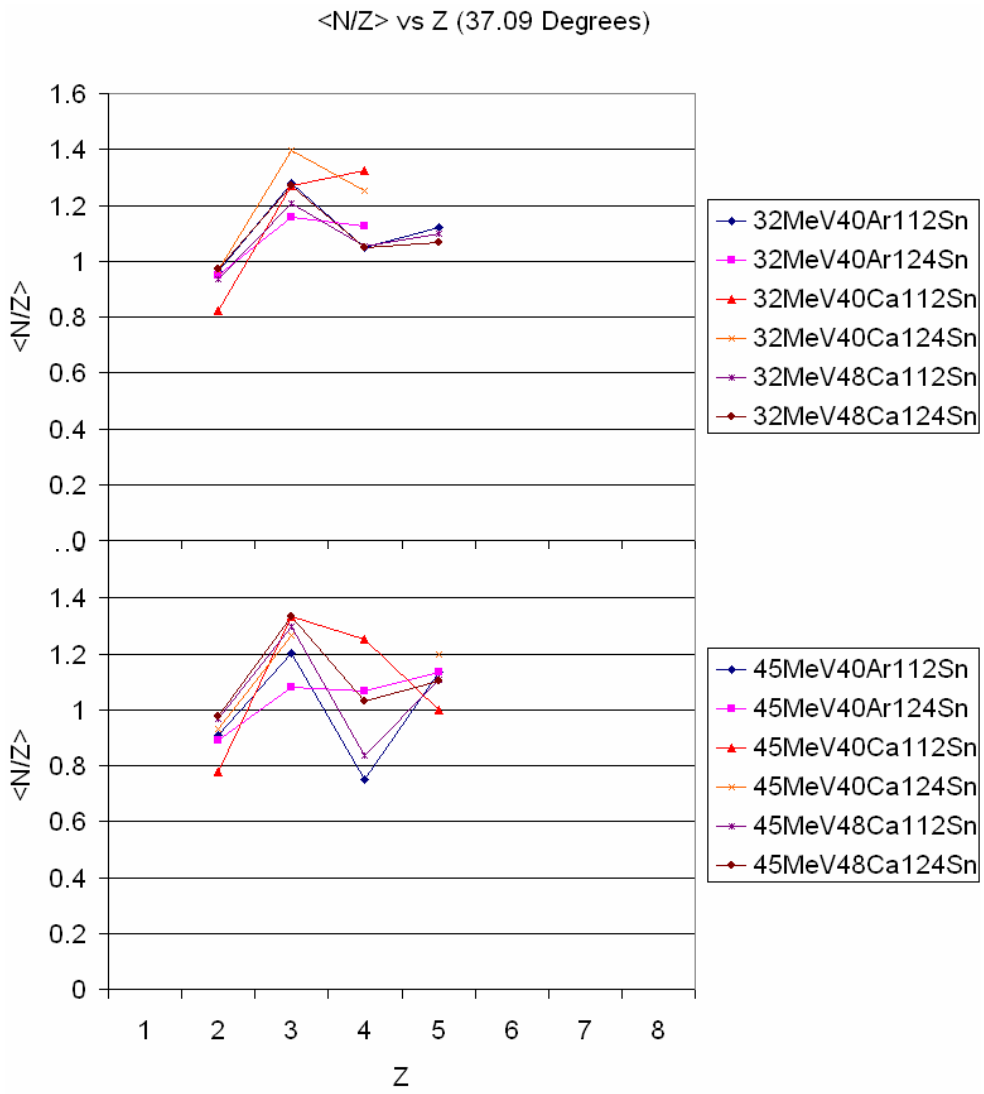


FIG. 191. (Color online) Mean N/Z versus Z plot of the 32 MeV systems (top) and 45 MeV systems (bottom) at 37.09 degrees.

# VITA

**August Lawrence Keksis**

## EDUCATION

Ph.D., Texas A&M University, Nuclear Chemistry, May 2007

B.S., Northern Arizona University, Chemistry (Certified by the American Chemical Society) and Biology, May 2000

Minor, Northern Arizona University, Physics, May 2000

## EXPERIENCE

Graduate Assistant Research, Texas A&M University (2001-2007)

Graduate Assistant Teaching, Texas A&M University (2000-2003)

## SELECTED AWARDS, SCHOLARSHIPS, AND ASSISTANTSHIPS

Robert A. Welch Foundation Pre-Doctoral Graduate Fellowship, Texas A&M University funds Graduate Assistant Research (2001-2007)

Teaching Assistantship, Texas A&M University (2000-2003)

## SELECTED AFFILIATIONS

American Physical Society (Since 2004)

American Chemical Society (Since 2000)

## SELECTED PUBLICATIONS

Heavy-residue isoscaling as a probe of the symmetry energy of hot fragments. G.A. Souliotis, D.V. Shetty, A. Keksis, E. Bell, M. Jandel, M. Veselsky, and S.J. Yennello. Physical Review C **73**, 024606 (2006)

## CONTACT INFORMATION

August Keksis can be reached through Sherry Yennello at the Cyclotron Institute, Texas A&M University, College Station, Texas, 77843-3366